From X-ray tomography to the first X-ray plenoptic camera for nanoparticles bio-localization

Elena Longo

université PARIS-SACLAY

NNT : 2018SACLX104

Thèse de doctorat

From X-ray tomography to the first X-ray plenoptic camera for nanoparticles bio-localization

Thèse de doctorat de l'Université Paris-Saclay
préparée à l'École Polytechnique

École doctorale n°572 Ondes et Matière (EDOM)
Spécialité de doctorat: Optique et Photonique

Thèse présentée et soutenue à Palaiseau, le 20/12/2018, par

Elena Longo

Composition du Jury :

Sophie Kazamias Professor, Université Paris-Sud , France (UMR CNRS PXI)	Président
Alexandra Fragola Professor, Université Pierre et Marie Curie Paris VI (UMR 8213)	Rapporteur
Jean-Claude Kieffer Professor, Centre Énergie Matériaux Télécommunication	Rapporteur
Philippe Zeitoun PhD, Laboratoire d'Optique Appliquée (UMR 7639)	Directeur de thèse
Ombeline De La Rochefoucauld PhD, Imagine Optic	Co-Directeur de thèse
Lucie Sancey PhD, Institute for Advanced Biosciences (U1209 UMR 5309)	Invitée

Acknowledgements

I would like to express my most sincere gratitude to all those who supported and helped me during my PhD.
I will start by thanking my supervisors Dr. Ombeline De La Rochefoucauld and Dr. Philippe Zeitoun. Thanks for having believed in my potential. It was a pleasure and honour working with you. I could not have better advisors. I hope we will continue to share ideas in future. I would like to thank my colleagues and friends: Daniel Adjei, Domenico Alj, Carla Alves, Yasmina Azamoum, Olivier Delmas, Isabel Gonzalez, and Francesco Massimo. I am grateful to have you fraternally by my side. I take the opportunity for thanking also Thuy Le, Ying Li, the former PhD students Jayanath Koliyadu and Hugo Dacasa Pereira and, the visitors Manuel Cotelo and Charlotte Herzog. I extend my acknowledgements to all people working at LOA (researchers, students, secretaries, engineers and technicians) for making me feel at home.
I wish to thank also Dr. Lucie Sancey, always present to support my thesis work, and Dr. Alessia Cedola and her team in Rome for making me passionate at X-ray tomography. Thanks to Prof. Alberto Bravin for guiding me in several experiments at ESRF. Thanks to Dr. Benoit Larrat and Dr. Christel Marquette for having me included in their projects.
Thanks to all people from Imagine Optic. My PhD roots grow there. Thanks again for your warm welcoming. Thanks to Dr. Hamed Merdji for motivating me to start this career and thanks to all VOXEL members and to my dear friends from MEASE.
Finally, I conclude with a special thought to my mum, my sister and my boyfriend that strongly encouraged me to never give up!

Résumé

Ce travail de thèse décrit deux techniques d'imagerie 3D dans le domaine des rayons X pour localiser, de manière non invasive et à faible dose, des nanoparticules théranostiques dans les tissus biologiques et dans les cellules.
Les nanoparticules théranostiques ouvrent de nouvelles frontières dans la recherche oncologique. Le mot "théranostique" provient de la fusion de deux termes: "thérapeutique" et "diagnostique" et souligne le fait que ce type de nanoagents exerce une double activité. D'une part, grâce à leurs propriétés diagnostiques, ils aident à visualiser la tumeur lorsqu'ils sont combinés à plusieurs techniques d'imagerie (telles que l'imagerie par résonance magnétique - IRM, la tomographie par émission de positrons - PET, la tomographie, l'imagerie optique). D'autre part, ils renforcent l'effet létal des rayons X sur les cellules cancéreuses lors de traitements par irradiation.
Dans ce cadre, la pénétration et la localisation de nanoparticules au sein des organismes doivent être surveillés pour établir des évaluations et des protocoles cliniques et précliniques. La question de la distribution des nanoparticules joue un rôle fondamental pour limiter tout effet toxique et pour prédire leur capacité de radiosensibilisation tumorale. À l'échelle nanométrique, les techniques de microscopie permettent d'observer l'internalisation de nanoparticules dans les cellules; tandis qu'à grande échelle MRI et PET réussissent seulement à montrer globalement que les nanoparticules ont atteint leur objectif, étant limité par une faible résolution spatiale. Jusqu'à présent, la seule technique capable de donner une certitude sur la présence de nanoparticules localisées dans les tissus (et donc sur une échelle intermédiaire) est le LIBS, la spectroscopie de plasma produit par laser. Bien qu'elle ait une résolution spatiale de quelques micromètres, elle a le désavantage d'être une méthode invasive.
Le manque de méthodes d'imagerie 3D non invasives à moyenne échelle a motivé ce travail de thèse. Ici, l'utilisation de la tomographie X par contraste de phase est proposée comme outil d'imagerie complémentaire aux techniques bien consolidées mentionnées ci-dessus. Elle permet d'observer les structures internes d'un échantillon sans le perturber et d'obtenir des reconstructions 3D à partir d'une série d'images 2D acquises sous différents angles. De plus, le contraste de phase permet de récupérer des détails anatomiques importants qui, autrement, ne pourraient pas être observés avec une tomographie standard, car les matériaux biologiques ont de faibles variations de coefficients d'absorption.
Cependant, la tomographie implique la l'absorption d'une dose considérable de rayonnement potentiellement nocif pour les échantillons biologiques. Obtenir un bon compromis entre la qualité de l'image et la dose absorbée par les rayons X est un sujet très important aujourd'hui. Cette thèse fait partie d'un projet européen FET, appelé VOXEL (Volumetric X-ray Extremely Low dose), qui, selon nous, apportera une perspective de changement en entraînant une réduction drastique de la dose absorbée par les rayons X, par rapport aux méthodes classiques de radiographie par rayons X. VOXEL se divise en deux branches: l'une visant à réaliser un prototype compact de microscope plénoptique à rayons X mous pour l'imagerie cellulaire dans la "fenêtre d'eau" et l'autre, une caméra plénoptique à rayons X dur pour l'imagerie des petits animaux. Une caméra plénoptique capture les composants spatiaux et angulaires de la lumière et est capable de réaliser des images 3D après une seule

exposition. Au cours de ma thèse, j'ai travaillé spécifiquement sur le développement d'un microscope plénoptique à rayons X mous au Laboratoire d'Optique Appliquée.

Le premier chapitre présente les concepts généraux de la tomographie à rayons X et de l'imagerie par contraste de phase. La méthodologie utilisée pour la reconstruction et l'analyse des images et la suppression des artifices est décrite.

Dans le deuxième chapitre, la tomographie X par contraste de phase est présentée comme une méthode valable pour localiser différents types de nanoparticules théranostiques (nanoparticules de gadolinium, d'or et de platine) dans des organes de souris. Les images ont été acquises à ESRF (European Synchrotron Radiation Facility) en collaboration avec CNR-Nanotec (Rome, Italie) et l'Institute for Advanced Biosciences (IAB-Grenoble, France). Des résultats nouveaux et inattendus ont été obtenus concernant la répartition des nanoparticules dans les métastases cérébrales causée par le mélanome. Les résultats obtenus révèlent également la capacité de la technique à visualiser les pigments de mélanine dans le mélanome.

Le troisième chapitre présente les résultats de la détection de plaques amyloïdes dans la maladie d'Alzheimer's après l'administration de nanoparticules chargées de gadolinium. Le but de l'expérience était de comprendre le mécanisme de diffusion et de distribution des nanoparticules, une fois que la barrière hémato-encéphalique ouverte par des ultrasons focalisés. Ce travail a été réalisé en collaboration avec l'ESRF, CNR-Nanotec, IAB and NeuroSpin Lab (CEA, Saclay et Grenoble).

Le chapitre quatre explique en détails la théorie et le fonctionnement de la caméra plénoptique visible dont s'inspire le projet VOXEL. Le traitement des données pour obtenir la refocalisation des images et pour visualiser les différents points de vue de la scène acquise est expliqué.

Dans le cinquième chapitre, le premier prototype de microscope plénoptique à rayons X mous a été décrit. C'est un microscope compact fonctionnant dans la "fenêtre d'eau" avec la nouveauté de l'adjonction d'une matrice des lentilles de Fresnel placée devant le détecteur. L'une des applications futures possibles de la caméra plénoptique à rayons X mous serait l'imagerie de nanoparticules dans des cellules avec une résolution spatiale de 100 nm.

Contents

List of Figures

Introduction

In recent years, the use of nanoparticles has attracted attention in various fields like paints, cosmetics or pharmaceutics. In particular, the development of metal-based theranostic nanoparticles is nowadays a new frontier of oncological research [8]. The word "Theranostics" derives from the fusion of two terms: "therapeutic" and "diagnostics" and it stresses the fact that this kind of nanoagents exert a double activity. On one hand thanks to their diagnostic properties, they help visualizing the tumor when combined with several imaging techniques (such as Magnetic Resonance Imaging -MRI, Positron Emission Tomography -PET, Tomography, Optical imaging). On the other hand, they enhance the lethal effect of X-rays on cancer cells during irradiation treatments [9, 10, 11, 12].
In this framework, nanoparticles penetration and localization inside the organisms need to be monitored for establishing clinical and pre-clinical evaluations and protocols. The issue of nanoparticles distribution plays a fundamental role to limit any toxic effect and to predict their capability of tumor radiosensitization. Up to date numerous in-vitro, ex-vivo and in-vivo studies at large and at small scales have been performed to observe nanoparticles in tissues and in cells. MRI and PET are 3D techniques but they show only globally the presence of nanoparticles in tumors without providing any information about their exact position, since they are limited by a spatial resolution of few millimiters in-vivo, and down to sub-100 μm ex-vivo [13, 14, 15]. Optical techniques, such as Laser Induced Breakdown Spectroscopy (LIBS) or Transmission Electron Microscopy (TEM) are considered as pseudo-3D techniques. They are able to achieve high spatial resolutions (10 μm and few tens of nm, respectively), but at the cost of slicing the specimen [16, 1]. They require very thin samples with thickness of few micrometers. The images of the sample slices can be stacked to create 3D models but with the possibility of an imperfect alignment and at the prize of loosing information from the sample part that has been removed during the sectioning. At cellular scale there is also

fluorescence microscopy. In order to visualize the nanoparticles, it requires the use of fluorophore crafted on nanoparticles surface at the risk of altering the nanoparticles penetration and aggregation dynamic [17, 18, 19].
The demand of nanoparticles bio-localization at a median scale resolution motivated this thesis work. Here, the use of X-ray Phase-Contrast Tomography (XPCT) is proposed as diagnostic imaging tool complementary to the well consolidate above mentioned techniques. X-ray tomogaphy has the advantage of being non invasive and of visualising the entire organ down to its structural features. The technique consists in acquiring multiple 2D images at many angles for numerically producing 3D images. If combined with phase-contrast imaging, it allows discriminating anatomical details of soft tissues that otherwise would not be possible to observe with standard absorption tomography [20].
In order to achieve a volumetric reconstruction up to thousands X-ray projections may be necessary. Thus, the radiation dose delivered to the sample is high. X-ray absorbed doses are potentially harmful for human. Therefore, for ethics reasons, there is a strong limitation also for animal imaging. Moreover, considering biological imaging a high irradiation dose may induce damages also in living cells [21, 22]. Thus, during X-ray cell tomography it is often preferred to use frozen than living cells.
Getting a good trade-off between image quality and X-ray absorbed dose is a hot topic today.
This thesis is part of a European FET project, named VOXEL (Volumetric X-ray Extremely Low dose), that we believe will bring a change perspective by leading to a drastic reduction of the X-ray absorbed dose, compared to traditional X-ray imaging methods. VOXEL splits in two branches: one aiming at prototyping a compact soft X-ray plenoptic microscope for cell imaging in the "water window" and, the other a hard X-ray plenoptic camera for small animal imaging.
A plenoptic camera is a device capable of producing 3D images in a single exposure. Thanks to a main lens and a microlens array coupled to a detector, the spatial and angular components of the light rays can be collected [23]. At the moment, this technology exists only for the visible light and VOXEL ambition is to transfer it to the X-ray domain.
During my thesis, I worked specifically on the "water window" prototype that is today under test at Laboratoire d'Optique Appliquée, while the hard X-ray prototype is under construction at Imagine Optique- Bordeaux.

In Chapter 1 of this manuscript, the general concepts of X-ray tomography, the problem of image reconstruction and the phase-contrast approach are discussed. Moreover, the protocol adopted for the data treatment of the XPCT images illustrated in the following chapters is made known. It is provided a detailed description of the steps accomplished to reconstruct the 2D virtual slices from the projections datasets and the techniques used for attenuating common artefacts are described.

In Chapter 2, the results obtained in the framework of resolving nanoparticles distribution in mice organs (kidney, liver, spleen, brain and lung) doped with gadolinium, gold or platinum nanoparticles are shown. The images were acquired at European Synchrotron Radiation Facility (ESRF) in collaboration with CNR-Nanotec (Roma, Italy) and Institute for Advanced Biosciences (Grenoble, France). Raw data were entirely processed in our institute. In particular, new and unexpected results were obtained regarding nanoparticles repartition intra- and inter-melanoma mouse brain metastases. Moreover, XPCT was used to achieve high-resolution insights of brain structures and to visualize melanin pigments distribution in melanoma tumor samples.

In Chapter 3, the results regarding the detection of amyloid plaques loaded with gadolinium-based nanoparticles are displayed. Recently, nanoparticles are also used to mark amyloid plaques in model mice of Alzheimer's disease. In collaboration with CNR-Nanotec, IAB and NeuroSpin Lab (CEA, Saclay and Grenobe), XPCT images of mouse brain samples in advanced state of Alzheimer's disease were acquired at ESRF synchrotron during an expirement I led. The goal of the experiment was understanding the mechanism of diffusion and distribution of nanoparticles, once the brain-blood barrier is permeated through focused ultrasound [24]. Several cases were examined and their XPCT images are here illustrated.

In Chapter 4, the plenoptic camera is introduced. We built our own traditional plenoptic camera system for collecting images with visible light and testing its special features. Within this chapter the meaning of light field is explained. The camera capability of creating sub-aperture images and the refocusing algorithm are presented and illustrated in the visible.

In Chapter 5, the first prototype of soft X-ray plenoptic microscope is described. Altough synchrotron radiation-based X-ray tomography for cell imaging is a benchmark for measurements in the "water window" [2], we designed a compact desktop-size plenoptic soft X-ray microscope based on a classical microscope developed by Wachulak and collaborators [7]. A matrice of Fresnel zone plates was added to make it work as a plenoptic camera. "Water window" is the spectral range comprised between oxygen K-shell ($\lambda = 2.3\ nm$) and carbon K-shell ($\lambda = 4.4\ nm$) [25]. This is a wavelength range suitable at imaging hydrated cells, because water is transparent whereas carbon-based structures strongly absorb. One of the possible future application of the soft X-ray camera would be imaging nanoparticles in cells with 100 nm spatial resolution.

Lastly, a brief summary of the work done during my thesis and the perspectives for future developments are reported.

Chapter 1

X-ray tomography imaging: the Phase-Contrast approach

The word "tomography" derives from the union of two Greek words: "tomos", slice, and "graphō", to write. Tomographic imaging is a 3D non-destructive method capable of producing virtual cross-section images of objects of any composition by using different sources (X-rays, neutrons, ultrasound, visible light, magnetic resonance, etc.). It is a versatile technique applied in many fields: radiology, biology, archeology, oceanography, material science. Thanks to its non-invasive nature, it is considered particularly suitable at investigating biological samples for pre-clinical and clinical applications.

This thesis deals with X-ray tomography and, it focuses on a specific tomographic approach: X-ray Phase-Contrast Tomography (XPCT) carried out with synchrotron light source.

Typically, classical X-ray absorption tomography allows determining the 3D spatial distribution of the attenuation coefficients of an object by placing the detector very close to the sample. In an XPCT experiment the detector is placed farther away from the sample, instead. The image formation process is purely based on refraction of X-rays by the sample and, if an appropriate phase-retrieval algorithm is implemented, a phase map can be finally retrieved. Compared to classical absorption tomography, XPCT offers the advantage of better discriminating the sample inner components if suffering of poor X-ray contrast.

A tomography experiment at a synchrotron radiation facility consists of several steps: beamtime request, sample preparation, image acquisition and data recon-

struction process. Specially, the reconstruction of XPCT images requires a specific and long data treatment. Synchrotron beamlines make available softwares for the reconstruction of the collected data. As the beamtimes are short, it is very important during the allocated shifts to make a fast qualitative control of the acquired images for optimizing the acquisition. The full reconstruction work and the quantitative image analysis are often postponed to the end of the beamtime and, performed at the user's home institution.
The first part of this chapter introduces X-ray tomography and describes the non-trivial problem of image reconstruction from a tomographic dataset. Then, the in-line phase-contrast technique and the phase-retrieval approaches for homogeneous and inhomogeneous materials are presented. In the second part of the chapter, the image processing techniques used for the practical reconstruction of the data collected in this thesis are described. It is explained step by step how the virtual slices of the sample were obtained from the acquired projections by using the open-source SYRMEP Tomo Project software and, how the most recurring artefacts in X-ray tomography were fixed by using FIJI plugins. Moreover, the approach of image matching necessary to compare images of the same sample acquired in different configurations is described. Finally, it gives a glance to the most common volume rendering techniques adopted for the 3D visualization of the measured organs.

1.1 X-ray tomography

X-ray tomography is a 3D non-intrusive imaging method that allows the visualization of the inner structures of a sample through a series of cross-sections, as if a virtual sectioning of the body was carried out. Its development results from the lack of depth information in radiography images, where the volume of an object is compressed into a single 2D image and many structures overlap on the same plane. More precisely, an X-ray tomography measurement is capable of supplying information about the 3D spatial distribution of the attenuation coefficients within any object.
The cross-section images are obtained from a sequence of 2D images of a sample acquired at many angles. These multi-angle views are called "projections", or also "radiographies". In case of parallel beam (as for the data of this thesis and illustrated in Fig. 1.1), each projection renders the total attenuation of the X-rays

propagating across the sample [26].

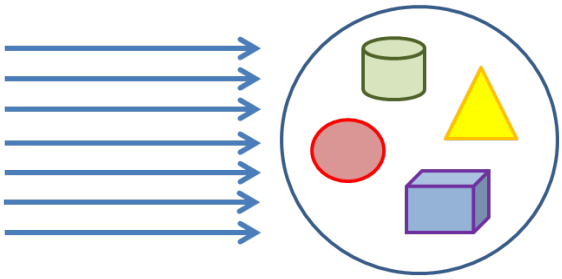

Figure 1.1: A sample of non-uniform composition backlighted by a parallel X-ray beam.

Since it is not possible to distinguish inner structures from one single projection, the sample is rotated over wide angles with a constant tiny angular increment (see Fig. 1.2).

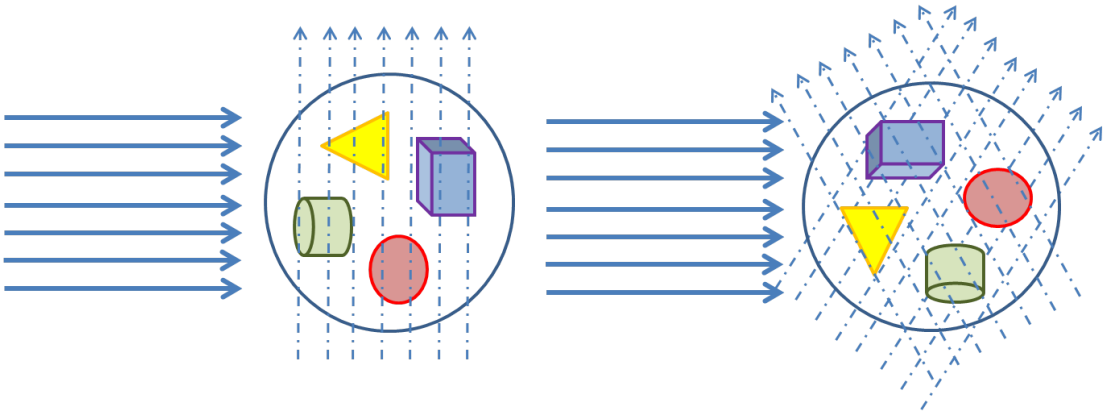

Figure 1.2: Drawing illustrating X-rays passing across the sample following rotation.

This leads to other equispaced lines that overlap to the previous ones until the sample is completely covered. The more the number of the views of the sample may be obtained, the more its internal components may be distinguished after an appropriate image reconstruction process [27].
The total rotation of the sample usually covers 180°. When the sample is too large in respect with the horizontal field of view of the camera, it may be rotated over 360° in order to cover its entire horizontal extension. This strategy is called "half-acquisition" mode and it requires a special step, named *sinogram stitching*, during the image reconstruction process. As explained farther in the paragraph "Data reconstruction process", this supplementary operation allows to have sinograms as

if they were acquired over 180°, but with a horizontal field of view twice larger than a normal sinogram.
Furthermore, before each tomographic measurement, a series of "flat-field" images, i.e. images of the background without the sample, and "dark-images", i.e. images with the X-ray shutter closed, are acquired with the aim of normalizing the collected projections during the reconstruction step. X-ray tomographic imaging may be achieved with laser-driven [28, 29, 30, 31] or synchrotron X-ray source. Performing X-ray tomography experiments with synchrotron radiation has the advantage of getting high-resolution images with a good signal-to-noise ratio. In addition, thanks to the large available photon flux, samples are usually exposed for a short time during the measurements.

1.1.1 Approaches to image reconstruction

The image reconstruction process allows determining the 3D spatial distribution of the attenuation coefficients of an object without knowing *a-priori* its inner composition. Recovering sample cross-sections from a set of projections is not a trivial mathematical problem. In non-ideal cases the objects are composed of different materials and hence, they have variable density and absorption coefficients [27]. As consequence, the Lambert-Beer law must be adapted for non-uniform objects. The shined object may be imagined subdivided into multiple smaller pieces (as illustrated in Fig. 1.3), each of them distinguished by a certain attenuation coefficient μ_n and a length l_n.

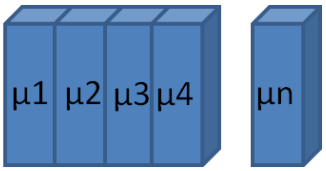

Figure 1.3: Discretization of non-homogeneous sample in order to achieve image reconstruction.

Thus, the Lambert-Beer law (equation 5.17 in Appendix B) becomes:

$$I = I_0 e^{-\mu_1 \Delta l_1} e^{-\mu_2 \Delta l_2} \dots e^{-\mu_n \Delta l_n} = I_0 e^{-\sum_{n=1}^{N} \mu_n \Delta l_n} \tag{1.1}$$

From which it follows that:

$$-\ln\Big(\frac{I}{I_0}\Big) = \sum_{n=1}^{N} \mu_{\mathrm{n}} \Delta l_{\mathrm{n}} \tag{1.2}$$

When Δl tends to zero, the summation becomes the integration over the full length of the object:

$$p = \int \mu(l) dl \tag{1.3}$$

This line integral, p, denotes the total X-ray beam attenuation along a straight ray path. A set of line integrals at a given angle originates a projection image, and a tomographic dataset comprises total attenuation measurements obtained at different angles and, at different distances from the center according to the shape of the object under study. The Fourier Slice Theorem is used to reconstruct the slices of an object.

1.1.2 Fourier Slice Theorem

Let be $f(x, y)$ the object to reconstruct, and let be $p(t, \theta)$ a projection of $f(x, y)$ taken at angle θ, where t is the distance of the projected rays from the center of the object. Let be (s, t) a new rotated coordinate system, where the axis s is parallel to the bundle of X-rays crossing the sample at angle θ. In the new coordinate system (Fig. 1.4), at a given angle θ the projection of a point (x, y) will have coordinates:

$$\begin{cases} t = x\cos\theta + y\sin\theta \\ s = -x\sin\theta + y\cos\theta \end{cases} \tag{1.4}$$

and the image $f(x, y)$ may be represented by $f'(t, s)$.
Therefore, a projection at angle θ is:

$$p(t, \theta) = \int_{-\infty}^{\infty} f'(t, s) ds \tag{1.5}$$

and its Fourier transform is:

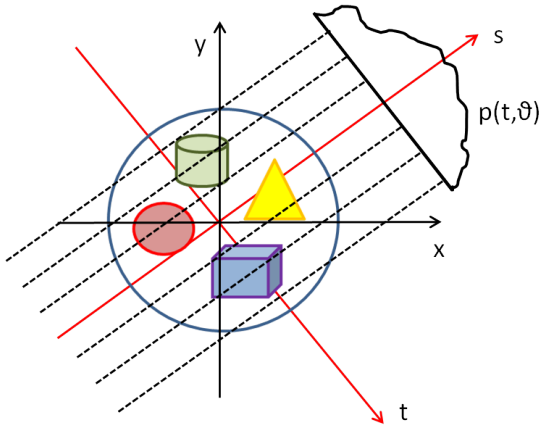

Figure 1.4: Schematic representation showing the relationship between the coordinate systems (x, y) and (s, t).

$$P(\omega, \theta) = \int_{-\infty}^{\infty} \int_{-\infty}^{\infty} f'(t, s) e^{-i2\pi\omega t} ds dt \tag{1.6}$$

By applying the coordinate transformation, the Fourier transform of the projection can also be written in the following way:

$$P(\omega, \theta) = \int_{-\infty}^{\infty} \int_{-\infty}^{\infty} f(x, y) e^{-i2\pi\omega(x cos\theta + y \sin\theta)} dx dy \tag{1.7}$$

whereas the Fourier transform of the function to reconstruct, $f(x, y)$, is:

$$F(u, v) = \int_{-\infty}^{\infty} \int_{-\infty}^{\infty} f(x, y) e^{-i2\pi(xu+yv)} dx dy \tag{1.8}$$

The variables (u,v) define straight lines in the Fourier domain. The following relationship between the coordinates:

$$\begin{cases} u = \omega \cos\theta \\ v = -\omega \sin\theta \end{cases} \tag{1.9}$$

makes the right-hand sides of equations (1.7) and (1.8) equal:

$$F(\omega \cos\theta, \omega \sin\theta) = P(\omega, \theta) \tag{1.10}$$

Thus, it has been demonstrated that at a given angle θ the Fourier transform of a projection is a 2D slice in the Fourier domain and subsequenty, this can be extended to all other projections acquired over the range from 0 to π. By using the inverse Fourier transform, the object $f(x, y)$ can finally be reconstructed. Fig. 1.5 illustrates in a schematic manner the Fourier Slice Theorem. In this representation the 2D Fourier transform of the entire object is depicted with a grey rectangle while the 2D Fourier transform of a parallel projection is identified by the red line. As consequence of the rotation, there will be multiple red lines passing through the center and corresponding to the 2D Fourier transforms of all the collected projections.

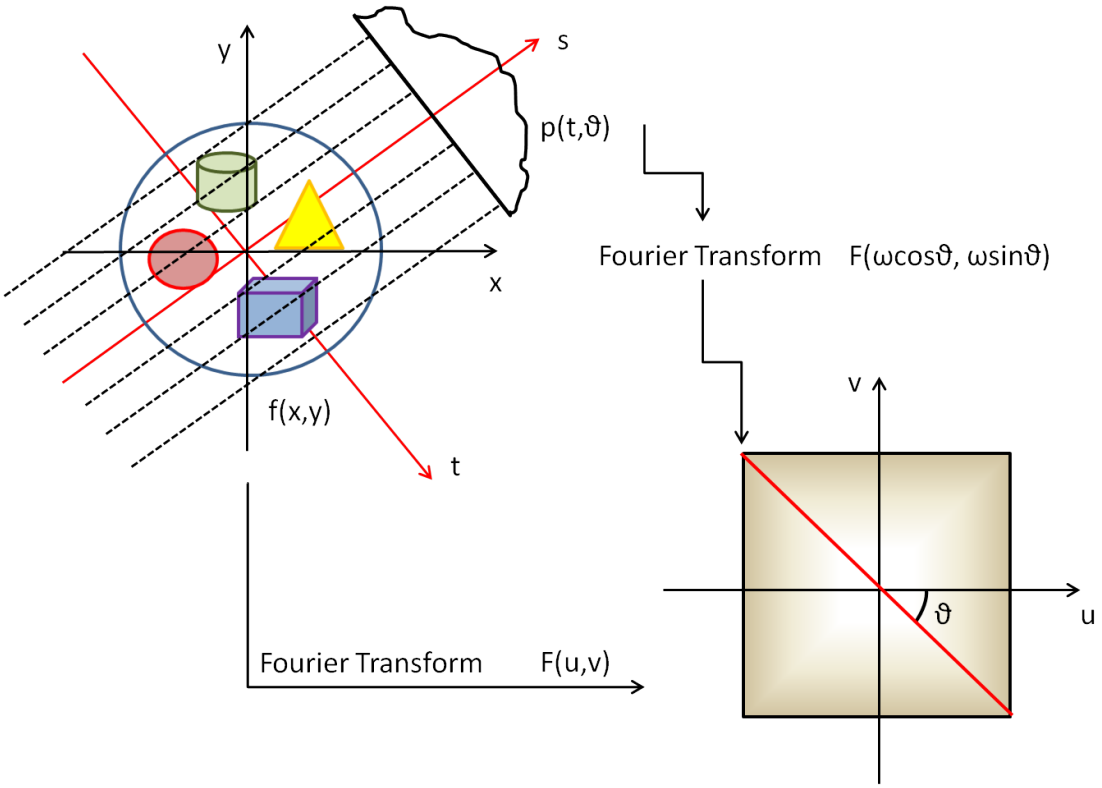

Figure 1.5: Schematic representation of the Fourier Slice Theorem: the Fourier transform of a parallel projection is a slice (here indicated as a red line) of the 2D Fourier transform of the object $f(x, y)$ (drawn like a grey rectangle). Following rotation, the 2D Fourier transform of the object will be covered by multiple red lines passing through the center corresponding to the collected projections during the aquisition.

1.2 Sinogram images

Sinograms are an alternative representation of the acquired projections. A single sinogram is a 2D matrix that is obtained by using the collected projection data. Let's imagine to extract one row from the projection image obtained at angle θ_1 and, to extract the same row from the subsequent projection image acquired at angle θ_2 and, so on. As it is described in Fig. 1.6a, by horizontally stacking the same projection line as a function of all the angles at which the tomography was performed, a 2D matrix is obtained and it is called *sinogram*. Thus, a sinogram is composed of a total number of rows equal to the total number of projections (hence, of angles) and, its number of columns is equal to the width of the field of view of the detector; while the total number of produced sinograms is equal to the height of the field of view of the detector (Fig. 1.6a). In other words, the full set of sinograms corresponds to the projection of the entire object.
A sinogram is mathematically defined by the Radon transform:

$$R(t,\theta) = \int_{-\infty}^{\infty}\int_{-\infty}^{\infty} f(x,y)\delta(x\cos(\theta) + y\sin(\theta) - t)dxdy \tag{1.11}$$

The Radon transform is obtained by applying a delta function on the line integral, introduced previously. A sinogram looks like several overlapping sinusoids (Fig. 1.6b), because the Radon transform of an off-center point is a sinusoid.
The inverse Radon transform provides the solution for retrieving a function from its line integrals. It means that in the tomography framework, the use of the inverse Radon transform allows retriving the cross-sections of the object. The reconstruction process leads to a number of cross-sections, or slices, equal to the number of available sinograms. There are severals mathematical approaches that use the inverse Radon transform to retrieve the cross-sections of an object: the most popular is the Filtered Back Projection (FBP) algorithm that will be described in more details in the second part of this chapter as this is the one we used to treat our experimental data.

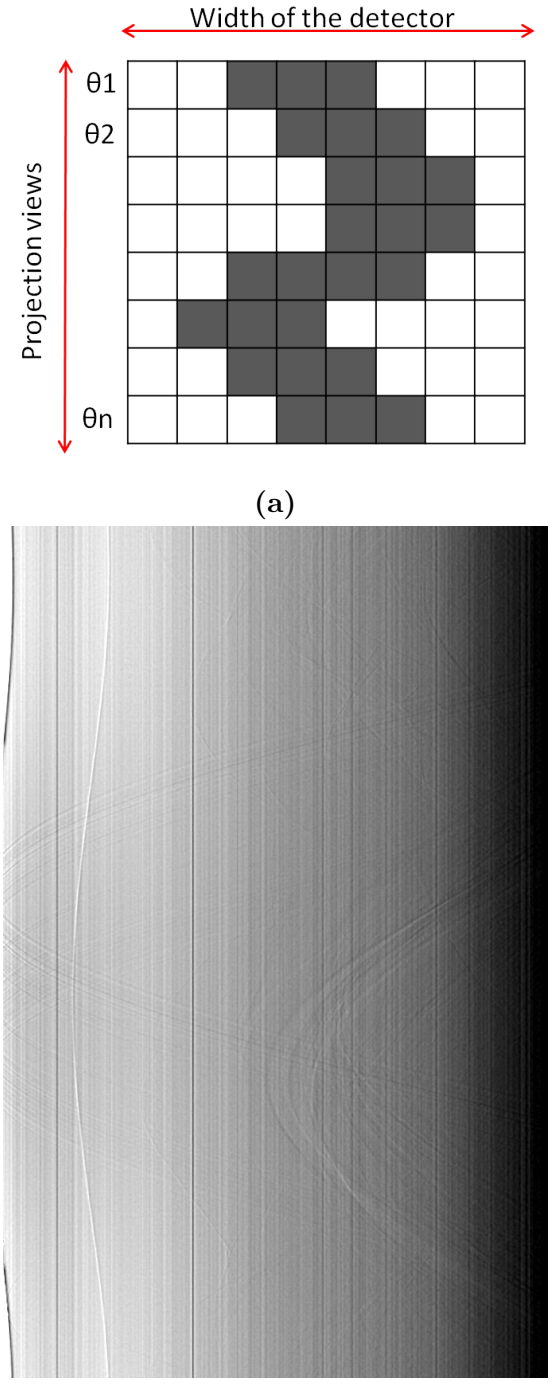

(a)

(b)

Figure 1.6: (a) Sinogram matrix. (b) Sinogram image.

1.3 X-ray Phase-Contrast Tomography

1.3.1 Theory of phase-contrast imaging

Biologic tissues are known to have weak contrast properties. This makes challenging the segmentation process of their X-ray images and, the subsequent creation of 3D models. XPCT offers the solution to overcome this limit by providing contrasted images.

Phase-contrast approach has ancient roots. It started in 1933 with Fritz Zernike's work on phase-contrast method with its fast application to biomedical world [32]. A second step was done in 1948 by Dennis Gabor's work on holography [33]. In 1965 Ulrich Bonse and Michael Hart demonstrated X-ray holography by crystal interferometry [34]. In 1986 Abraham Szöke proposed the idea of internal source holographic microscopy [35]. The first demonstration was done in 1995 by Anatoly Snigirev at ESRF with a propagation geometry and a detection of Fresnel Fringes [36]. In 1996, Wilkins et al., at CSIRO, demonstrated in line holography with micro-focused X-ray tube [37].

The main physical phenomenon behind phase-contrast imaging is X-ray refraction. When X-rays pass through the sample, according to the composition and structure of the object, they are refracted at the interfaces. Thanks to an appropriate propagation distance set between the sample and the detector, some rays concentrate on some paths while inducing a vacancy of rays right next to them. This leads to the measurement at the detector plane of peaks and valleys in correspondence of the object boundaries, as it is illustrated in Fig. 1.7.

The fringes that appear in the image are typical of the near-field imaging regime, thereby the Fresnel diffraction equation is valid. To fulfill the near-field condition, the distance between the object and the detector, z, has to be smaller than the square of the smallest distinguishable feature, d, in the imaged object divided by the wavelength of the radiation [38]:

$$z << \frac{d^2}{\lambda}. \tag{1.12}$$

The optimal distance, z, should be set in order to be shorter than the critical distance, z_c:

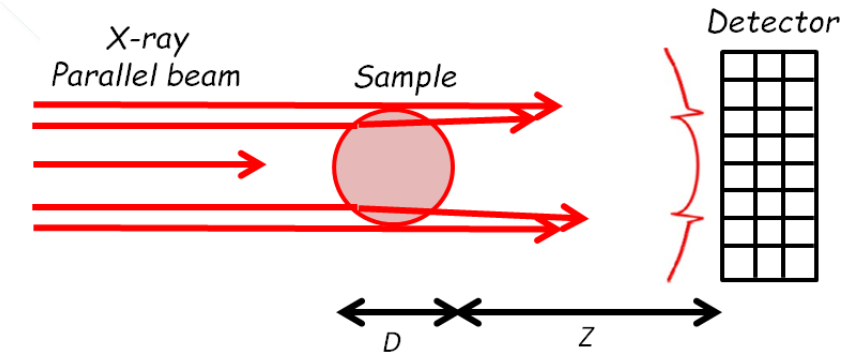

Figure 1.7: Layout of an in-line phase-contrast tomography set-up, with a sample embedded in an X-ray parallel beam.

$$z_c = \frac{(2\Delta)^2}{\lambda} \tag{1.13}$$

where Δ is the pixel size and, λ is the wavelength of the used radiation. Typically, z_c can vary between 1 mm and 100 m for pixel sizes ranging between 0.1 μm and 50 μm and, energies comprised between 5 keV and 120 keV [38].
For instance, in our phase-contrast experiments the projections were recorded by a CMOS camera connected to an optical system having a final pixel size of 3 $\mu m \times$ 3 μm. For measurements at 76.9 keV, 79.2 keV, 79.9 keV, and 82.2 keV, it was set a propagation distance of 11 m, while acquisitions at 48.5 keV and 51.5 keV were done both at 11 m and at 2.3 m.
When the distance sample-detector becomes longer and longer, the fringes broaden and the near-field regime is replaced by the intermediate regime, where diffraction fringes are visible [39].
In a phase-contrast experiment, the profile beam recorded by the detector is a mixture of attenuation and phase-shift. These two physical parameters are respectively related to the imaginary, β, and real part, δ, of the X-ray refractive index of a material (Appendix C). Both δ and β are strongly influenced by the energy of the incoming radiation. For light elements, δ is several orders of magnitude greater than β at the same energy [40]. Therefore, the variations in soft tissue density induce stronger phase-contrast than absorption-contrast [20]. This explains why XPCT is more suitable at discriminating the inner components of a soft tissue that otherwise would not be possible to identify by standard absorption tomography.

Phase-contrast may be achieved through several techniques, such as propagation-based imaging [36], analyzer-based imaging [41, 42], grating interferometry [43, 44], edge-illumination [45]. These approaches differ by the experimental set-up, by the image-signal provided and by the amount of radiation dose delivered to the sample [20]. This thesis focuses only on the in-line propagation-based method, whose layout scheme is presented in Fig. 1.7.

The propagation-based method is free from aberrations, it does not use optics. It has the advantage of imparting a reduced radiation dose to the specimen [37, 46, 47]. The final contrast of the image depends on several factors, such as: the pixel size of the detector, the image reconstruction process, the energy of the radiation and the divergence of the beam [48, 20]. In order to better illustrate the concept of phase-contrast imaging using free propagation (technique used in chapters 2 and 3), it is displayed three images achieved by 3D ray-trace code (developed by M. Cotelo from Universidad Politecnica de Madrid, Spain and run and treated by T. T. T. Le from Imagine Optic). The code is considering the propagation, using Snell law at interfaces, and absorption (Beer-Lambert law). Intrinsically, the rays are treated as independent from each other, meaning a fully incoherent beam. The three images have been obtained by placing a detector at 5 cm, 1 m and 10 m from the sample exit. The same data treatment has been applied to the three images (Gaussian blur $\sigma = 3$ and LUT inversion) to clean up moiré fringes coming from the different sampling frequencies from the detector (9 μm pixels, 2500 $\times$ 2500) and the refracted rays that have non-uniform frequency due to refraction.

The sample was a 1 cm diameter sphere made of brain with a core mimicking a 1 mm of diameter tumor loaded with 9% of gadolinium. The X-rays were tuned at 51.5 keV leading of $\beta = 4.11 \times 10^{-11}$ and $\delta = 8.82 \times 10^{-8}$ for the brain and $\beta = 1.84 \times 10^{-9}$ and $\delta = 8.70 \times 10^{-8}$ for the tumor. The brain is placed in air with $\beta = \delta = 10^{-12}$. About 10 millions rays were launched in a parallel beam mimicking the ESRF experiments.

On Fig. 1.8a, one can see the two spheres projected on 2D plane with the gadolinium being much whiter than the brain. The detector is placed at 5 cm from the sample. In this modelling some rays go around the brain leading to a dark grey background. A line-out has been performed at the centre of the image and the result is displayed on Fig. 1.8b. Apart a residual modulation coming from the moiré fringes, that are pure artefact, we observe a smooth diminution of the signal from the edges to the central part.

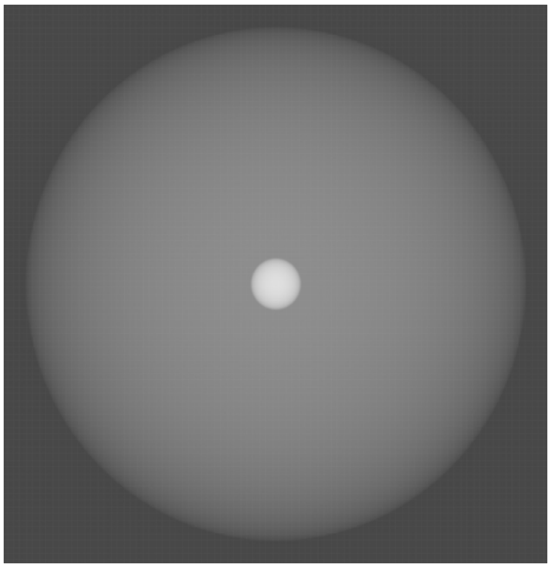

(a)

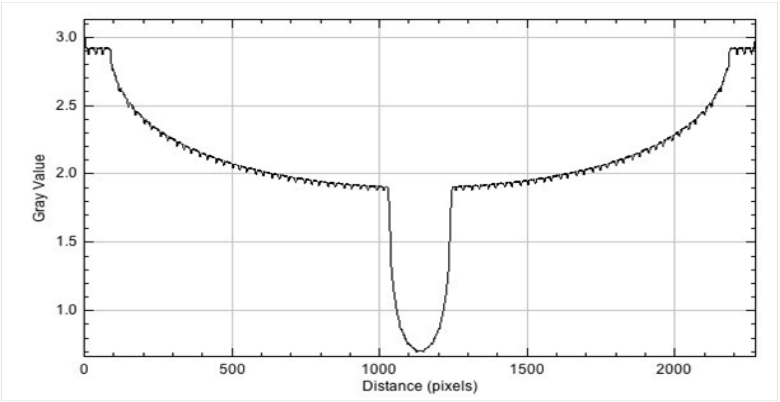

(b)

Figure 1.8: (a) Image achieved by 3D ray-trace code by considering the detector at 5 *cm* from the sample. (b) Line-out performed at the centre of Fig. 1.8a, where a smooth diminution of the signal from the edges to the central part can be observed.

By moving the detector at 1 *m* away from the sample (Fig. 1.9a) and using the same rays exiting from the sample than in the precedent figure, we observe that the image of the brain is less contrasted as compared to the background than for Fig. 1.8a. Also, we observe a very light over-intensity ring on the brain edge. This is confirmed by the line-out displayed on Fig. 1.9b.

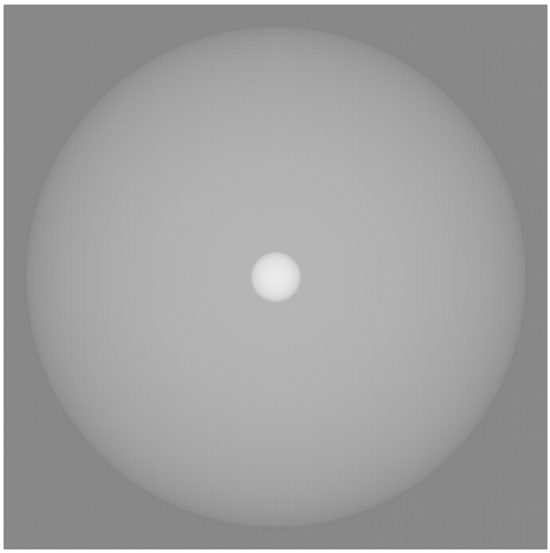

(a)

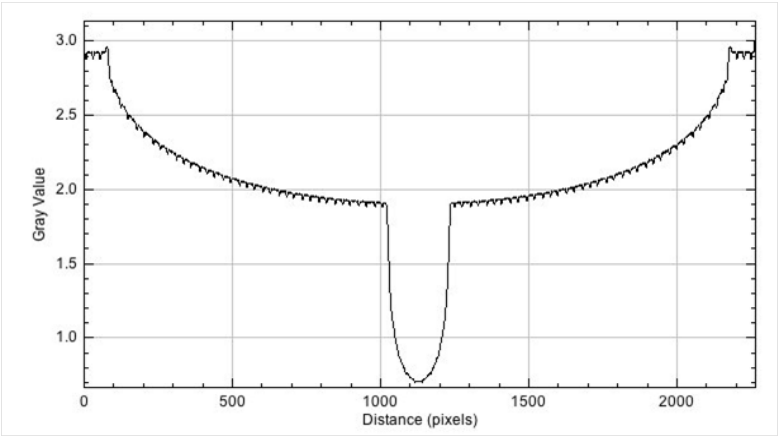

(b)

Figure 1.9: (a) Image achieved by 3D ray-trace code by considering the detector at 1 m from the sample. (b) Line-out performed at the centre of Fig. 1.9a.

Finally, we placed the detector 10 m away from the sample that corresponds roughly to the distances used during ESRF experiments. The image on Fig. 1.10a displays a very clear and well-contrasted double ring (whiter for the inner part and much darker in the outer part). Although difficult to observe, a ring appeared also around the gadolinium core. The line-out (Fig. 1.10b) shows intense over-intensities on the brain edge (about 30% intensity enhancement) accompanied by a weak depletion in the inner part of the brain. A peak less intense appears also

around the gadolinium edge. The effect is weaker since rays are strongly absorbed in gadolinium.

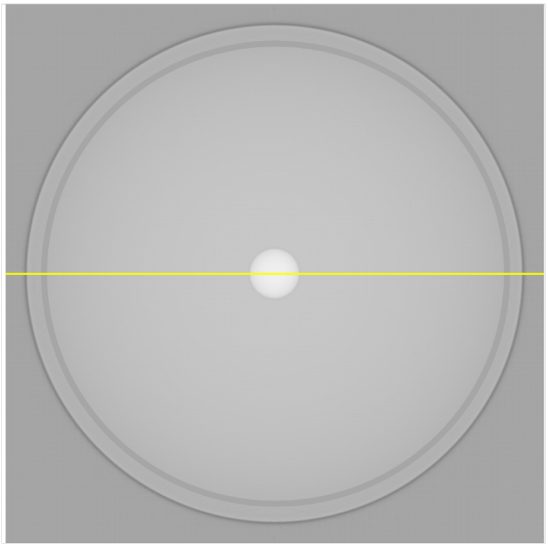

(a)

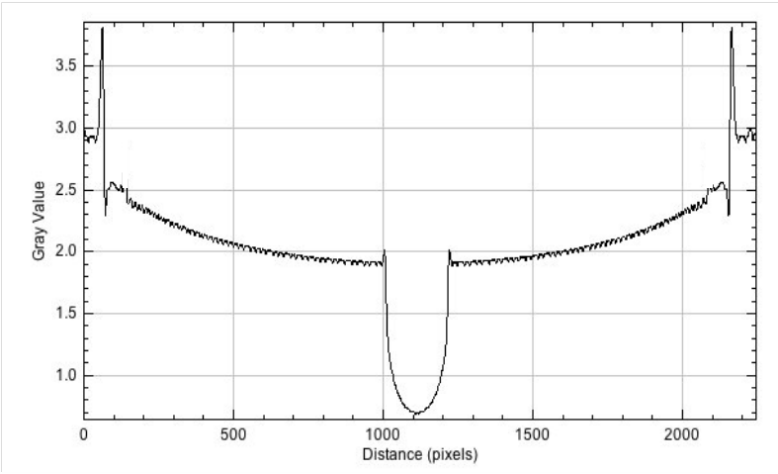

(b)

Figure 1.10: (a) Image achieved by 3D ray-trace code by considering the detector at 10 m from the sample. (b) Line-out performed at the centre of Fig. 1.10a showing intense over-intensities on the brain edge followed by a weak depletion in the inner part of the brain.

This simulation shows that phase-contrast imaging, in general, does not rely on beam coherence but is only due the deflection of incoherent rays inside the sample.

We would like to note that using coherent beam for the backlighting will lead to the generation of a hologram. Since the real part of index of refraction (δ) is very small, the fringes coming from phase-contrast imaging are visible only by placing the detector far away. For very large distances, not displayed here, the ring trends to shade. The optimal distance depends on the sample characteristics (index of refraction, density variation and shape).

1.3.2 Phase retrieval

In propagation-based phase-contrast experiments, the projections recorded by the detector contain the phase-shift induced by the sample and, the transmitted radiation resulting from the attenuation produced by the sample inner components. This imaging modality allows distinguishing materials on the basis of their refractive index and attenuation properties [49].
Phase and intensity are linked through the transport of intensity equation, according to which the lateral Laplacian of the phase is proportional to the longitudinal gradient of intensity (Eq. 1.14) [50]. Under specific assumptions, Paganin et al. solved this equation to recover the phase [51] and thus, the spatial distribution of the parameter δ. Their algorithm is valid for homogeneous samples and it is one of the most popular in this field. Its mathematical derivation will be shown in the following paragraph. Other phase-retrieval approaches presented in literature are based on the assumption of large Fresnel numbers [52], or on the dissection of multi-component materials [49, 53] in case of non-homogeneous materials.
Anyway, phase-retrieval is not a mandatory step to have the final slices. As the lateral Laplacian of the phase enhances the external and internal countours of the object allowing the edges visualization of the sample, cross-sections are informative even without the implementation of a phase-retrieval algorithm. In Fig. 1.11 are compared an edge-enhanced image obtained withouth phase-retrieval (Fig. 1.11a) and a phase-retrieved image achieved with Paganin's algorithm (1.11b).

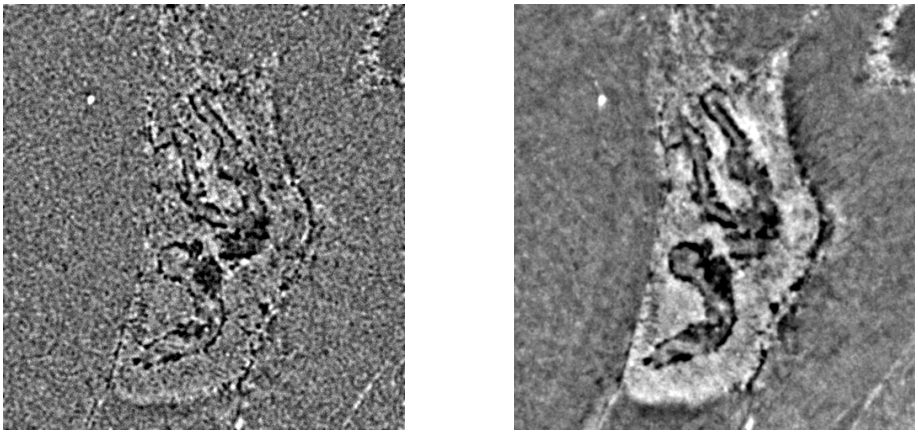

(a) **(b)**

Figure 1.11: (a) Edge-enhanced slice showing a mouse brain tumor. (b) Phase retrieved slice showing a mouse brain tumor.

This paragraph repeats the mathematics described by Paganin and collaborators in [51] for obtaining the decoupling of the phase from the intensity of a recorded projection.
The phase-retrieval approach derived by Paganin is based on the solution of the transport of intensity equation under paraxial approximation [50]:

$$\nabla_\perp \cdot (I(\mathbf{r}_\perp, z)\nabla_\perp \varphi(\mathbf{r}_\perp, z)) = -\frac{2\pi}{\lambda}\frac{\partial}{\partial z} I(\mathbf{r}_\perp, z). \tag{1.14}$$

This equation derives from the Helmholtz equation and it describes the evolution of the intensity of a propagating monochromatic scalar electromagnetic wave. The intensity and the phase of the beam are indicated by $I(\mathbf{r}_\perp, z)$ and $\varphi(\mathbf{r}_\perp, z)$, respectively; whereas λ is the radiation wavelength and $\mathbf{r}_\perp$ is the position vector lying in the plane perpendicular to the optical axis. The paraxial approximation establishes the constraint that all the X-rays passing through the sample propagate at small angles with respect to the axis of the system.
In order to extract the phase from the equation (1.14), the algorithm initially relies on a series of assumptions:

1. The point source of X-rays is far away, leading to collimated illumination and unit magnification.

2. The incident radiation is a monochromatic plane wave of uniform intensity over the area occupied by the sample.

3. The object under examination is made up of a single material; i.e. it has a homogeneous composition.

4. The object is sufficiently thin.

Because of the assumption n^o2, the intensity radiation at the exit plane from the object ($z = 0$) may be well approximated with the Lambert Beer's Law (Appendix B):

$$I(\mathbf{r}_\perp, z = 0) = I_0 e^{-\mu T(\mathbf{r}_\perp)}. \tag{1.15}$$

Here, I_0 is the intensity of the incident radiation at the entrance of the sample, μ is the linear attenuation coefficient and $T(\mathbf{r}_\perp)$ the projected thickness of the object onto the detector plane. It is assumed that the detector is at a distance z from the sample. As it is required by the condition n^o4, if the object is thin enough, the phase of the transmitted radiation at $z = 0$ is proportional to the projected thickness through 1.16 [37]:

$$\varphi(\mathbf{r}_\perp, z = 0) = -\frac{2\pi}{\lambda}\delta T(\mathbf{r}_\perp). \tag{1.16}$$

By replacing in (1.14) the intensity and the phase at $z = 0$ as they are defined in the equations (1.15) and (1.16) respectively, the transport of intensity equation becomes:

$$-\frac{\delta}{\mu} I_0 \nabla_\perp^2 e^{-\mu T(\mathbf{r}_\perp)} = \frac{\partial}{\partial z} I(\mathbf{r}_\perp, z = 0). \tag{1.17}$$

When the detector plane is sufficiently close to the sample, the right-hand side of the equation (1.17) may be approximated as follows:

$$\frac{\partial}{\partial z} I(\mathbf{r}_\perp, z = 0) \approx \frac{I(\mathbf{r}_\perp, z) - e^{-\mu T(\mathbf{r}_\perp)} I_0}{z}. \tag{1.18}$$

By replacing the right-hand side of equation (1.17) with the right-hand side of equation (1.18) and by grouping the terms, it results that:

$$\left(-\frac{z\delta}{\mu}\nabla_{\perp}^{2} + 1 \right) e^{-\mu T(\mathbf{r}_{\perp})} = \frac{I(\mathbf{r}_{\perp}, z)}{I_0} \tag{1.19}$$

and that may be re-arranged in the following way:

$$I_0 e^{-\mu T(\mathbf{r}_{\perp})} = \frac{I(\mathbf{r}_{\perp}, z)}{1 - z\delta\mu^{-1}\nabla_{\perp}^{2}}. \tag{1.20}$$

The image at the exit from the sample (at $z = 0$) and, the phase-contrast image produced onto the detector (at z) can be expressed through the Fresnel diffraction equation written in terms of Fourier transform. Thus, the image at $z = 0$ results:

$$I_0 e^{-\mu T(\mathbf{r}_{\perp})} = \frac{I_0}{2\pi} \iint \mathcal{F}\{e^{-\mu T(\mathbf{r}_{\perp})}\} e^{i\mathbf{k}_{\perp}\cdot\mathbf{r}_{\perp}} d\mathbf{k}_{\perp} \tag{1.21}$$

and the image at z:

$$I(\mathbf{r}_{\perp}, z) = \frac{1}{2\pi} \iint \mathcal{F}\{I(\mathbf{r}_{\perp}, z)\} e^{i\mathbf{k}_{\perp}\cdot\mathbf{r}_{\perp}} d\mathbf{k}_{\perp} \tag{1.22}$$

where $\mathcal{F}\{\}$ is the Fourier transform. By replacing (1.21) and (1.22) in (1.20) and by isolating the term containing the projected thickness, one get:

$$\mathcal{F}\{e^{-\mu T(\mathbf{r}_{\perp})}\} = \frac{\mathcal{F}\{I(\mathbf{r}_{\perp}, z)\}/I_0}{z\delta\mu^{-1}|\mathbf{k}_{\perp}|^2 + 1}. \tag{1.23}$$

By executing the inverse Fourier transform, it can be extracted the projected thickness:

$$T(\mathbf{r}_{\perp}) = -\frac{1}{\mu} ln\left(\mathcal{F}^{-1}\left\{ \frac{\mathcal{F}\{I(\mathbf{r}_{\perp}, z)\}/I_0}{z\delta\mu^{-1}|\mathbf{k}_{\perp}|^2 + 1} \right\} \right). \tag{1.24}$$

The parameters β and μ are linked by means of the X-ray refractive index according to the following relationship:

$$\mu = 4\pi\beta/\lambda. \tag{1.25}$$

Paganin's algorithm is still valid even if few assumptions stated at the beginning are not fulfilled, as for instance: the constraint that the source is infinitely distant from the object or the condition that the object has to be homogeneous. In fact, this mathematical approach works for a system with magnifications different from unit, as with a microfocus X-ray souce [54] and for a sample made up of a mixed composition but poorly absorbing, like a biologic material [38]. In this specific case of a non-homogeneous material, the phase-map can be obtained by arranging the equations (1.16) and (1.25) in the equation (1.24):

$$\varphi(\mathbf{r}_\perp) = \frac{\delta}{2\beta} ln\left(\mathcal{F}^{-1}\left\{\frac{\mathcal{F}\{I(\mathbf{r}_\perp, z)\}/I_0}{[z\delta\lambda/4\pi\beta]|\mathbf{k}_\perp|^2 + 1}\right\}\right). \tag{1.26}$$

Thus, it results that the phase-map is dependent on the ratio δ/β, rather than on their absolute values [38]. This makes the phase-retrieval algorithm valid for all those samples in which the average ratio δ/β is constant [51]. The *a priori* knowledge of an object composition helps in determining the exact proportion of each component of a material. Most of biological materials are approximatively considered homogeneous, despite their density variation. This is permitted especially above 30 keV, as Compton scattering dominates in attenuation and, as consequence, δ and β are proportional to the local density of an object [20] (Appendix C). This favours that their ratio is considered constant throughout the sample [51, 38]. The image reconstruction problem becomes more complicated if the object under investigation is composed of many very different materials; for instance, an organ doped with high-Z metal-based nanoparticles. The values of δ and β for a high-Z metals are several magnitude order greater than those of a biological material; thus, the approximation that the ratio δ/β is constant all over the sample fails. In this case, the simplification of reconstructing the images regarding tissues with nanoparticles like-homogeneous materials breaks down. For mixed materials the refractive index map $n(r)$ is expected to be a mix of soft tissue, $n(r_1)$, and nanoparticles, $n(r_2)$, refractive indexes [49]. The challenging part of this thesis will be demonstrating how to isolate the signal due to the weak concentration of nanoparticles from the signal due to tissue. See apendix C for the calculation of δ and β for compunds.

1.4 Data reconstruction process

The tomography images showed in this thesis were reconstructed by using the open-source software: SYRMEP Tomo Project [55]. All the solutions offered by SYRMEP Tomo Project are implemented in ASTRA Matlab toolbox [56]. The software allows working on large datasets collected at synchrotron facilities. It is conceived for converting the projections saved as TIFF, or EDF files, into TDF (Tomo Data Format) files. TDF belongs to HDF5 [57] file format that is suitable to handle large amount of data and store together raw data and experimental metadata information, such as: used energy, camera pixel size, and distance sample-camera [58]. SYRMEP Tomo Project has a graphical user interface (GUI) composed of: a side menu with the steps to carry out during the work of image reconstruction; a window for visualizing the images and for adjusting the degree of "brightness/contrast" and, of zooming in and out; a region to inform the user about the progress of the running jobs (see Figure 1.12).

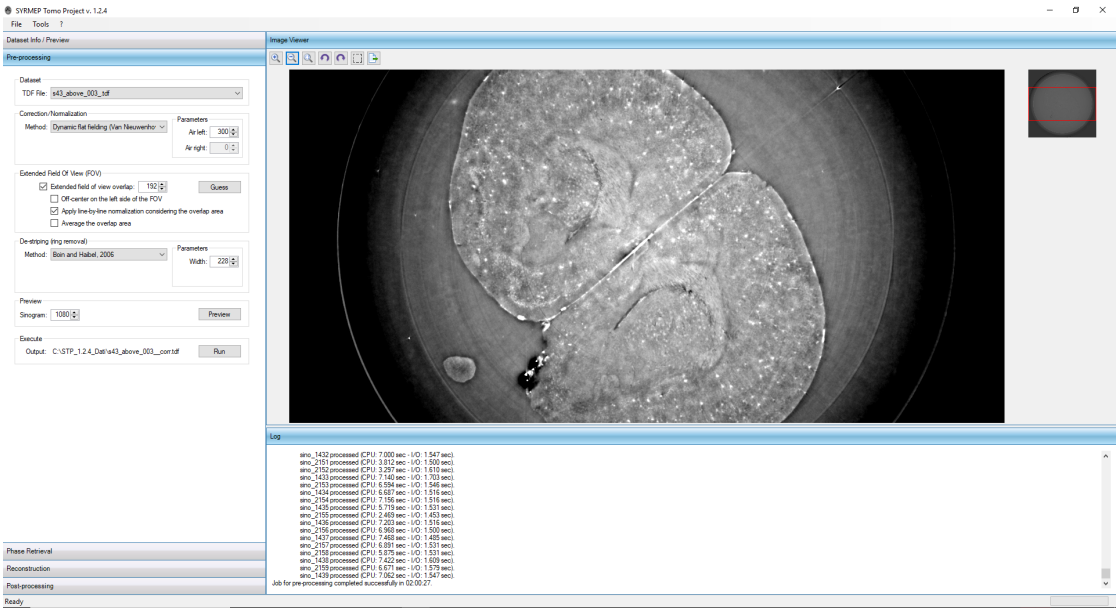

Figure 1.12: Graphical interface of SYRMEP Tomo Project software.

The workflow for the reconstruction of the volumetric datasets divides in five fundamental steps: *dataset preview*, *pre-processing*, *phase-retrieval*, *reconstruction*, and *post-processing*.
It is useful as a first step to look at both the projections and sinograms of the

sample. This can be done through the *dataset preview*. It shows the metadata and can give a quick look on the collected measurements by switching from projection-order to sinogram-order and vice-versa. An example of XPCT projection of a melanoma is illustrated in Fig. 1.13a. X-ray projections may be affected by noise due to instabilities of the X-ray beam, such as a low photons count, or due to the possible presence of dust and scratches accumulated on the screen of the detector. In fact, it is possible to notice impurities (white spots) due to the optical system connected to the detector in the projection of Fig. 1.13a. These defects in addition to a mis-calibration of the detector can lead to the formation of ring artifacts [27, 59]. To correct the initial projections, "flat-field" and "dark-field" projection images are used during the *flat-field correction* in the software *pre-processing* phase. As mentioned previously, a certain number of "white" projection images are acquired without the sample at the beginning and at the end of each measurement. They are referred as "flat-field" images. Similarly, an equal number of images is recorded with the shutter closed and are said "dark" images. The *flat-field correction* is a normalization procedure essential for improving the quality of the images that must be reconstructed. The projections (P) of the sample are normalized (N) with dark (D) and flat field (F) images according to the ratio [60]:

$$N = \frac{P - D}{F - D} \tag{1.27}$$

Flat-field correction is followed by *sinogram stitching*, and *ring-removal* operations. When the samples are too large to be imaged entirely in the horizontal field of view of the camera, the choice of the half-acquisition approach is made: the samples are rotated over 360° rather than 180°. In half-acquisition mode (as for the data presented in this thesis), the sinogram stitching is required. This step transforms the 2D projections originally acquired over 360°, in 2D projections recorded over 180° but with a width twice the conventional one. Consequently, sinograms are twice larger. In order to perform the operation of *sinogram stitching*, the software is conceived to suggest the most appropriate center of rotation [61]. If the center of rotation proposed by the software does not fit appropriately, it can be adjusted subequently by the user after looking at the preview of a reconstruced slice. In Fig. 1.13c an example of stitched sinogram for a mouse brain sample is displayed. The software also helps to soften the ring artefacts that may occur in the final reconstructed slices by treating the sinograms directly. In fact, the presence of

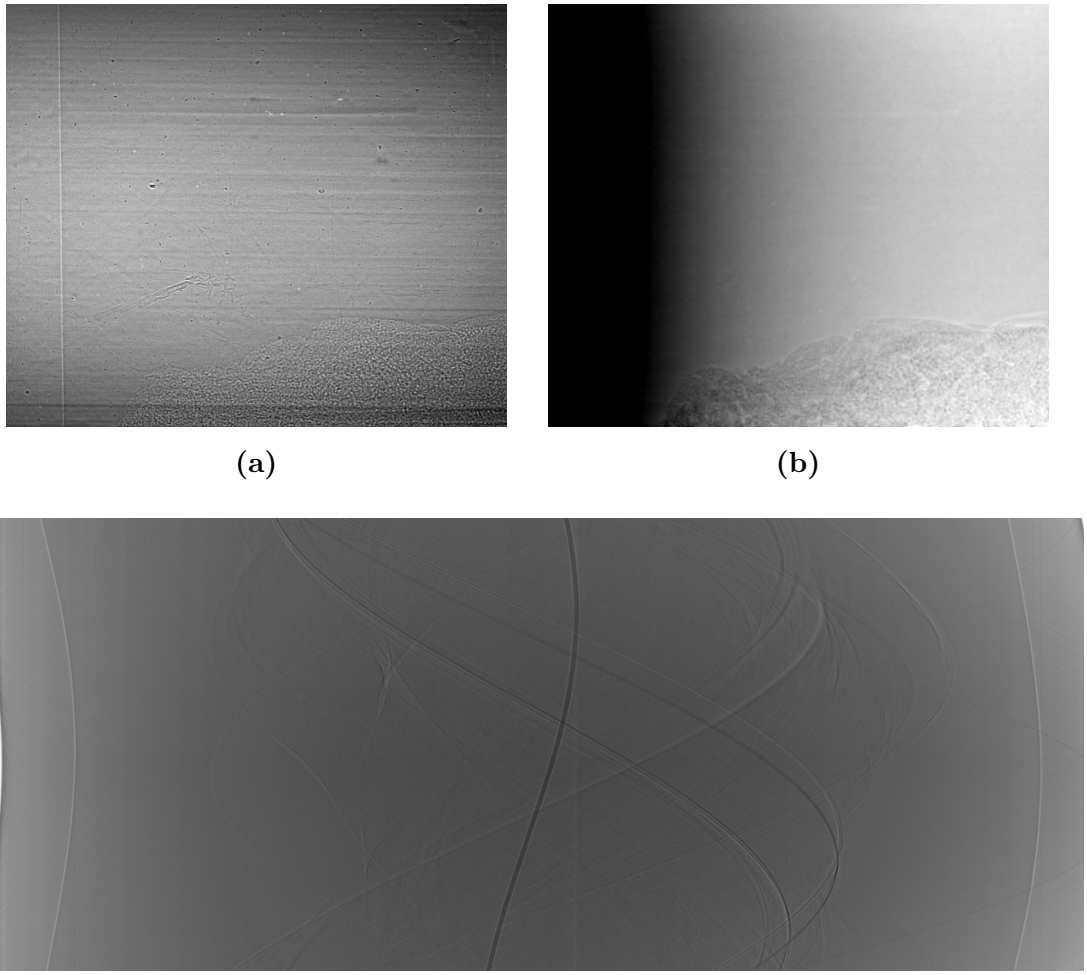

(a) **(b)**

(c)

Figure 1.13: (a) 2D XPCT projection of a melanoma. (b) 2D XPCT projection of the same sample in Fig. 1.13a after the implementation of Paganin's algorithm. (c) Stitched sinogram for a mouse brain sample.

possible rings can be identified *a priori* by observing if anomalous vertical stripes are visible in the sinogram images, as in the case of Fig. 1.13c where few thick vertical lines overlap the multiple sinusoids. The software allows the user to use one of the following ring removal filters: Raven [62], Boin and Haibel [63], Munch [64], Oimoen [65].
To get a phase-shift map, a phase-retrieval algorithm can be applied for disentangling the phase from the intensity. Thus, the next step after the pre-processing, is indeed the *phase-retrieval*. In this section of the software pipeline, two algorithms

are available: Paganin′s method [51] implemented for solving the transport of intensity equation [50]; and, Moosman′s approach based on the projected version of the contrast-transfer function [52].
Paganin′s algorithm was used to treat the data of this thesis. For instance, Fig. 1.13b illustrates the phase-retrieved projection of a raw projection capturing a melanoma view (Fig. 1.13a) after the implementation of Paganin's algorithm.
The last step to complete the reconstruction process consists in the application of a tomographic *reconstruction* algorithm. SYRMEP Tomo Project offers the possibility of choosing among the traditional Filtered Back Projection (FBP) algorithm and algebraic reconstruction techniques, such as: Simultaneous Iterative Reconstruction Technique (SIRT) [66], Simultaneous Algebraic Reconstruction Technique (SART) [67], Conjugate Gradient Least Squares (CGLS) [68], Equally Sloped Tomography (EST) [69], Minimum Residual FBP (MR-FBP) [70]. FBP method is the most common approach and it is widely recommended in case of large datasets, whereas the algebraic techniques may be more efficient with a limited number of projections [55].
Finally, the *post-processing* window allows cropping the final images and calibrating their gray scale values.
The images reported in this manuscript were obtained according to this protocol: normalization with conventional and dynamic flat-field correction, sinogram stitching, ring removal on sinogram images by choosing one of the ring removal filters listed before and tuning its specific parameters according to a visual assessment of preliminary reconstructed slices, phase retrieval implementation through Paganin's method and slices reconstruction with FBP algorithm in combination with Shepp-Logan filter.
Filtered Back-Projection algorithm is an alternative implementation of the Fourier Slice Theorem. As it was mentioned before, the theorem states that the Fourier transform of a projection is a line passing through the origin in 2D Fourier space. Although the theorem proposes a solution to the problem of reconstruction of tomography images, it is difficult to implement because the sampling pattern in the Fourier space is in polar coordinates. To perform a 2D inverse Fourier transform, these samples must be interpolated on a Cartesian grid and this is not an easy step as it could produce errors that compromise the appearance of the final image [27].
The Back-Projection algorithm relies on the idea of roughly estimating the origi-

nal image by back propagating the acquired projections through the object, along the directions in which the views were originally acquired. In this way, the final back-projected image is given by the sum of all back-projected views. But back-projection from many directions results in a denser sampling near the origin and a sparser sampling away fom the origin. This non-uniform sampling leads to final blurred images.
To reduce this blurring effect, a high-pass ramp filter is used in combination with the back-projection. This approach is known as *Filtered Back-Projection*. The filtering operation can be applied before or after the back-projection step. If the back-projection is performed first, the unblur operation consists in the use of a 2D filter, afterward; if the filtering is applied before the back-projecton, the operation is simpler since each projection has to be convolved with a 1D filter.
To derivate the back-projection formula, let start from the inverse 2D Fourier transform of the image function $f(x, y)$ in Cartesian coordinate:

$$f(x,y) = \int_{-\infty}^{\infty}\int_{-\infty}^{\infty} F(u,v)e^{j2\pi(xu+yv)}dudv \tag{1.28}$$

and let switch to polar coordinate system:

$$f(x,y) = \int_{0}^{2\pi} d\theta \int_{0}^{\infty} F(\omega\cos\theta, \omega\sin\theta)e^{j2\pi\omega(x\cos\theta+y\sin\theta)}\omega d\omega \tag{1.29}$$

By applying the Fourier Slice Theorem, the Fourier transform of the image function can be replaced with the Fourier transform of its projection at angle θ:

$$F(\omega\cos\theta, \omega\sin\theta) = P(\omega,\theta) \tag{1.30}$$

Consequently, the inverse 2D Fourier transform results:

$$f(x,y) = \int_{0}^{2\pi} d\theta \int_{0}^{\infty} P(\omega,\theta)e^{j2\pi\omega(x\cos\theta+y\sin\theta)}\omega d\omega \tag{1.31}$$

For parallel sampling geometry, this relationship is valid among the projections:

$$p(t,\theta+\pi) = P(-t,\theta) \tag{1.32}$$

Similarly, for their Fourier transforms:

$$P(\omega, \theta + \pi) = P(-\omega, \theta) \tag{1.33}$$

Therefore by taking into account this symmetry property and by using the coordinate system shown in Eq. 1.4, Eq. 1.31 becomes:

$$f(x, y) = \int_0^{\pi} d\theta \int_{-\infty}^{\infty} P(\omega, \theta)|\omega| e^{j2\pi\omega t} d\omega \tag{1.34}$$

$P(\omega, \theta)|\omega|$ is the Fourier transfom representing a projection at angle θ in the spatial domain, filtered by a function whose frequency domain response is $|\omega|$. This is known as filtered back-projection and states that the reconstructed image at the location (x, y) is the sum of all filtered projection samples passing through that point. Eq. 1.34 can also be rewritten as follows:

$$f(x, y) = \int_0^{\pi} g(xcos\theta + y \sin\theta) d\theta \tag{1.35}$$

since

$$g(t, \theta) = g(x \cos\theta + y \sin\theta) = \int_{-\infty}^{\infty} P(\omega, \theta)|\omega| e^{j2\pi\omega(x \cos\theta + y \sin\theta)} d\omega \tag{1.36}$$

The function $|\omega|$ is not integrable; therefore, a band-limited filter has to be introduced at this point. The most common filters are: Ram-Lak that uses a rectangular window; Shepp-Logan that uses a sync window [71] and Hamming that uses a generalized Hamming window.

1.5 Post-Processing via FIJI

By means of the open-source software FIJI [72], the reconstructed datasets have been visualized in sequence and, in some cases, subjected to post-processing treatments for correcting minor remaining artifacts and enhancing the data quality. The software offers a wide choice of filters and plugins for different applications. As basic step after the reconstruction, it allows setting brightness/contrast levels

in order to distinguish and emphasize anatomic features of the sample.
The following sections are dedicated to a detailed description of the plugins used to reconstruct the slices presented in this manuscript.

1.5.1 Filtered Gaussian blurred image

A recurring artefact in the reconstructed slices is the presence of an over-saturated central disk that covers the underlying structural information of the sample, as in Fig.1.14a. This inconvenience can be corrected by subtracting the "Gaussian Blur" filter of the image.
"Gaussian Blur" is a low-pass filter attenuating the high frequencies. The filter creates an image blurring effect through a convolution of the original image with the 2D Gaussian function [73]:

$$g(x,y) = e^{-\frac{x^2+y^2}{2\sigma^2}} \tag{1.37}$$

The degree of smoothing of the image is related to the standard deviation, σ, of the distribution. The quality of the resulting image depends on how the user sets the optimal value for σ. If σ is too high, the filter has no effect on the image, the central artefact is untouched. On the other hand, if σ is too small the subtracted image will be edge-enhanced too much, instead. The user has the task of finding the best compromise between artefacts suppression and image conservation. Fig. 1.14b shows the resulting image after the subtraction of a Gaussian blur filter with $\sigma = 50$.

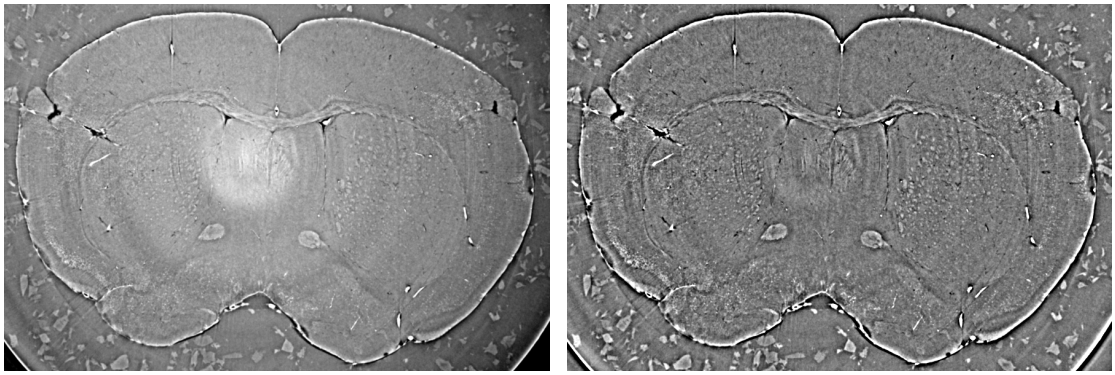

(a) **(b)**

Figure 1.14: (a) Original XPCT image showing a whiter disk at the center. (b) XPCT image obtained by the subtraction from Fig. 1.14a of its Gaussian blur filtered image with $\sigma = 50$.

1.5.2 Ring artefact removal

Ring artefacts are the most annoying since they compromise the appearance and the quantitative analysis of the images. They might be due to impurities in the scintillator or mis-calibration of the X-ray detectors [27, 59]. These defects affect the recording of the projections by generating unrealistic concentric circles, or semicircles that superimpose to the final slices after the reconstruction process. Although sinograms are subjected to de-stripe filtering in the pre-processing step implemented in SYRMEP Tomo Project, it may happen that filter parameters are not appropriately tuned with the fear of suppressing features of the specimen. As a consequence, some rings continue to be present in the final images. Here, it will be shown how to correct ring artefacts in the post-processing phase by using the open-source software FIJI. The solution lies in the application over the reconstructed polar slices of the "Stripe Filter" contained in the "Xlib" plugin developed by Munch et al. [64]. This filter is based on the implementation of the Gaussian filter in the Fourier domain on decomposed images by a 2D discrete wavelet transform. Fig. 1.15a illustrates a XPCT image of a mouse brain reconstructed with the standard pipeline presented in the previous paragraph: residual dark and bright rings compromise the interpretation of the figure and hide anatomic structures. The adopted strategy for preserving the original image comprises the following steps:

1. Conversion of the slice with ring artefacts to polar coordinates by means of ImageJ "Polar Transformer" plugin. In this way the rings in the input image (Fig. 1.15a) become vertical stripes in the polar system (see Fig 1.15c);

2. Decomposition of the image in polar coordinates by Daubechies wavelets by choosing an appropriate decomposition level through the option Stripe Filter of "Xlib" plugin of FIJI. In mathematical terms, this command corresponds to the decomposition of a 2D-signal into four terms:

$$f(x,y) = \sum_{j}\sum_{k} C_{\mathrm{L(j,k)}}\Phi_{\mathrm{L(j,k)}}(x,y) + \sum_{i=1}^{L}\sum_{j}\sum_{k} C_{\mathrm{h(i,j,k)}}\Psi_{\mathrm{h(i,j,k)}}(x,y) + \sum_{i=1}^{L}\sum_{j}\sum_{k} C_{\mathrm{v(i,j,k)}}\Psi_{\mathrm{v(i,j,k)}}(x,y) + \sum_{i=1}^{L}\sum_{j}\sum_{k} C_{\mathrm{d(i,j,k)}}\Psi_{\mathrm{d(i,j,k)}}(x,y) \tag{1.38}$$

   where the first term is a low pass term, and the remaining are horizontal, vertical and diagonal terms respectively; where $C_{\mathrm{L(j,k)}}$, $C_{\mathrm{h(i,j,k)}}$, $C_{\mathrm{v(i,j,k)}}$, $C_{\mathrm{d(i,j,k)}}$ are coefficients; $\Phi_{\mathrm{L(j,k)}}$ is the scaling function, and $\Psi_{\mathrm{h(i,j,k)}}$, $\Psi_{\mathrm{v(i,j,k)}}$, $\Psi_{\mathrm{d(i,j,k)}}$ are Daubechies wavelets[64].

3. Damping the Fourier transform of f(x,y) through the multiplication of its coefficients with a Gaussian function:

$$g(\hat{x},\hat{y}) = 1 - e^{-\frac{\hat{y}^2}{2\sigma^2}} \tag{1.39}$$

   The value σ represents the width of the filter in the vertical direction.

4. The "Stripe Filter" automatically generates the inverse wavelet transform of the inverse Fourier transform of the Gaussian filtered image (see Fig1.15d).

5. Conversion back to Cartesian coordinates by means of "Polar Transformer" plugin (see Fig.1.15b).

The final image obtained through this protocol (Fig. 1.15b) shows how ring artifacts have successfully been suppressed.

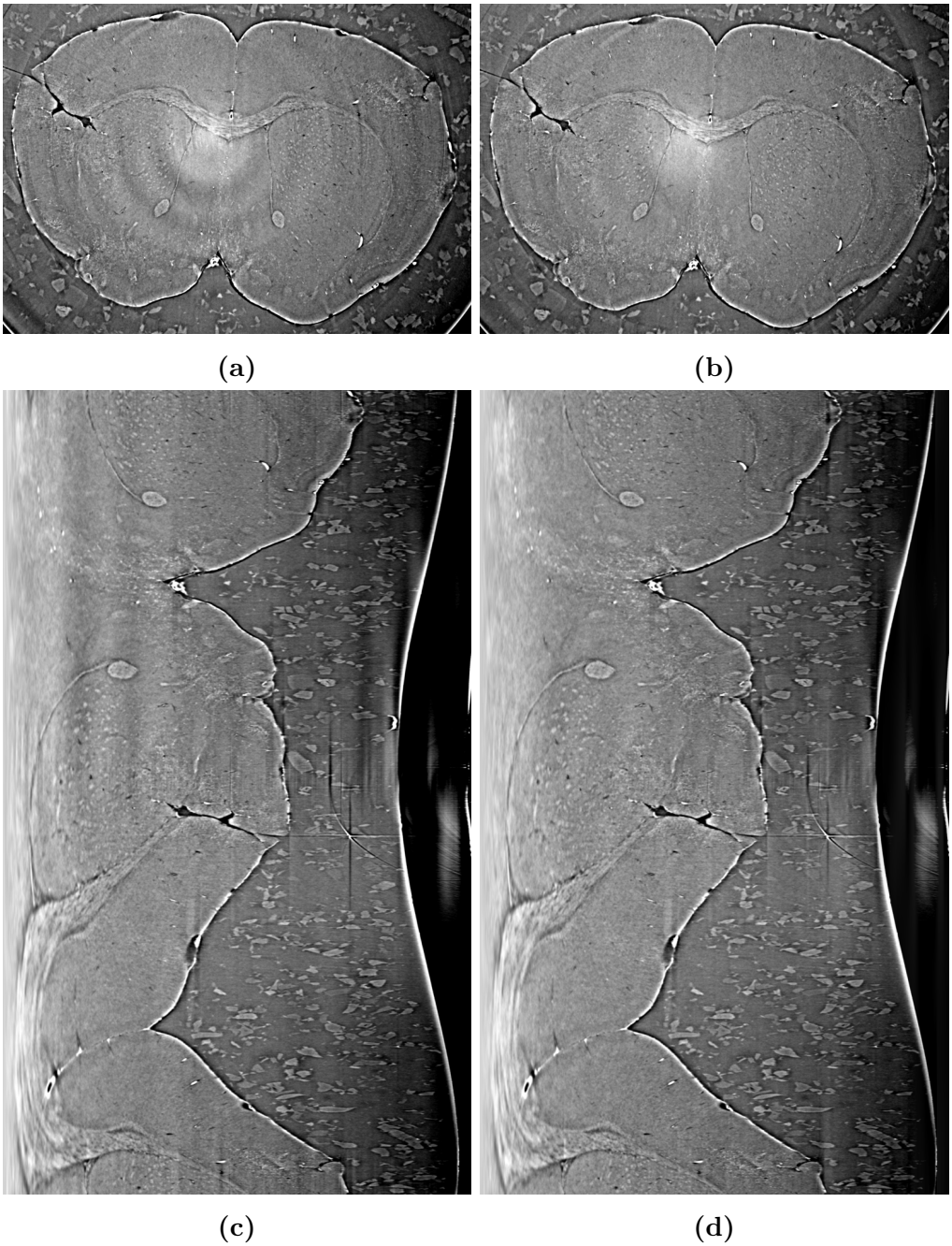

Figure 1.15: (a) XPCT image with ring artefacts. (b) XPCT image corrected by Stripe Filtering with parameters DB24, level = 7, $\sigma = 4$. (c) Image 1.15a converted into polar coordinates. (d) Image after the stripe filtering operation in polar coordinates.

The parameters of "Stripe Filter" have been set with a qualitative criterion: the

optimal values were chosen on visual assessment until the rings disappeared completely.

1.5.3 Volume rendering techniques

Volume rendering is a display technique used for reducing a set of 2D sequential images that form a volume into a single 2D view. Maximum intensity projection and minimum intensity projection are a variant of direct volume rendering [27]. A maximum intensity projection figure is obtained by projecting onto a plane the brightest pixels encountered by a set of parallel imaginary rays passing through the volume. This kind of graphical representation allows standing out the densest structures like highly absorbing objects. An example of maximum intensity projection image is shown in Fig. 1.16.

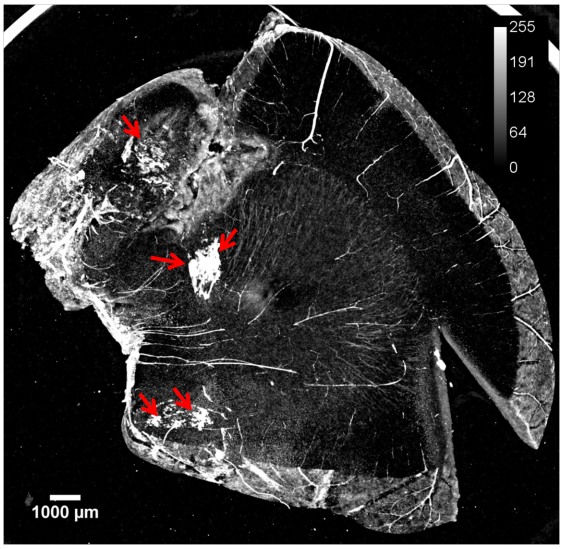

Figure 1.16: Maximum intensity projection image of a mouse brain stack of slices corresponding to a thickness of 1.5 mm. Owing to the presence of gadolinium nanoparticles injected in the sample and accumulated in tumors, the image allows recognizing the multiple metastases (displayed in white and indicated by red arrows) developed in the mouse brain.

This image shows a mouse brain section with multiple metastases filled with gadolinium nanoparticles (white masses indicated by red arrows) and, in white a set of not perfused vessels. Analogously, a minimum intensity projection image is produced through the projection of the minimum pixel values met by a ray

along a line. This sort of image is useful for identifying the points with the lowest attenuation coefficients, such as empty vessels or air pathways. An example of minimum intensity projection is displayed in Fig. 1.17 and reveals the pattern of empty vessels after the perfusion of a mouse brain.

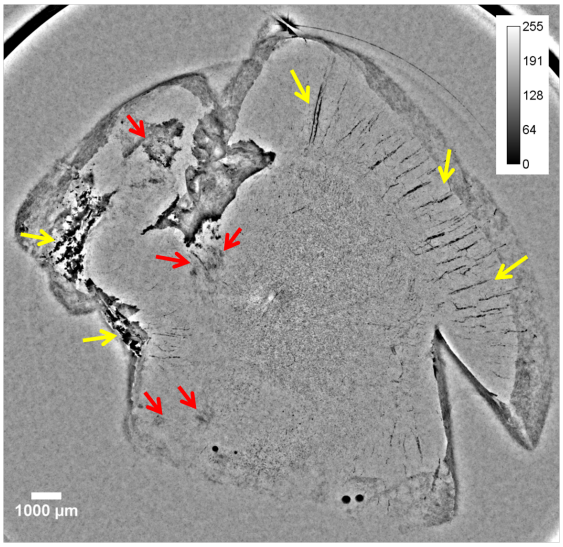

Figure 1.17: Minimum intensity projection image of the same mouse brain stack of slices seen in Fig. 1.16. As indicated by the red arrows, the image allows recognizing the shadows of the metastatic masses and trasversal (black spots) and longitudinal empty vessels as those indicated by the yellow arrows.

The intensity of maximum and minimum projections depends on the length of the projection path; to limit intensity fluctuations, it is recommended to perform the projections over small sections instead of the entire volume of the object [27]. The images of maximum and minimum intensity shown in this thesis were created by using FIJI. The software was used also for producing new images by combining maximum and minimum projection images through basic mathematical operations, such as the image depicting the mouse liver vasculature in Fig. 1.18. For instance, this image was obtained from the subtraction of maximum-minimum images of the same sample section. The image shows two main veins, recognizable for their large diameters and wide bifurcations, surrounded by a tangled net of peripheral arteries.
Another example of combined volume rendered image is displayed in Fig. 1.19 for which the ratio of maximum and minimum projection images of the same stack of slice was taken. It shows the vessels pattern in the mouse brain.

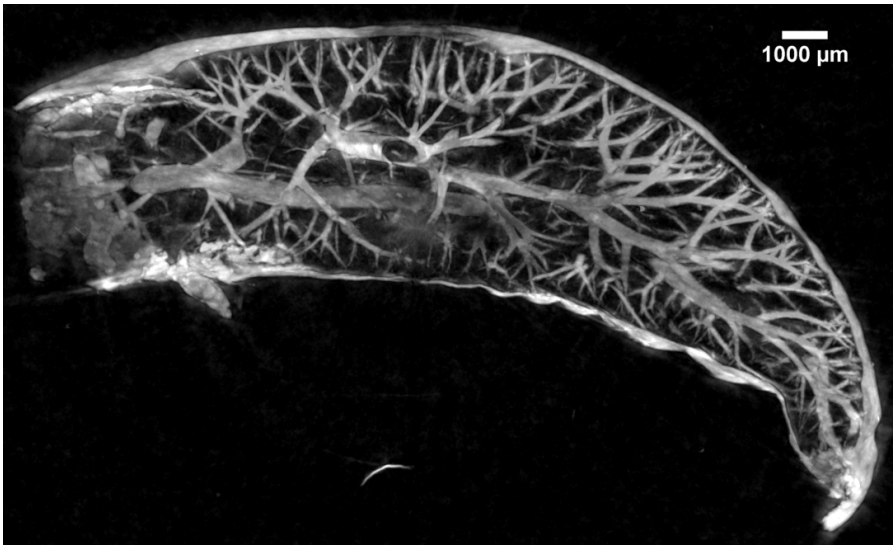

Figure 1.18: Volume rendered image depicting mouse liver vascular network. The image was obtained from the difference between the projections of maximum and minimum pixel values of a liver section thick 2.06 mm.

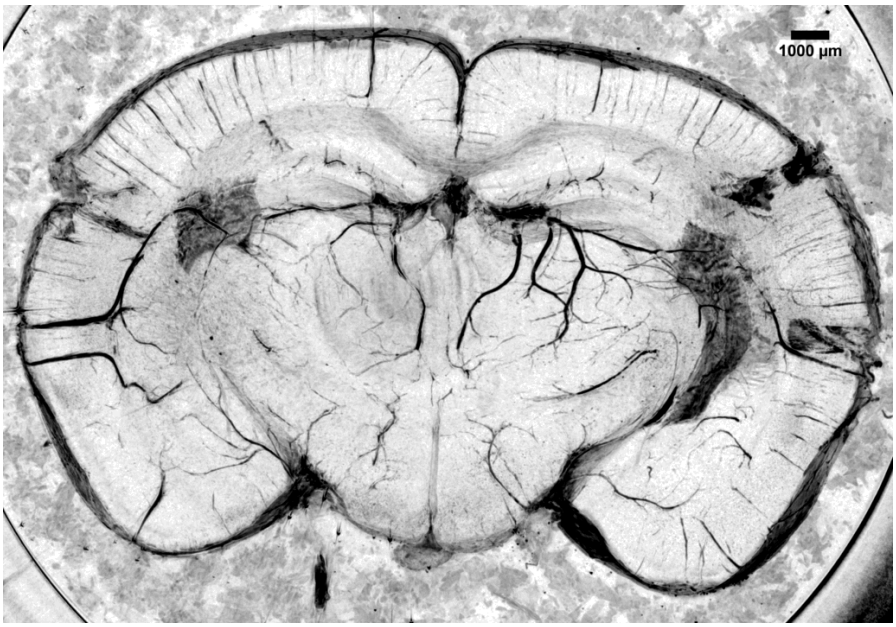

Figure 1.19: Volume rendered image depicting a thin section of the mouse brain vascular network. The image was obtained from the ratio between the projections of maximum and minimum pixel values.

1.6 Visualizations of 3D organ models

Volume visualization allows the visual representation of a full dataset, or of a part of it, by superimposing a sequence of 2D aligned images. The volume visualization relies on two basic steps: segmentation and classification of the voxels.
The segmentation is realized by evaluating the voxel intensity distribution in a histogram, where the horizontal axis represents all existing voxel values, and the vertical axis the number of voxels with that intensity. Different tissue types may be differentiated according to their composition and density. A large number of voxels with the same intensity indicate a region made up of a homogeneous material. The classification step allows discriminating how individual voxels contribute to the final image, instead [74]. Generally, the voxel values are mapped to the optical properties of the material to be represented through one or more transfer functions, depending on lightening model. In standard cases, colours and opacity are assigned to voxels [75]. The 3D visualization of the organs explored in this thesis was performed by using the open-source software VolView [1]. The software has a graphical interface that shows sagittal, coronal and axial planes (Appendix D) at the same time and produces volume representations by superimposing the slices, previously pre-processed and aligned. The user may rotate the volume around one of the three orthogonal axes and may adjust its appearance through a side panel that allows setting opacity and colours. Voxels are mapped by a linear piece-wise function. The user may enhance the structures of interest in the volume by the control points at the end of each segment of the function. Different colours describe different types of material. Opacity function allows making transparent less relevant structures such as the outer surface of an object, and enhanced the visualization of anatomic features normally hidden, such as vessels and nanoparticles uptake. For instance, in Fig. 1.20 the 3D volume rendering of a mouse spleen is displayed. The representation in false colours scale shows the densest spleen areas varying from orange to green.

[1] http://www.vtk.org/

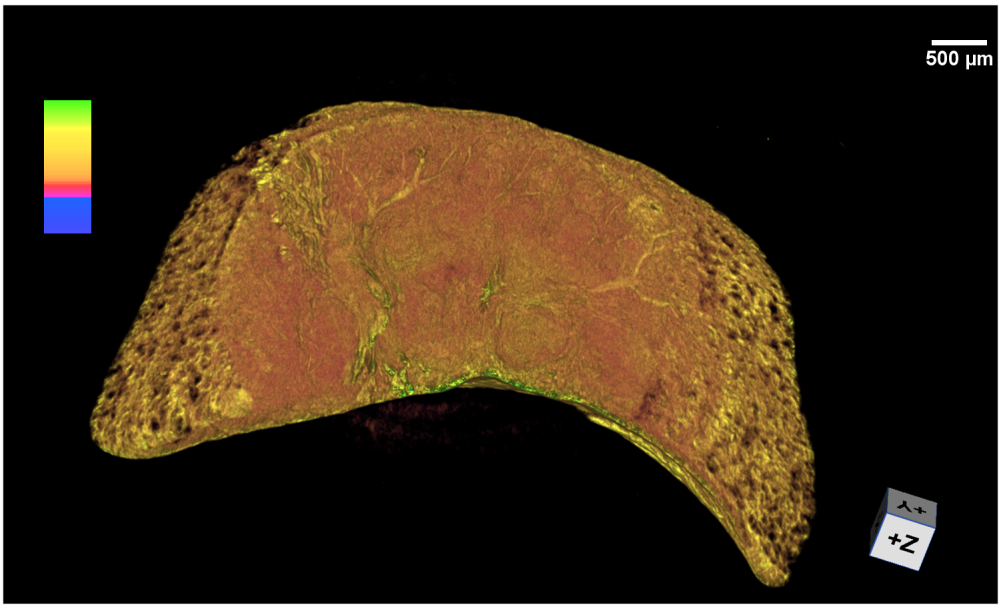

Figure 1.20: 3D visualization in false colours of a mouse spleen. The highest intensity pixels (from orange to green) correspond to the densest parts of the spleen.

1.7 Summary

The first part of this chapter summarized the theoretical aspects on which X-ray tomography is based and, the problem of image reconstruction. Mathematical dissertations of the main theorem (Fourier Slice Theorem) and algorithms (Paganin's phase retrieval and FBP) used are included.
This first general part was necessary to intoduce the tomography imaging method adopted in this thesis: X-ray Phase-Contrast Tomography (XPCT). XPCT has been chosen to resolve nanoparticles distribution in several mice organs for different pre-clinical evaluations. One of the main objectives of this thesis is to demonstrate how to discriminate nanoparticles signal from the surrounding tissue. As it was mentioned, the problem of image reconstruction for an inhomogeneous material is challenging and the adopted strategy will be illustrated in the next chapters.
In the second part of the chapter, the image processing strategies adopted for the XPCT data treatment have been described. The steps accomplished by Syrmep Tomo Project for the production of the virtual slices of the sample from its projections have been explained in detail.
Although the software used for the XPCT image reconstruction supports a de-ring

operation; some minor artefacts could continue to affect the final images. Therefore, descriptions of the main FIJI plugins applied in the post-processing phase for the improvement of the reconstructed slices have been reported.
FIJI software was also used for obtaining volume rendered images through the projection of maximum intensity pixel values, minimun intensity pixel values and by performing combinations of the previous volume rendered images through different mathematical operations. Furthermore, with FIJI it was possible to correlate stacks of slices belonging to different datasets.
The 3D volume visualizations and segmentations in false colour scale were realized through Volview software, instead.

Chapter 2

Application of tomographic imaging in Theranostics

Within this chapter, new and unprecedented XPCT images of mice tissue loaded with three different types of theranostic agents are illustrated. Theranostic nanoparticles are a promising point of strength of oncological research. They are ultrasmall agents useful at the same time for therapeutic and diagnostic purposes. Thanks to their small size, nanoparticles can permeate and passively accumulate in tumors. In addition, owing to their metallic atoms they enhance the tumor visualization and the tumor radiosensitization effects.
In this framework, we explored the potentiality of the XPCT approach as a novel and complementary median-scale imaging method to resolve nanoparticles distribution in tissues. Here we present the reconstructed images after a XPCT experiment carried out at the biomedical beamline ID17 at European Synchrotron Radiation Facility (ESRF Grenoble, France). The investigation was performed in collaboration with CNR-Nanotec (Rome, Italy), Institute for Advanced Biosciences (Grenoble, France) and Institut Lumière-Matière (Lyon France) and, the full data processing was done at Laboratoire d'Optique Appliquée (Palaiseau, France).
To introduce our results, a brief summary of the state of the art about nanoparticles imaging at large and small scales is reported. Then, the problem of nanoparticles elimination is treated. Three distinct cases are examined: a mouse kidney containing gadolinium loaded nanoparticles, gold zwitterionic nanoclusters retained in a mouse liver and a mouse spleen with platinum nanoparticles. Subsequently, the images of a mouse lung affected by carcinoma and reporting multiple

metastases loaded with nebulized gadolinium nanoparticles are displayed. Then, high-resolution images showing gadolinium nanoparticles repartition in multiple melanoma brain metastases are illustrated, followed by the visualization of melanin pigments distribution in melanoma tumor layers. In conclusion, the use of K-edge subtraction imaging for isolating nanoparticles signal from the surrounding tissue components is discussed.

2.1 Imaging of theranostic nanoparticles: state of the art

Nanoparticles penetration and distribution in living organisms is a problem of a crucial importance for pre-clinical evaluations. Many imaging techniques at different scales are adopted to monitor nanoparticles behavior, from their interaction with constituents of the cell, up to their arrangement in organ tissues.
At cellular level there are several optical techniques with a resolution of some hundreds of nanometers allowing the visualization of nanoparticles internalization in cells, such as confocal microscopy, fluorescence microscopy, transmission electron microscopy (TEM), two-photon microscopy, photo-activated localization microscopy (PALM) and stochastic optical reconstruction microscopy (STORM) [76, 17, 77, 78, 79]. However, nanoparticles detection by fluorescence techniques requires the application of fluorophores, but at the risk of misrepresenting the real nanoparticles distribution since external probe can detach from nanoparticles [16].
At higher-scales Laser Induced Breakdown Spectroscopy (LIBS) has been performed to get insights about nanoparticles location in biological tissues with few tens of μm of spatial resolution [1]. Even if pseudo-3D representations were achieved [80], it showed some limitations. It is an invasive method, implying an irreversible cut of the sample into sections few μm thick. Consequently, by focusing on a specific area, it loses sight of the whole organ and makes challenging the full three-dimensional visualization of nanoparticles distribution in an organism. Moreover, because of laser ablation LIBS could damage surface tissue [81] and remove part of the nanoparticles [16].
Diagnostic techniques such as Magnetic Resonance Imaging (MRI) and Positron Emission Tomography (PET) are often used at organ-scale or body-scale and provide 3D information, but they are strongly limited by low resolution (few mm

in-vivo and sub-100 μm ex-vivo) [13, 14, 15]. Due to their resolution, they can only globally show if nanoparticles reached their target but they are not suitable to find them precisely in a tissue. From this, we concluded that 3D high-resolution nanoparticles localization in body organs is still a topic to better investigate.
This thesis focuses on the three-dimensional mapping of nanoparticles by means of X-ray Phase Contrast Tomography (XPCT). XPCT is non-destructive multi-scale technique that, thanks to the strong X-ray penetration power, allows the imaging of the inner tissues of an organ without any physical manipulation of the sample itself and, at the same time it permits of visualizing anatomical features on a median scale between few mm (MRI and PET) and sub-μm (microscopy techniques) [82, 83]. Medical X-ray diagnostics relies on the different absorption properties of the elements constituting the imaged material. Soft tissues, like biological materials, are mainly composed by light atoms (80% of water and a bit less than 20% of carbon), thus they are characterized by low absorption and low capacity of providing contrast in radiological images; whereas heavy metals (gadolinium, gold, platinum, bismuth) are very absorbing. Some are used as contrast agents. Since theranostic nanoparticles are made up of metals with high Z-numbers and tend to form clusters of different size and shape after the injection, the detection of nanoparticles through XPCT images is based on the contrast differences produced by nanoparticles with respect to surrounding tissues.

2.2 Experimental conditions

All the examined samples were removed from mice at different times after the administration of gadolinium, gold or platinum nanoparticles.
The gadolinium-loaded nanoparticles used in this thesis are named AGuIX® and they are mainly described in [84, 85]. Briefly, AGuIX® are made up of a polysiloxane matrix surrounded by DOTAGA (1,4,7,10-tetraazacyclododecane-1-glutaric anhydride- 4,7,10-triacetic acid)-gadolinium^{3+} chelates and exhibit a hydrodynamic diameter of about 3 nm. Today they are under clinical experimentation and, clinical trials phase I has been already completed. These kind of nanoparticles were provided by NH TherAguiX [86] and administered in many of the samples presented in this thesis. Indeed, we examined their biodistribution in mice kidney, lungs and brain.
The gold nanoclusters have a zwitterionic coating that provides high stability in

water [87] and a hydrodynamic diameter of roughly 2.3 nm [88]. They were also provided by Institute for Advanced Biosciences and we examined only a mouse liver containing this kind of theranostic nanoparticles.
The platinum-based nanoparticles have a hydrodynamic diameter of roughly 6.2 nm. They were provided by Institute for Advanced Biosciences and we examined their biodistribution in a mouse spleen.
All samples were immobilized with Agar-Agar gel in Eppendorf tubes and placed on a high-resolution rotation stage. The samples were illuminated with a quasi-monochromatic X-ray parallel beam according to the in-line phase-contast geometry (see Chapter 1).
The beam available at ID17 beamline has a minimum size equals to 10.0 $\times$ 51.0 μm^2, and a maximum size equals to 150.0 x 7.0 mm^2 [89]. Due to a Si(111) double bent Laue crystal, beam monocrhomaticity is $\Delta E/E \simeq 10^{-4}$ in the energy range 25-150 keV [90].
The projections were recorded by a CMOS camera connected to an optical system having a final pixel area of 3 $\mu m \times$ 3 μm. The propagation distances and the energy acquisition varied according to the examined samples and they are specified for each shown sample in the following sections. Because of the narrow field of view of the camera (7 mm $\times$ 6.4 mm), all the samples were measured in half-acquisition (i.e. over 360°) and virtually divided in more pieces along the vertical axis. Each piece of the tomographic scan resulted in 4000 projections. The acquisition time of the projections was 0.07 s for a single-projection.

2.3 Renal clearance

It is known that long term retention of nanoparticles in organisms could induce toxicity [91, 92, 93, 12]. Therefore, in the pre-clinical evaluation phase monitoring their metabolism, accumulation, distribution and clearance is of fundamental importance. As starting point for the localization of the nanoparticles in biological tissues by XPCT, we focused on the renal elimination of the above-mentioned gadolinium-based nanoparticles, AGuIX®.
In previous pre-clinical studies it was found that AGuIX® are mainly eliminated through kidneys and that one day after their administration less than 0.2% of the injected dose was detected in other mice organs [94, 95, 85, 96, 97, 19]. More in detail, Laser Induced Breakdown Spectroscopy (LIBS) allowed accurately study-

ing the kinetics of elimination of AGuIX® thanks to its sensitivity to the chemical composition of the scanned materials [1, 19]. LIBS is a label-free technique used to quantify multichemical elements in biological tissues. It consists in focusing laser pulses on the surface of a sample in order to create a plasma and then get an elemental map pixel by pixel. This map is retrieved by extracting the emission lines of atoms and ions excited by the high plasma temperature [16]. In Fig. 2.1, it is shown a map of nanoparticles distribution by means of LIBS scans.

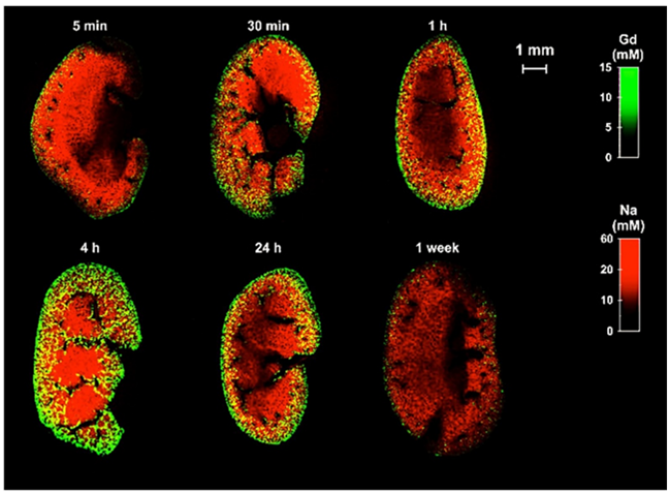

Figure 2.1: LIBS coronal sections of murine kidneys from [1]. The images show a quantitative map of gadolinium and sodium in kidneys from 5 minutes up to 1 week after nanoparticles injection. The images were acquired with 40 μm spatial resolution.

Fig. 2.1 depicts the coronal sections of several mouse kidneys removed at different times (from five minutes to 1 week) after the intraveneous injection of AGuIX®. The images were recorded at 40 μm spatial resolution and are the superimposition of gadolinium (green) and sodium (red) maps. Since sodium is a constitutive element of the kidney, it was homogeneously detected all over the kidney whereas gadolinium was found mainly all around the cortex. This study reveals that the peak of accumulation of nanoparticles in kidney is three hours after their administration. Today, LIBS represents the most accurate 2D imaging approach to identify nanoparticles in biological materials as it can discern between endogenous and exogenus compounds of a specimen.
XPCT provides also high-resolution images at the organ scale but despite LIBS it does not compromise the integrity of the sample. This thesis aims at showing

that XPCT can be considered as a complementary tool to LIBS measurements. To test XPCT capabilities in locating nanoparticles, a mouse kidney was extracted 3 hours after the injection of AGuIX® nanoparticles and then, subjected to XPCT measurements. In Fig. 2.2, it is shown the 3D representation of an inner section of the kidney. The volume was created by superimposing a part of the virtual reconstructed XPCT slices of the kidney. The segmented image in false colour scale displays the highest intensity pixels in red/dark orange. This is the signal due to the presence of nanoparticles that were detected mainly in the peripheral region of the kidney and near the main collecting ducts. The remaining kidney tissue is represented in green. This result is in good agreement with the LIBS image depicting the case of a kidney 4 hours after injection of gadolinium nanoparticles, and it pushed us to deepen this issue of nanoparticles biolocalization by XPCT.

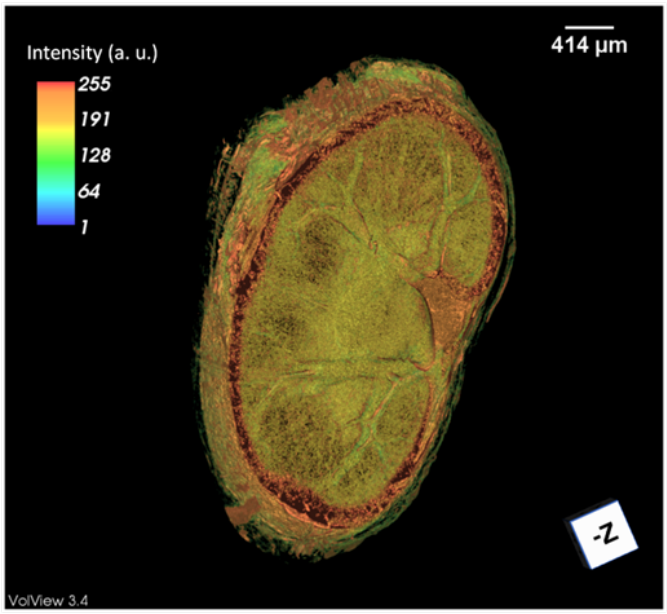

Figure 2.2: 3D visualization of a segmented piece of kidney. The image displays in red/dark orange the gadolinium nanoparticles and in green the renal tissue. According to this view, nanoparticles are distributed in the peripheral region of the kidney and in minor concentration next to the main vessels.

2.4 Liver elimination

Generally, nanoparticles with a size comprised between 20 and 200 nm are eliminated by the reticuloendothelial system (RES) [19]. This system includes the macrophages, the Kupffer cells placed in the liver and the reticular cells placed in the lungs, spleen, bone marrow and lymph nodes.
Nanoparticles design influences their life time in-vivo and their elimination process. Specifically, the key parameters conditioning nanoparticles pharmacokinetics, tumor uptake, biodistribution and retention are size, shape, chemical composition, surface coating, electric charge [92]. For instance, positively or negatively charged nanoparticles demonstrated to have short half-lives in blood and to be cleared mostly by liver and spleen [98]; thus reducing the possibility of accumulation in tumors. Conversely, nanoparticles coated with pegylated or zwitterionic molecules showed longer half-lives time in the vascular system, instead [98, 99]; thus increasing tumor uptake and the possible benefits deriving from therapies [88]. Liu and collaborators showed that gold nanoclusters coated with glutathione may reach a good trade-off between fast renal clearance and early passive tumor accumulation [100], while Xie and collaborators investigated their radiosensitization capabilities [101]. Thus, today there is a growing interest in the development of new gold nanoclusters with other surface coatings.
In this framework, the behaviour of zwitterionic gold nanoclusters in glioblastoma mouse model was observed with the support of multimodal imaging techniques, such as in-vivo whole body fluorescence imaging, LIBS and XPCT [88]. Within this collaboration with Institute for Advanced Biosciences, the use of XPCT was required to get complementary visualization of gold particles in liver tissue. We imaged a mouse liver 5 hours post-injection of 600 μM in 200 μL of $AuZwMe_2$ (zwitterionic gold nanoclusters). XPCT was performed at 82.20 keV, above gold K-edge. The propagation distance between the liver and the camera was set at 11 m. The virtual slices were reconstructed according to the protocol described in Chapter 1 with a ratio $\delta/\beta = 300$.
In Fig. 2.3 a 2D reconstructed XPCT slice is shown. Thanks to the high-resolution and the phase-contrast technique, the full anatomy of the liver is displayed with impressive sensitivity [102]. From the fully reconstructed dataset, it seems that gold nanoparticles scattered everywhere in the soft tissue giving a bright appearance to the tissue. As indicated by the red arrows, white areas made up of very small spots are mainly accumulated close to the hepatic vessels. This gives a

promising idea that it could be the signal of the presence of gold nanoparticles captured by the Kupffer cells present in the liver [103].

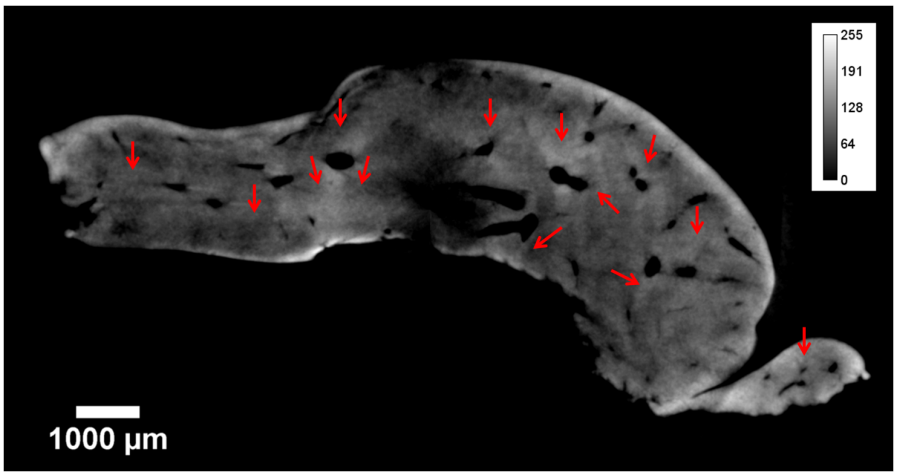

Figure 2.3: 2D XPCT virtual slice of the mouse liver where the red arrows indicate possible liver areas with gold nanoclusters accumulations.

Fig. 2.4 shows a section of the liver vasculature. From this visualization, bright spots are enhanced into peripheral small arteries. This could be due to the presence of a small concentration of nanoparticles still entrapped into the vasculature at the moment of the sacrifice.

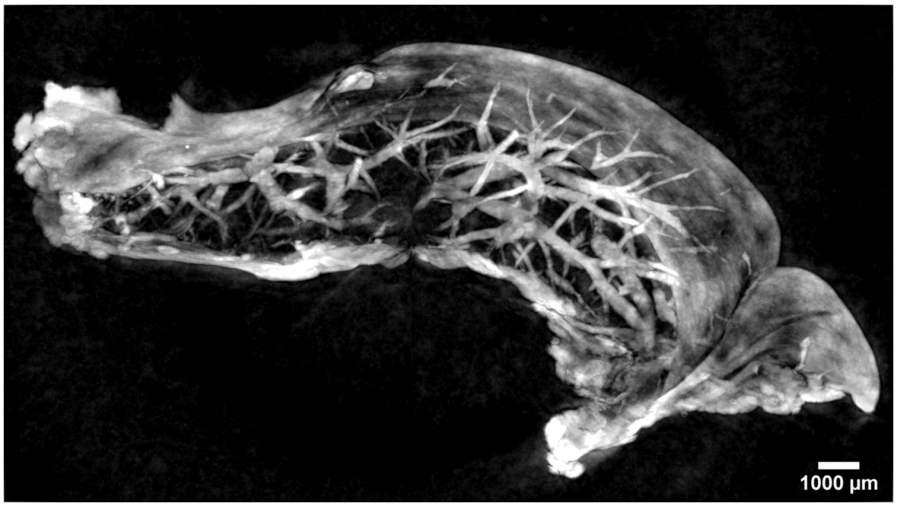

Figure 2.4: Volume representation of a liver section showing the vasculature. Some vessels appear brighter than others, very probably because of entrapped nanoparticles.

In Fig. 2.5, it is shown a 3D reconstruction of a thin piece of liver enabling the map visualization of densest areas in yellow. The image shows a homogeneous distribution of the highest pixel values pushing us to believe that gold nanoclusters are homogeneously distributed in the liver. XPCT is in agreement with LIBS measurements as described in [88].

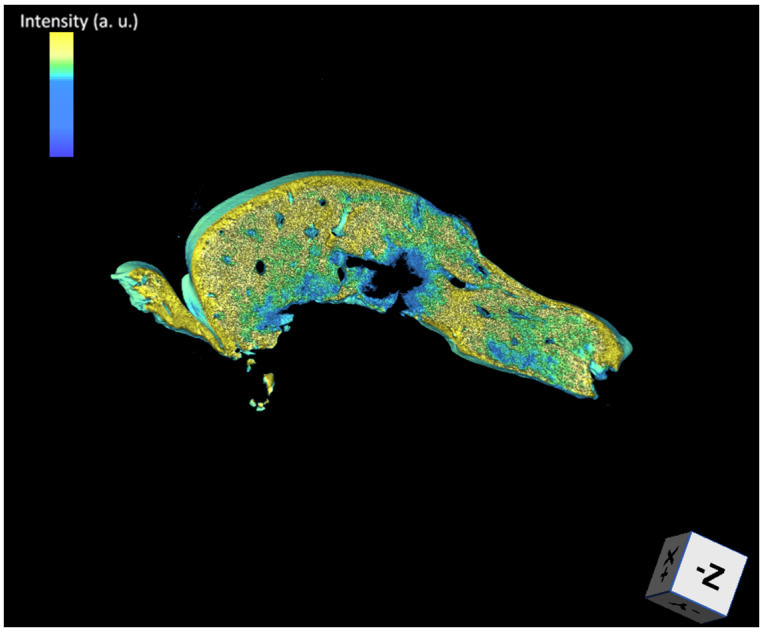

Figure 2.5: 3D rendering of a small portion of mouse liver (600 μm thickness). The representation in false colours shows in yellow the hepatic regions with the highest pixel values, i.e. the liver regions at highest density. This signal can be associated to the diffuse presence of gold nanoclusters retained in the liver.

In addition, Fig. 2.6 displays four different views of the entire 3D rendered liver. As it can be seen, a non-uniform yellow patina coats the liver surface and very dense regions were detected also in the liver tissue and visualized in orange. These could be the signatures of the scattered homogeneous signal produced by gold nanoparticles retained in the liver, while it is not clear yet the origin of the intense signal measured on the liver external surface. It could be due to gold deposition or it could be an artefact due to a not well tuned ratio δ/β [104]. Data treatment is still under process to deepen this unexpected effect.

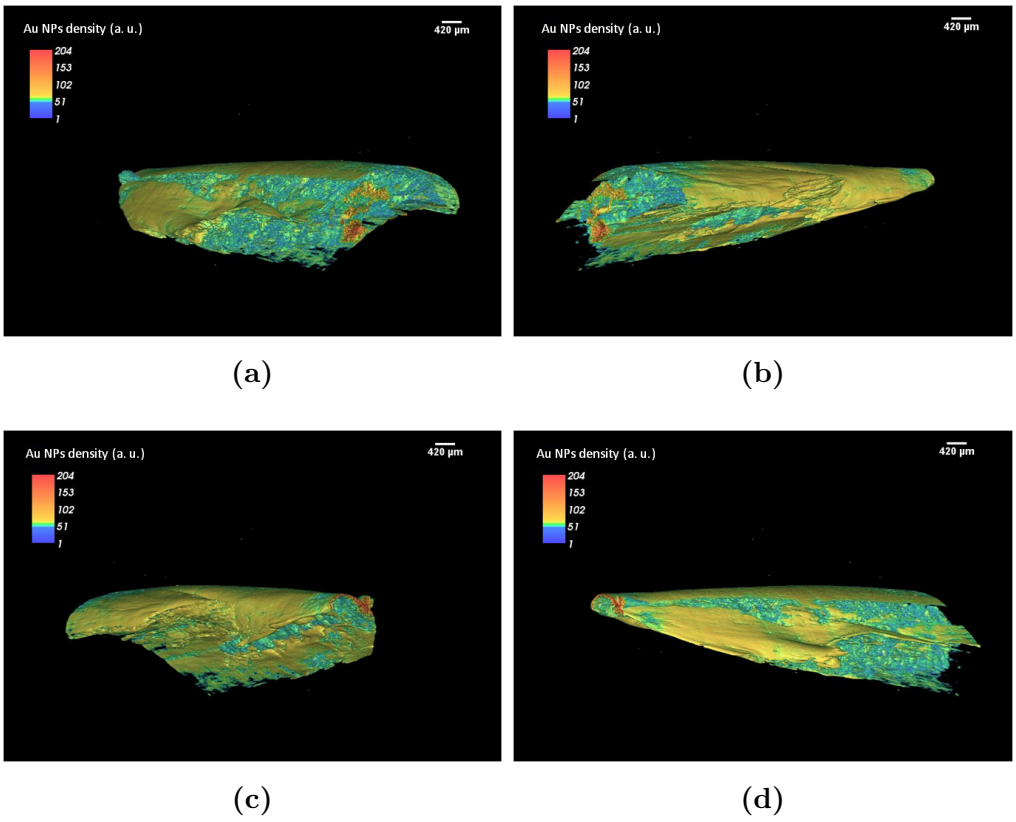

Figure 2.6: 3D visualization in false colours at different angles of the entire mouse liver.

2.5 Spleen elimination

Within this section, the XPCT images of a mouse spleen removed 5 *min* after the injection of 100 μL pure solution of platinum nanoparticles are displayed. The raw data were obtained with a propagation distance of 11 m and an energy of 79.9 keV, a value slightly above platinum K-edge. The phase-retrieval algorithm was implemented with a ratio $\delta/\beta = 73$. Here below, two spleen cross-sections (Fig. 2.7 and Fig. 2.9a) are displayed. The XPCT technique allowed achieving a spleen insight rich of details. For instance by looking at Fig. 2.7, it can be observed that B-cells, pointed by green arrows, can be well-discriminated from the red pulp, in turn indicated by orange arrows.

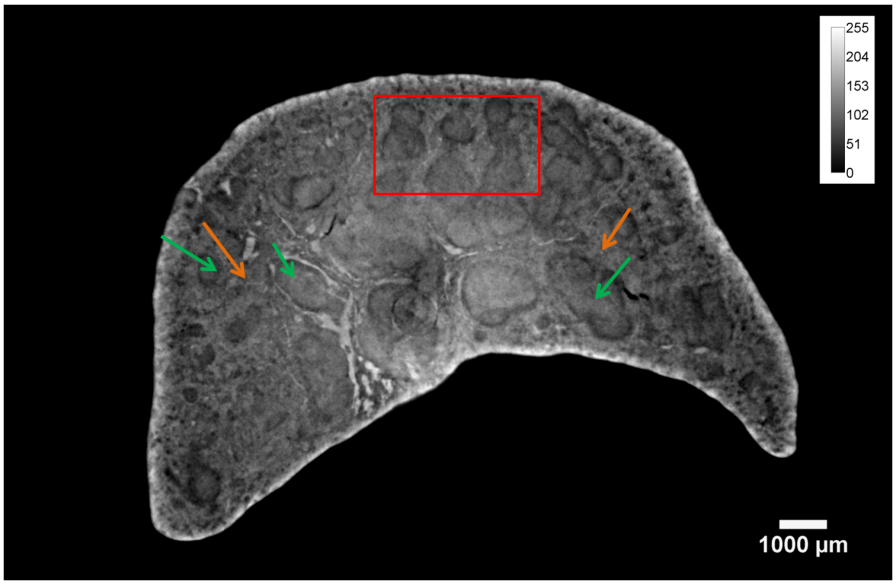

Figure 2.7: 2D XPCT virtual slice of the mouse spleen. Green arrows indicate the B-cells, while orange arrows the red pulp. The red rectangle highlights a spleen region where we detected signal attributable to the presence of platinum nanoparticles.

If we focus on the red rectangle superimposed to Fig. 2.7 (magnified also in Fig. 2.8a), a signal that could be attributable to platinum nanoparticles was found. As it can be seen, several hyper-intense dots, pointed by red arrows, were detected in the red pulp next to the marginal zone of the spleen cells. By looking at the full volume dataset has been excluded that this signal might belong to vessels. In addition, these white dots were compared to the resulting signal coming from the average of a stack of slices selected around this region of interest in Fig. 2.8a. The average map is displayed in Fig. 2.8b and it is represented in a colour scale from green to white. As it can be seen, the spleen tissue, coloured in green, is quite uniform, except for few bright white dots in the red pulp, whose visualization is enhanced by the red arrows.

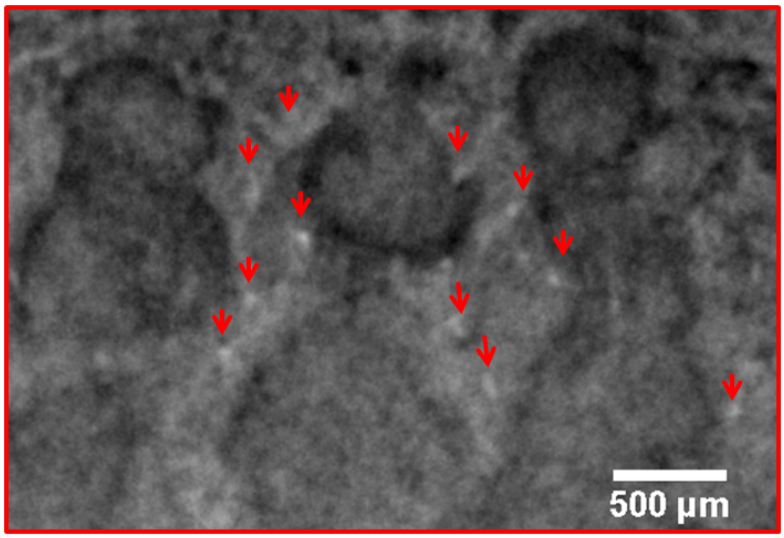

(a)

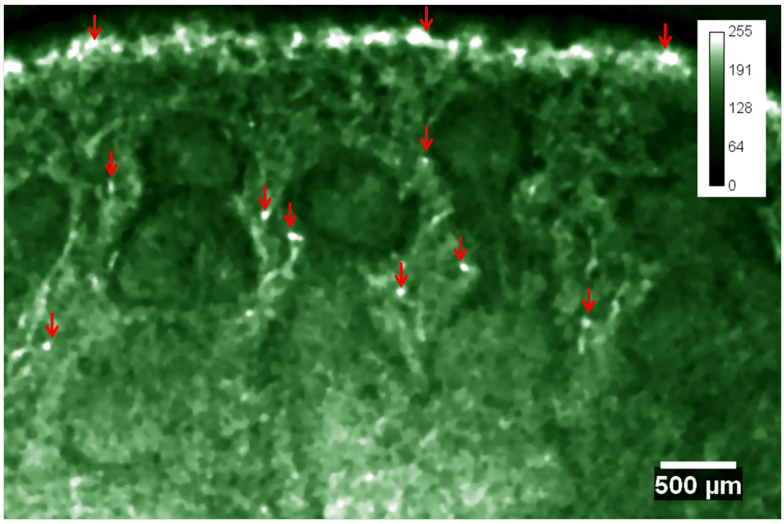

(b)

Figure 2.8: (a) Magnified region of interest within the red rectangle in Fig. 2.7. The red arrows focus on some dense spots detected in the red pulp, next to the marginal zones of the B-cells. (b) Image resulting from the calculation of the average of a stack of slices taken around the region of interest shown in Fig. 2.8a. The image is in false colours and it allows enhancing highest intensity pixels by the white colour. As indicated by the red arrows, the most intense signal was detected in the red pulp and in some points on the spleen edge. These dense points could be due to clusters of platinum nanoparticles.

Similar white spot deposits were detected at other depths in the spleen and also

in peripheral region, as it is illustrated in Fig. 2.9a. The region within the red rectangle is magnified in Fig. 2.9b. Red arrows helps to visualize the possible accumulations of platinum nanoparticles in the red pulp.

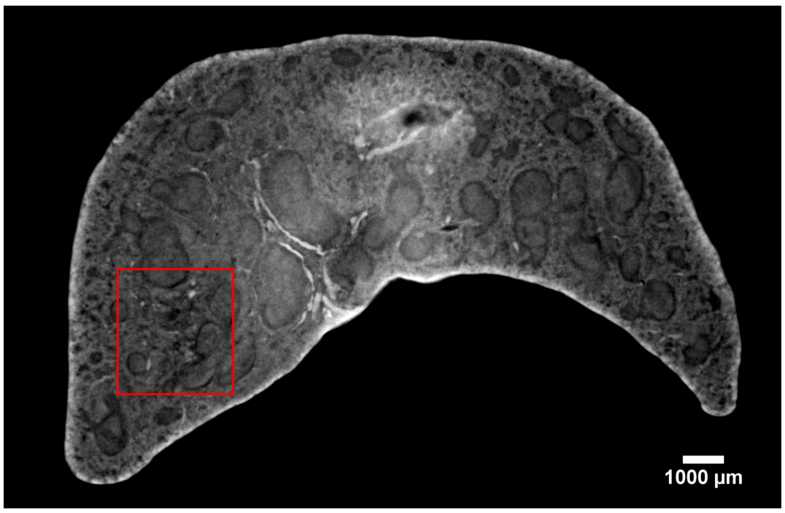

(a)

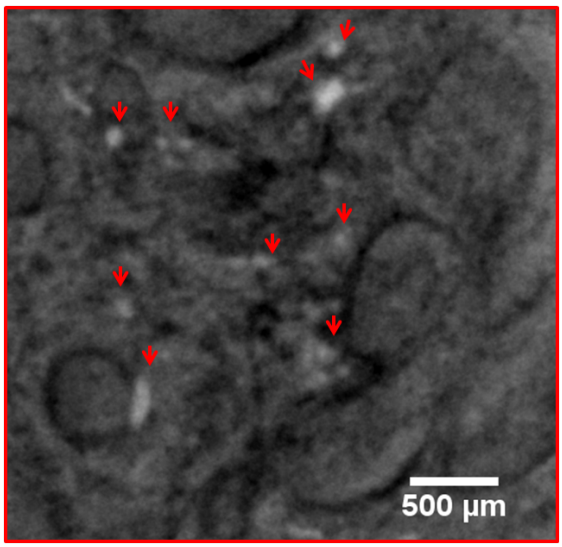

(b)

Figure 2.9: (a) 2D XPCT image of the mouse spleen extracted at another depth from the volumetric dataset. The red rectangle highlights a peripheral region rich of hyper-intense white spots. (b) Close-up of the red rectangle in Fig. 2.9a. Red arrows show the possible platinum accumulation in the spleen tissue.

The presence of nanoparticles in the red pulp, very close to the B-cells has been confirmed also by LIBS measurements. A LIBS slice (courtesy of Dr. Lucie Sancey) is shown in Fig. 2.10. In this representation, platinum nanoparticles are identified as yellow points, whereas phosphore and iron that are constitutive elements of the spleen are labeled in blue and pink, respectively.

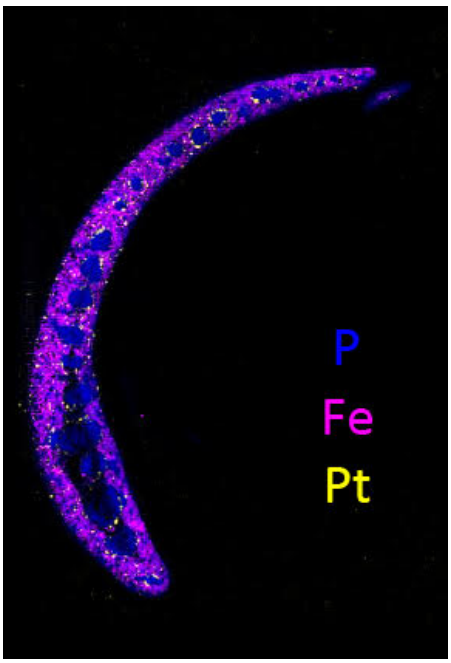

Figure 2.10: LIBS image showing the main elements composing the spleen. Phosphorus is depicted in blue, iron in pink and platinum in yellow. According to LIBS measurements, a few content of platinum nanoparticles was located in the red pulp (here in pink) next to the B-cells (here in blue).

2.6 Imaging of gadolinium nanoparticles in lung carcinoma

Malignant lung cancers are named carcinomas. They can be due to small cell lung cancer (SCLC) or non-small cell lung cancer (NSCLC) and represent the leading cause of tumor mortality worldwide [105]. The failure of anticancer treatments is linked to the inability of getting high concentrations of drugs in tumor sites and to the high radio-sensitivity of the lungs [106]. Next to local chemotherapy, inhalation of aerosolized drugs is a promising option for delivering larger doses and finer particles into the lungs [107, 108].
In recent years, the administration of high-Z elements based-nanoparticles has become a tempting strategy to enhance the X-rays effects in tumor sites [109, 110, 111, 106]. In this scenario in collaboration with the Institute for Advanced Biosciences and Institut Lumière-Matière, we examined the nanoparticles distribution in an implanted carcinoma that originated multiple metastases in a mouse lung sample. The lungs were explanted 1 hour after the administration of nebulized AGuIX® nanoparticles. The goal of the XPCT experiment was to evaluate the target efficiency of tumor sites from the gadolinium compounds. Here below, a series of preliminary 2D XPCT images are illustrated. Lungs are huge organs; mouse lungs have roughly a height of 1.5 *cm*. This required the acquisition of many datasets to cover the entire vertical extension of the organ. In Fig. 2.11, a 2D XPCT virtual slice depicting a lung cross-section is illustrated. A high-resolution inset of the area under the red rectangle in Fig. 2.11a is shown in Fig. 2.11b. Thanks to the natural contrast and the synchrotron high brightness, a sophisticated discrimination among different soft tissues was achieved. The close-up of Fig. 2.11b displays, by a red arrow, a density change in the lung tissue that we believe is caused by a cancer lesion. This irregular object has a bright appearance, very probably due to the contrast enhancement produced by the gadolinium nanoparticles retained inside.

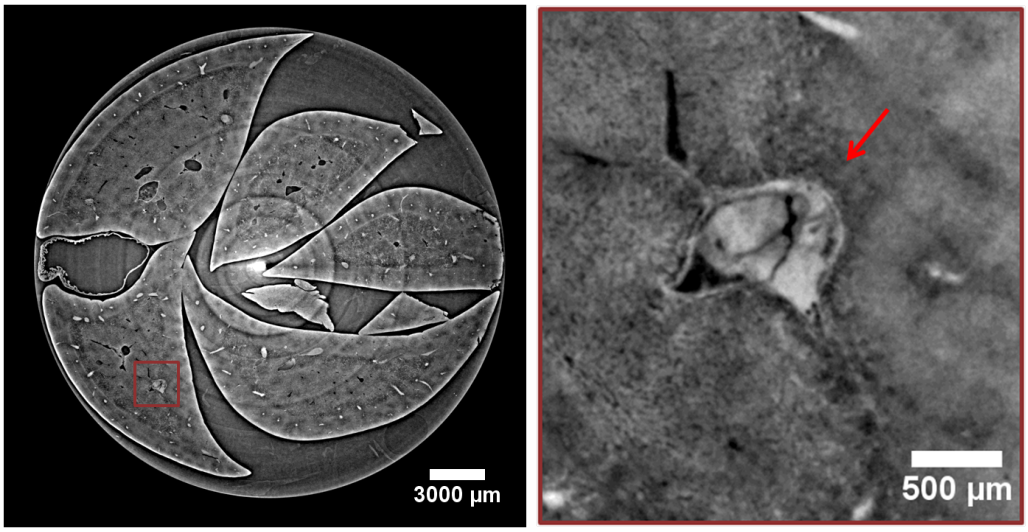

(a) **(b)**

Figure 2.11: (a) 2D XPCT image of the mouse lungs carrying carcinoma metastases. (b) High-resolution close-up of the red rectangle depicted in Fig. 2.11a. The image denotes a sudden change of the lung tissue density, very probably due to the presence of a meatastasis.

In Fig. 2.12a, it is illustrated a tiny volume reconstruction with three regions of interest highlighted by red, yellow and green rectangles and magnified in Fig. 2.12b, 2.12c, 2.12d, respectively. As pointed by the coloured arrows, all of them show suspicious masses of high intensity. They could be lung malignancies and according to the grey scale map of XPCT images their white colour is justifiable for the conspicuous presence of nanoparticles. They are surrounded by multiple black spots representing transversal vessels in the reading of XPCT images. Thus, very reasonably these white and irregular masses could be vascularised pulmonary metastases.

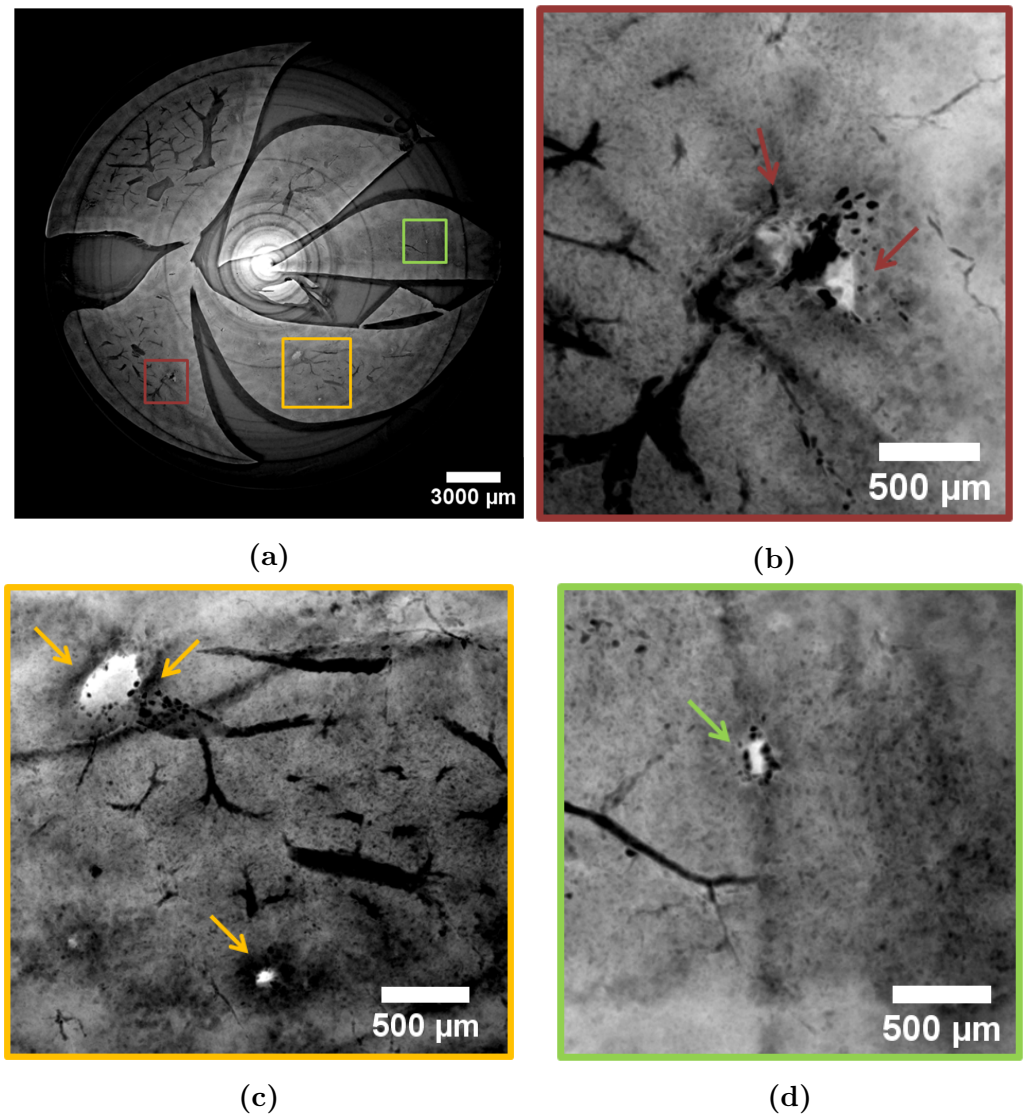

Figure 2.12: (a) Volume representation of a thin mouse lung section. (b) High-resolution close-up of the red rectangle depicted in Fig. 2.11a. The image denotes a sudden change of the lung tissue density, very probably due to the presence of a metastasis enhanced by gadolinium nanoparticles. This abnormal structure is pointed by red arrows. (c) High-resolution close-up of the yellow rectangle depicted in Fig. 2.11a. The yellow arrows indicate abnormal bright structures that could be metastases filled with gadolinium. (d) High-resolution close-up of the green rectangle depicted in Fig. 2.11a. By a green arrow the image shows another suspicious metastasis.

Finally, the image of maximum projection intensities illustrated in Fig. 2.13a

gives an insight of the lung extensive vasculature. The red rectangle captures an important detail found in the lower part of the lung. As it can be seen from its high-resolution close-up in Fig. 2.13b, multiple white spots were detected in a tissue area surrounded by the tangled net of vessels. They could be accumulations of gadolinium nanoparticles, whose signal was enhanced by the projection of the maximum intensity pixels.

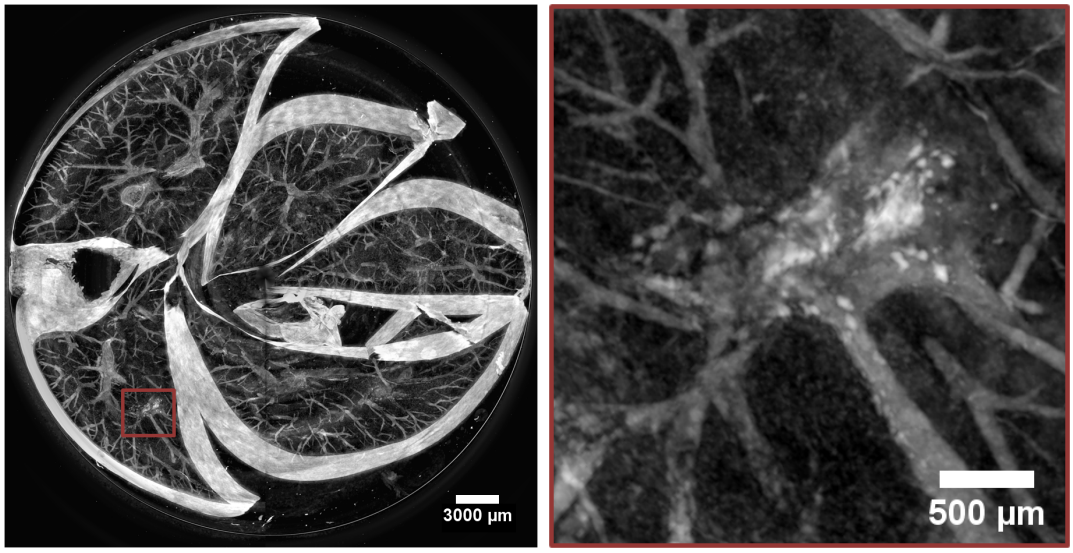

(a) **(b)**

Figure 2.13: (a) Volume representation of a thin lung section depicting the vessels pattern. (b) High-resolution close-up of the red rectangle depicted in Fig. 2.13a. This sub-figure denotes the accumulation of dense objectes (very probably nanoparticles) in correspondence of the irregular mass detected in Fig. 2.12a and 2.12b.

2.7 Resolving 3D biodistribution of nanoparticles inside melanoma brain metastases

Melanoma is one of the most aggressive skin cancers and shows a strong tendency to metastasize [112]. 60 % of melanoma patients develop multiple metastases in the central nervous system and the survival patient rate is very low (5-19 % according to the location and number of metastases) [113, 114]. Brain metastases are among the most difficult tumors to treat because the blood-brain barrier (BBB) hampers large molecules, such as anti-cancer medications, from entering the brain

[115]. Surgical resection and brain radiotherapy demonstrate to be only palliative cares [116, 117, 118]. Moreover, tissue irradiation by radiotherapy may induce the cell necrosis of healthy tissues surrounding the tumor volumes [119].
In recent years, the administration of theranostic biocompatible nanoparticles to eradicate this kind of cancers is under experimentation. Thanks to their physical and chemical properties, these nanoagents are small enough to passively cross the blood-brain barrier and accumulate in cerebral tumors [120, 121]. It has been demonstrated that they enhance the tumor visualization by multi-modal imaging techniques and increase the tumor radiosensitization [9, 10, 109, 110, 111, 1, 106]. Following the interaction between the X-rays and their metal components, nanoparticles produce a shower of Auger and photo-electrons that, in turn, produce reactive oxygen species inducing damages to the DNA of the tumor cells and leading to tumor subsequent destruction [122, 123, 124]. This strategy circumscribes the therapy to the malignancy region and leads to minor side effects in the healthy tissue. Therefore, the knowledge of nanoparticles repartition in tumors and retention in healthy tissues is fundamental for optimizing radiotherapy protocols and to predict the effects of irradiation.
Within this section, it is presented for the first time a XPCT study on the distribution of AGuIX® nanoparticles in melanoma brain metastases of different size and at different locations inside the brain. It is known that XPCT is suitable to detect tumors in mice brains for pre-clinical evaluations [44]. Thus, it was feasible to characterize the number of metastases formed inside the brain, their position and their morphology. It was chosen to image a mouse brain sacrificed one hour after the administration of the gadolinium nanoparticles, since very often irradiation is accomplished at this time [125, 126, 127]. XPCT provided unprecedented insights of the complex internal structure of each individual melanoma metastasis grown in the brain. In this work, the XPCT images were compared with MRI and histology results. XPCT was performed first, then MRI on the ex-vivo intact brain and, at the end, histology since it requires the sectioning of specific slices from the full brain. The XPCT volumetric dataset of the brain with metastases was compared with the volumetric dataset of a control brain, with some images illustrated in the next paragraph.

2.7.1 XPCT images of a healthy mouse brain

A healthy mouse brain without AGuIX® nanoparticles was used as control sample for characterizing the metastatic regions and identifying nanoparticles in the sick brain. The sample was imaged at 51.5 keV with a propagation distance of 11 m. Here below in Fig. 2.14, 2.15, 2.16, four coronal cross-sections of the brain are shown. The 2D XPCT views were selected at different depths in the volumetric dataset, starting from mid-depth of the brain (Fig. 2.14) up to the cerebellum (Fig. 2.16). As it can be seen, the tissue shows a uniform density in all of them and no evidence of morphological changes attributable to the presence of tumor lesions was found.

Figure 2.14: 2D XPCT coronal image of the healthy brain sample selected at mid-depth of the brain.

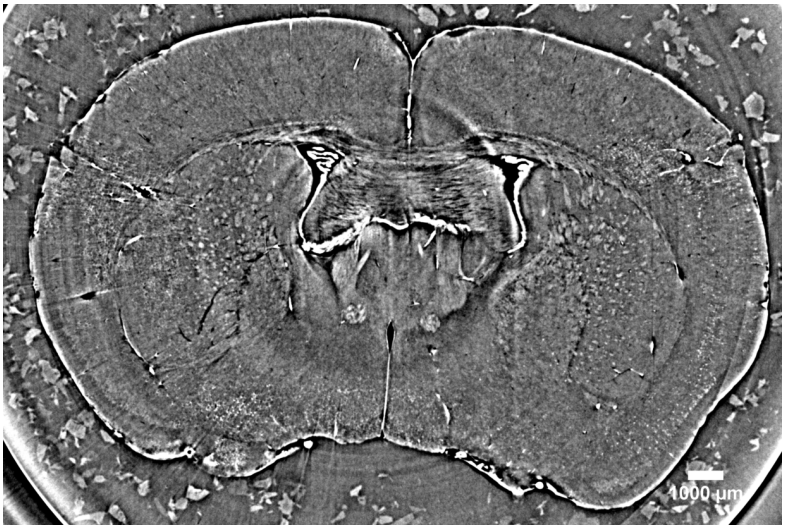

Figure 2.15: 2D XPCT coronal image of the healthy brain.

Figure 2.16: 2D XPCT coronal image of the healthy brain sample showing the cerebellum.

A brain volume representation is illustrated in Fig. 2.17. This sample was not perfused post-mortem; therefore its vasculature looks white due the presence of hemoglobin in the vessels. It is the only intense signal found during the imaging of this control brain. In Fig. 2.17, the healthy ventricle is framed by the yellow box. It can be observed that the structure appears normal with well defined boundaries

and crossed by white vessels organized according to a specific pattern.

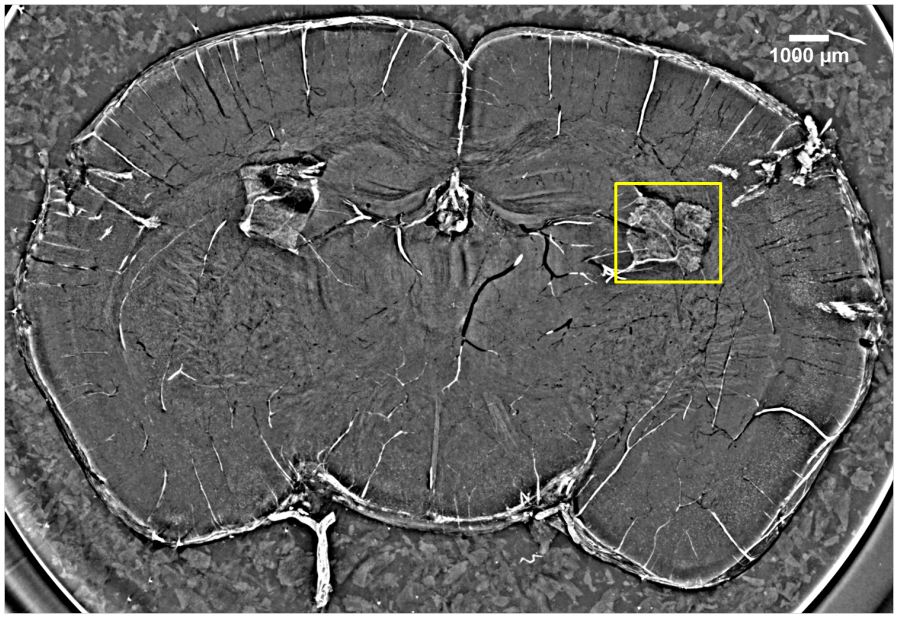

(a)

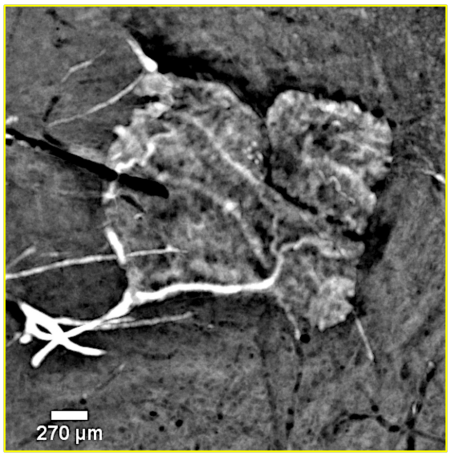

(b)

Figure 2.17: Brain reconstruction 732 μm thick. The yellow rectangle highlights the lateral venticle. The ventricle has well-defined boundaries and does not show abnormalities.

2.7.2 Classical imaging techniques for visualising brain tumors

In Fig. 2.18a, it is displayed an image of the sample used as model of brain melanoma metastases loaded with AGuIX® nanoparticles. The black arrow in Fig. 2.18a displays the point of injection of tumor cells B16F10 through the cortex. This large cancerous lesion is the main one, other metastases are also present at the posterior side of the brain. They are illustrated in Fig. 2.18b. Due to the high and irregular content of melanin, the external metastases are recognizable by their black colour.

(a) **(b)**

Figure 2.18: (a) Image of the mouse brain carrying the melanoma primary tumor. The black dot on the left upper hemisphere, indicated by the black arrow, represents the injection point of the tumor cells. (b) Picture of the back side of the mouse brain. This view allows observing the melanoma metastases (in black) spread on the external surface of the brain.

Nanoparticles were administered intravenously twelve days after the tumor implantation, when the metastases were highly spread. It was expected that the nanoparticles crossed the blood-brain barrier and penetrated inside the tumor and the multiple metastases before sacrificing the mouse one hour later. The mouse brain was subjected to XPCT measurements, MRI and histology in order to detect and compare the biodistribution of nanoparticles inside the different cancer lesions. Since melanomas are characterized by a high content of melanin, histology

analysis was carried out for distinguishing melanin aggregates in the brain and it confirmed the presence of melanoma. The histology image in Fig. 2.19 displays an axial slice of the brain, where the large brown dot (indicated by the yellow arrow) in the left hemisphere is the primary melanoma. At high magnification, the histology reveals the presence of tumor cells, that were clearly seen due to their specific chaotic arrangement and to the production of black melanin pigmentation. This tumor grew in correspondence of the point of injection of the tumor cells seen in Fig. 2.18a. However, this kind of investigation does not provide any evidence about the location of nanoparticles inside the melanoma.

Figure 2.19: (a) Histology image of the brain with a $\times 2.5$ objective. The yellow arrow indicates melanin aggregation typical of melanomas.

The brain was also undergone to a MRI scan. A coronal view was selected from the T_1[1] sequence (Fig. 2.20a). The yellow arrow shows how deep the tumor took place in the brain cortex compared to the injection site. The tumor shape is evidenced thanks to AGuIX® nanoparticles that are T1-MRI positive contrast agents, i.e. the tumor filled with gadolinium is imaged in white.
The MRI zoomed view in Fig. 2.20b provides an apparent homogeneous nanoparticles distribution in the tumor lesion, at the current spatial resolution (60 μm). The same cancerous lesion was detected by XPCT at higher resolution. The results are shown in the following paragraphs.

[1]Relaxion time measuring how quickly the longitudinal magnetization recovers to its ground state.

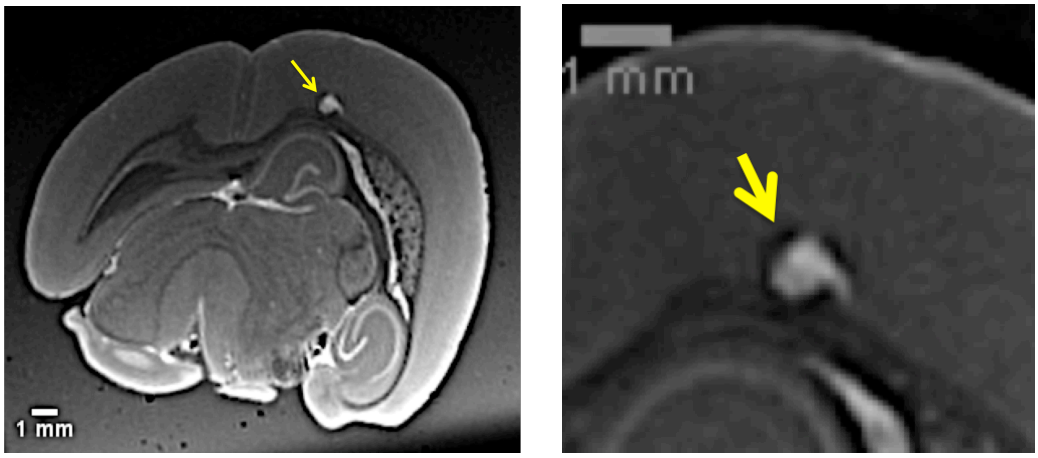

(a) **(b)**

Figure 2.20: (a) MRI image, coronal view. The yellow arrow points the main melanoma lesion developed in the mouse brain cortex in correspondence of the point of the injection of tumor cells. (b) Close-up of the MRI image on the tumor showing an apparent homogeneous distribution of nanoparticles.

2.7.3 XPCT images of the mouse brain with melanoma metastases

In this paragraph the XPCT brain images collected at 51.5 keV and acquired with a propagation distance of 2.3 m are shown. The virtual slices were reconstructed with a ratio $\delta/\beta = 73$. The volumetric information provided by XPCT revealed that the primary lesion induced the growth of multiple metastases of different size and at a different location in the brain, resulting in a different impact of nanoparticles penetration inside them. Thanks to its high-resolution, XPCT allowed resolving nanoparticles position inside the metastatic regions, while leaving the brain intact.
Here below, 2D virtual slices, volume renderings and 3D representations of the brain are shown. Referring to the XPCT grey scale maps, the 2D images show the high-density areas of the brain in white due to the contribution of gadolinium nanoagents, and the low-density areas in dark grey and black. This latter is the case of empty areas, transversal vessels, bloodstains and melanin.
Fig. 2.21a is a 2D slice showing by means of coloured rectangles three regions of interest. The volume renderings of the regions under the yellow and red rectangles are displayed in Fig. 2.21b and Fig. 2.21c.

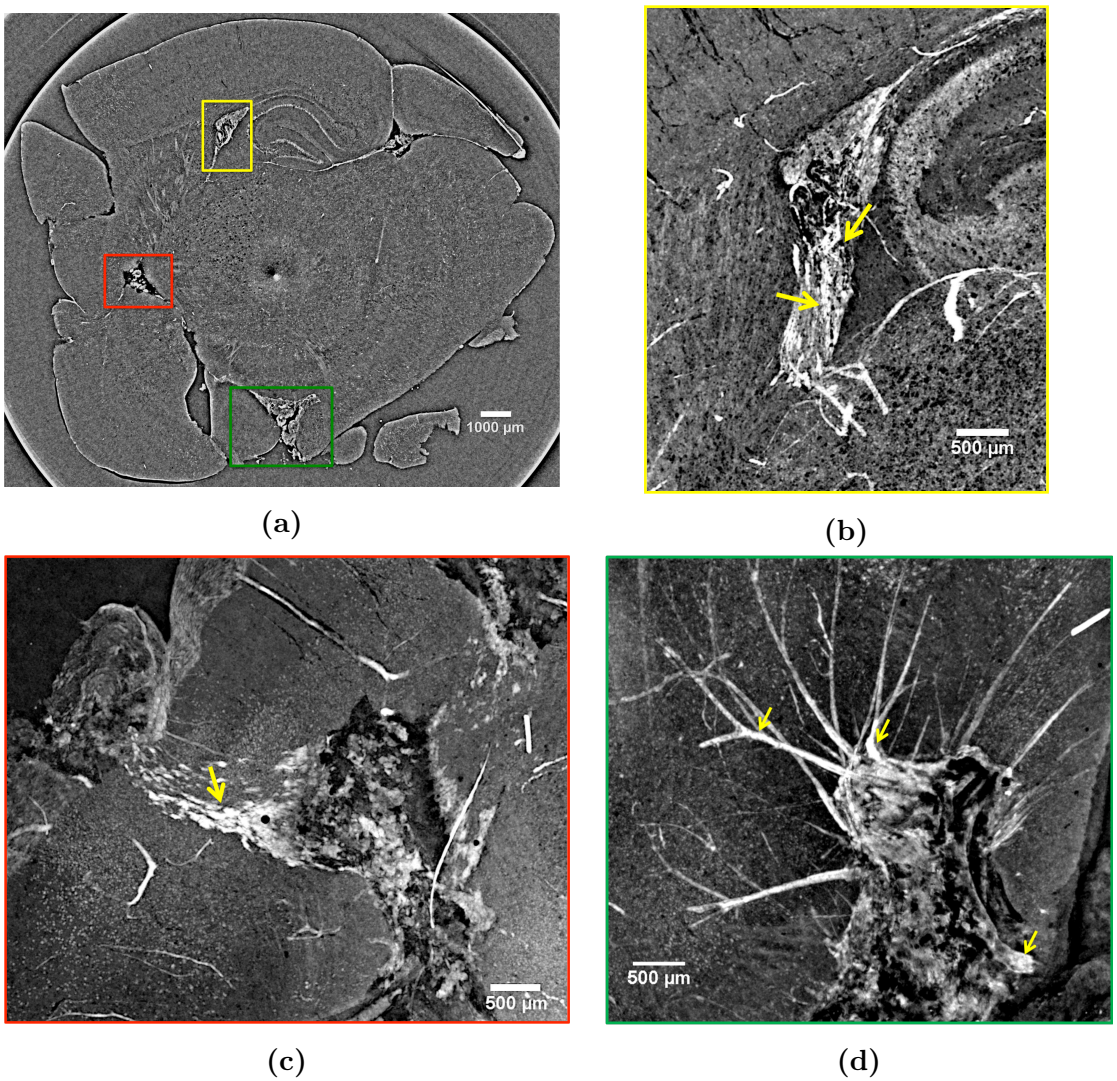

Figure 2.21: (a) Mouse brain cross-section with metastases highlighted under coloured rectangles, whose volume renderings are displayed in Fig. 2.21c, 2.21b and 2.21d. (b) Volume visualization of a portion of brain containing a metastasis grown in the lateral ventricle. The yellow arrows indicate the non-homogeneous accumulation of nanoparticles inside the tumor tissue. (c) View on the point of injection of tumor cells and on the amount of nanoparticles (white small objects pointed by the yellow arrow) delivered up to the tumor. A great amount of gadolinium could not permeate the tumor membrane and remained localized at the edges with the healthy tissue as indicated by the arrow. (d) Volume reconstruction of the metastasis developed in the inferior part of the brain and illustrated under the green box in Fig. 2.21a. Yellow arrows show nanoparticles accumulated in the metastasis, especially in the front part and nanoparticles entrapped in the vessels.

In the red close-up image (Fig. 2.21c), it is possible to identify the point of injection of the melanoma cells through the cortex and the tumor that originated more deeply in the cortex. The tumor is recognizable because of the sudden change of density of the cerebral tissue. Unlike the lower-resolution MRI image, here it is shown that nanoparticles (in white) followed a curved trajectory up to a bottleneck point without filling completely the tumor volume. A little amount of gadolinium successfully reached the central core of the tumor, while the remaining amount of permeated nanoparticles remained localized mainly on one side of the tumor, as indicated by the yellow arrow. Metastatic melanoma tumors are known to be well-vascularised; therefore, the large black stains visible at the edges with normal tissue might be bloodstains caused by the particular tendency of melanoma vessels to bleed [128], or melanin pigments. The yellow rectangle in Fig. 2.21a shows a metastasis invading the lateral ventricle. From its volume reconstruction in Fig. 2.21b, it is clear that a certain quantity of gadolinium extravasated from the hemorrhagic flow and deposited in the tumor tissue. Nanoparticles stayed concentrated in the central part (see yellow arrows in Fig. 2.21b) of the tumor close to the blood hemorrhage and left uncovered some parts of the metastatic region. The green box in Fig. 2.21a indicates the tumor cells that developed in the inferior part of the brain. A volume rendering of this brain region is illustrated in Fig. 2.21d. The metastasis exhibits a deformed mass pushing the neighboring normal tissue on the front side. Nanoparticles were mainly detected next to the bleed zones and in the upper part of the malignancy. Similarly to the other imaged metastases, also this one contains an abundant bleeding. The bloodstains correspond to the lowest density pixels rendered in black. The metastasis is surrounded by multiple vessels. The image clearly shows the nanoparticles entrapped inside the vasculature because the mouse was sacrificed before all the dose was delivered to the tumor (see the yellow arrows). This metastasis is also represented in a 3D image in false colour scale, shown in Fig. 2.22.

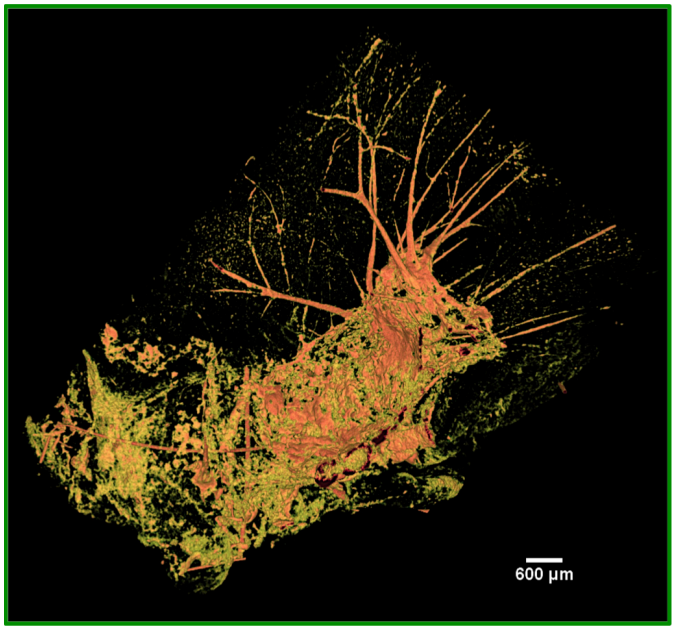

Figure 2.22: 3D segmented visualization in false colours of the area under the green box in 2.21a. The highest intensity pixels, displayed in orange, correspond to the densest pixels: gadolinium nanoparticles.

The stronger signal in orange corresponds to the high gadolinium density. The 3D view helps in observing that nanoparticles did not cover the tumor homogeneously and that a weak amount was still entrapped in the vascular system.
The 2D cross-section in Fig. 2.23a shows two other regions of the brain with metastases: the yellow rectangle shows at a new depth the metastasis developed in the lateral ventricle (whose zoom is illustrated in Fig. 2.23b) and, the red box two small metastases originated in a posterior structure of the brain. From the close-up of Fig. 2.23b, it can be observed that this metastasis has an irregular shape and produced a considerable variation of the cerebral tissue density. Nanoparticles filled this structure and produced its contrast enhancement in respect with the surrounding normal brain tissue. The tumor mass seems pushing the surrounding healthy tissue and it is driven by a large amount of blood vessels (black dots). Whithin the tumor, many bright dots (signature of the gadolinium) can be distinguished. They are mainly extravasated close to bloodstains, and in minor concentration in other points of the metastasis farther from the blood traces.

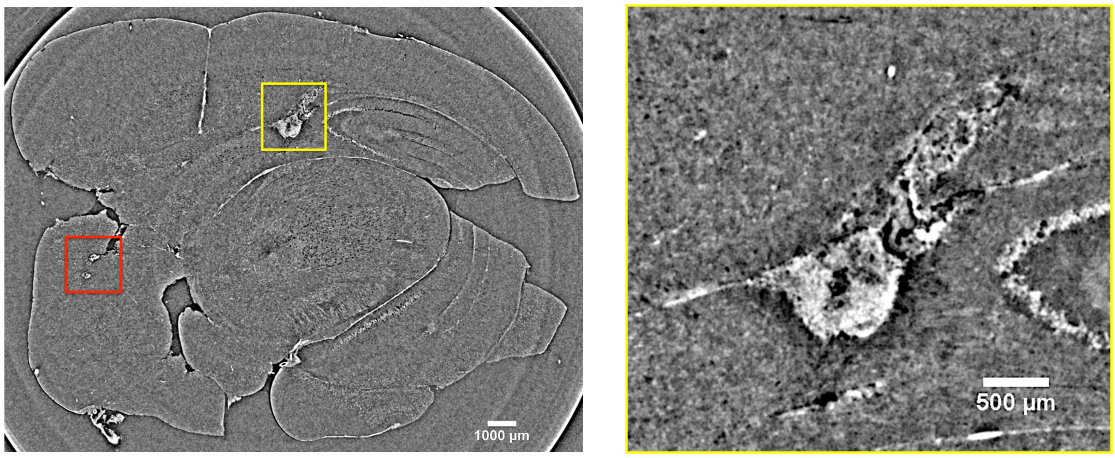

(a) **(b)**

Figure 2.23: (a) 2D XPCT slice showing two tumor lesions under the red rectangle in a posterior structure of the brain and, a metastasis developed in the lateral ventricle under the yellow box. (b) Close-up illustration of the metastasis invading the lateral ventricle.

In Fig. 2.24 and 2.25 are illustrated the projections of maximum and minimum intensity values of a stack of 120 slices selected around the red region of interest in Fig. 2.23a. The projection of maximum intensity in Fig. 2.24 reveals the pattern of distribution of gadolinium nanoparticles inside the tumor tissue (white area) and the pattern of arterioles connected to the metastasis.
The projection of minimum intensity in Fig. 2.25 shows the brain tisue inhomogeneity due to the presence of the tumor. The brain region marked by the tumor is dark in respect with the surrounding healthy tissue characterized by a rich concentration of black spots, especially in the upper part of the metastasis. This black signal could come from a mixture of vessels and melanin. Furthermore, the image shows also that the two metastases are connected by means of a blood vessel (longitudinal view of the vessel).

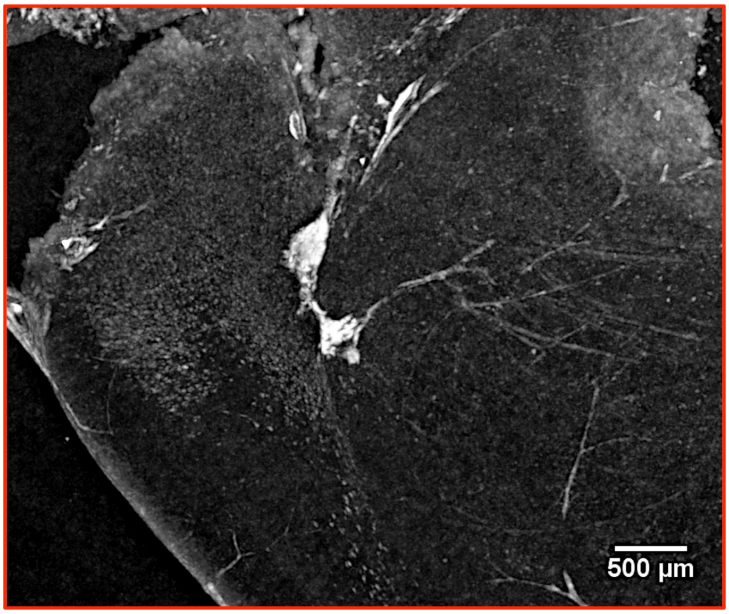

Figure 2.24: Maximum intensity projection of the area under the red rectangle in Fig. 2.23a.

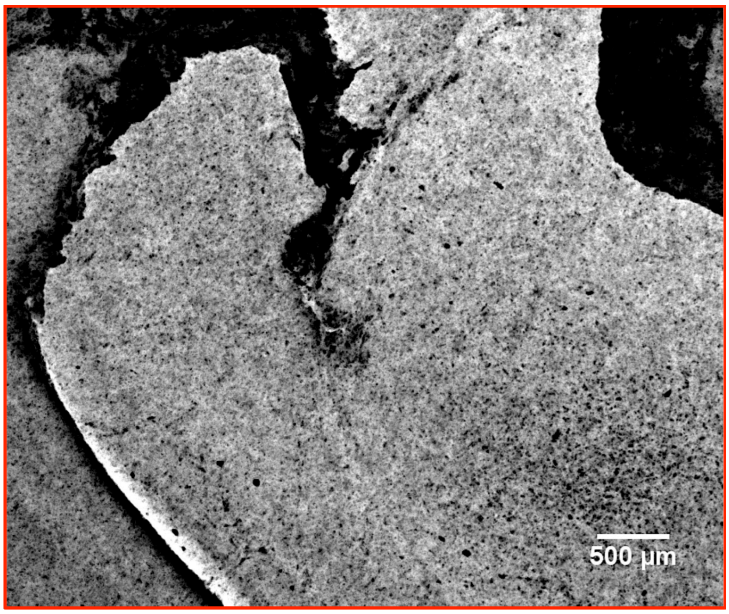

Figure 2.25: Minimum intensity projection of the same area in Fig. 2.23a.

Fig.2.26 is the sum of the maximum and minimum intensity projections. From this volume rendering, it is possible to visualize in high-resolution how nanoparticles

are distributed inside the tumor lesion (Fig. 2.26). Nanoparticles are strongly accumulated in the bottom part of the tumor, supposedly fed by arterioles; whereas the upper part presents some shadow regions, very probably metastasis parts less loaded with nanoparticles. Furthermore, from Fig. 2.26 it is also possible to notice small white clusters in the vessels (indicated by the yellow arrow) corresponding to a little amount of nanoparticles entrapped in the circulatory system.

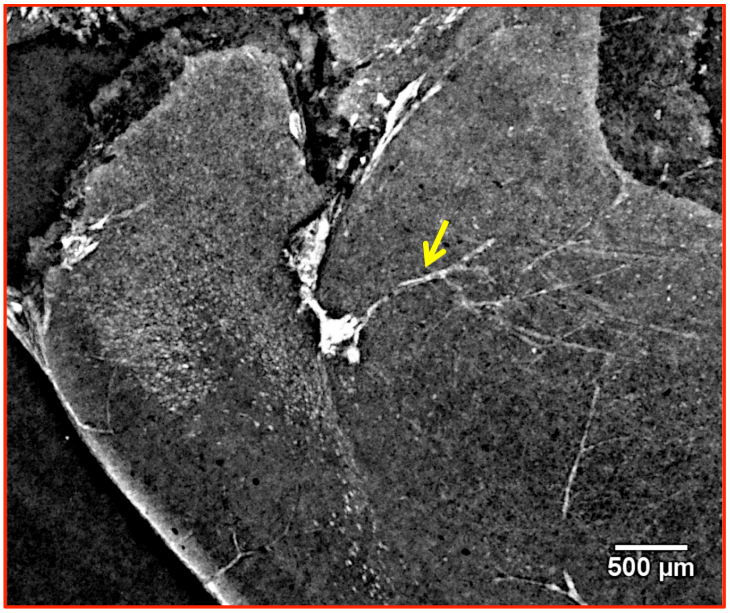

Figure 2.26: Sum of the previous maximum and minimum intensity projections (Fig. 2.24 and Fig. 2.25).

Fig. 2.27a is a volume reconstruction showing three metastases grown in the bottom part of the brain. In Fig. 2.27b, one may recognize a malignancy developed in the thalamus (pointed by the yellow arrow) and another one close to the pituitary gland (orange arrow). Both of them are located near brain peripheral regions and are surrounded by a dense vasculature delivering a great amount of nanoparticles. In particular, the release of nanoparticles close to the pituitary gland is facilitated by a stronger alteration of the blood-brain barrier. The metastases of Fig. 2.27c are a prototype of very well-loaded tumors exhibiting a quasi-homogeneous nanoparticles distribution. The strong signal detected in the surrounding vessels might be the proof that not all the injected nanoparticles were delivered to the tumor, as they did not have enough time to reach their target within one hour. The yellow arrows in the close-up of Fig. 2.27c displays small metastases at early

stage of formation, well-vascularised and filled with gadolinium nanoparticles.

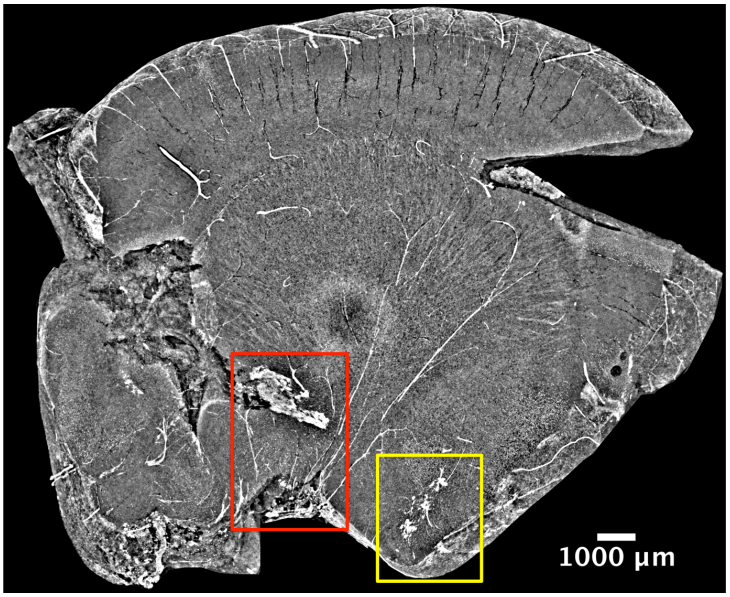

(a)

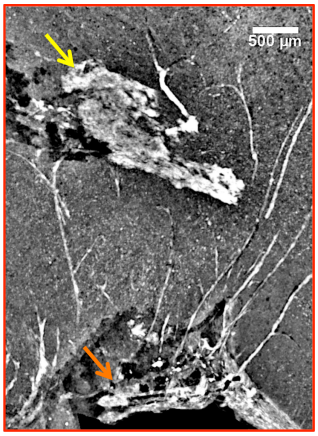

(b)

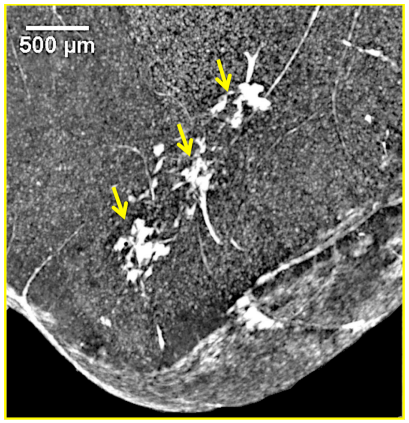

(c)

Figure 2.27: (a) Brain volume reconstruction 732 μm thick. Red and yellow rectangles highlight big and small metastases originated in the lower part of this view of the brain. (b) Visualization of a metastasis invading the thalamus (see yellow arrow) and one developed close to the pituitary gland (orange arrow). (c) Yellow arrows point to some small metastases in early formation.

In conclusion, with this work we demonstrated that nanoparticles have a different

targeting approach because of the heterogeneity of the metastases. The high-resolution images showed a complex nanoparticles repartition, different from case to case, that would lead to diverse radio-enhancement responses following irradiation. Thus, XPCT insights found that one hour after nanoparticles injection might be early to perform tumor irradiation. A longer delay after administration should favour the delivery to tumors of greater amount of nanoparticles that at this time is still entrapped in the vasculature. We believe that this finding could be useful for the design of more efficient treatments.

2.8 High-resolution images of melanoma

Melanoma is a very widespread skin cancer. According to the *American Cancer Society*, its incidence rate increased in the last 30 years [129]. Even if dermoscopy is currently the best clinical method to detect melanoma, the early diagnosis is crucial and challenging [130].
Melanomas arise from melanocytes, cells predisposed to the production of melanin [131], a dark pigment determining skin and hair colours. Melanoma lesions are characterized by a high-density and cahotic repartition of these melanin pigments, whose size become larger as the melanoma progresses [132]. As melanin distribution is related to the cells from which the disease may arise, melanin map in melanomas can act as marker for this kind of tumor [133, 132]. In this framework, XPCT was used to detect melanin pigments in a mouse sub-cutaneous melanoma tumor removed from the mouse body. In principle, the choice of imaging an isolated tumor was carried out to test the capability of XPCT approach in imaging a poor natural contrast tissue like a tumor. To have the possibility to well retrieve the irregular tumor vasculature, the sample was not perfused after explantation. Futhermore as XPCT is a 3D label-free technique, it was thought that it could be suitable to visualize the volumetric melanin distribution even in deep layers of the melanoma. Fig. 2.28a is a 2D cross-section extracted from the tumor volumetric dataset. Even if this reconstruced tumor layer shows some superimposed residual rings, it worths to notice the cahotic distribution of melanin pigmentes (black spots), arranged mainly along the external tumor edges. Thanks to the high-resolution of our imaging technique, melanin aggregates of different sizes and shapes were visualized, as it can be observed in the close-ups of Fig. 2.28b and 2.28c, corresponding to the areas under the yellow and green rectangles of Fig.

2.28a.

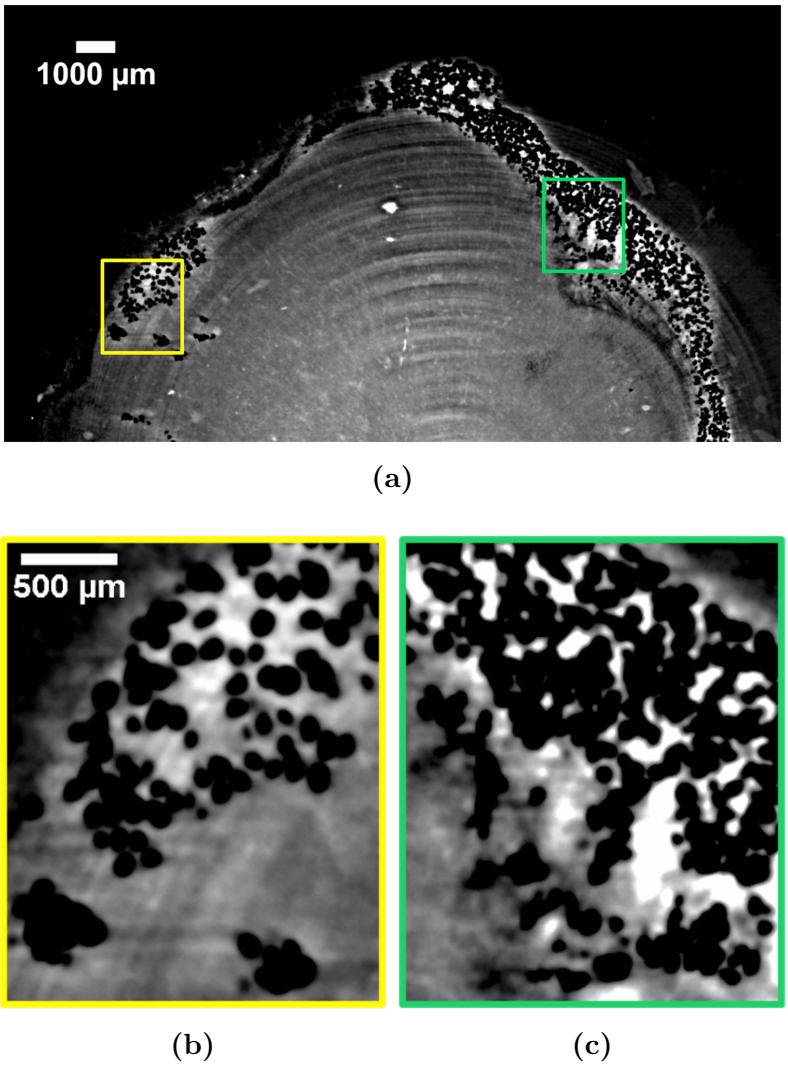

Figure 2.28: (a) 2D cross-section of a sub-cutaneous tumor showing cahotic melanin aggregation (black spots). Two magnified views are illustrated in (b) and (c).

Fig. 2.29a is a 3D surface plot of a cropped melanoma volume. It displays melanoma vasculature comprising vessels of different diameters and a dense presence of melanin pigments. The image was obtained from the maximum intensity projection of a melanoma section. By analyzing the sample layer by layer from the top (part of the sub-cutaneous tumor supposed to be close to the mouse skin) to the bottom (farther from the mouse skin), a different melanin concentration was observed. Higher density melanin pigments were detected in the layers closer to

the mouse skin. It was observed the melanin concentration decreased in the deeper tumor layer. Fig. 2.29b is a volume visualization concerning an inner section of the tumor, far from the skin. As it can be seen, the amount of detected melanin pigments is very weak in respect with the previously shown images. Few black spots were detected around the edges of the tumor and close to the peripheral vessels. Conversely, this volume visualization enhance the irregular network of little empty vessels, whereas bigger vessels filled with blood are imaged in white.

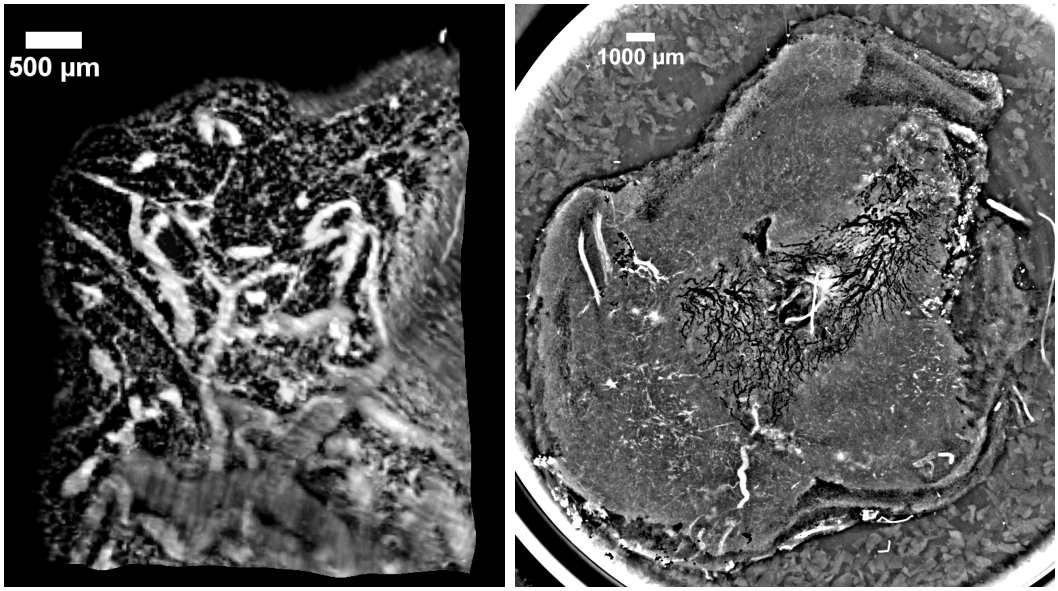

(a) **(b)**

Figure 2.29: (a) 3D surface plot of a melanoma cropped section 390 μm thick. (b) Volume visualization of an inner melanoma section 600 μm thick.

2.9 Subtraction of images around gadolinium K-edge

Within this section we would like to show some preliminary results we got by the K-edge subtraction method. The case under study is the brain sample model of melanoma metatastases and containing gadolinium nanoparticles. Gadolinium absorption coefficient as well as it is refractive index are far superior to those of the soft tissue components (see Appendix C), as it is the case for a brain sample. With the aim of better discriminating the gadolinium signal due to the possible presence

of nanoparticles in tumor, we decided to record XPCT projections of the mouse brain below and above gadolinium K-edge energy located at 50.2 keV. Therefore two datasets were reconstructed, one at 48.5 keV, corresponding to the images acquired below gadolinium K-edge and, another at 51.5 keV, corresponding to the images collected above gadolinium K-edge.

To support this kind of image analysis, the alignment of two different slice sequences is mandatory since the subtraction operation has to involve exactly the same cross-section of the sample in both datasets. The alignment and correlation operations can be achieved by means of an image registration process. The image registration step allows finding similarities among images acquired by different techniques or under different experimental conditions, such as different time or energies. Moreover, it is also widely used to compare patient's images with anatomical atlases in the medical imaging field [134].

The selected slices for the K-edge subtraction operation were first compared by visual assessment, by detecting similar morphological features like external edges or inner contours. Then, the images considered as similar as possible were subjected to a cross-correlation analysis by using ImageJ Correlation plugin [135]. The algorithm behind this ImageJ plugin estimates a local statistics within each local region of defined size in two aligned images (the source image and the target image). The available statistics for correlating the images are: average, standard deviation, skewness, kurtosis and directionality of the local pattern. For each selected statistics the cross-correlation coefficient is calculated:

$$r = \frac{\sum_{i=1}^{m}\sum_{j=1}^{n}(f(m_i,n_j)-\overline{f})(g(m_i,n_j)-\overline{g})}{(mn-1)\sigma_f\sigma_g} \tag{2.1}$$

where m and n are the number of local regions in the horizontal and vertical directions; $f(m,n)$ and $g(m,n)$ the local values for the chosen statistics; $\overline{f}$ and $\overline{g}$ the mean values of the whole images; whereas σ_f and σ_g their standard deviations. Furthermore, the plugin produces a correlation map showing the differences between local areas and create a plot showing the correlation between the two images.

In Fig. 2.30, two similar brain images acquired at different energies are compared.

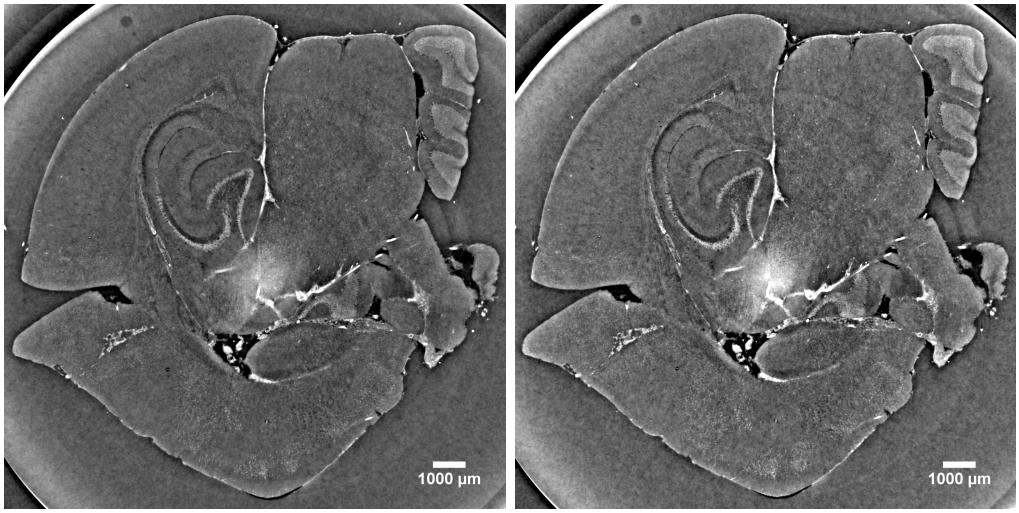

(a) **(b)**

Figure 2.30: (a) 2D XPCT brain image acquired at 48.5 keV. (b) 2D XPCT brain image acquired at 51.5 keV.

On the left, Fig. 2.30a was obtained at 48.5 keV, while on the right Fig. 2.30b was obtained at 51.5 keV. The correlation plot in Fig. 2.31a shows that these two images are well-correlated with a correlation coefficient equal to 0.71, while Fig. 2.31 shows the 2D correlation map between the slice in Fig. 2.30a and that in Fig. 2.30b.

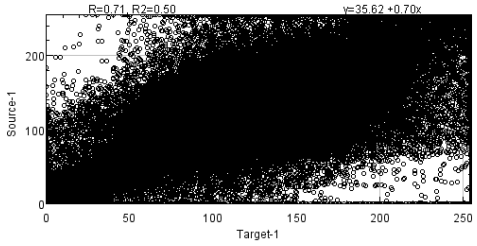

(a)

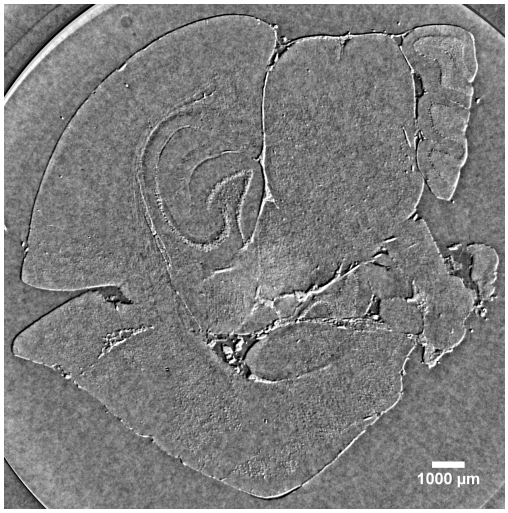

(b)

Figure 2.31: (a) Correlation plot between the slice in Fig. 2.30a and that in Fig. 2.30b. The images have a positive correlation equal to 0.71. (b) 2D correlation map between the slice in Fig. 2.30a and that in Fig. 2.30b. This map shows the local differences between the two images according to the average of patches of 3 pixels size.

Once shown how correlation between two dataset is performed, we may focus on image subtraction. In Fig. 2.32, the 2D XPCT brain slice acquired at 48.5 keV (Fig. 2.32a) is compared with the 2D XPCT brain slice obtained at 51.5 keV (Fig. 2.32b). As first test, we phase-retrieved the projections with the same ratio $\delta/\beta = 73$. The choice of this ratio was motivated by the fact that low ratios could better enhance the presence of heavy metals deposited in the brain tissue.

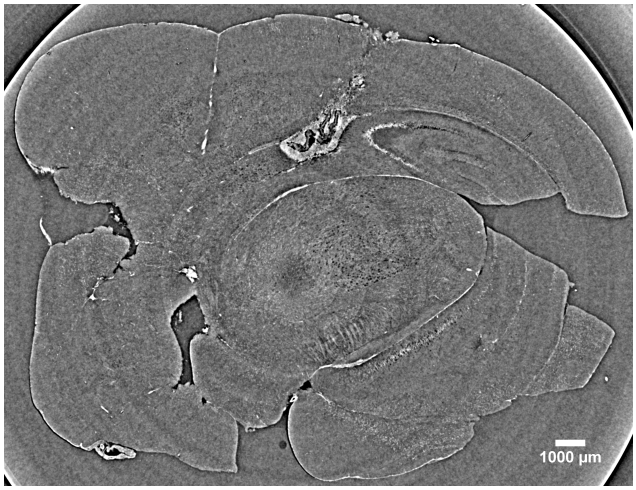

(a)

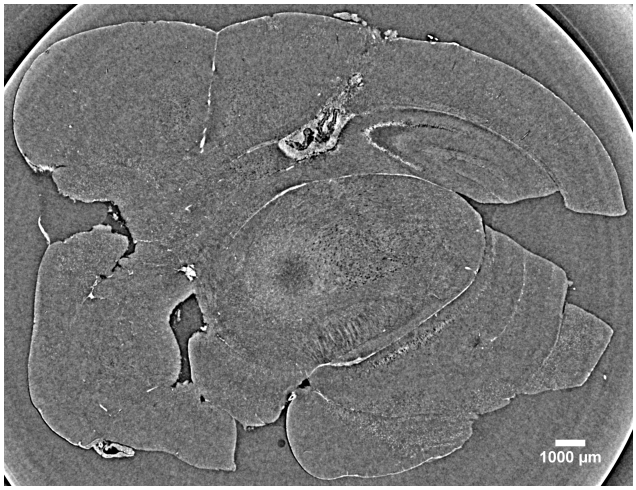

(b)

Figure 2.32: (a) 2D XPCT mouse brain image at 48.5 keV. (b) 2D XPCT mouse brain image at 51.5 keV.

K-edge subtraction method is usually applied in absorption tomography to isolate the contrast agent contribution from the remaining content of the X-ray image. In case of the phase-contrast approach, the issue of K-edge imaging is not trivial. The behavior of the real (δ) and imaginary (β) parts of the refractive index have to be taken into account. As δ values of gadolinium are higher below K-edge than above K-edge, we considered the subtraction operation between the image taken at 48.5 keV and that at 51.5 keV. The result is displayed in Fig. 2.33a with two magnified insets over the tumors: one under the cortex in Fig. 2.33b and another

in the lower part of the brain in Fig. 2.33c.

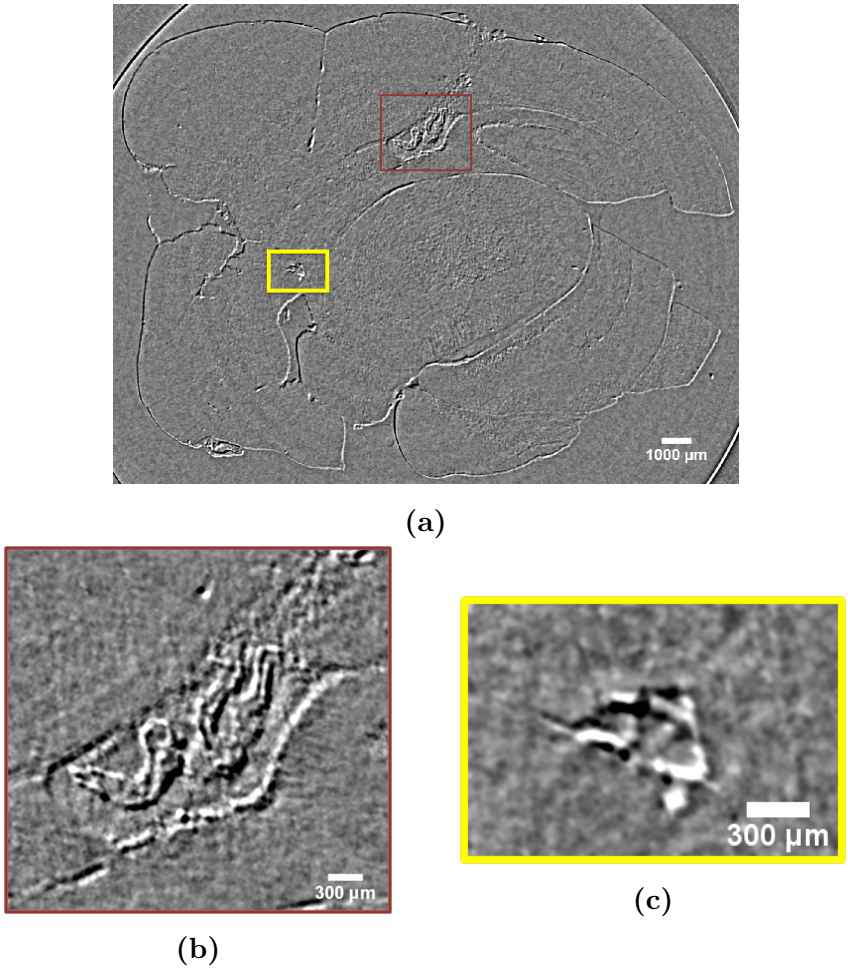

Figure 2.33: (a) 2D XPCT image obtained following gadolinium K-edge subtraction operation between the images in Fig. 2.32a and 2.32b. (b) Close-up visualization on the big tumor developed under the brain cortex (red rectangle in Fig. 2.33a). (c) Close-up visualization on the small tumor in the lower part of the brain (yellow rectangle in Fig. 2.33a).

We may notice that most of the signal located inside the brain is now near the noise (i.e. comparable to the level of the signal outside the brain). This result is logical since such a small change in photon energy leads to a negligible change in the index of refraction of the brain (4.6×10^{-11} at 48.5 keV and 4.11×10^{-11} at 51.5 keV). Only the edges remain visible as coming from the phase-contrast technique. In comparison, the images of the two tumors remained quite visible

and still well contrasted as compared to the brain. This is an interesting result confirming the presence of gadolinium and also the usefulness of the technique.
In order to better understand the interest of K-edge subtraction, we calculated the index of refraction for the brain and for the brain doped with two different concentrations of gadolinium (Fig. 2.34 and Fig. 2.35).

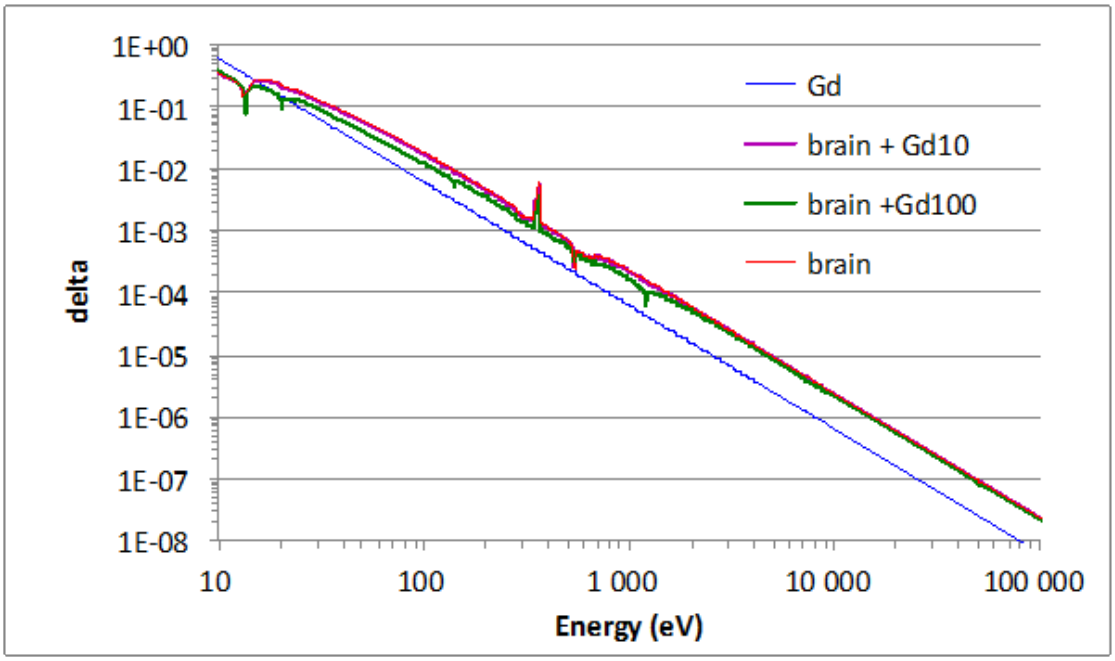

Figure 2.34: δ versus photon energy for pure gadolinium (blue), brain doped with 10 atoms of gadolinium (purple), 100 atoms of gadolinium (green) and undoped brain (red).

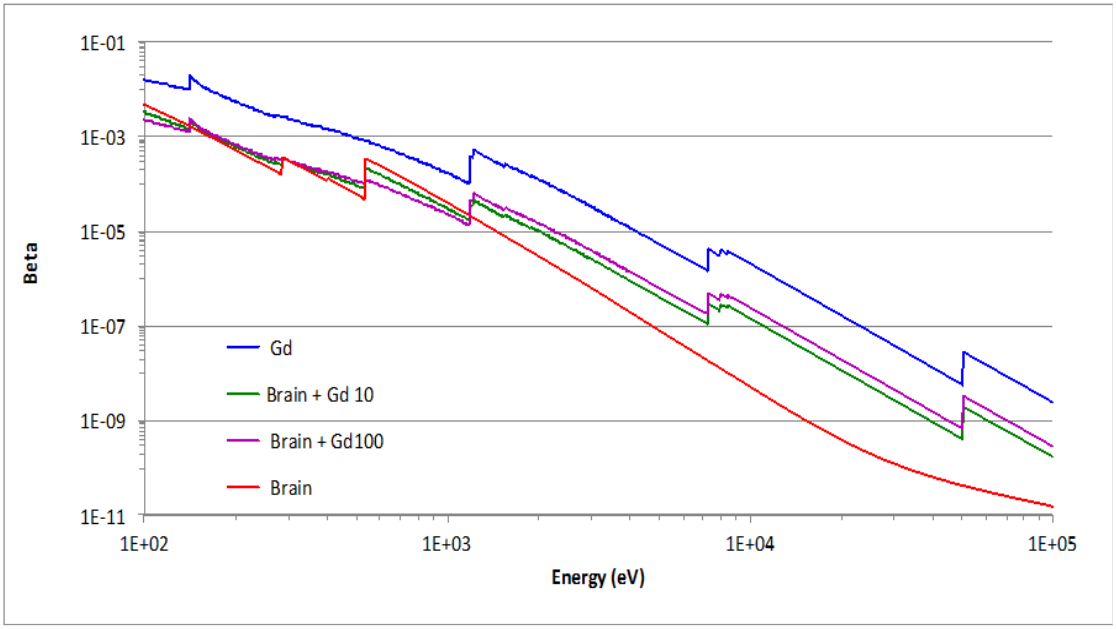

Figure 2.35: β versus photon energy for pure gadolinium (blue), brain doped with 10 atoms of gadolinium (purple), 100 atoms of gadolinium (green) and undoped brain (red).

Since we have no element to estimate the real concentration, and since it may change from tumor to tumor, we took two arbitrary values as a demonstration for this test. We thus modified the brain composition (taken from NIST website) $C_{14}H_{11}O_{71}N_2$ by adding 10 or 100 atoms of gadolinium i.e. 10% to 100% doping. The new compositions are thus $C_{14}H_{11}O_{71}N_2Gd_{10}$ and $C_{14}H_{11}O_{71}N_2Gd_{100}$. For δ (Fig. 2.34), i.e. the real part of the index of refraction, the adjunction of gadolinium has nearly no impact, all over the considered energies. Just around 30 eV, 100 eV and 1 keV (i.e. N, M and L-edges) one may observe the influence of gadolinium. Such drop also exists for the K-edge but is barely noticeable. It may be observed directly on the values of delta and only if 100 atoms of gadolinium is added. In that case, delta varied by 5% around the K-edge to be compared to 3% for undoped brain. For the imaginary part of the index of refraction, β, that is linked to absorption, even 10 atoms over 98 atoms from the initial brain molecule induces a strong shift of the value, in particular above 1 keV (Fig. 2.35). For brain doped with 10 atoms of gadolinium, at 48.5 keV, β equals 4.6×10^{-10} and 1.84×10^{-9} at 51.5 keV leading to a variation of the linear attenuation coefficient of 7 cm^{-1}. Based on Fig. 2.33, the main tumor may be approximated (very roughly)

as a sphere of 1 mm in diameter. In that case, changing the photon energy from 48.5 keV to 51.5 keV should induce a diminution of the signal by about 50%. The same calculation gives a theoretical drop of transmission of 70% if the brain is doped with 100 atoms of gadolinium. This value is very likely too high but it shows that the K-edge subtraction technique associated with a good estimate of the tumor size may lead to an estimation of the gadolinium doping. The phase contrast is still useful to enhance the shape of the tumor.
The next test we would like to accomplish is the image subtraction between two energies very far, such as 35 keV and 51.5 keV. We believe that by considering a larger energy gap, we could achieve more informative images as δ for gadolinium and brain molecules do not have the same variation with photon energy. We believe that 3 energies will be an optimum to disentangle gadolinium from the rest of the brain without delivering high doses to the sample.

2.10 Summary

Within this chapter new results about nanoparticles biolocalisation by XPCT are discussed. The chapter begins with a premise on what are the imaging technques currently in use today. It emerges the lack of imaging tools at a median scale between few and hundreds of microns. We proposed XPCT as a good alternative to fill this gap since it is a high-sensitive and non-destructive method. Therefore is is suitable to investigate biomaterials. Multiple pre-clinical problems were investigated, from nanoparticles clearance process up to nanoparticles uptake and retention in tumors. In more detail, we showed the renal clearance of gadolinium nanoparticles, the hepatic retention of gold zwitterionic nanoclusters and the spleen elimination of platinum nanoparticles. We displayed some preliminary results about the identification of lung carcinoma metastases thanks to nebulized gadolinium nanoparticles.
The heart of the chapter is the study carried out about gadolinium nanoparticles localization in melanoma brain metastases. This work showed a complex repartition of the nanoparticles due to metastases hetereogenity. We believe it will have a positive impact on future clinical protocols. In addition, high-resolution insights of melanoma layers showing the distribution of melanin pigments are illustrated.
Finally, some tests done by K-edge subtraction to isolate nanoparticles signal from that of the surrounding tissue are reported.

Chapter 3

Detection of amyloid plaques loaded with gadolinium nanoparticles

Alzheimer's disease is a complex neurodegenerative illness that attacks different parts of the brain at the same time. It is characterized by the accumulation of extracellular β-amyloid (Aβ) aggregates, more commonly known as "senile plaques", and by abnormal intracellular aggregations of tau protein, called neurofibrillary tangles [136]. Detecting amyloid deposits in the brain in a non-invasive manner sounds as a promising strategy for early diagnosis and, for accelerating the discovery process of new drugs that could slow down the cognitive decline that the disease causes.

Currently, neuroimaging techniques like MRI and PET provide structural information but can not discriminate between different amyloid deposits at various stage and of different morphology, because of their low spatial resolution [137, 138]. Thus, the development of more direct approaches in combination with active targeting would lead to more sensitive results. Recently, it was found that in-vivo MRI with the injection of gadolinium-based contrast agent (Gd-DOTA, Dotarem) can enhance the detection of amyloid plaques and help to follow the progression of Alzheimer's disease [139]. Later, it was also proved that the gadolinium-based nanoparticles AGuIX® (also mentioned in Chapter 2) enhance contrast more efficiently than Dotarem [11] and, if they are functionalized with specific peptide ligands (PIB), grafted on their surface, these nanoparticles are able to target spe-

cific amyloid fibrils [140].
Pinzer and co-workers demonstrated in 2012 that phase contrast X-ray imaging, using gratings, was an efficient tool for detecting amyloid plaques in mice brain [83]. The experiment was performed at 25 keV to ensure a strong diffrence between the indexes of refraction of the plaques and of the brain. However, Pinzer highlighted that a total dose of 3×10^4 Gy was required which is lethal, preventing the use of living mice, but still below the threshold of 10^6 Gy for inducing damages. As a perspective work, they propose to work at higher photon energy to strongly reduce the X-ray absorption.
Therefore, motivated by the promising results obtained by high photon energy XPCT for bio-locating nanoparticles in mice organs, we also performed XPCT for better understanding the diffusion and distribution mechanism of AGuIX® and AGuIX-PIB nanoparticles in mice brains model of Alzheimer's disease. The data collection was performed at ESRF in collaboration with NeuroSpin (CEA Saclay and Grenoble, France), Institute for Advanced Bioscences (Grenoble, France) and CNR-Nanotec (Rome, Italy), and I was the principal investigator of the experiment. The XPCT image reconstruction process was accomplished at Laboratoire d'Optique Appliquée.

3.1 Experimental conditions

We collected the images of six 20-22 months old male mice brains affected by Alzheimer's disease and, four 20-22 months old male mice wild type as reference models. The brains were imaged under these conditions: with or without nanoparticles and with or without blood-brain barrier opening protocol. The blood-brain barrier is made up of tight junctions that permit the passage of only small molecules. Thus, it protects and isolates the cerebrospinal fluid from any pathogenic substance carried by the blood. With the aim of promoting the delivery into the brain of a greater amount of nanoparticles, the blood-brain barrier of some mice were locally opened with a non-invasive method under experimentation at NeuroSpin laboratory. Firstly, nanoparticles were administered intravenously in combination with circulating microbubbles; then, low intensity focused ultrasounds were applied in-vivo directly to the mice brains to induce the barrier disruption. Furthermore, ultrasound technology is expected to be a new potential therapeutic approach to reduce the amyloid load [141].

Each mouse brain had an approximate size of 1 $cm \times 1\ cm \times 1.5\ cm$. The amount of AGuIX® or AGuIX-PIB nanoparticles intravenously administered to mice was equal to 10 μmol. All mice were sacrificed between 3-4 hours after nanoparticles injection and they were ex-sanguigno fixed in paraformaldehyde (PFA). Before euthanasia, some brains were imaged by in-vivo MRI to locate and to quantify the uptake of gadolinium in the brain. In addition, after XPCT experiment the brains were submitted to post-mortem high-resolution MRI (30 μm isotropic spatial resolution). Sample preparation and MRI measurements were carried out at NeuroSpin laboratory.
The XPCT experiment was performed at 48.5 keV and 51.5 keV, i.e. at two energies selected immediately below and above gadolinium K-edge (50.2 keV). This choice of the energies was made because gadolinium refractive index, especially at 51.5 keV, is different from that of iron, zinc and copper that are the metals contained in the amyloid plaques [142]. We thought we could better discriminate gadolinium signal from that of the endogenus metals of the plaques by K-edge subtraction operations (see Chapter 2, paragraph 2.8.1).
All the brain projections were acquired with a drift distance of 11 m and a camera pixel size of 3 μm. The images displayed in this chapter are those collected at 51.5 keV and reconstructed with the ratio $\delta/\beta = 112$.

3.2 XPCT results

To start, two images of the healthy control brain are illustrated in Fig. 3.1. Thanks to the high-brightness of the synchrotron radiation and the phase-contrast approach, high-resolution images were achieved. The natural contrast and the fixation with paraformaldehyde enabled a good visualization of many inner brain features. For instance, the brain slice in Fig. 3.1a is rich of details in the midbrain region indicated by red arrows. This image displays also the lateral ventricles by yellow arrows. Due to their intense signal, very probably they still contain blood traces inside. Both Fig. 3.1a and 3.1b show the hippocampal region (green arrows) at different depths. It can be observed that in a healthy brain the cerebral cortex (the peripheral region of the brain pointed by blue arrows in Fig. 3.1a) is free of imperfections. The visible faint white spots are the weak signal coming from the cell cortex and not sharply visible with this current spatial resolution. Conversely, XPCT succesfully imaged the myelin fibers, as it is showed by the yellow arrows

in Fig. 3.1b. This is not a trivial infomation, as it is not obvious to be able to visualize them with routine neuro-imaging techniques.

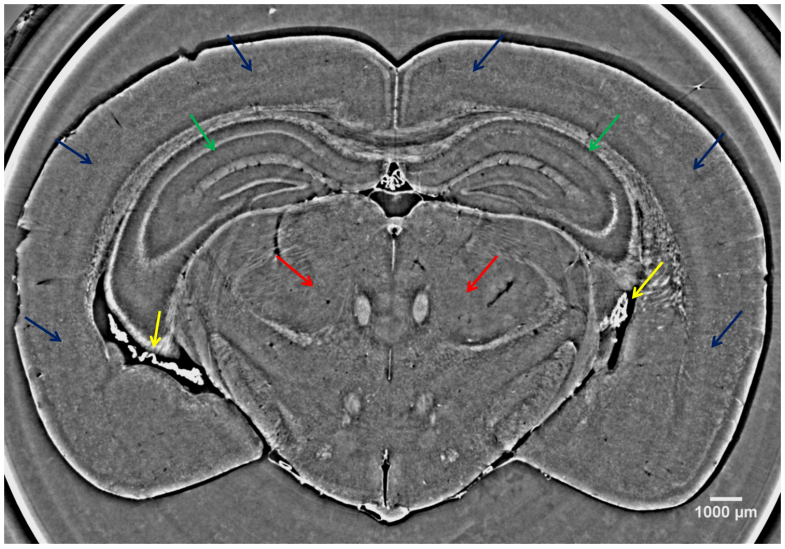

(a)

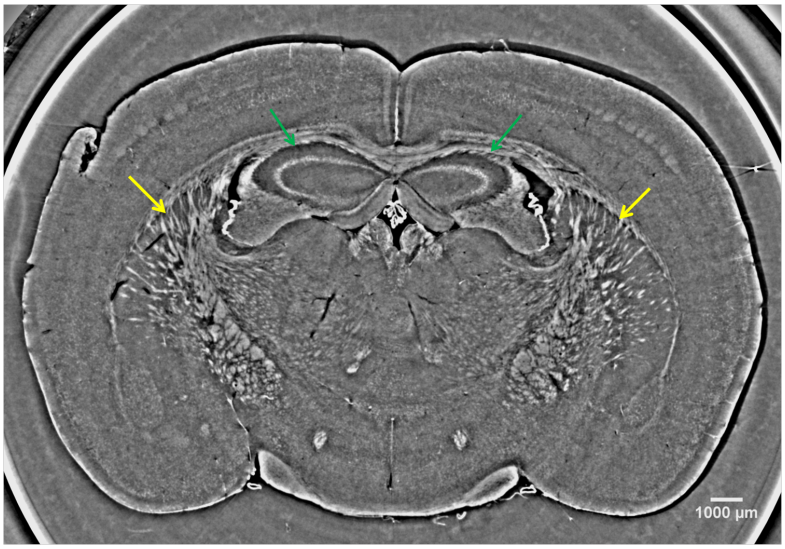

(b)

Figure 3.1: 2D XPCT virtual slices of the healthy mouse brain chosen at two different depths. (a) This insight offers a good visualization of the cerebral cortex (blue arrows), midbrain region (red arrows), lateral ventricles (yellow arrows) and the hippocampal formation (green arrows). (b) This brain insight shows the myelin fibers (yellow arrows) in addition to the anatomical features seen in Fig. 3.1a.

Myelin fibers are considered as markers of many neurodegenerative diseases and their imaging plays a crucial role in monitoring lesions in the white matter [143]. In Fig. 3.2a a piece of brain volume representation enhancing the visualization of the myelin fibers is shown. The image was obtained by the maximum intensity projection of a sequence of XPCT brain slices. In Fig. 3.2b, a magnified inset cropped from Fig. 3.2a is displayed. This view allows distinguishing single axons and their orientation. This result seems to be promising in the use of XPCT as method to map myelin fibers in brains.

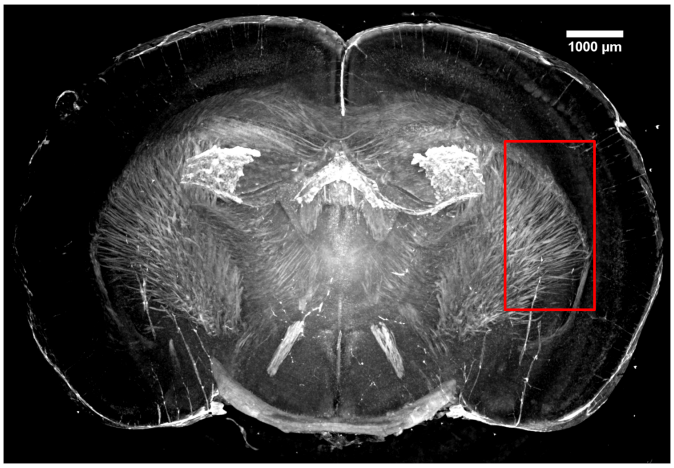

(a)

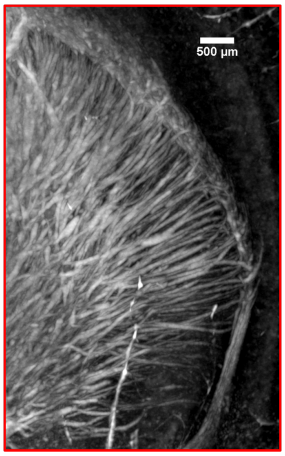

(b)

Figure 3.2: (a) Brain volume representation focusing on the myelin fibers visualization. (b) High-resolution close-up of the fibers indicated within the red rectangle in Fig. 3.2a. From this close-up, individual axons can be identified.

Fig. 3.3 is an insight of a healthy mouse brain whose blood-brain barrier was opened to let penetrate not-functionalized nanoparticles, i.e. AGuIX®. Few intense signals were detected in few points of the midbrain tissue and pointed by red arrows. They could be attribute to deposits of nanoparticles clusters. The presence of nanoparticles in this sample was also confirmed by the MRI measurements performed by our collaborators in NeuroSpin. However, it has been noted that the amount of nanoparticles detected throughout the brain volume was very low. This could be due to a low injected amount of nanoparticles, to nanoparticles difficulty to cross the blood-brain barrier despite its local opening or, in the opposite case to an early and fast cleaning. Moreover, it can not be excluded that a small amount of nanoparticles remained trapped in the vessels.
The first conclusion we reached with this set of measurements is that XPCT could find clusters of nanoparticles in the control brain even if their concentration was weak.

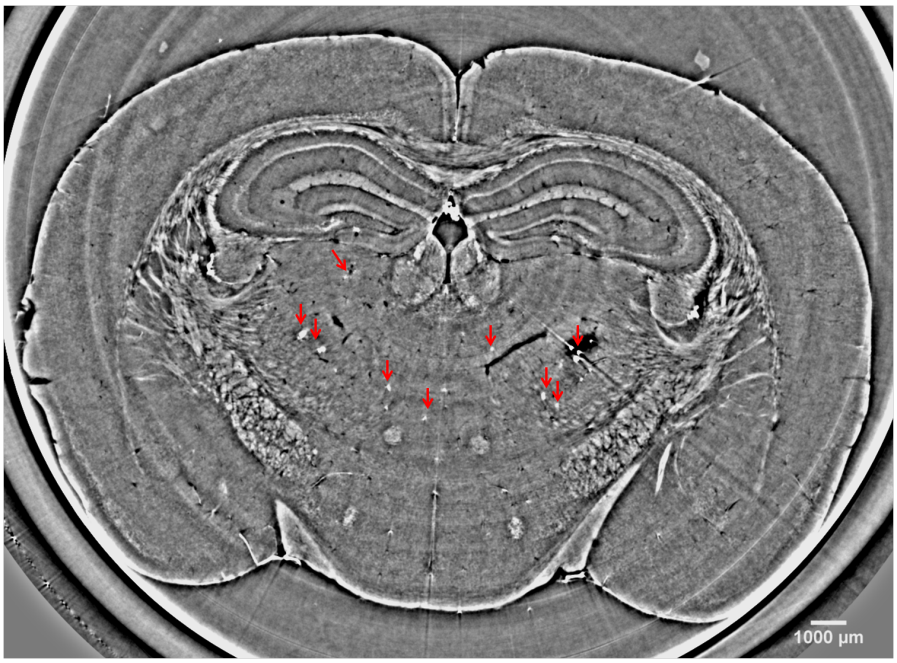

Figure 3.3: 2D XPCT slice of a healthy brain injected with non-functionalized nanoparticles. Red arrows point to some dense spots in the midbrain region. Very probably they are nanoparticles deposits in the brain matter.

In Fig. 3.4a the brain of a transgenic mouse carrier of the Alzheimer's disease in advanced state is shown.

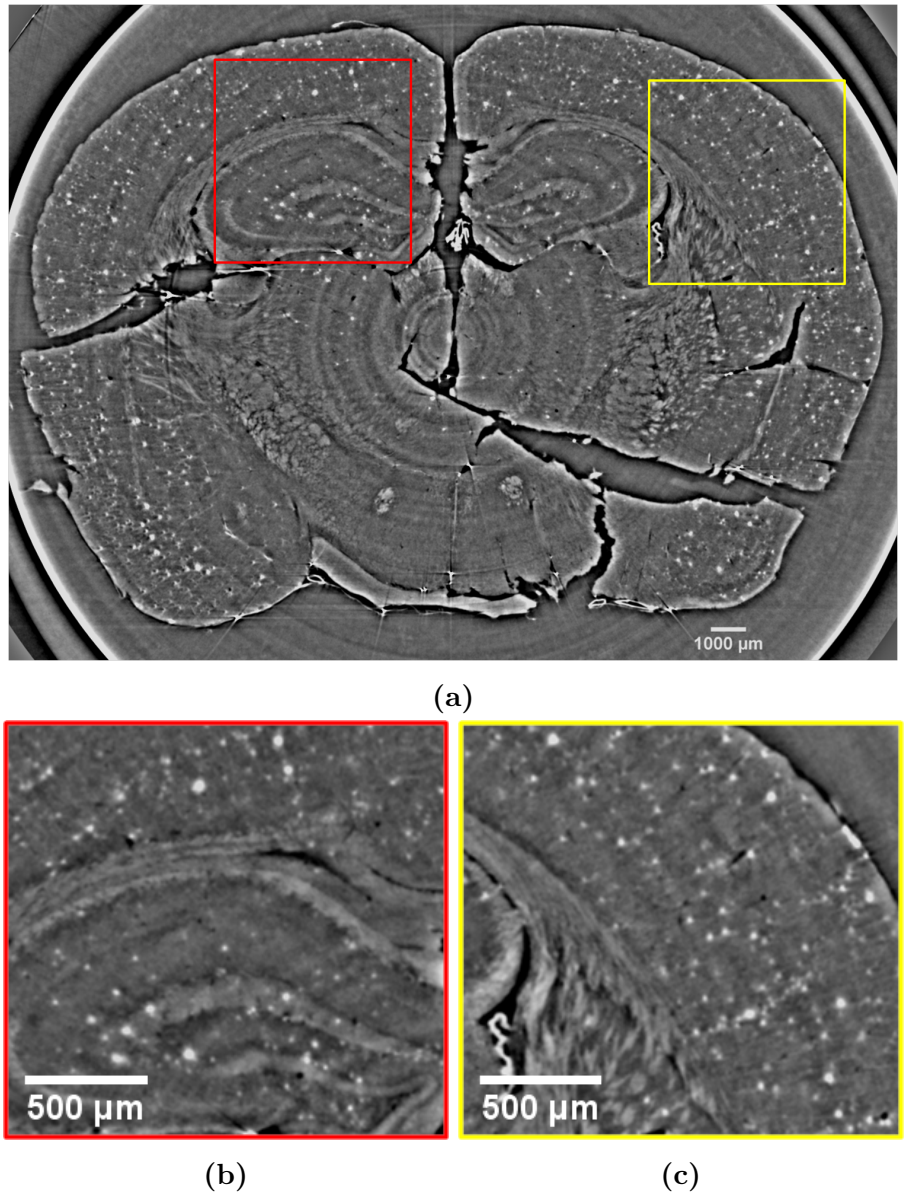

Figure 3.4: (a) 2D XPCT virtual slice of the mouse brain used as control model for the study of the Alzheimer's disease. The white intense spots spread throughout the cortex and the hippocampal region are the amyloid plaques. (b) Close-up of the red rectangle of Fig. 3.4a. This cropped image shows amyloid deposits (white spots) in the hippocampus. (c) Close-up of the yellow rectangle of Fig. 3.4a. This cropped image offers a view of the amyloid deposits (white spots) invading the cortex.

The brain does not contain nanoparticles. XPCT was able to identify the onset

of the disease. The brain shows numerous small white dots spread throughout the cortex and the hippocampus. They are the amyloid plaques, a mixture of iron, zinc and copper, that the disease is used to produce in specific regions of the brain [144, 145]. Typically, the amyloid plaques have a central dense core and can be also surrounded by a diffused light corona [146]. The intense spots detected by XPCT agree with this description. In the healthy brain (Fig. 3.1), such amount of white dots were not present. This structural change confirms that what we see are the amyloid plaques. Amyloid plaques can be clearly seen in the hippocampus (Fig. 3.4b) and in the cortex (Fig. 3.4c). The images have a good contrast and, thanks to the powerful resolution, plaques of different sizes and conformations can be observed. We estimated plaques with width comprised between 20 μm and 110 μm and we observed that some plaques are more rounded and others more elongated. This result is in good agreement with previous works [147, 83]

The images we obtained reproduce at higher resolution published data about amyloid detection in mice by grating interferometer based differential phase-contrast [83]. Our images were achieved with a volume voxel $3 \times 3 \times 3$ μm^3 against the images in [83] collected with a set-up having a volume voxel of $7.4 \times 7.4 \times 7.4$ μm^3.

The 2D XPCT images of the mouse brain affected by Alzheimer's disease and doped with functionalized gadolinium nanoparticles (AGuIX-PEG-PIB) are displayed in Fig. 3.5a and 3.5b. Also in this case the blood-brain barrier was locally opened with the ultrasound approach.

Having now knowledge of the structural changes induced by the disease to the brain anatomy, amyloid plaques can be immediately recognized in the brain displayed in Fig. 3.5. The demanding task in this sample image analysis is distinguishing the functionalized nanopaticles from the plaques. The plaques are widely diffused in the cortex and in the hippocampus, and both the plaques and the gadolinium-based nanoparticles theoretically provide a white signal in the XPCT images. So, this makes it very difficult to localize the functionalized nanoparticles in the brain.

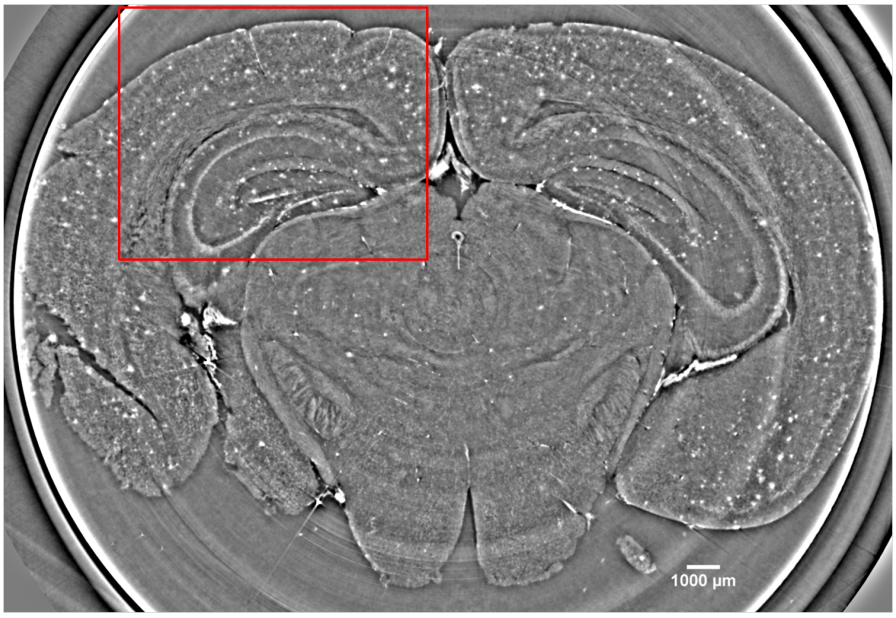

(a)

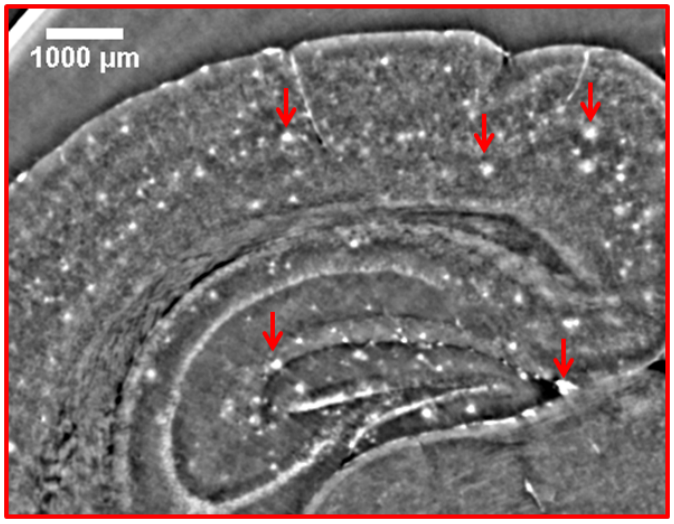

(b)

Figure 3.5: (a) 2D XPCT virtual slice of the mouse brain affected by Alzheimer's disease and injected with functionalized nanoparticles. (b) Cropped image from Fig. 3.5a focusing on the left hippocampus region of the mouse brain. The red arrows show hyper-intense structures.

Nevertheless, we observed (Fig. 3.5b) some hyper-intense spots that are much whiter on the image than the average spots that we identified previously as coming

from the plaques. It might be an indication of successful targeting of AGuIX® on few plaques. Regarding, the well-known disparity of plaque morphology and chemical composition, this might be also an artefact. We thus investigated further the variation of the index of refraction between characteristic plaques and plaque loaded with gadolinium (Fig. 3.6 and 3.7).

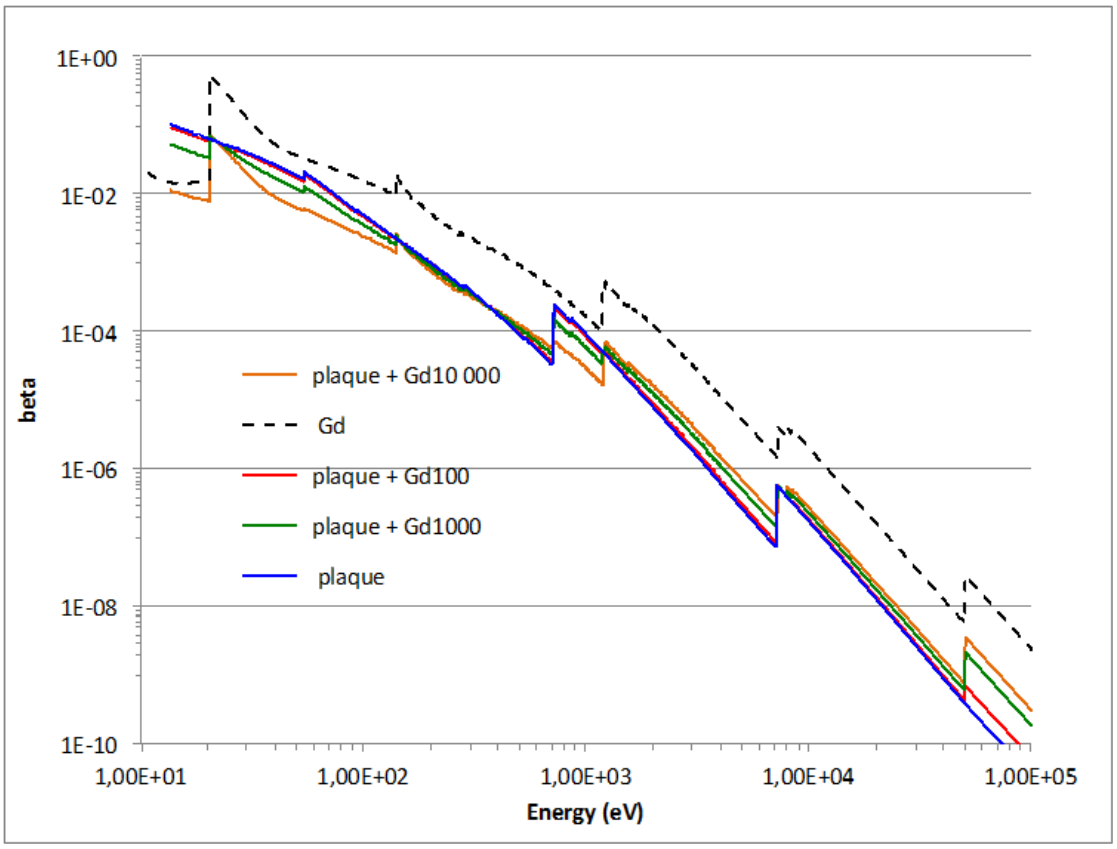

Figure 3.6: β versus photon energy for pure gadolinium (dotted black), plaque doped with 100 atoms of gadolinium (red), 1000 atoms of gadolinium (green), 10 000 atoms (orange) and undoped plaque (blue).

We used three very different concentrations of gadolinium to infer the impact on the images. The concentrations were chosen arbitrary since we have so far no indication about them. For the imaginary part relating to absorption, even a small doping of gadolinium changes its value. For only 100 atoms of gadolinium, i.e. 11 molecules of AGuIX®, over 3900 atoms contained in typical plaques ($C_{400}H_{670}O_{119}N_{15}S_2Fe_{2700}$), the value of beta rises from 3.6×10^{-10} to 7.0×10^{-10}.

Higher concentrations lead to stronger changes with beta equals 2.1×10^{-9} and 3.1×10^{-9} for 1,000 and 10,000 atoms of gadolinium, respectively. This last concentration is barely realistic but it was useful to test the variation of delta (Fig. 3.7).

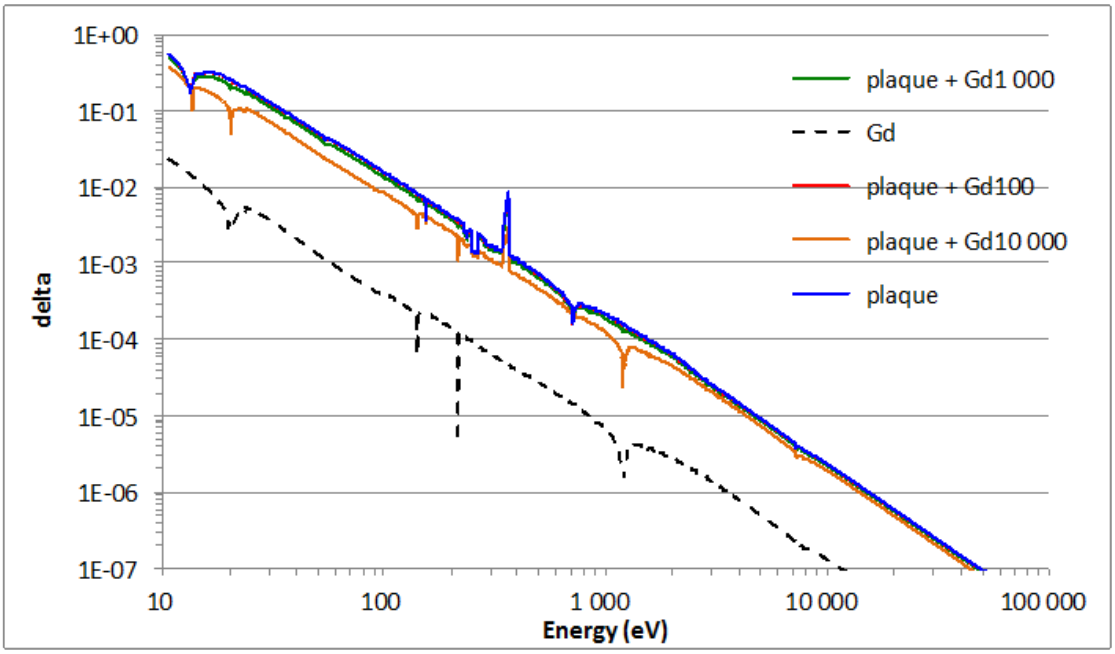

Figure 3.7: δ versus photon energy for pure gadolinium (dotted black), plaque doped with 100 atoms of gadolinium (red), 1000 atoms of gadolinium (green), 10 000 atoms (orange) and undoped plaque (blue).

As previously observed (Chapter 2, paragraph 2.8.1) for the tumor in brain, only very strong and thus unrealistic concentrations of gadolinium may significantly change the real part of the index of refraction. δ exhibits several drops but only few of them are characteristic of the gadolinium transitions at about 20 (O-edge), 140 (N-edge), 270 (M-edge), 1200 (M-edge) and 50 000 eV (K-edge). This last peak is not visible due to the vertical scale used to make visible the tiny changes in δ. Once again, it appears the K-edge subtraction imaging technique would give measurable effect only due to the change of absorption. Assuming the plaques to be spheres of with either 20 or 110 μm in diameter, as given by our measurement, we may estimate the variation of absorption between pure plaques and gadolinium-doped plaques. For 20 μm plaques, 100 atoms of gadolinium will increase the absorption by about 30% and 80% for doping as high as 1,000. Higher doping is not realistic.

Even 1,000 atoms is probably a maximum possible doping. For larger plaques of 100 μm, the absorption becomes much bigger increasing by 80% for 100 atoms of gadolinium. Pure AGuIX® sphere with 100 μm diameter will have a much stronger absorption. As a conclusion, the hyper-intense dots that look quite different from other spots might be plaques doped with gadolinium. The complete treatment of the data by comparing images acquired below and above gadolinium K-edge may give a confirmation that very few plaques were effectively doped with gadolinium. Indeed for 100 μm plaque doped with 100 gadolinium atoms, the variation of signal below and above K-edge should be around 60% that is high enough for being above any experimental noise. For 20 μm plaques, the variation of intensity will be around 20%. This shows that only strong doping or large plaques will give to intensity variation above noise. Fluorescence X-ray tomography [148] or nano-tomography may be more appropriate tools for detecting gadolinium in amyloid plaques. Finally, the higher resolution used in this experiment as compared to previous ones was letting us expect to observe clustering of AGuIX® on some plaques meaning a plaque with on one side a hyper-intense and very localised dot. This was not observed. The plaques for which there is indication of gadolinium loading look homogeneous like if the AGuIX® was distributed all over the plaque. This issue might be investigated with nano-tomography, either by fluorescence or phase-contrast.

3.3 Summary

In this chapter the preliminary results about the detection of gadolinium nanoparticles in mice brains model of Alzheimer's disease were shown. To identify the anatomical changes induced by Alzheimer's disease to an aged brain, firstly a healthy mouse brain was shown. Secondly, a control brain with not-functionalized nanoparticles (AGuIX®) is displayed. This was a fundamental test to understand the ability of the technique in visualizing the nanoparticles uptake in brain tissue. Subsequently to observe the structural changes caused in the brain by this neurodegenerative disease, a brain with Alzheimer's but without nanoparticles was studied. The high-resolution of the technique permitted to discriminate amyloid plaques of different sizes and structures. Then, the challenging case of an Alzheimer's model brain with functionalized nanoparticles (AGuIX-PIB) was examined. The discrimination of nanoparticles signal from that of amyloid deposits

appeared very hard. We have some indications letting us believe that we observed few plaques loaded with AGuIX-PIB. Very likely, the amount of functionalized nanoparticles crossing the blood-brain barrier was low, as it was proved by the images depicting the control brain with not- functionalized nanoparticles. In addition the chosen parameter δ/β to phase-retrieve the images was probably not the most appropriate to enhance nanoparticles signal and better discriminate it from those of the amyloids. However we believe that nanoparticles could be more easily detected throughout the brain by the K-edge imaging approachtested in Chapter 2 and still under development.

Chapter 4

Plenoptic imaging

Within this chapter another 3D imaging technique is presented, the so-called plenoptic imaging. We worked on the transposition of the plenoptic technique into the X-ray domain. We believe that with this technology the radiation dose transmitted to biological samples during measurements may be drastically reduced. The transposition of plenoptic to X-rays is the heart of the VOXEL FET-open European project, developed wihtin a collaboration of 7 European teams.
Plenoptic imaging relies on the use of a camera composed of a main lens and a microlens array. Thanks to the lenslet, different views over a narrow range of angles are recorded at the same time. This makes feasible the 3D reconstruction of a scene in a single exposure. Plenoptic imaging shows a certain similarity with limited angle tomography, where few projections, obtained following rotation of the sample, are enough to produce a volume [149, 150, 151]. In addition, plenoptic imaging has the ability of changing the viewpoint of the photographed scene and of digital refocusing unblurred objects. Digital refocusing is the heart of this technology as it allows performing a virtual sectioning of a 3D scene (volume) along the optical axis, where each section corresponds to a different depth and its thickness is equal to the depth resolution. In the framework of VOXEL project, we used our knowledge of plenoptic imaging in visible light to build the first model of soft X-ray plenoptic microscope (which will be presented in the following chapter 5). This chapter explains the theory behind plenoptic camera and shows the tests we carried out with visible light by using plenoptic camera 1.0.

4.1 State of the art: early works and developments

The primitive idea of using a lens array for capturing different points of view of a scene in a single exposure was introduced in the 1908 by Lippman and named "integral photography" [152]. Twenty years later, Ives improved Lippman′s design by inserting a main lens with a large diameter [153]. Afterwards, Adelson and Bergen gave the definition of plenoptic function [154] and Adelson and Wang conceived a camera prototype that they called "plenoptic camera", in which a main lens was focused on a matrix of microlenses [155]. But they never realized it. Levoy and Hanrahan introduced the simplification of the plenoptic function and demonstrated that for describing light flowing from every direction is sufficient a four dimensional function, said "light field" [156]. Indeed, the word light field has more ancient roots: in 1936 Gershun defined as light field the vector indicating the irradiance at a given point and direction [157]. Many approaches for the light field data treatment have been suggested during the years leading to progress in 3D photography. Levoy and Hanrahan proposed an image-based rendering method to render the scene from any arbitrary point of view from light field data and a method to compute images from virtual apertures [156]. Isaksen validated this last approach [158] and later, it was called "synthetic aperture photography" [159]. Recently, Ng realized the first hand-held plenoptic camera and developed a fast computational method for digitally performing refocusing [160]. Ng′s thesis had a great impact in the modern digital photography; thus, he decided to found Lytro [161], a company dedicated to the production of visible light field cameras. Light field technology resulted very attractive for the digital photography market and for its various applications ranging from microscopy [150] to cinema. Lumsdaine and Georgiev designed a new class of plenoptic cameras with higher spatial resolution than Ng′s model and more flexible geometry. They called it "focused plenoptic camera" or "plenoptic camera 2.0" [162]. Adobe Systems [163] is currently the leading industry of this new generation of 3D cameras. Among the changes made to the early plenoptic device, it worths mentioning also the model promoted by Raytrix [164] in which the lens array is composed of alternating microlenses with three different focal lengths.

4.2 Principle of plenoptic function

4.2.1 Plenoptic function and light field

In a homogeneous medium, such as free space, light rays propagate on straight lines. With the intent of representing the total geometric distribution of light rays travelling up to the image sensor and of quantifying rays for computer vision applications, Adelson and Bergen defined a function named "plenoptic" [154]:

$$P = (\theta, \phi, \lambda, t, x, y, z) \tag{4.1}$$

According to this definition, each light ray is identified by means of seven variables. The couple (θ, ϕ) indicates the angular coordinates linked to the direction of the ray, λ is the wavelength of the light radiation, t is the time, and (x, y, z) are the spatial coordinates that locate each spatial point through which the light ray passes. Under a series of suppositions that remain valid in the framework of image formation, plenoptic function can be resized up to four variables. The assumptions taken into account are the following [165]:

1. Light ray does not vary with time; thus, t can be neglected.
2. Light is monochromatic; hence, λ can be neglected.
3. Two spatial coordinates are enough to locate a ray, since light trajectory does not change in a region free of occluders; consequently, the third spatial coordinate can be omitted.

In this way, the 4D simplified version of the plenoptic function depends only on two angular and two spatial components (θ, ϕ, x, y) and, it is also known in literature as "light field" [156], or "lumigraph" [166] in computer science slang; whereas the amount of light travelling along a light ray is often referred as "radiance". To measure four dimensions (two angular and two spatial components), both a lens and a lens array are needed.

4.2.2 Plenoptic camera and conventional camera

A conventional camera is made up of a main lens and a sensor. The plenoptic camera differs form the traditional ones for the presence of an array of microlenses

placed in front of the sensor [160, 23]. The addition of this element changes the way of sampling the light rays. Whereas in a conventional camera, the main lens collects light cones to let them converge to a single pixel onto the image sensor, in the plenoptic camera there is an intermediary step. The main lens gathers light from different viewpoints of the photographed scene over its aperture diameter and forms an image onto the microlens plane. Each microlens covers a matrix of pixels of the sensor and individually originates a micro-image, or sub-image, onto the sensor plane. Thus, the resulting image is composed of a grid of sub-images, in turn made up of a grid of pixels. The acquired images by a plenoptic camera are a 2D flattening of the 4D sampled light field. An exemplary diagram comparing the image formation modes in the two cameras is illustrated in Fig. 4.1.

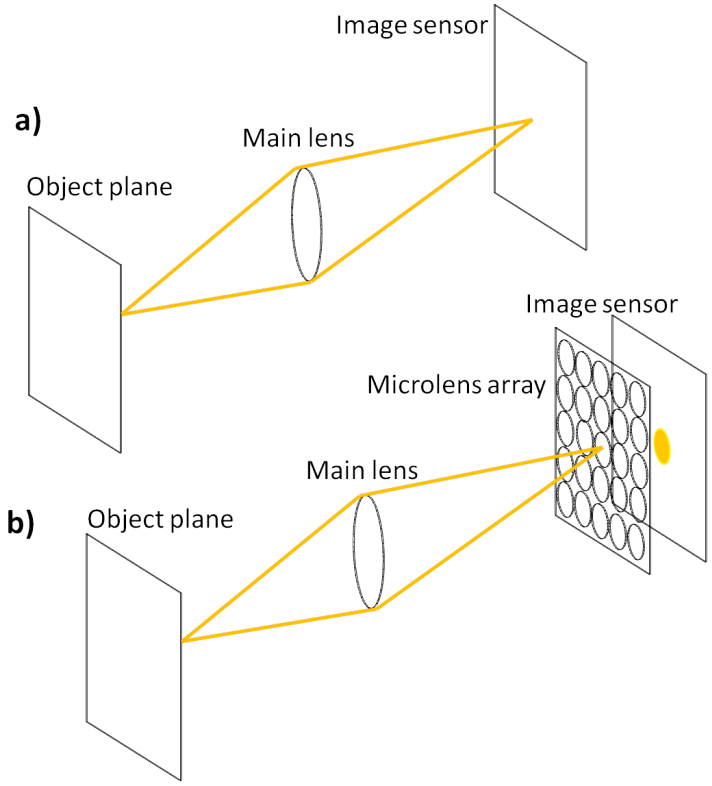

Figure 4.1: Layouts illustrating the mechanism of image formation **a)** for a normal camera **b)** for the plenoptic camera. Microlenses and distances are not in scale.

The specialty of plenoptic camera lies in the fact that it can store at the same time and in a single exposure the spatial and angular components of the light rays reaching the sensor. Through the angular information, it is possible to recover

the depth of the objects in the scene and to shift the focus where the rays should have ideally terminated. This refocusing step is achieved computationally after the picture is taken. However, in order to have angular resolution spatial resolution is sacrificed in the final rendered images.

4.2.3 Two-planes parametrization and ray trace representation

The 4D light field flowing into the camera can be described by means of a two-plane parameterization that it will prove to be particularly helpful when the digital refocusing problem will be dealt with. Let be (u, v) and (s, t) two imaginary planes transverse to the optical axis that cross the main lens and the microlens array respectively, like in Fig. 4.2.

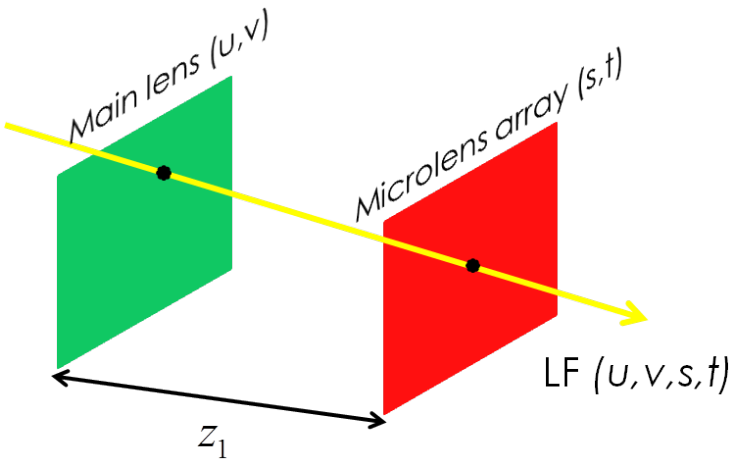

Figure 4.2: Sketch of the two-planes parameterization.

The radiance along a given ray may be denoted as $LF(u, v, s, t)$. With the (u, v) coordinates we refer to the directional or angular components of the light field. The point of intersection between the light ray and plane passing through the main lens determines the direction at which the light illuminates the sensor. The spatial coordinates, indicated with the (s, t) couple, show which microlens is crossed by the light ray. The radiance sampling can be illustrated through a Cartesian 2D ray-space diagram [23, 165], like the one displayed in Fig. 4.3, where the directional axis is plotted versus the spatial axis.

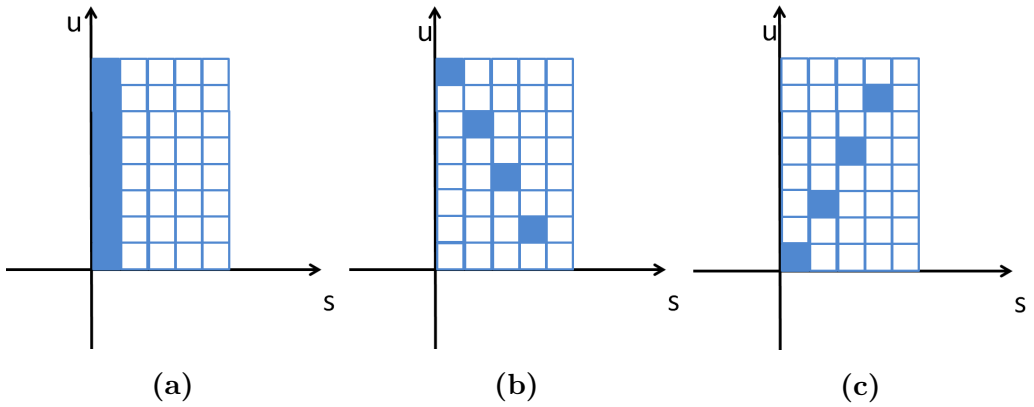

Figure 4.3: Cartesian 2D ray-space diagram. (a) Light field if the object is in-focus. (b) Light field if the object is farther from the camera. (c) Light field if the object is closer to the camera.

In this graphic (Fig. 4.3), each micro-image is represented as a vertical stack while pixels depicted as blocks. The diagram helps to figure out what pixels are hit by the light rays during the process of image formation. For an in-focus object, all the pixels composing a sub-image are illuminated. This can be represented with a straight vertical line, as shown in Fig. 4.3a. In the case of a blurred object, the situaton is different. Light rays impinge onto pixels belonging to different microlenses. For a blurred object, the line is tilted. If the light cone converges before the lenslet (see Fig. 4.3b), the line has a negative angular coefficient; whereas if the convergence is after the lenslet, the line results tilted with a positive slope (see Fig. 4.3c) [165].

4.3 Theoretical design of a plenoptic camera

The drawing in Fig. 4.4 summarizes the parameters involved in the optical design of the plenoptic camera. The aperture diameters of the main lens and of the microlens array are indicated with d_1 and d_2, respectively. Similarly, it is denoted with f_1 the focal length of the main lens and, with f_2 that of the microlens array. The separations between the different elements are called z_0, z_1 and z_2:

- z_0 is the distance between the in-focus plane and the main lens;
- z_1 is the distance between the main lens and the microlens array;

- z_2 is the distance between the microlens array and the CCD plane.

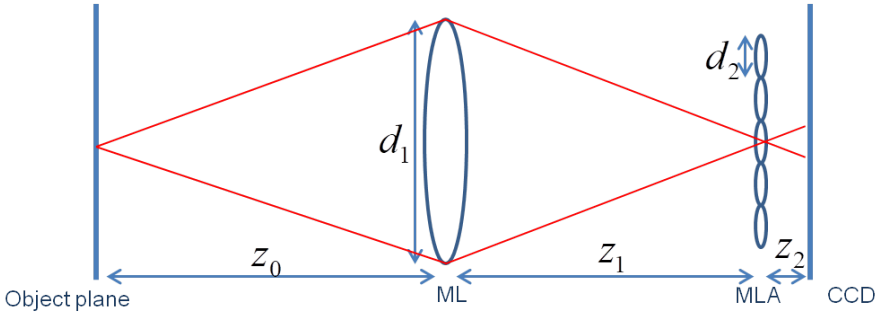

Figure 4.4: Optical scheme of the plenoptic camera with the notation adopted in this thesis.

We will see later that in case of refocusing a fourth distance, z'_1, is needed. According to this criterion of notation, the lens equation can be written as:

$$\frac{1}{z_0} + \frac{1}{z_1} = \frac{1}{f_1} \tag{4.2}$$

For the traditional plenoptic camera, the CCD is placed one focal length away from the microlens array:

$$z_2 = f_2 \tag{4.3}$$

in order to have the microlenses focused at infinity.
The plenoptic camera 2.0 allows gaining spatial resolution at the expense of the angular resolution. This design is composed of a main lens, a microlens array and a detector behind the lenslet, but the optical configuration totally changes, as shown in Fig. 4.5.

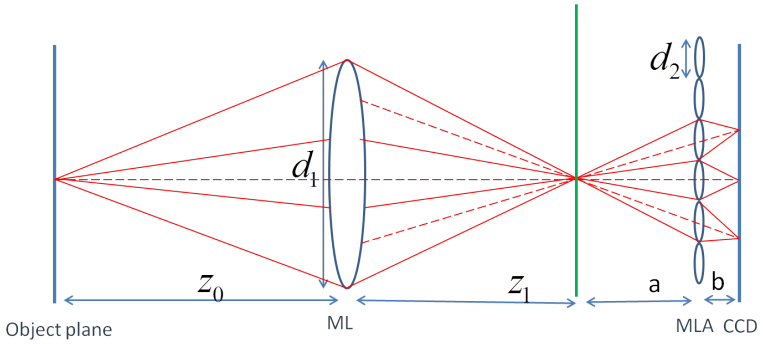

Figure 4.5: Layout illustrating the design of plenoptic camera 2.0.

The main lens originates an image onto a plane in front of the microlenses following the thin lens equation 4.2. The microlenses are focused on the image plane of the main lens instead of being focused at the optical infinity. This new class of cameras is also referred as "focused plenoptic camera" [162]. The distance between the sensor and the microlens array is not limited anymore equal to the focal length, f_2, of the microlens. The sensor may be placed at a distance $b > f_2$ or $b < f_2$ from the microlens array. The microlens array, positioned at a distance a from the intermediate image plane re-images the object. The image formation by the microlens array satisfies the thin lens equation:

$$\frac{1}{a} + \frac{1}{b} = \frac{1}{f_2} \tag{4.4}$$

If $b > f_2$, the main lens creates a real image in front of the microlenses; if $b < f_2$, the main lens generates a virtual image behind the microlens array and then the image is picked up by the microlenses and reimaged on the sensor. Thanks to this new optical design, the microlenses capture entire portions of the scene according to the position that they occupy in the array, as if they were a series of micro-cameras.

This configuration involves some changes in the ray space-diagram and in the image rendering. Each micro-image rather than being represented as a vertical strip in the Cartesian grid, it is now a tilted stack sampling both spatial and angular distribution of the radiance. Thus, at a spatial position the angular components are sampled across different microlenses rather than within each single micro-image [167].

The 2.0 version of the plenoptic camera was designed to achieve better spatial reso-

lution than traditional plenoptic camera, where the number of microlenses dictates the spatial resolution. In fact, the traditional plenoptic camera suffers from the fact every microlens counts as a final output pixel in the rendered image. Thus, the resulting image is made up of few pixels.

4.4 Resolutions of a plenoptic camera

In this section, we will retrieve different key parameters when designing a plenoptic camera.

4.4.1 Depth of field in photography

Let consider the scheme in Fig. 4.6 that proposes the simple case of a lens producing an image onto the image plane.

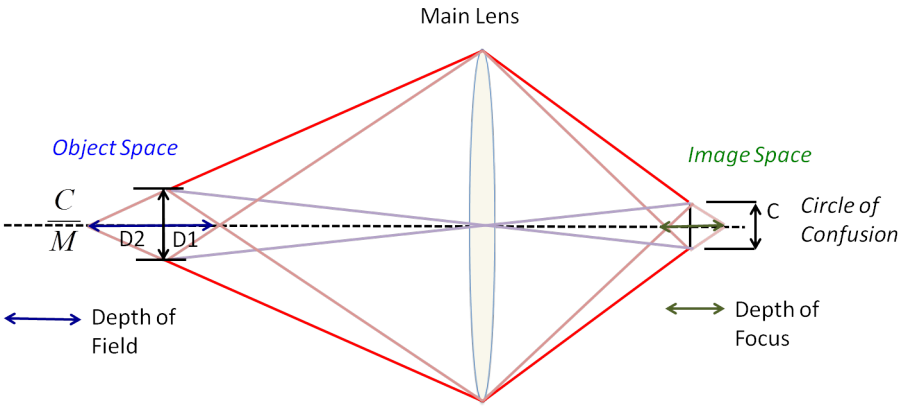

Figure 4.6: Layout enhancing the depth of field.

Let call D_1 and D_2 the two parts of the depth of field separated by the in-focus subject, represented with the vertical black line in the object space. Let z_0 the distance between the in-focus object and the main lens and, z_1 the distance between the main lens and the image plane.
For an out-of-focus object, a circle of confusion spot (vertical black line in the image space) is imaged on the sensor plane and its size is indicated with C. The in-focus object has a size C/M, where M is the magnification.
To express D_1 and D_2 as a function of the other available parameters, let's go

forward by estabilishing relationships between similar triangles, i.e. the small one having as side C/M and as height D_1 and, the big one having as height $z_0 - D_1$ and as side f/N that is the main lens aperture written as function of its focal length f and f-number N.

$$\frac{D_1}{C/M} = \frac{z_0 - D_1}{f/N} \tag{4.5}$$

and

$$\frac{D_2}{C/M} = \frac{z_0 + D_2}{f/N} \tag{4.6}$$

D_1 and D_2 are derived:

$$D_1 = \frac{C{\cdot}N{\cdot}z_0^2}{f{\cdot}z_1 + C{\cdot}Nz_0} \tag{4.7}$$

and

$$D_2 = \frac{C{\cdot}Nz_0^2}{f{\cdot}z_1 - C{\cdot}Nz_0}. \tag{4.8}$$

It follows that the depth of field (DOF):

$$DoF = D_1 + D_2 = \frac{2{\cdot}z_0^2{\cdot}f{\cdot}z_1{\cdot}C{\cdot}N}{f^2{\cdot}z_1^2 - C^2{\cdot}N^2{\cdot}z_0^2} \tag{4.9}$$

The second term at the denominator is much smaller than the fist term, therefore the DoF formula can be approximated to:

$$DoF = D_1 + D_2 = \frac{2{\cdot}z_0^2{\cdot}C{\cdot}N}{f{\cdot}z_1} = \frac{2z_0C{\cdot}N}{f{\cdot}M} \tag{4.10}$$

By rewriting z_0 from the thin lens equation, it results:

$$z_0 = f\left(\frac{M+1}{M}\right) \tag{4.11}$$

and by replacing z_0 in Eq. 4.12, it follows that:

$$DoF \approx \frac{2 \cdot C \cdot N}{M} = \frac{C}{NA \cdot M}. \tag{4.12}$$

where NA is the numerical aperture of the lens ($NA = 1/2N$). From Equations 4.7 and 4.8 it follows that the depth of field is asymmetrical around the in-focus object plane.

4.4.2 Resolutions plenoptic camera 1.0

Levoy and collaborators [150] expressed all the resolutions of a traditional plenoptic camera. We will re-write them here using our notations. Resolutions are limited by diffraction; therefore the effective pixel size is given by the maximum between the pixel size of the detector (Δps) and the diffraction limit spot size as defined by the Sparrow criteria (R_{obj}), with

$$R_{obj} = \frac{0.47 * \lambda * M}{NA}. \tag{4.13}$$

With NA the object-side numerical aperture ($NA = d_1/2z_0$), and M, the magnification ($M = z_1/z_0$). Light field camera provides four different types of resolution: directional, spatial, lateral and axial resolution. The directional resolution, (N_u, N_v), equals the number of pixels underneath each microlens as each microlens covers a defined number of pixels (see Fig. 4.7a).

$$N_u = \frac{d_2}{max(\Delta ps, R_{obj})}. \tag{4.14}$$

The spatial resolution, (N_s, N_t), is given by the number of microlenses in the array, N_2:

$$N_s = N_2. \tag{4.15}$$

Indeed, $(N_u \times N_s) \times (N_v \times N_t)$ leads back to the total number of pixels of the CCD. The spatial sampling rate is denoted with (Δs, Δt) and it coincides with the size of a microlens. The directional sampling rate is indicated with (Δu, Δv), instead. The directional sampling rate is defined as the ratio between the lens aperture

diameter and the directional resolution that is equivalent to the product between the pixel size, Δps, and the ratio between the distances z_1 and z_2:

$$\Delta u = \Delta v = \frac{d_1}{N_u} = \Delta ps \frac{z_1}{z_2} \tag{4.16}$$

A simplifying layout showing the relationship between the directional sampling rate and the involved optical elements is illustrated in Fig. 4.7b.

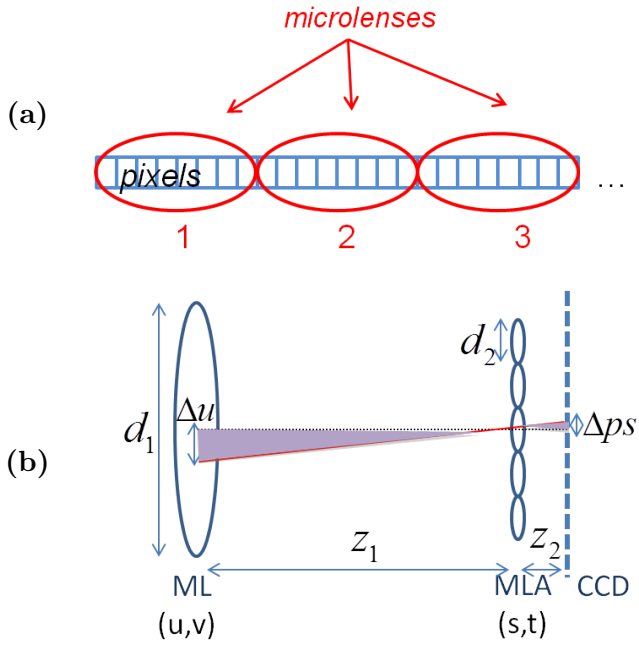

Figure 4.7: (a) Scheme to understand microlens array role in the design of a light field camera. Microlenses are represented with red circles. Every single microlens covers a defined array of pixels, here single pixels are drawn as blue squares. (b) Scheme showing the optical parameters involved in the definition of spatial and directional sampling rate of the light field camera.

The lateral resolution provides the size of an effective pixel on the object plane and it is defined as the ratio between the microlens size and the magnification, M, of the system:

$$Res_{lat} = \frac{d_2}{M}. \tag{4.17}$$

The axial resolution determines the depth resolution of the image (equivalent to the depth of field of an image taken by a conventional camera). The depth resolution is the distance comprised between the nearest point in-focus and the farthest one in the object space. The depth resolution is the sum of two terms: a geometric one and another one related to wave optics:

$$Res_{depth} = \frac{d_2}{M \cdot NA} + \frac{\lambda}{NA^2} \tag{4.18}$$

The axial resolution establishes the depth refocusing capability of the camera within a 3D scene. We refer to the total axial resolution (i.e. the whole 3D photographed scene) as plenoptic depth of field. The plenotic depth of field (DoF_{pleno}) corresponds to Eq. (5.3) in Levoy [150] and it is equivalent to calculate the depth of field in case of one small microlens:

$$DoF_{pleno} = \frac{N_u \cdot d_2}{M \cdot NA} + \frac{\lambda}{NA^2} \tag{4.19}$$

while the field of view (FoV) corresponds to the size of the sample that can be imaged and it is:

$$FoV = N_s \cdot Res_{lat} = N_2 \cdot \frac{d_2}{M} \tag{4.20}$$

With a plenoptic camera from one acquisition, a volume of size: $FoV \times FoV \times DoF_{pleno}$ can be reconstructed.

4.5 Experimental results: plenoptic camera 1.0

4.5.1 Camera set-up

Here, the design of our visible camera prototype is described. The system was built for simulating the plenoptic camera mode of operation and for testing refocusing. A descriptive picture of the set-up mounted in laboratory is shown in Fig. 4.8.

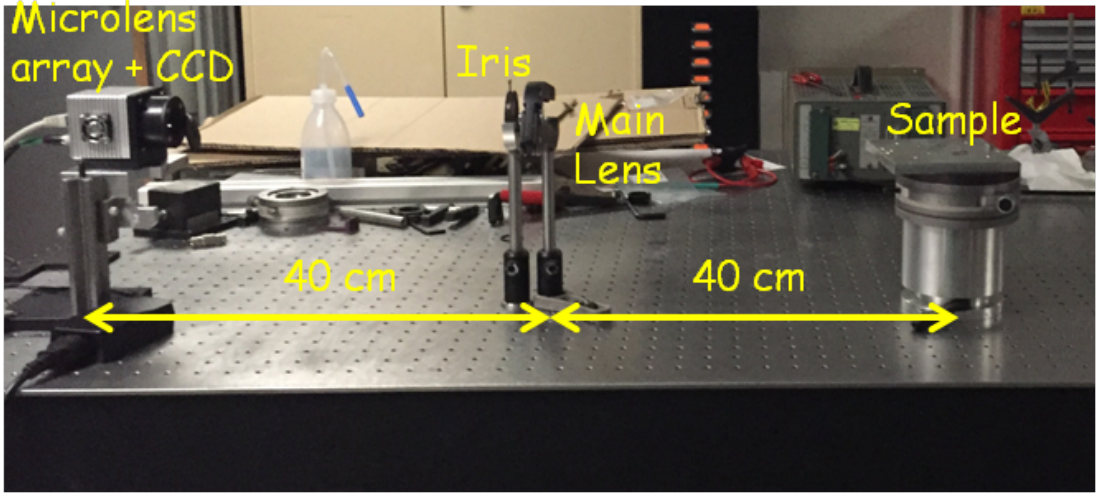

Figure 4.8: System simulating the plenoptic camera mode. It includes a wavefront sensor with 128 × 128 microlenses, an iris, a main lens 200 *mm* focal length. The lens was used in configuration $2f/2$f. The distance microlens aray main lens was fixed at 40 *cm*.

As it was mentioned above, the conventional plenoptic camera comprises a main lens, a microlens array and an image sensor. The peculiarity of our set-up was to capture the light field by using a Shack-Hartmann wavefront sensor that is typically employed for measuring the angles of the rays incoming on each lens and the lens aberrations. It is a device in which microlens array and a CCD image sensor are coupled. The microlenses have the same focal length and are focused on the CCD placed behind them. In particular, we used a wavefront sensor provided by the firm Imagine Optic [168].
The wavefront sensor chosen for our experiment consists of 128 × 128 microlenses squared packed. This lens array is fixed, one focal length away from the sensor plane. Each microlens has a pitch size of 110 μm and covers a matrix of 16 × 16

pixels onto the CCD sensor. The CCD has 14.6 $\times$ 14.6 mm^2 internal frame for a total number of 2048 $\times$ 2048 pixels. The full resolution of the captured light field images is 128 $\times$ 128 in the spatial axis and 16 $\times$ 16 in the directional axis. As main lens of the system, a plano-convex lens with 200 mm focal length was chosen and used in configuration $2f/2f$. Thus, it was kept a fixed distance of 40 cm between the main lens and the wavefront sensor, whereas the distance object-main lens was initially set to 40 cm and then, slightly varied of few centimeters in order to change the focus of the camera from time to time. A simple lamp was used as illuminating source of the photographic scene. To regulate the aperture size of the main lens and to produce round sub-images onto the CCD, an iris was introduced immediately after the main lens.

The experiment consisted in acquiring images of small objects placed on a stage with adjustable height at a certain distance one from each other, in order to have subjects at different depths. For instance, Fig. 4.9 shows some photographed test objects whose rendered light field images will be shown later in this chapter. On the left column of Fig. 4.9, conventional pictures of the recorded scene are displayed, whereas the corresponding raw light field images acquired with our camera prototype are illustrated on the right column. As the field of view of our light field camera prototype was narrow, the acquired images result restricted to the 3D scene within the red circles superimposed on the conventional pictures in the left column. Precisely, Fig. 4.9a shows a business card with the in-focus name *Raphael* 3.5 cm behind a out-of-focus ruler on the foreground. Fig. 4.9b shows two wine corks distant from each other by 9 cm, where the cork on the foreground is in-focus and that on the background is blurred.

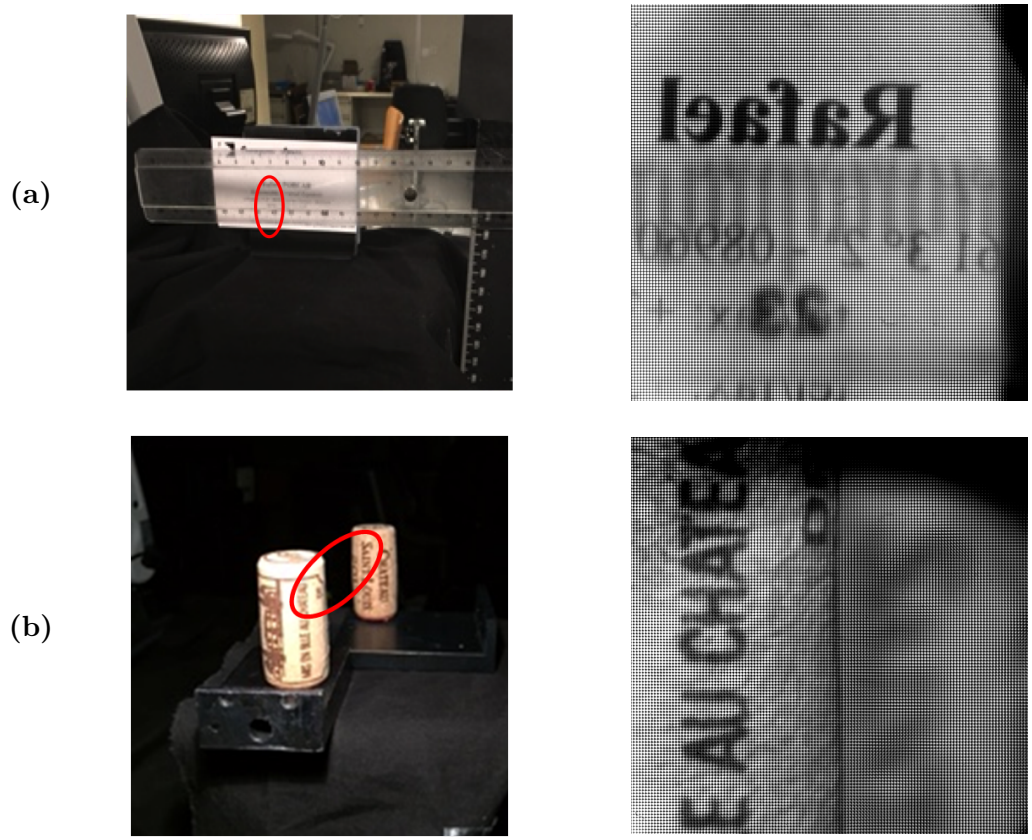

Figure 4.9: On the left column, some test objects photographed by a mobile camera. The red circle superimposed to the images shows the restricted field of view recorded by our plenoptic camera. On the right column, the light field images taken with our plenoptic camera prototype.

4.5.2 A glance at a light field image

In this paragraph, a deeper analysis of a raw light field image is achieved. Fig. 4.10 is another example of raw image acquired with our light field camera.

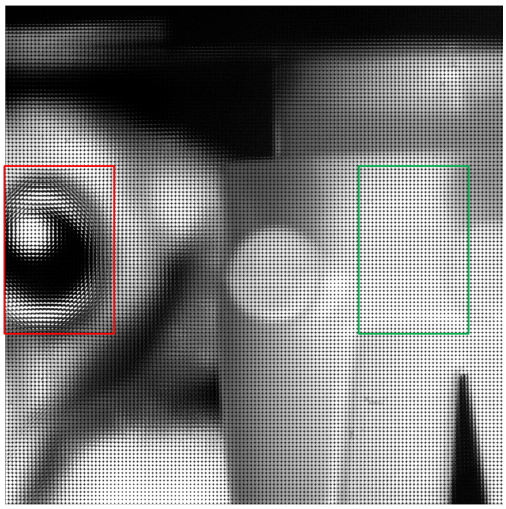

(a)

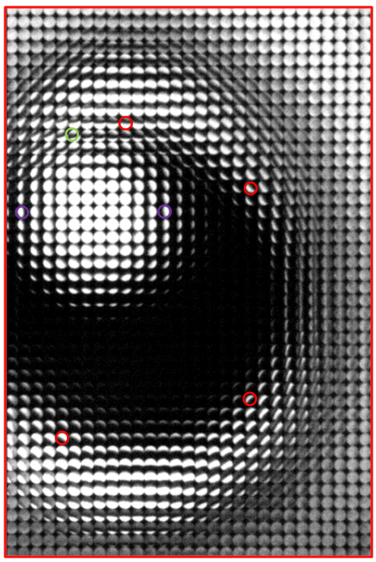

(b)

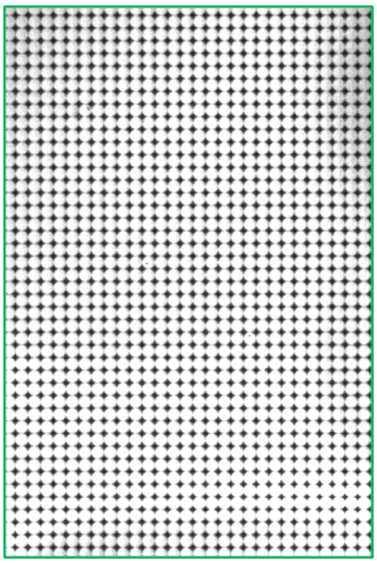

(c)

Figure 4.10: (a) 16 × 16 × 128 × 128 Raw light field image depicting two toys 3.5 *cm* far. (b) Zoom on the sub-images composing the dog′s eye image on the background. (c) Zoom on the sub-images composing the object image on the foreground of the 3D photographed scene.

The two photographed objects are two toys, displayed in Fig. 4.11.

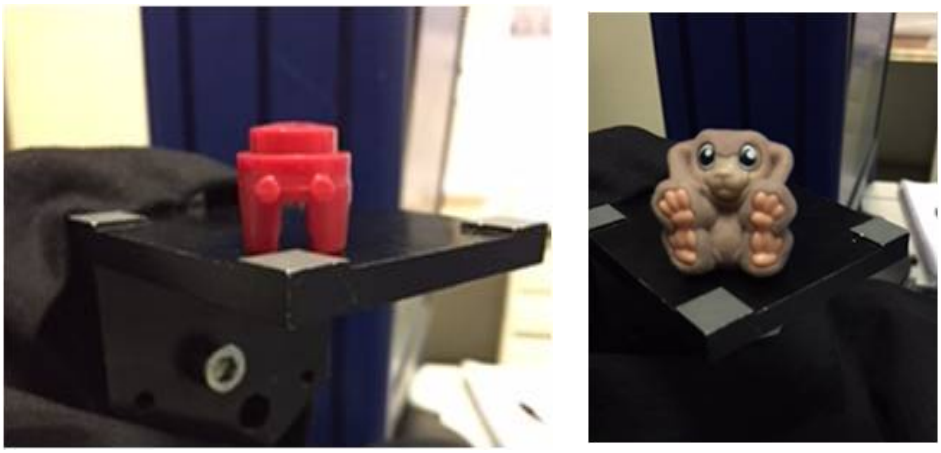

(a) **(b)**

Figure 4.11: Images showing the toys photographed by our plenoptic camera in Fig. 4.10.

As it can be seen, a raw light field image looks like a normal picture, macroscopically. Looking at it more closely, it can be noticed that it is composed of a pattern of small disks. These circular images are called sub-images and, each of them shows a precise area of the object seen from one single microlens, depending on the position that it occupies on the array. The captured 3D scene in Fig. 4.10 portrays a sharp toy on the foreground and a blurred dog on the background. The two objects are 3.5 *cm* distant from each other. The effects of sharpness and bluriness are due to the fact that light comes from different planes in the object space. Superimposed to the image, there are two coloured rectangles enhancing these two different features of the framed scene. By carefully examining these zoomed regions, we can notice that for an in-focus object, like in Fig. 4.10c, the grid of circular images is regular and each disk is well filled and illuminated the same way. For an out-of-focus object, like the dog′s eye on the background, sub-images are cropped, as it can be observed in the close-up of Fig. 4.10b. If we follow the superimposed red circles around the edge of the eye in anticlockwise way, starting from the bottom to the top, we notice that the sequence of the sub-images is reversed at a certain point. The sub-images at the bottom of the eye are filled half in black (lower part) and half in white (higher part), and the colors alternate in the sub-images at the top of the eye (black in the higher part and white in the

lower part). Those indicated by green circles have a tiny black stripe at the center, while those within the violet circles show sub-images filled only on one side: on the left for those at the left side of the eye and, only on the right for those at the right side of the eye. The filling factor of the sub-images is strictly linked to the departure position of the light rays travelling up to the image sensor.

4.5.3 Illustration of perfect matching

As it was mentioned, the number of pixels underneath a single microlens determines the directional resolution of the captured light field. A fundamental condition for achieving the best directional resolution is that the microlenses are focused at the optical infinity [160]. To have that, the CCD plane is placed one focal length away from the microlens array and hence $z_2 = f_2$.
The directional resolution does not rely only on the sharpness of the sub-images, but also on their size. Sub-images too small, or too large to overlap one with another, degrade the resolution. Therefore, the aperture size of the main lens and that of the microlenses have to be necessarily adjusted in order to cover as many pixels as possible for getting sharp and distinct sub-images [23]. In practice, this means to match the f-number of the main lens with that of the microlenses [155]. The f-number is a dimensionless number obtained by the ratio between the focal length of a lens and its effective aperture. In our set-up, thanks to an iris placed in front of the main lens, the aperture size of the main lens was adjustable to adapt to the f-number of the microlenses.
Fig. 4.12 shows how the quality of the captured images changes by varying the aperture size of the iris. When the f-number of the main lens is smaller than that of the microlenses, the amount of light passing through the main lens creates on the CCD plane circular images too big that tend to overlap each other (see Fig. 4.12a). When the f-number of the main lens matches the f-number of the microlenses, sub-images achieve the best filling factor and the maximal directional resolution is obtained (see Fig. 4.12b). When the f-number of the main lens is greater than that of the microlenses, a significant amount of light is lost and the sub-images originated on the CCD plane are cropped. Macroscopically, the images appear dark and directional resolution is wasted (see Fig. 4.12c).

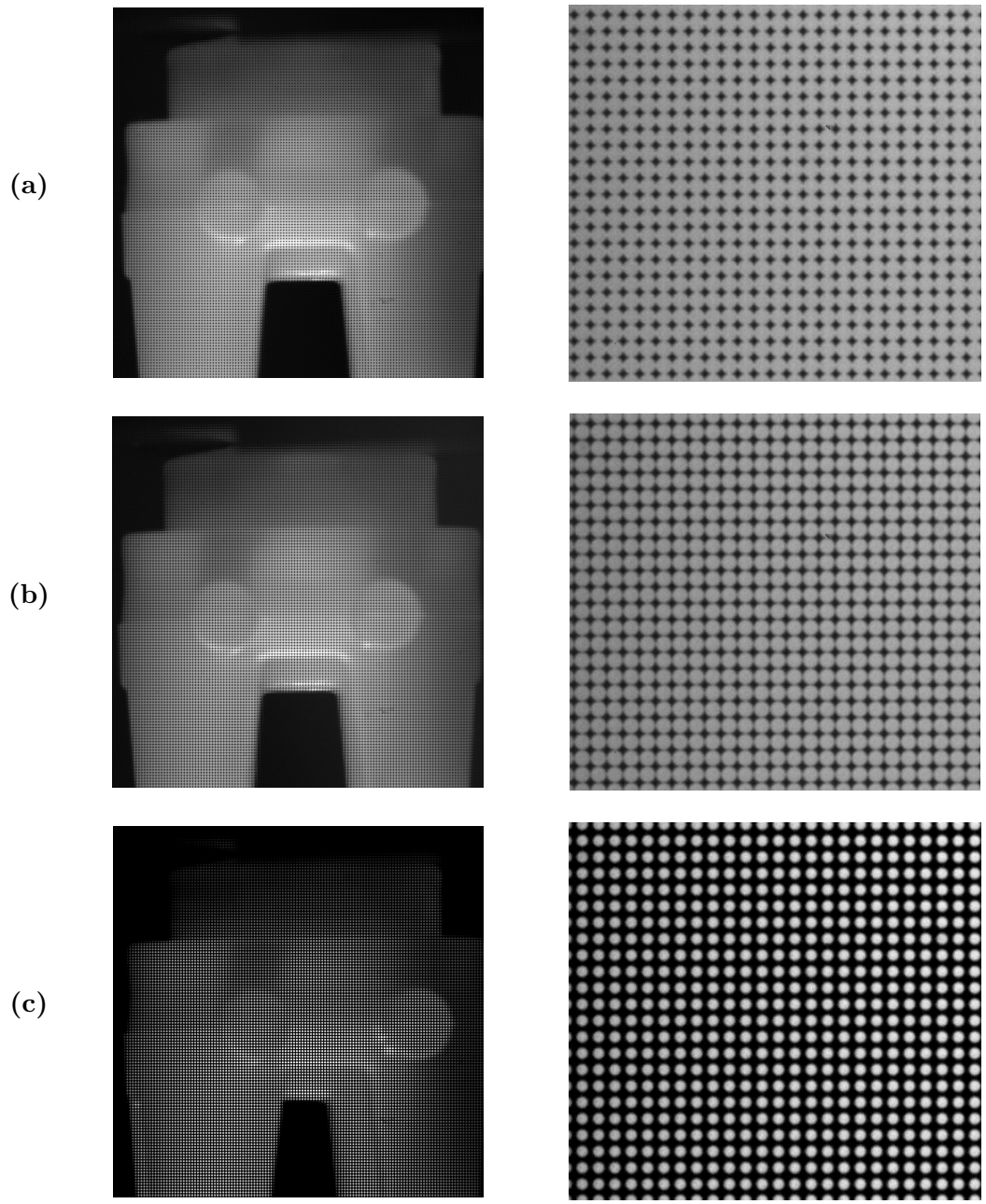

Figure 4.12: Images on the left column show raw light field images acquired for different configurations. Images on the right column are a zoom of the images on the left. (a) Image taken with an aperture size of the main lens bigger than that of the microlenses. Sub-images tend to overlap. (b) Image taken with an aperture size of the main lens matching the aperture size of the microlenses. Sub-images show the best filling factor. (c) Image taken with an aperture size of the main lens smaller than that of the microlenses. In this configuration, directional resolution is wasted.

4.6 Plenoptic 1.0 imaging

4.6.1 Sub-aperture images

A second way to display the light field is through *sub-aperture images* [23], as illustrated in Fig. 4.13.

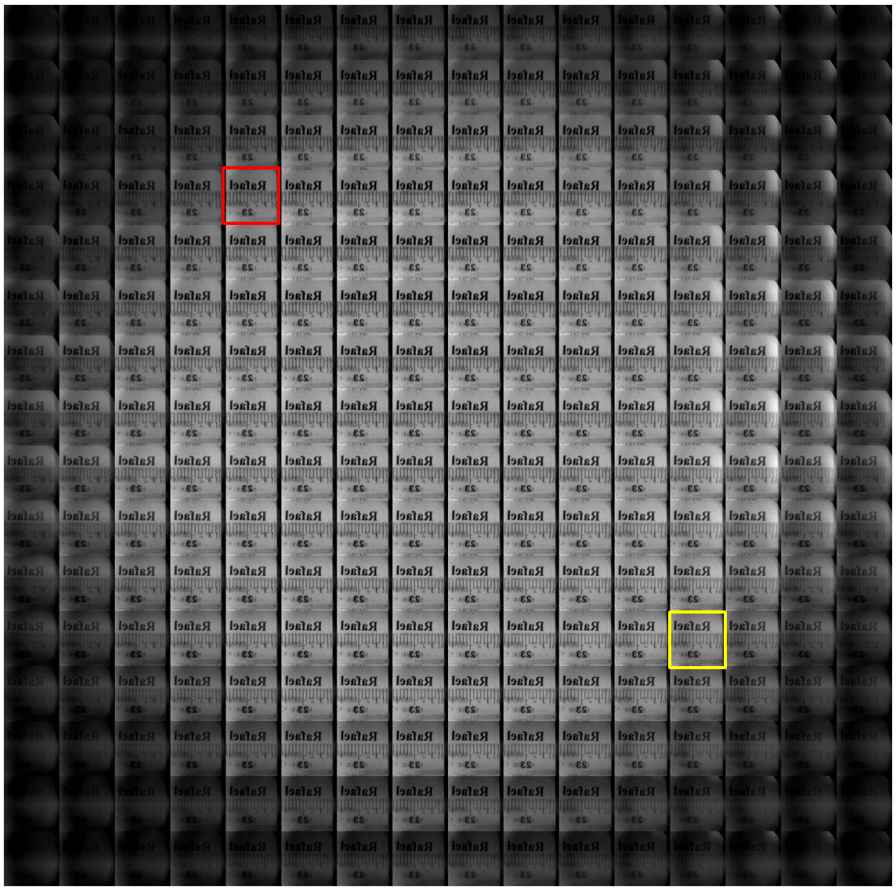

Figure 4.13: Sub-aperture images of the light field recorded in Fig. 4.9a

The *sub-aperture images* of the recorded scene are visualized underneath of a circular area (looking as a big eye) that repoduces the field of view seen by the main lens aperture. This kind of light field representation can be obtained by the 4D light field tranposed matrix. In other words, each sub-aperture image is built by extracting the same pixel of coordinates (u, v) from each microlens. Thus, the final image is composed by $u \times v$ *sub-aperture images* and in turn, each of these figures is made up of $s \times t$ pixels.

Each sub-image displayed in Fig. 4.13 shows the photographed scene according to a given (u, v) position on the main lens plane. More precisely, as (u, v) coordinates sample the directions of the incoming light rays through the main lens, each sub-aperture image shows a different perspective of the recorded scene. Moving virtually from one sub-aperture image to another demonstrates the change of perspective that can be achieved by a light field camera [160].
Moreover, sub-aperture images result u-times sharper than a light field picture taken with the full aperture of the main lens, since the sub-aperture images correspond to pictures taken with numerical aperture u-times smaller. In particular, the sub-aperture images of Fig. 4.14 are 16-times sharper than the raw light field image in Fig. 4.9a. The sharpness of the *sub-aperture images* can be notice in the close-ups of Fig. 4.14.

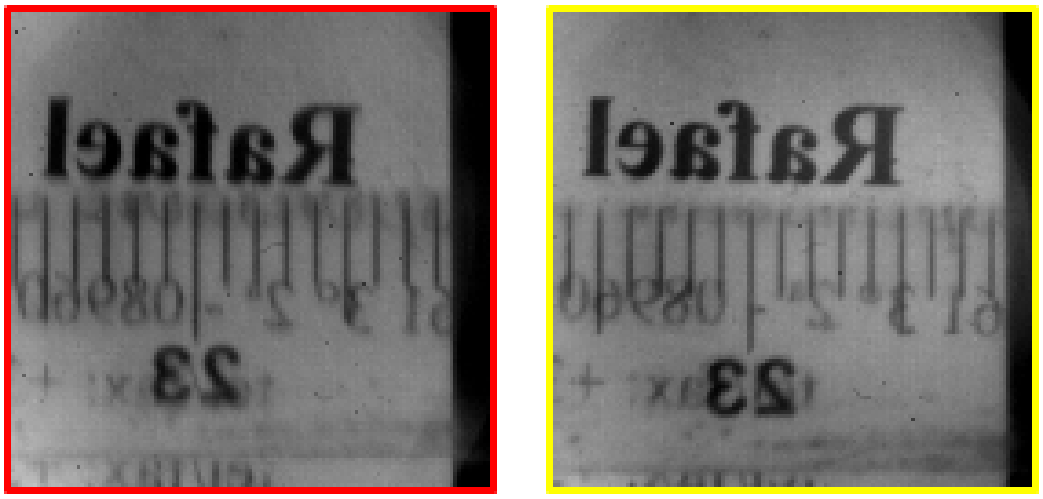

(a) **(b)**

Figure 4.14: *Sub-aperture images* extrapolated from Fig. 4.13. (a) Sub-image highlighted by the red rectangle in Fig. 4.14. (b) Sub-image highlighted by the yellow rectangle in Fig. 4.14.

These images are two sub-aperture images selected from two opposite sides of the main lens aperture. Fig. 4.14a corresponds to the sub-image highlighted by the red rectangle in Fig. 4.13, whereas Fig. 4.14b to that under the yellow rectangle. Although these figures look quite similar, they show parallax effects. By looking at them more carefully a series of differences due to the parallax phenomenon can be noticed, as for instance by focusing on the name "Raphael". In Fig. 4.14a, the

name “Raphael” appears immediately above the ruler, whereas it is shifted of few pixels higher in Fig. 4.14b.

4.6.2 Ray-tracing

When a picture is taken, there could be sharp subjects and blurred ones. These lighting effects can be understood by tracing back the light rays up to the photographed subjects. Fig. 4.15 shows the luminance profiles of three different situations that can occur when an image is achieved by a light field camera.

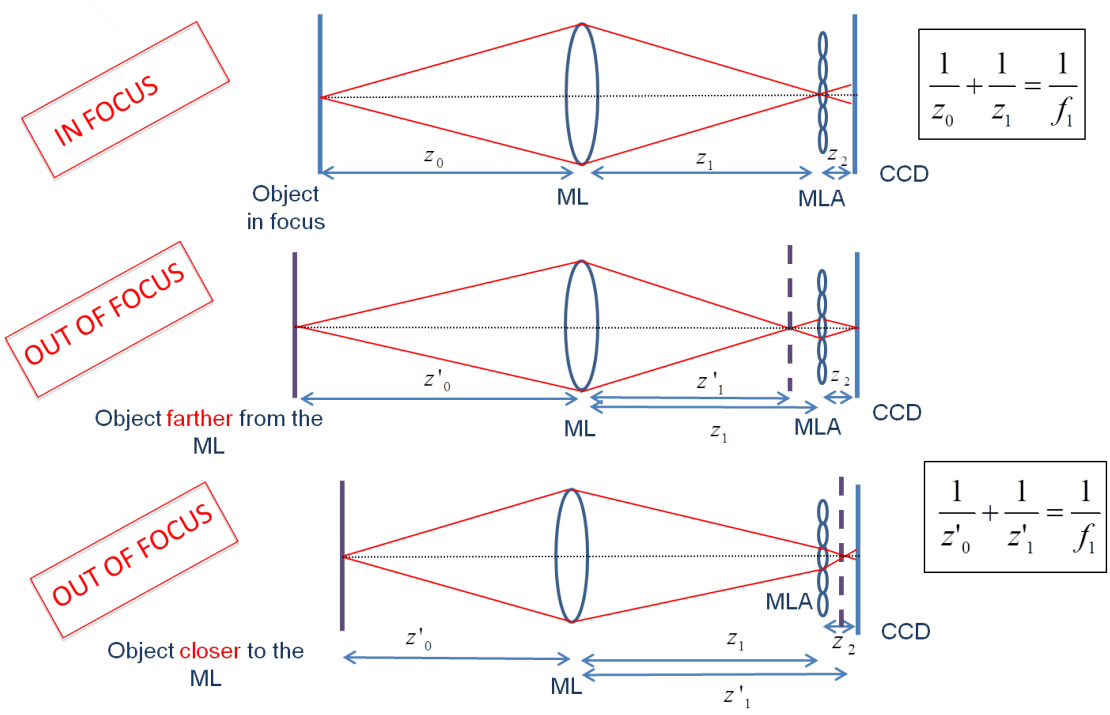

Figure 4.15: Ray-tracing schemes.

When the photographed object is in-focus, rays departing from the object plane are brought to a single convergence point at the microlens plane (scheme at the top of Fig. 4.15). Then, every single microlens originates a bright disk onto the CCD plane.
When there are subjects not rightly placed at the focalization (or in-focus) plane in the object space, consequently they appear blurred in the recorded picture. If the out-of-focus object is on a plane behind the focalization plane, it results farther

from the main lens. The light rays converge to a point on the plane z_1'; then, they diverge when they invest the microlenses and converge back to a point on the sensor plane (scheme in the middle of Fig. 4.15).
If the out-of-focus object is on a plane in front of the focalization plane, it results closer to the main lens. The light rays converge onto the plane z_1' between the microlens array and the image sensor and, they finally end up onto the CCD with different spatial locations (scheme at the bottom of Fig. 4.15).
In both misfocused cases the imaged objects would have result in-focus at the plane z_1'. The specialty of the plenoptic camera is to bring these out-of-focus objects to focus after the picture was taken. Thanks to the presence of the microlens array in the camera design, the depth information of the scene is preserved and the correct focus can be simply restored by means of a refocusing algorithm. So, the plane z_1' can be also called *refocused* plane.

4.6.3 Digital refocusing

In conventional photography, when light impinges on the sensor the resulting image is proportional to the received irradiance at each pixel [169, 23]. In a plenoptic camera, every microlens covers a matrix of pixels, instead. Therefore, the image rendering from the raw light field pictures is more complex. By taking into account the two-planes parameterization introduced previously and the imaging equation for the formation of the images from the classic radiometry [170, 160, 23], the resulting 2D image from the recorded 4D light field can be obtained through the weighted integral of the light rays passing through the main lens:

$$I(s,t) = \frac{1}{z_1^2} \int \int LF(u,v,s,t) \cos^4 \theta du dv \tag{4.21}$$

The angle θ is the incidence angle that rays make with the sensor plane. The $\cos^4 \theta$ term is sometimes referred as the optical vignetting factor. It represents the reduction effect due to rays arriving onto the sensor plane from oblique directions. Under paraxial approximation, i.e. by assuming that light rays form small angles with the image plane, it can be neglected as it would result equal to 1. Thus, the equation for the image formation is simplified:

$$I(s,t) = \frac{1}{z_1^2} \int \int LF(u,v,s,t) du dv \tag{4.22}$$

It means that the computed image from the collected light field is obtained by summing all the directions covered by each microlens. Or else, each microlens acts as an output pixel and the final image has a spatial resolution equal to the number of microlenses.
The focus of a blurred image can be corrected computationally, thanks to a refocusing process. The algorithm consists in virtually changing the separation between the main lens and the microlens plane, by exchanging the microlens plane with the plane where the focus would have been ideally obtained, as it is illustrated in the diagram of Fig. 4.16.

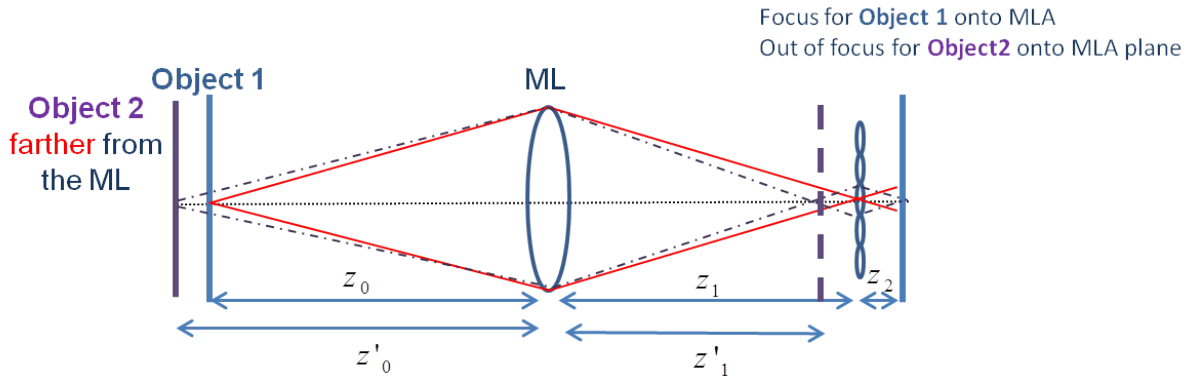

Figure 4.16: Optical scheme illustrating the case of refocusing of an object placed farther from the main lens.

In order to compute an image with a new focus at a distance z'_1, the light field at the desired depth should be re-parameterized and expressed as a function of the known light field [158] (see Fig. 4.17).

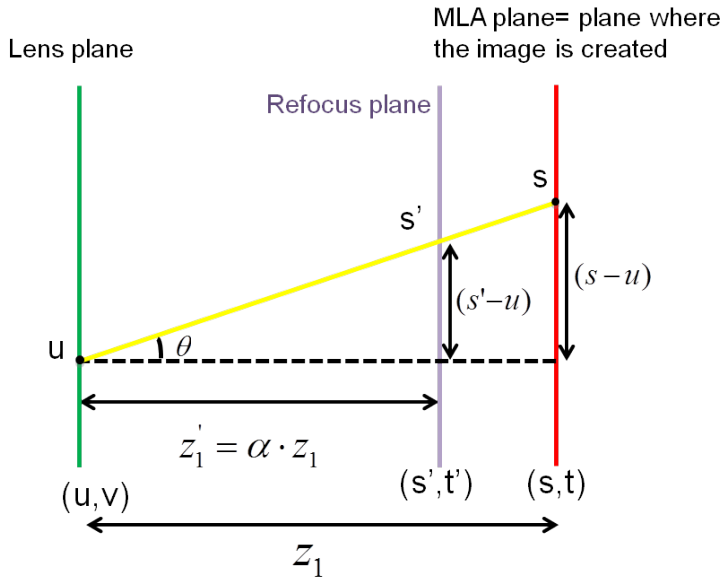

Figure 4.17: Parameterization scheme to perform digital refocusing.

Let be α the relative depth between the refocused plane and the measurement one, $\alpha = z'_1/z_1$. Let assume that $u \in (u, v)$ and that the point $s \in (s, t)$. The new coordinate $s' \in$ (s, t) can be derived from Thales theorem:

$$\frac{(s-u)}{z_1} = \frac{(s'-u)}{z'_1} \tag{4.23}$$

$$(s-u) = \frac{z_1}{z'_1}(s'-u) = \frac{(s'-u)}{\alpha} \tag{4.24}$$

$$s' = u + \alpha(s-u) \tag{4.25}$$

The coordinate s belonging to the measured light field expressed as a function of s' is:

$$s = u + \frac{(s'-u)}{\alpha} \tag{4.26}$$

Similarly, identical relationships are valid for the other two coordinates t and v. Thus, the refocused light field in terms of the measured light field will be [23]:

$$LF_{z_1'}(u,v,s',t') = LF_{z_1}\left(u, v, u + \frac{(s'-u)}{\alpha}, v + \frac{(t'-v)}{\alpha}\right) = \tag{4.27}$$

$$LF_{z_1}\left(u, v, u\left(1-\frac{1}{\alpha}\right) + \frac{s'}{\alpha}, v\left(1-\frac{1}{\alpha}\right) + \frac{t'}{\alpha}\right). \tag{4.28}$$

By means of the refocusing parameter α, the refocusing operation consists in performing a shearing of the light field of an angle ψ in the ray-space diagram:

$$\psi = \tan^{-1}(1-\alpha) \tag{4.29}$$

When the refocusing parameter is one, the rendered image shows the blurred and in-focus objects how they originally looked in the raw images. A refocusing parameter minor than unit can refocus out-of-focus objects farther from the main lens; whereas a refocusing parameter major than unit can bring to focus blurred objects placed closer to the main lens. A summary scheme is shown in Fig. 4.18.

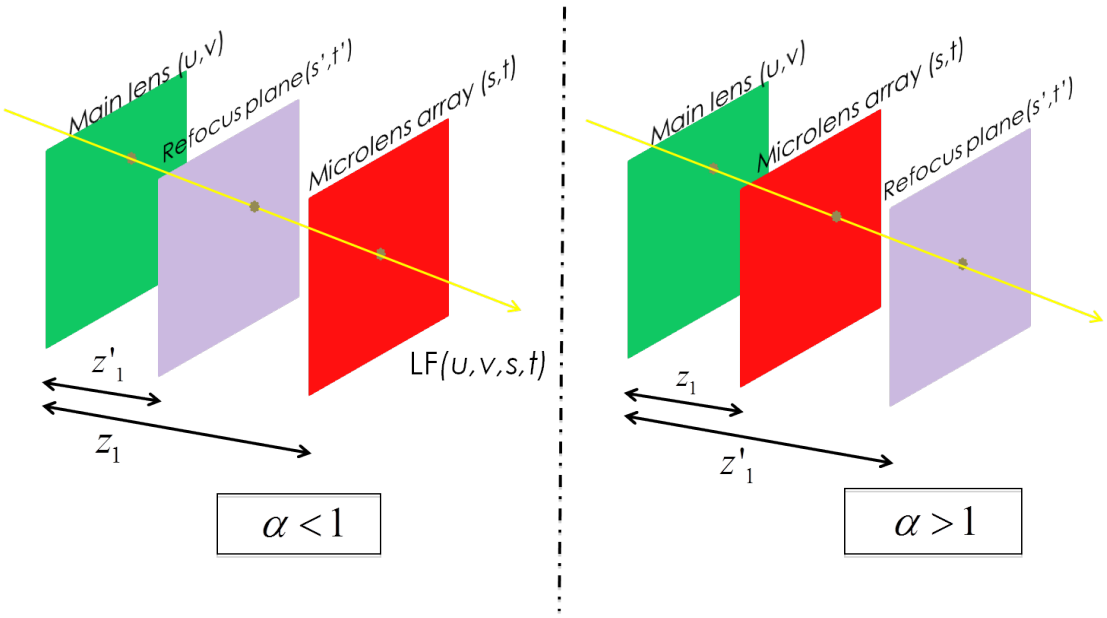

Figure 4.18: Drawing showing the role of the refocusing parameter.

The replacement in equation 4.29 of the light field with new coodinates ensures that the refocused image is obtained by summing the pixels underneath a microlens overall directions:

$$I_{z_1'}(s,t) = \frac{1}{\alpha^2 z_1^2} \int\int LF\left(u, v, u\left(1 - \frac{1}{\alpha}\right) + \frac{s'}{\alpha}, v\left(1 - \frac{1}{\alpha}\right) + \frac{t'}{\alpha}\right) dudv \quad (4.30)$$

This method recalls previous imaging works in which sub-aperture images were shifted and then summed for rendering an image [159].

4.6.4 Examples of digital refocused images

This paragraph shows the results obtained after the application of the refocusing algorithm over the raw images shown in Fig. 4.9.
The first case concerns a business card, with the name *Raphael* in view on the background, placed 3.3 *cm* behind a transparent ruler on the foreground. The corresponding rendered image at $\alpha = 1$ is illustrated in Fig. 4.19a, whereas the successful attempt to bring the ruler in-focus is shown in Fig. 4.19b. This result was achieved with $\alpha = 1.125$

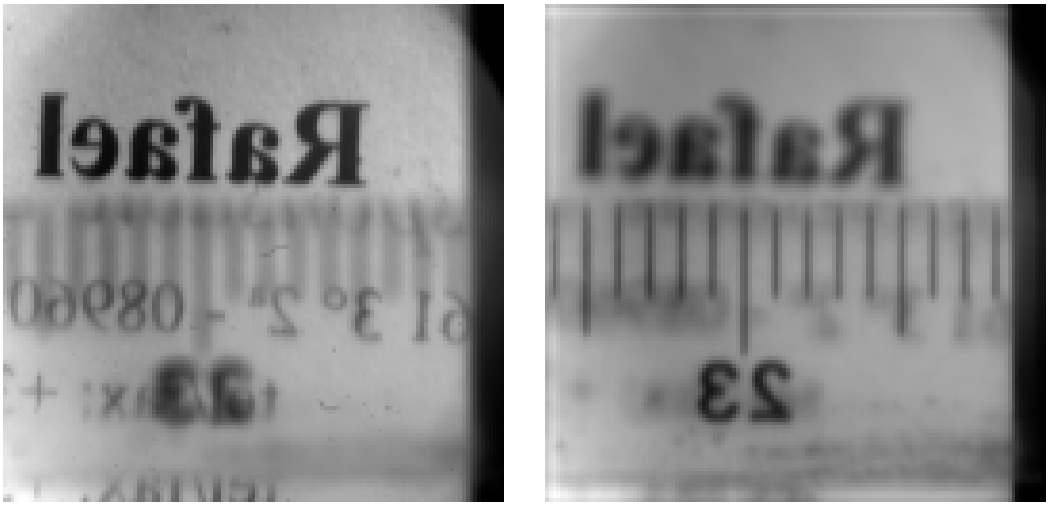

(a) **(b)**

Figure 4.19: (a) Rendered image on the background with α=1. (b) Rendered image on the foreground with α=1.125.

The second case illustrates two wine corks distant 9 *cm* from each other. The rendered image with $\alpha = 1$ in Fig. 4.20a shows a sharp cork on the foreground

whereas a second cork is on the background and the letters on its side are unrecognizable due to the blurring. This second cork was brought to focus with a refocusing parameter $\alpha = 0.88$ while the cork on the foreground became blurred.

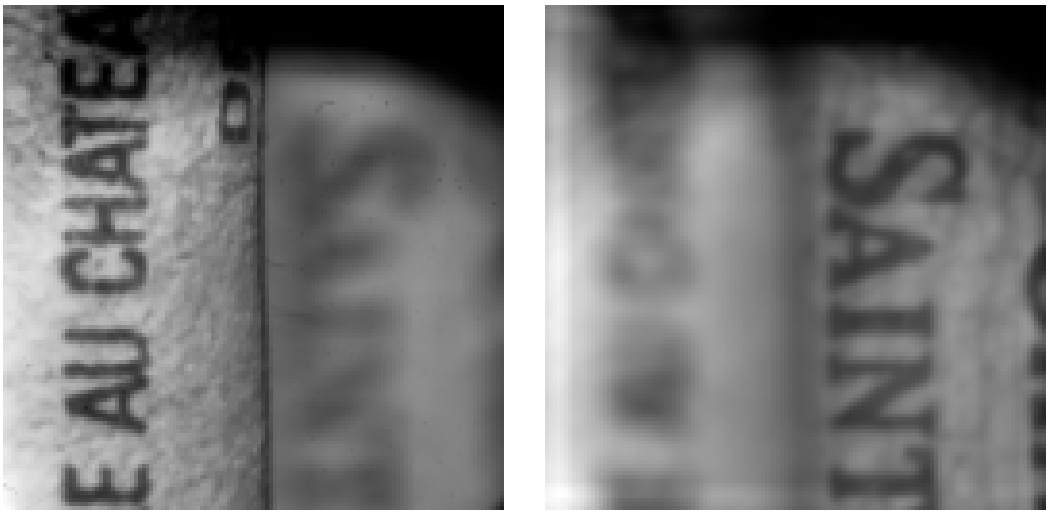

(a) **(b)**

Figure 4.20: (a) Rendered image on the foreground with $\alpha = 1$. (b) Rendered image on the background with $\alpha = 0.88$.

The range of focal depths ($|z_1 - z_1'|$) whereby the exact focusing is estimated by the following relationship:

$$|z_1 - z_1'| = \frac{N_u}{d_1} \Delta s z_1' \tag{4.31}$$

where N_u is the directional resolution, d_1 the diameter of the main lens aperture, Δs the spatial sampling rate. Thus, it follows that the sharpness of refocused photographs is linked to the directional resolution [160].
By merging the only in-focus objects, images with an extended depth of field may be achieved, as it is displayed in Fig. 4.21a and Fig. 4.21b.

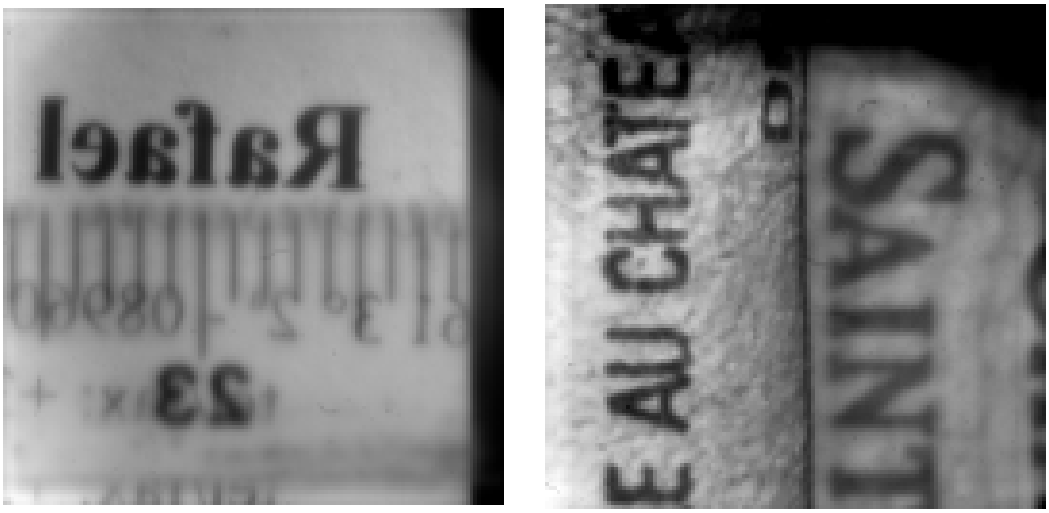

(a) **(b)**

Figure 4.21: (a) Extended depth of field obtained from the average of the images with $\alpha = 1$ and $\alpha = 1.125$. (b) Extended depth of field obtained from the average of the images with $\alpha = 1$ and $\alpha = 0.88$.

4.7 Towards the 3D rendering

Fig. 4.22a is a segmented copy of the image in Fig. 4.20a, where the cork on the foreground is displayed in black and the blurred one on the background in white. A 3D surface plot of this same image is presented in Fig. 4.22b. This view gives the feeling of depth between the elements present on the scene. Both images were obtained by using FIJI open-source.

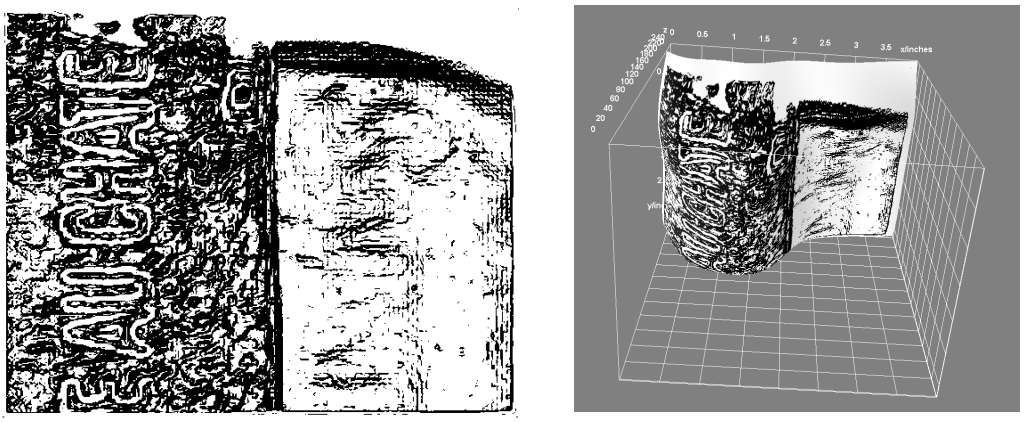

(a) **(b)**

Figure 4.22: (a) Segmented corks. The in-focus cork on the foreground is depicted in black, whereas the out-of-focus cork on the background is visualized in white. (b) 3D surface plot of the light field segmented image in Fig. 4.22a.

By using Volview software, a rough 3D estimation of the two corks was made. This volume rendering was realized by superimposing a stack of segmented refocused slices at different depths. In Fig. 4.23a a frontal view of the two corks is displayed, whereas Fig. 4.23b shows a side perspective from the top. For our system, a voxel is a parallelepiped whose side is given by the depth resolution and the height by the lateral resolution of the camera.

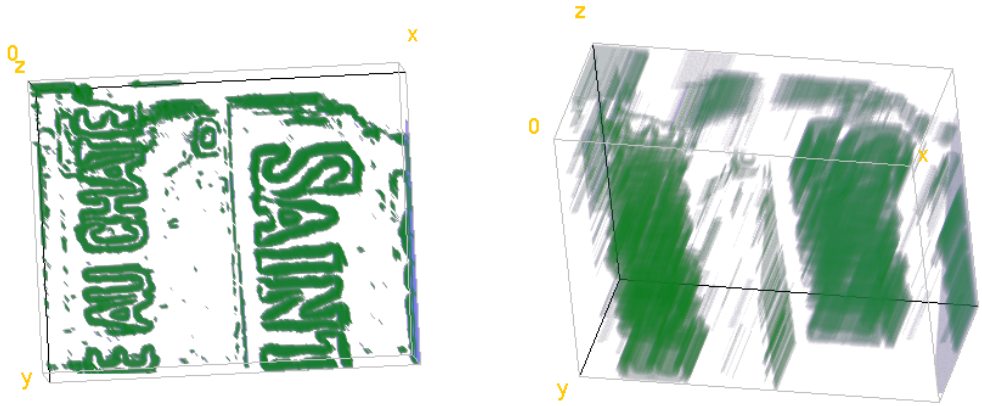

(a) **(b)**

Figure 4.23: (a) Frontal view of the two 3D rendered corks. (b) Lateral view of the two 3D rendered corks.

4.8 Summary

This chapter dealt with the theory of light field camera and shows different tests performed with visible light before its first transposition to the X-rays.
Plenoptic camera (or light field camera) is a special device able to record 3D images in one single exposure. This is achieved thanks to a microlens array placed in front of an image sensor. The combination of the optical elements, main lens and microlens array, allows sampling the directional and spatial components of the light field flowing into the camera. The knowledge of the spatial and angular components of the light field is the strength to retrieve information about the depth that the objects occupy on the scene.
In fact, the camera offers the advantage of virtually changing the focus of a photograph after the picture is taken. By computationally re-sorting the light rays to where they would have ideally terminated, blurred subjects can be brought to focus and sharp objects can be made blurred. Digital refocusing is equivalent to virtually slicing a 3D scene in many paralell planes, whose thickness is equal to the depth resolution of the recorded scene. Thus, a light field camera may produce different images where every subject is in-focus and by combining them, an image with extended depth of field can be obtained.
Furthermore, the camera allows shifting the viewpoint of the photographed 3D

scene. Owing to the many views recorded in a narrow range of angles, the light field camera behavior can be compared to limited angle tomography.
Within this chapter, our light field camera prototype for acquiring light field images was shown. A wide variety of objects were photographed to test the advanced image treatment required by this typology of camera. The mathematical definition of light field was deepened and the multiple properties of the camera were experimentally explored. In particular, a section of the chapter was dedicated to the description of the mathematical algorithm behind digital refocusing.

Chapter 5

Soft X-ray plenoptic camera

In the framework of VOXEL (VOlumetric X-ray Extremely Low dose) project, we developed a soft X-ray plenoptic microscope for cellular imaging at Laboratoire d'Optique Appliquée. Today, the references for biological imaging are in the visible range. A lot of well-estabilished techniques with resolutions down to few nanometers are known, such as confocal microscopy, fluorescence microscopy, transmission electron microscopy (TEM), two-photon microscopy, photo-activated localization microscopy (PALM) and stochastic optical reconstruction microscopy (STORM). All the above-mentioned techniques need multiple views to reconstruct a 3D image. Plenoptic microscope has been demonstrated by Levoy and collaborators opening the way of 3D reconstruction from a single view [150]. Our goal is to further push this work by transposing plenoptic microscope to the soft X-rays for achieving a high-resolution microscope with the plus value offered by plenoptic imaging. This thesis work was oriented to develop a soft X-ray plenoptic microscope, that is a microscope suitable to image cells in the so-called "water window" region. "Water window" is the energy range comprised between the oxygen absorption K-edge (543 eV, 2.3 nm) and the carbon K-edge (284 eV, 4.4 nm) (Fig. 5.1). In this interval, high natural contrasted X-ray images can be achieved as water is transparent and organic materials absorb much more than water [25]; thus, the use of contrast agents is not required.

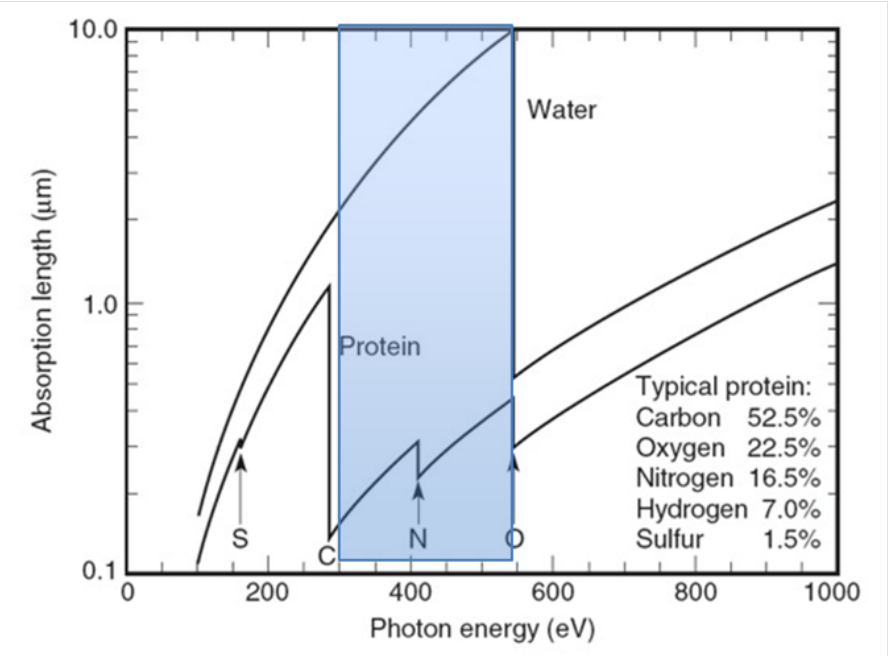

Figure 5.1: Protein and water absorption lengths versus photon energy. The atomic edges of the different components constituting a protein are shown from [2].

Today, the best microscopy images in the "water window" were realized by soft X-ray tomography that is now considered as a benchmark in this domain [171]. In literature there are mentioned several works of soft X-ray tomography that in combination with Fresnel zone plates could achieve extremely high-resolutions, such as 60 *nm* by [172], 50 *nm* by [2, 173] and 10 *nm* by [174]. For instance, Fig. 5.2 shows a orthoslice of a Schizo-saccharomyces pombe with a spatial resolution of 50 *nm* [3, 4]. The accurate discrimination among several cellular components favoured the 3D segmentation and visualization of all the structures, as shown in Fig. 5.2.

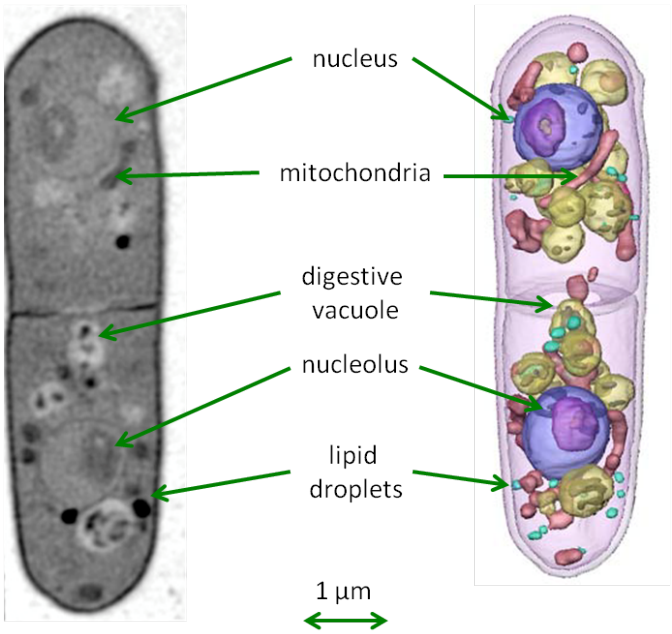

Figure 5.2: Imaging of a Schizo-saccharomyces pombe by soft X-ray tomography. On the left, an orthoslice of the imaged cell. On the right, 3D segmentation of the organelles according to this colour map: nucleus in blue; nucleolus in orange; mitochondria in red; vacuoles in white; lipid-rich vesicles in green. Image from [3, 4].

The main concern related to X-ray tomography is the X-ray dose that is transmitted to samples during the acquisition. Normally, since the X-ray radiation is harmful, cells are cryo-immobilized to prevent damages. If the development of our soft X-ray plenoptic microscope will be sucessful, it will set up an important achievement for cellular imaging. Thanks to the refocusing ability of the camera, 3D images will be obtained ultimately in a single exposure and the technique will be applicable on living cells without having to freeze them [21, 22, 175]. In addition, we are developing a desktop size soft X-ray microscope that represents an attractive and friendly alternative to synchrotrons, as experiments at synchrotron facilities are not of easy accessibility. Furthermore, since soft X-rays revelead to be a good tool for locating metal-labeled proteins in single cells and to study their morphology [176, 177], we believe that our approach will have an important impact for bio-locating theranostic nanoparticles in living cells complementing the work shown in Chapters 2 and 3.
Within this chapter, the design of our soft X-ray plenoptic microscope is shown. Since conventional optics can not be used for the "water window" wavelengths,

it is provided an overview over the available optics for realizing the microscope and our choice of using Fresnel zone plate is discussed. Moreover, the role of each element of the set-up is described.

5.1 Available optics for a soft X-ray plenoptic experiment

5.1.1 Refractive lenses

Refractive lenses are optics commonly used for visible light as they have strong refraction index (n=1.5 to several units for glass); therefore, short focal lengths. For long time they have been considered inappropriate for focusing X-rays, especially soft X-rays, because absorption is strong in this energy range whereas refraction effects are too small. The X-ray refractive index is $n = 1 - \delta + i\beta$ (see Appendix C), with a typical δ comprised between 10^{-3} and 10^{-7}.
In literature, many attempts of building efficient X-ray refractive lenses are reported. Suehiro et al. proposed the use of X-ray refractive lenses made up of high-Z materials [178]. Michette discouraged the use of these lenses for soft X-rays, because absorption is the leading phenomenon in the "water window" region [179]. Conversely, Yang launched the idea of using X-ray refractive lenses for hard X-rays by using low Z-materials [180].
However, as $(1-\delta)$ is minor than 1, the lensmaker equation (5.1) estabilishes that refractive lens, rather than having a convex shape, must have a concave shape to focus X-rays:

$$\frac{1}{f} = (1-n)\frac{2}{R} \tag{5.1}$$

where R is the radius of the lens and n is the real part of refractive index. From here it follows that the focal length, f, is:

$$f = \frac{R}{2\delta} \tag{5.2}$$

Since f is inversely proportional to δ, a single refractive lens has a huge focal length (several meters to hundreds of meters) that makes an experiment unrealizable. A

good practical solution to remedy the absence of adequate optics was found by Snigirev et al. in the energy range 5-40 keV [5]. They proposed the use of a *compound refractive lens* (CRL), that is a linear array of concave lenses consisting of low-Z materials (such as boron, carbon, aluminium, polymers) to minimize the absorption.
A compound refractive lens is usually fabricated by drilling a block material with a series of N holes closely equidistant. Unlike of a single refractive lens, a compound refractive lens has the advantage of producing shorter focal lengths as the final focal distance is inversely proportional to the number of holes, N:

$$f = \frac{R}{2N\delta} \tag{5.3}$$

A schematic drawing illustrating the focusing differences between a single X-ray refractive lens and a compound refractive lens is shown in Fig. 5.3.

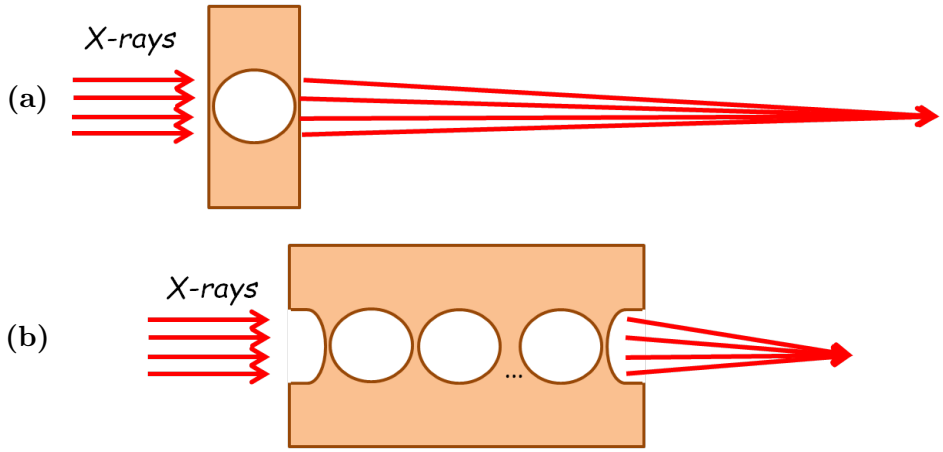

Figure 5.3: Drawing of a compound refractive lens, as illustrated in [5]. (a) An X-ray concave lens having a long focal distance. (b) A compound refractive lens consisting of N holes along the optical axis focusing X-rays at a distance N times shorter than that obtainable by a single X-ray concave lens.

This trade-off seems convincing also in the "water window" region, if a block material made up of beryllium is taken into account. For example, at 500 eV, a refractive lens fabricated in beryllium shows acceptable refractive properties $\delta = 1.46 \times 10^{-3}$ and, if we assume a radius $R = 100\ \mu m$, $f = 3.4\ cm$. So definitely, shorter focal lengths can be achieved by drilling a series of holes in a beryllium

block and thus having an array of lenses. However, the limit of strong absorption in the "water window" by any materials persists. The linear absorption coefficient of a material, μ, influences the calculation of the numerical aperture of a lens, as shown in Equation 5.4 [5]:

$$NA = 2R\left(\frac{2}{\mu RN}\right)^{\frac{1}{2}} \tag{5.4}$$

where

$$\mu = \frac{4\pi\beta}{\rho\lambda} \tag{5.5}$$

Thus, for a single lens made up of beryllium the numerical aperture is very small $NA = 4 \times 10^{-4}$. This disadvantage brought us to exclude the employement of a compound refractive lens for our plenoptic experiment.

5.1.2 Soft X-ray Mirrors

Ordinary mirrors operating at normal angles of incidence do not work with X-rays, as their reflectivity is very small; thus, specific multilayer coating mirrors were developed. They are composed of a stack of alternating layers of two materials having low and high refractive indexes [181]. Typically, the thickness of two consecutive layers, called bilayer, is half of the used wavelength, $\lambda/2$. As consequence, for a wavelength of 4 *nm* (as in the case of "water window"), the resulting thickness is 2 *nm*. This is a technological limit for the design of multilayers. Multilayers reflectivity is influenced by the number of periods and by intrinsic properties, such as absorption and roughness [182]. Today, the best reflectivity is around 25% in the "water window". Microscopes are often composed of two or more mirrors in order to correct the aberrations generated when using a large magnification over a large field of view. With such low reflectivity, even two mirrors will drop the efficiency to about 6%. This goes against our strategy to reduce the dose on the sample. Moreover, mirror shape affects the quality of the final images. Spherical mirrors were excluded *a priori* because they have strong aberration increasing very fast when they are tilted to let the reflected rays go to the detector. Ellipsoidal mirrors are effective to produce high quality images but they are very expensive

with prize reaching easily 50 to 100 of thousands of euro. Ellipsoidal mirrors were also excluded because of their purchase cost.

5.1.3 Fresnel zone plates

Fresnel zone plates are diffractive optics widely used in X-ray microscopy. They consist of several symmetric rings, named zones. Rings are alternately transparent and opaque. Light rays passing through transparent zones constructively interfer at the focus point. The innermost ring defines the first zone. By moving further away from the center, the other zones are numbered in ascendent order. The radius of the r_n zone is given by:

$$r_n{}^2 = n\lambda\Big(f + \frac{n\lambda}{4}\Big) \tag{5.6}$$

where λ is the wavelength, f is the focal length. For zone plates with low numerical aperture, the term $n\lambda/4$ can be neglected if compared to the focal length. Thus, the radius can more simply defined as:

$$r_n{}^2 = n\lambda f \tag{5.7}$$

The total number of zones, N, has important implications on some physical properties such as the resolution of a zone plate w, source bandwith $\Delta\lambda$ and efficiency. In a diffraction-limited optical system, the resolution is given by:

$$w = \frac{\lambda}{2NA} \tag{5.8}$$

where NA is the numerical aperture of the system and it is defined as the sine of the half angle of the cone light reaching the focus point. Thus:

$$w = \frac{\lambda}{2\sin\theta} \tag{5.9}$$

As the alternating zones behave as a diffraction grating with pitch $d = 2\Delta r$, the grating equation can be used:

$$\sin\theta = \frac{\lambda}{d} = \frac{\lambda}{2\Delta r} \tag{5.10}$$

By replacing Eq. 5.10 in Eq. 5.9, it is obtained that the resolution of a zone plate is set by the width of the outermost zone, Δr:

$$w = \Delta r \tag{5.11}$$

The zone plate radius can be directly related to the zone plate resolution through the following relationship:

$$w = \frac{\lambda f}{2r_N} \tag{5.12}$$

As the zone number increases, the width of zone progressively decreases from the center towards the edges. This can be observed following the direction of the red arrow in the TEM image with magnification $\times 8330$ displayed in Fig. 5.4, provided by [6].

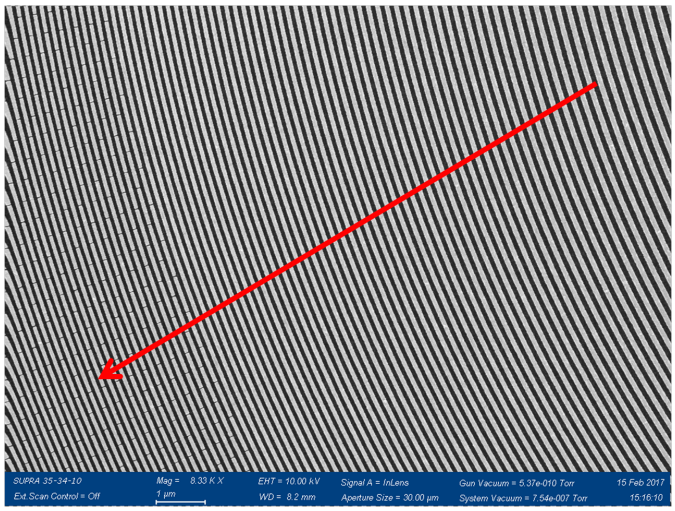

Figure 5.4: TEM image of a Fresnel zone plates made by 4473 lines zones provided by [6]. The image with magnification $\times 8330$ shows that the zones width progressively reduces towards the outer edge.

Nowadays, more and more sophisticated zone plates with very thin outer zone can be fabricated. Currently, the highest resolution available zone plates have a outer diameter below 15 nm[183]. Fresnel zone plates were chosen as the most suitable optics for our soft X-ray miroscope. However, they are very chromatic optics. Their focal length varies according to the selected wavelength:

$$f = \frac{2r_N w}{\lambda} \tag{5.13}$$

where f is the focal length, r_N and w are the radius and the width of the outer zone, respectively. To avoid chromatic blurring, the number of zones (N), must be less than the inverse relative spectral bandwidth $\lambda/\Delta\lambda$:

$$N < \frac{\lambda}{\Delta\lambda} \tag{5.14}$$

where $\Delta\lambda$ is the spectral width of the illuminating radiation [184]. Therefore as it will be shown farther, we needed to use a titanium filter to narrow the soft X-ray radiation and keep the source monochromatic.

5.1.4 Soft X-ray source

We chose to develop a desktop size soft X-ray source emitting radiation in the "water window" spectral range. In principle a solid, liquid or gas target can be employed to produce soft X-ray radiation in this energy range. However, solid targets have the disadvantage of debris production [185, 7] at the risk of damaging the optical system. Liquid-nitrogen based soft X-ray microscopes are known for the achievement of sub-50 nm of spatial resolution with emission at $\lambda = 2.88$ nm [186] and, of sub-60 nm at $\lambda = 2.48$ nm [187]. However, the proceeding for obtaining a liquid nitrogen target is complicated and it requires a constant supply of liquid nitrogen [7]. Another popular liquid target based soft X-ray microscope is that based on ethanol droplets emitting radiation at $\lambda = 2.88$ nm developed by Johansson et al. [188]. This desktop size microscope allowed to capture images with sub-50 nm of spatial resolution albeit with 5 min exposure time for image acquisition. We decided to use a gas puff target for preventing the limitation associated with the employment of a solid target source or a liquid target source. For instance, Wachulak et al. [7] designed a "water window" microscope through a nitrogen double-stream gas puff target source emitting in water window range at the wavelength of $\lambda = 2.88$ nm. In combination with a zone plate lens, their system allowed resolving features down to 60 nm with few seconds of exposure time. Similarly, we decided to develop a soft X-ray source based on nitrogen gas jet target. We generated nitrogen plasma by focusing a Nd:YAG pumping laser

(532 nm laser from SAGA/Thales [189]) with pulses of 5 ns duration, repetition rate 10 Hz and energy of 1 J by an $f = 300$ mm focal length lens onto the nitrogen puff target. Nitrogen jet was regulated by means of a pulse valve (GR020 from Attotech [190] illustrated in Fig. 5.5a) driven by a piezo electric disc that permits of tuning the gas release and the timing. The valve nozzle for the injection of nitrogen gas into the vacuum chamber has a maximum aperture diameter of 0.5 mm. The nozzle opens when a voltage to the piezo electric disc is applied and it may stay open up to a minimum time of 30 μs. The valve can support backing pressures up to 5 bars and it is cooled by a water cooling circuit. Fig. 5.5b displays the plasma generated above the gas valve by the interaction between the green laser and the nitrogen jet.

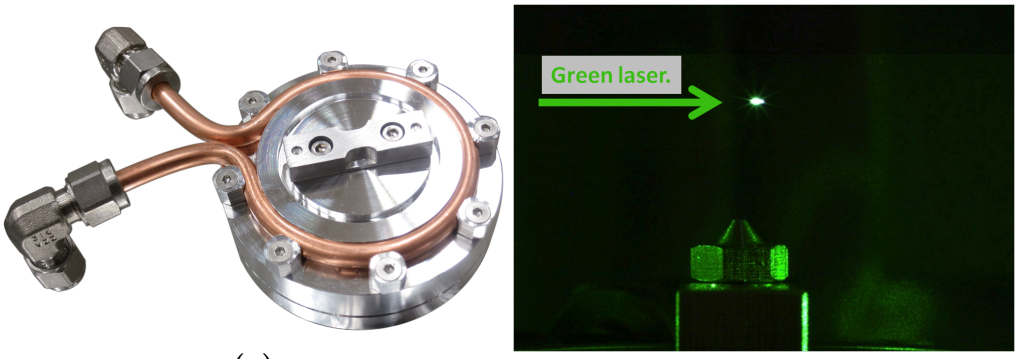

(a) **(b)**

Figure 5.5: (a) Image of the pulsed gas valve. (b) Image showing the plasma laser (white dot) created above the gas pulsed valve.

Finally, the produced soft X-ray radiation is incoherent and polychromatic. Since nitrogen plasma emits radiation in a broad range of wavelengths, including also visible light, a titanium filter was introduced before the sample, as demonstrated by Wachulak et al. [7]. The filter makes the radiation monochromatic, by narrowing the soft X-ray radiation as close as possible to the desired wavelength of $\lambda = 2.88$ nm, where there is a strong emission line from helium-like ions. In detail, we used a titanium filter 200 nm thick with a polyimide membrane, mounted on a circular Al-BA frame supplied by Luxel [191]. Fig. 5.6 shows the nitrogen plasma emission in red dashed line, the filtered nitrogen plasma emission in blue dashed line and, the theoretical transmission of the titanium filter in violet.

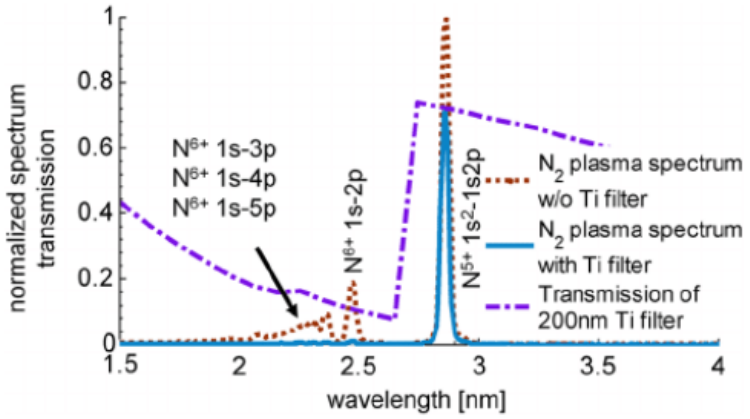

Figure 5.6: Transmission in the water window spectral range for the plasma unfiltered radiation (red dashed line), filtered radiation with the titanium filter (blue dashed line) and theoretical transmission of the titanium filter (violet dashed line) from [7].

5.2 Design of soft X-ray plenoptic camera

In Fig. 5.7 the scheme of the soft X-ray plenoptic microscope we built in Laboratoire d'Optique Appliquée is illustrated. Compared to [7], we introduced in the set-up a microlens array of Fresnel zone plates in front of the detector.

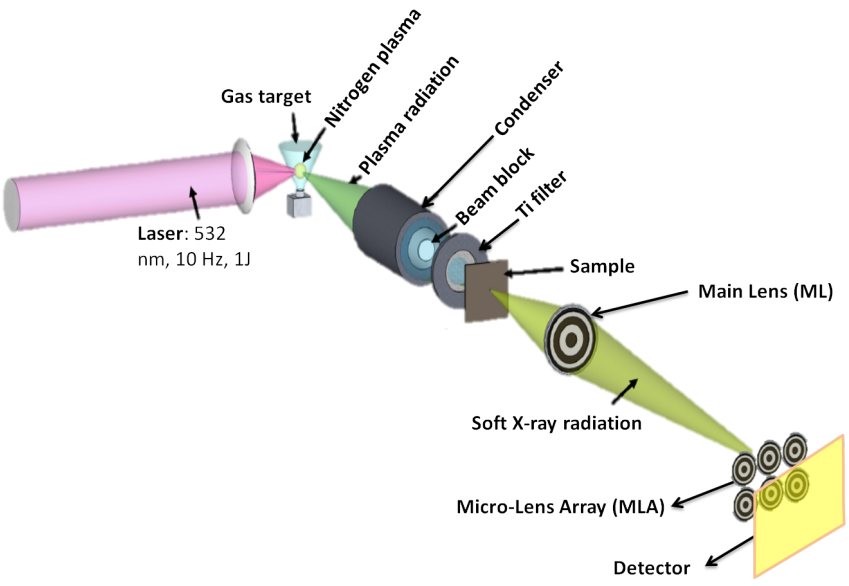

Figure 5.7: Design of the soft X-ray plenoptic camera.

Since a 600 *mm* long vacuum chamber was available, we decided to mount the microscope according to the geometry of the plenoptic camera 1.0 (see Chapter 4). A picture of the empty chamber is shown in Fig. 5.8.

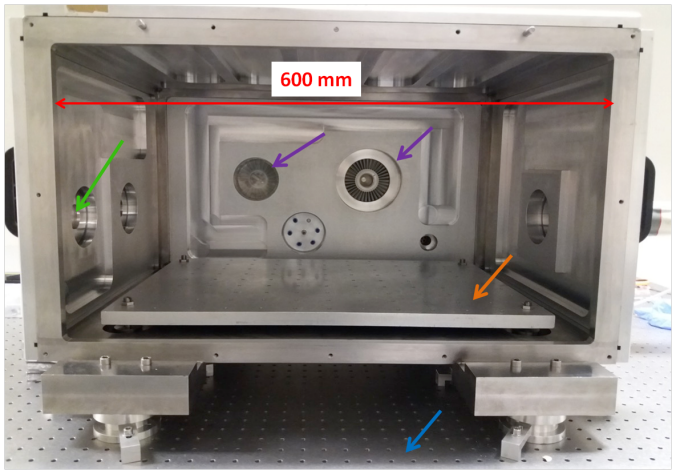

Figure 5.8: Image showing the vacuum chamber used for building the soft X-ray plenoptic microscope. The red arrow shows the length of the camera, the green arrow the entrance window for the green laser, the violet arrows the entrance flange for the turbomolecular pumps. The orange arrows points an additional vacuum breadbord we inserted in the vacum chamber and, the blue arrow the breadbord of the table. This double system ensures a very high dumping of vibrations coming from the pumps and from the floor.

An independent vacuum breadbord was placed into the chamber to hamper vibration and displacement caused by the pumps. The vacuum chamber is placed above an optical table, whose breadbord dumps vibration from the floor.
According to the scheme in Fig. 5.7, the soft X-ray radiation produced following the interaction between the green laser and the nitrogen jet, is collected and focused onto the sample by a condenser mirror. We used an ellipsoidal nickel-coated condenser mirror from Rigaku Innovative Technologies Europe s.r.o. [192]. The highest incidence angle on the inner surface of the condenser is about 2,5°, leading to a reflectivity of about 80% (see Fig. 5.9).

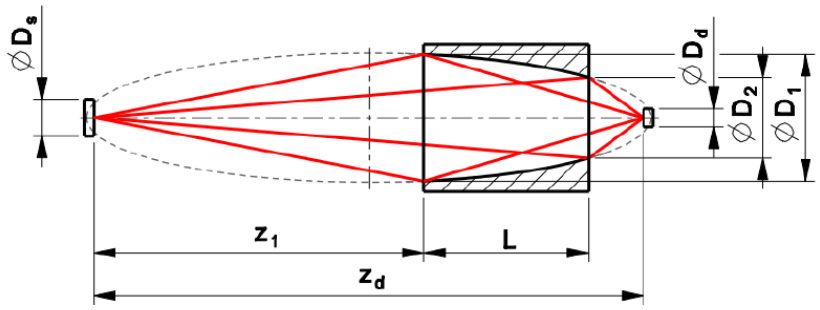

Figure 5.9: Drawing illustrating the features of the condenser.

The condenser has the following features: a length (L) of 60 mm, an entrance diameter (D_1) of 11.5 mm and an exit diameter (D_2) of 9.8 mm. The condenser was designed to have an exit numerical aperture, NA, of 0.1 in order to be equal to NA of the zone plate placed after the sample. The condenser we bought has the following features: source to focus distance (z_d) of 250 mm, and source to entrance aperture distance (z_1) of 130 mm. The scheme showing the condenser features is illustrated in Fig. 5.9, where D_s is the source diameter and D_d the output beam diameter from the condenser. The condenser was tested by the manufacturer with a visible source size of 25 μm and its focal spot is displayed in a 2D and in a 3D map false colours in Fig. 5.10 and 5.10b, respectively.

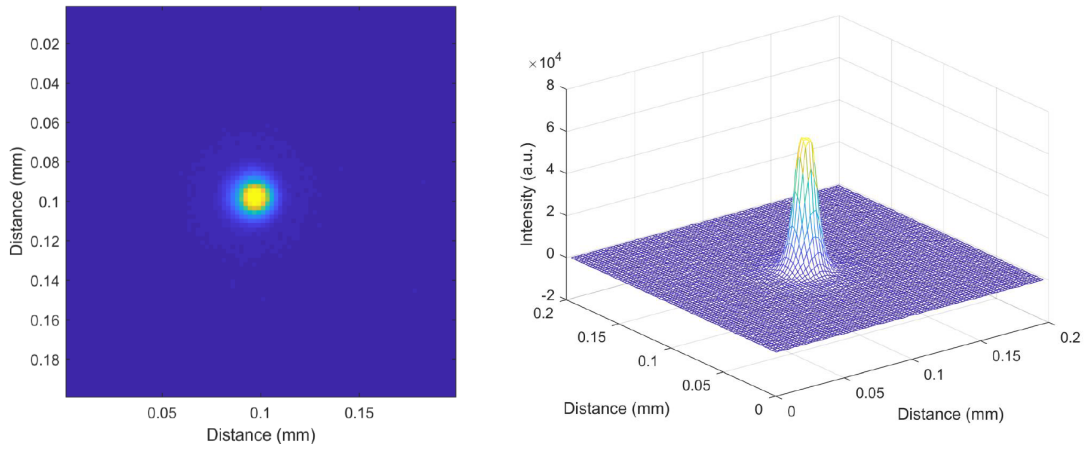

(a) **(b)**

Figure 5.10: (a) 2D image in false colours of the focal spot produced by the condenser from a 25 μm source size. (b) 3D map in false colours of the same focal spot shown in (a). Images provided by the manufacturer.

In Fig. 5.11 it is displayed how the focal spot produced by the condenser changes when the distance z_d is varied.

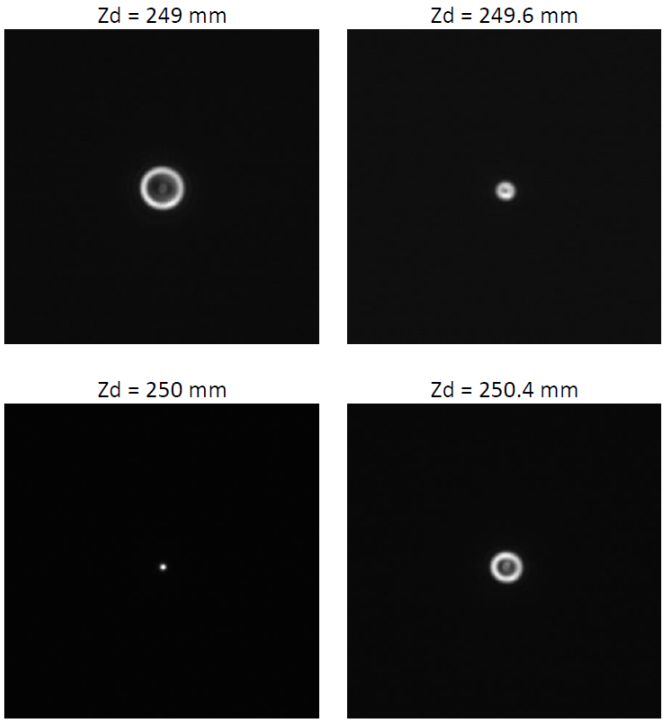

Figure 5.11: Out-of-focus images from a 25 μm source size. Images provided by the manufacturer.

It worths noticing that at distances slightly larger or shorter than $z_d = 250\ mm$ the focal spot is enlarged and it is composed of a series of concentric rings that do not allow a homogeneous shining of the sample. Fig. 5.12 depicts the gas valve and the condenser Rigaku, placed above a translation stage, inside the vacuum chamber. This small useful zone is compatible with the size along the propagation axis of few μm to few 10's μm for biological objects. However, this requires a careful positionning of the sample with a motorized stage. In Fig. 5.12, the preliminary version of the sample holder is mounted on the right of the condeser. It sets on a piezo translation stage for fine adjustment. The full system condenser plus sample is mounted on a translation stage to adjust for the distance source-condenser. Indeed, we felt that the gas jet with all the gas connections is difficult to move under vacuum. Therefore, it is the fix point of the experiment.

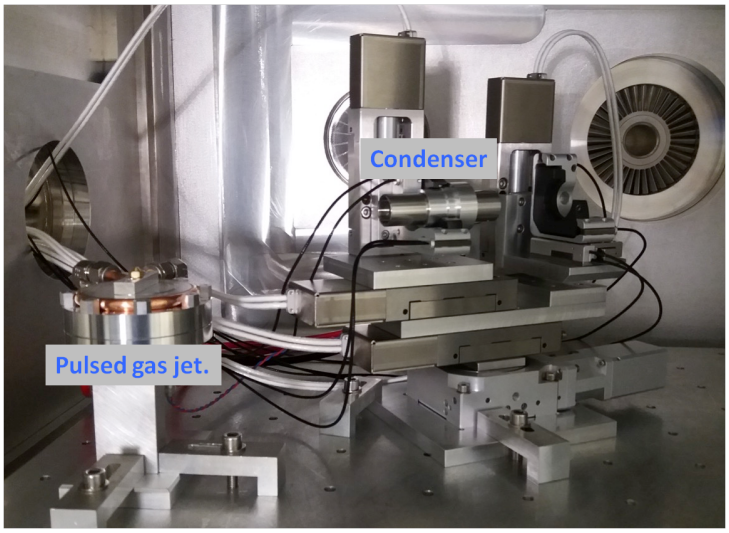

Figure 5.12: Image showing the gas valve and the condenser inside the vacuum chamber. The source to focus distance is equal to 250 *mm*.

Next to the exit diameter of the condenser a beam stopper of 3 *mm* was placed. This element was necessary to block the incoming straight radiation, because a minimum amount of hard X-rays could be generated during the plasma production at the risk of damaging the sample. With the presence of the beam stopper, only the radiation reflected by the walls of the condenser is collected. Moreover, a second stopper with an aperture size of 2 *mm* was fixed at 6 *cm* from the condenser exit to hamper that the remaining straight radiation coming from the space between the condenser and the first stopper could reach the sample. Then, the titanium filter was placed, as shown in Fig. 5.7, in order to produce monochromatic soft X-ray irradiation of the sample. The sample is imaged using as main lens a Fresnel zone plate having 320 μm diameter, with a first ring of 4 μm diameter and an outer zone width equal to 18 *nm*, leading to an intrinsic resolution of 18 *nm*. The Fresnel zone plate is composed of 4473 lines and it has a focal length of 2 *mm*. Fresnel zone plates were custom designed and supplied by Applied Nanotools Inc. [6]. Images of the zone plates are illustrated in Fig. 5.13 and Fig. 5.14. In Fig. 5.13a and 5.13b are shown the TEM images of the zone plate with magnification $\times 240$ and $\times 1340$, respectively.

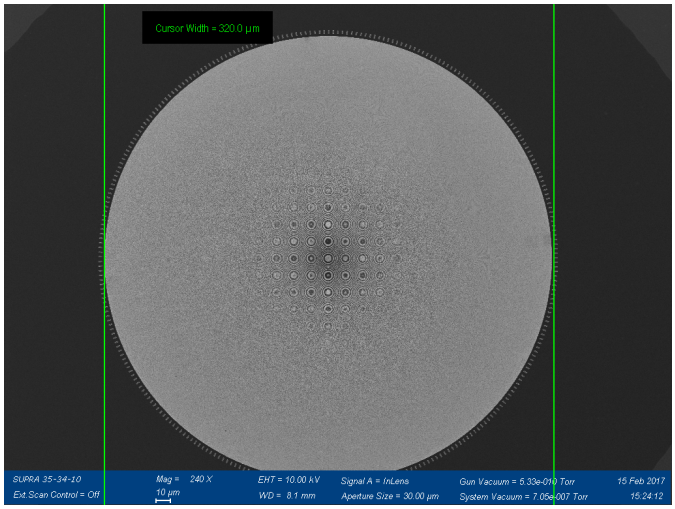

(a)

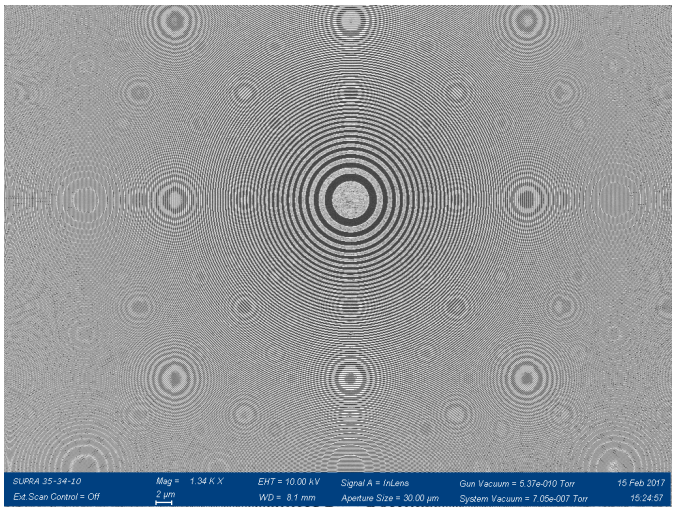

(b)

Figure 5.13: (a) TEM image with magnification ×240 of the zone plate we used as main lens in our plenoptic microscope. (b) TEM image of the same zone plate with magnification ×1340. The presence of many small circles not concentric with the central ring is due to moiré effect and are thus artefacts.

In Fig. 5.14 it is reported a TEM image of the zone plate with magnification ×68500. Thanks to the line profile drawn over the outer transparent zones, it can be seen that the distance bewteen two consecuitive peaks is 36 *nm*. This confirms that the outer zone width is 18 *nm*.

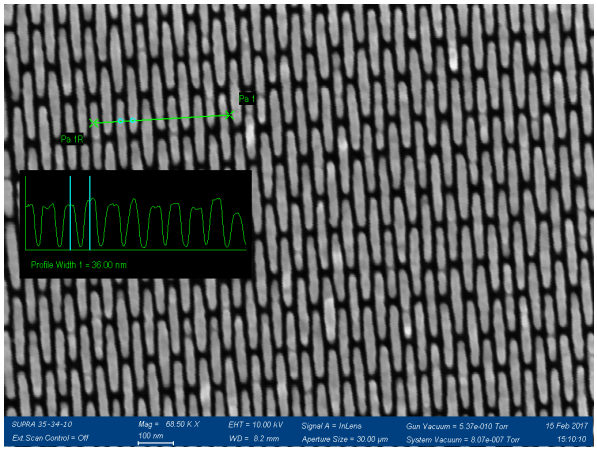

Figure 5.14: TEM image with magnification ×68500 showing that the width of the outer zone is 18 *nm*.

The numerical aperture of the zone plate was designed to match with the exit numerical aperture of the condenser and with the numerical aperture of the array of zone plates (NA= 0.08). To produce an image according to the design of the plenoptic camera 1.0, it was calculated a distance sample-main lens equal to 2.02 *mm*, main lens-microlens array equal to 154 *mm* and microlens array-detector equal to 17.78 *mm*. Fig. 5.15 shows the condenser (blue arrow), the main lens (yellow arrow) and the microlens array (red arrow) inside the vacuum chamber.

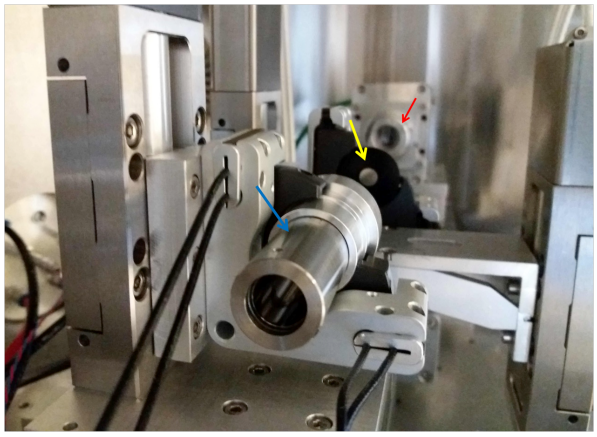

Figure 5.15: Image showing the condenser indicated by the blue arrow, the Fresnel zone plate (i.e. the main lens of the plenoptic camera) indicated by the yellow arrow and the array of Fresnel zone plates (i.e. the microlens array of the plenoptic camera) indicated by a red arrow.

Fig. 5.16a shows a visible microscope image of the array of Fresnel zone plates we bought from Applied Nanotools Inc. [6], while Fig. 5.16b is a SEM image.

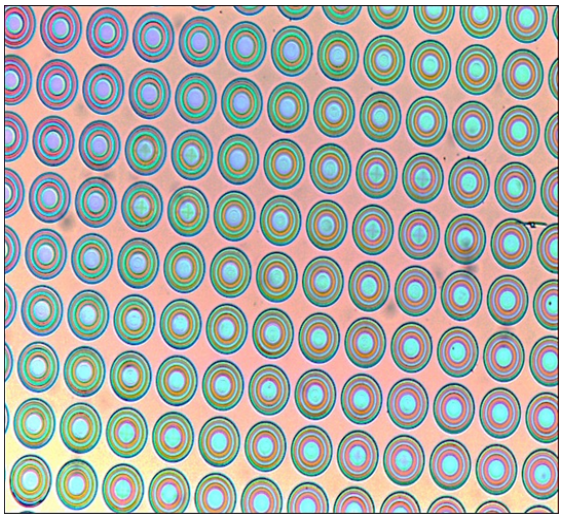

(a)

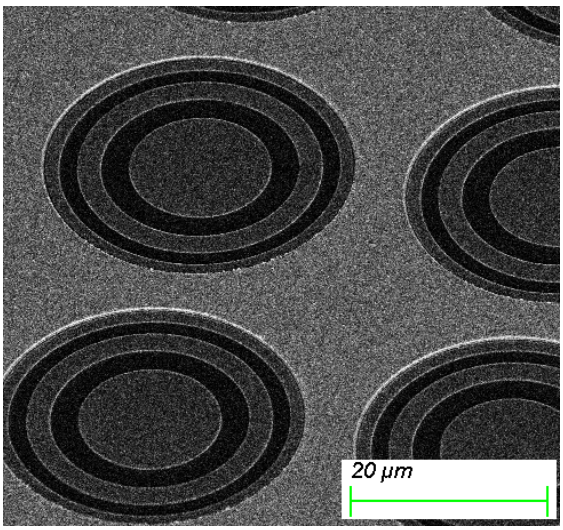

(b)

Figure 5.16: (a) Image showing the custom designed microlens array of Fresnel zone plates. (b) SEM image of the microlens array of Fresnel zone plates provided by the manufacturer.

It is a 170 nm thickness nickel 20×20 zone plate array lens optimized for focusing application at $\lambda = 2.8$ nm with a 300 nm gold blocker layer to minimize the zero-order transmission. The theoretical efficiency of the 1st order is above 11%

and the Si_3N_4 membrane transmission is around 73%, leading to a transmission of 8%. A single zone plate is composed of 5 numbers of lines and it has 17.78 mm focal length, 32 μm diameter and an outer zone width equal to 1.689 μm. The array has 37 μm periodicity. Microlenses were placed on a silicon nitride membrane with thickness equal to 50 nm and the substrate frame has a size of 5 $\times$ 5 mm^2. Finally, the CCD camera was placed behind the array of Fresnel zone plates. We are currently using a back-illuminated CCD camera with 2048 $\times$ 2048 pixels from Princeton Instruments [193]. The CCD is efficient for experiments set with visible light or with soft X-ray radiation, but it has the disadvantage that pixels are relatively big for a plenoptic experiment (pixel size is 13.5 μm).
The completed set-up is illustrated in Fig. 5.17.

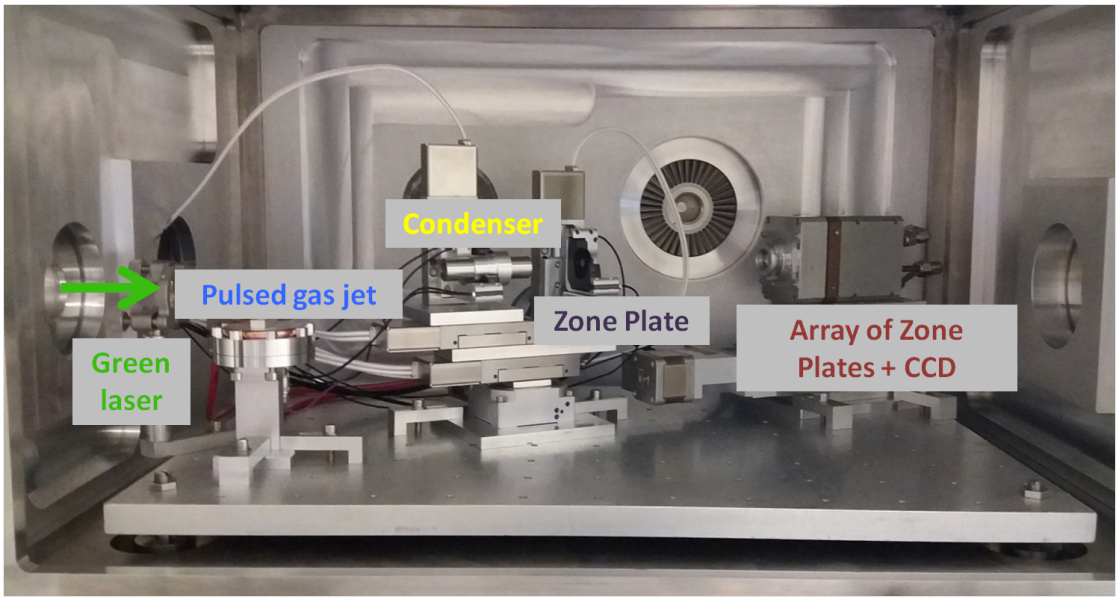

Figure 5.17: Image showing the soft X-ray plenoptic microscope inside the vacuum chamber.

For the first experiment, we still consider using the in-vacuum CCD camera. However, we are developing a system to attain better resolution by downsizing the pixel size. The system tested long time ago at LOA consists in a YAG:Ce crystal that converts the soft X-rays into green light. The crystal emission is thus imaged with a microscope ($\times$10) objective and a visible CCD. We are developing and soon testing a system that can stay under vaccuum without releasing hydrocarbon vapours. This system has a pixel size of about 1 μm. The key parameters of

the system are displayed in the table below. Interestingly, reducing the pixel size by one order of magnitude does not have any effect on the lateral resolution that stays at 488 nm but impacts strongly the number of sampled angles, N_u. This is a crucial parameter for 3D reconstruction. Two parameters may improve the lateral resolution: the NA of the main lens that has to be as large as possible and the diameter of the lenses inside the lens array. For these lenses going from 37 μm to 20 μm the resolution drops from 488 nm to 142 nm.

d1 (um)	Dpx (um)	d2 (µm)	Res lat (nm)	Res depth (um)	FoV (um)	DoFpleno (um)	Nu	Ns	dist tot (mm)
320	13,5	37	488	7	10	17	3	20	174
320	2	37	488	7	10	115	19	20	174
320	1	37	488	7	10	176	28	20	174
320	13,5	37	488	7	10	17	3	20	174
320	13,5	20	142	2	3	3	1	20	304
320	13,5	37	488	7	10	17	3	20	174
600	13,5	37	258	2	5	5	3	20	308

Figure 5.18: Table showing the key values parameters of some elements of the system.

Finally, it is important to remind that all this work has been done with the initial aim of reducing the dose received by the sample. Today, we consider that being able to get an image on a single exposure allows also to keep the sample in normal water while today for tomography the sample is cryogenized. To estimate the dose reduction for this experiment is finally rather simple. Indeed, all the experiment apart of the lens array is classical for soft X-ray tomography. Only the lens array modifies the total throughput. As discussed, this optic has 8% transmission. Considering that a high resolution tomography experiment requires a minimum of 100 views and more generally of 1,000 views, the total required dose should thus be reduced by a factor 8 to 80. This is quite important.

5.3 Conclusions

Within this chapter the soft X-ray plenoptic microscope realized at Laboratoire d'Optique Appliquée was described. The role of each component was introduced and the system is still open to technical improvements to achieve better theoretical resolutions. Firstly, we want to replace the current CCD camera with a crystal coupled to a visible CCD having 1 μm pixel size. The crystal is needed to convert the X-rays into green light and to collect the radiation by a 10× objective microscope. As a second modification, we want to replace the array of zone plates with an array of holes. Also, we want to replace the main lens, i.e. the Fresnel

zone plate, by a spherical mirror and an adaptive optics to emulate a low-cost ellipsoidal mirror.

Conclusions and perspectives

Nanomedicines open new horizons for the treatment of many diseases. Nanodrugs uptake, biodistribution and retention are important criteria that need to be considered during the pre-clinical phase of experimentation in order to get maximum efficiency while limiting any toxicity. Especially, the knowledge of the amount of nanoagents that effectively reached the target and that retained in healthy tissues are of fundamental importance for planning future clinical trials.
Today, numerous in-vitro, ex-vivo and in-vivo studies from cellular scale to full organs are performed to observe nanodrugs behaviour. Microscopy techniques based on the employment of fluorophores show nanocompounds uptake at cellular level. Laser Induced Breakdown Spectroscopy (LIBS) or Transmission Electron Microscopy (TEM) are pseudo-3D techniques that may achieve high-spatial resolutions (down to 10 μm and few tens of nm, respectively), but they require the sectionning of the specimen [16, 1]. Lastly, MRI and PET are routine 3D techniques that provide only macroscopic information, being limited by a spatial resolution of few millimiters in-vivo, and down to sub-100 μm ex-vivo. Thus, it emerges a lack of 3D non-invasive imaging technics in the resolution range between few microns up to few hundreds of microns.
This thesis proposes X-ray Phase-Contrast Tomography (XPCT) as a novel complementary method for bio-localization nanoparticles in tissues at the above mentioned empty scale (1-100's μm). XPCT is a well-established technique for imaging bio-materials in a non-destructive manner; we explored its capacity to detect nanoparticles in tumors, healthy organs and in brains affected by Alzheimer's disease.
However albeit X-ray tomography is a powerful imaging technique, it submits the specimens to a non-negligible X-ray dose radiation, potentially harmful for humans, living animals and cells. For instance, it is reported in literature that at 80 keV, in case of 340 projections, pixel size of 0.35 mm and slice thickness of

0.625 mm, the Computed Tomography Dose Index (CTDI) is estimated equal to 14.8 mGy [194]. Nowadays, there is a strong demand to discover and develop new techniques capable of producing X-ray images at lower doses. In this aim, this thesis also contributed to the development of a new compact soft X-ray camera for low dose cell-imaging in the "water window" region (4-40 nm). The work was focused on the transposition to the X-rays of the so-called plenoptic imaging, that is a 3D imaging technique well-known in visible light for its capacity to capture a 3D scene in a single exposure [23].

In Chapter 1 of this manuscript, the general concepts of X-ray tomography and of the phase-contrast approach were introduced. It was explained how the virtual cross-sections of a specimen can be retrieved from a dataset containing 2D images acquired at many angles. It was also described the processing protocol applied for reconstructing our XPCT data, the main techniques used for reducing some common artefacts and for rendering volume images.

In Chapter 2, the advantageous aspects of XPCT in the visualization of theranostic nanoparticles-loaded tissue were illustrated. Because of their radiosensitization ability, theranostic nanoparticles have become attractive to improve radiotherapy treatments of radioresistent tumors, such as melanoma metastases or lung carcinoma [120, 121]. Several mice organs containing different types of theranostic nanoparticles were investigated at the European Synchrotron Radiation Facility (ESRF Grenoble, France) in the framework of a collaboration between Laboratoire d'Optique Appliquée (Palaiseau, France), Institute for Advanced Biosciences (Grenoble, France), Institut Lumière-Matière (Lyon, France) and CNR-Nanotech (Rome, Italy). Thanks to the high-brightness of synchrotron radiation and to the high-resolution camera (3 μm pixel size), new and unprecedent results were obtained in the imaging of nanoparticles at median scale.
Different pre-clinical problems were examined. Firstly, the results obtained regarding the renal clearance of gadolinium nanoparticles, the hepatic retention of gold nanoclusters and the spleen elimination of platinum nanoparticles were shown. Then, the case of a mouse lung containing nebulized gadolinium nanoparticles was studied. Subsequently, it was reported a study about the repartition intra- and inter-melanoma mouse brain metastases of gadolinium nanoparticles 1 hour after administration, classical time of irradiation. It was found a heterogeneous distri-

bution of the nanoparticles intra- and inter-metastases, according to the location of the metastases in the brain and their size. We believe these new findings will have postive impact for the optimization of radiotherapy protocols. Moreover, it was illustrated XPCT ability in visualizing melanin pigments distribution in an extra-cutaneous melanoma sample. This sounds as a promising result for promoting the XPCT as bio-marker of melanin. Lastly, the preliminary results of the K-edge subtraction approach were shown.

In Chapter 3, the results regarding the use of gadolinium-based nanoparticles to mark amyloid plaques in mice brains model of Alzheimer's disease were displayed. In collaboration with NeuroSpin Laboratory (CEA, Saclay and Grenobe), CNR-Nanotech and Institute for Advanced Biosciences, several mice brains were examined at ESRF under my supervision as Principal Investigator. The goal of the study was understanding the mechanism of diffusion and distribution of nanoparticles, once the blood-brain barrier is permeated through focused ultrasounds.
Several cases were examined throughout the chapter. Firstly, a prototype of a healthy mouse brain was illustrated with the aim of recognizing farther the structural changes that a neurodegenerative disease like Alzheimer's can induce to a brain. Then, it was shown XPCT ability in detecting gadolinium nanoparticles in a healthy brain specimen, following the blood-brain barrier opening by ultrasounds. Then, the images of Alzheimer's model brain without nanoparticles and with functionalized nanoparticles were displayed.

In Chapter 4, the plenoptic technology and its general aspects were described. We built our plenoptic camera system working in the visible domain to test and understand its main properties, such as the multi-viewing and the refocusing.

In Chapter 5, the first model of soft X-ray plenoptic camera that we also named plenoptic microscope was illustrated. The work was directed within an European project called VOXEL (VOlumetric X-ray Extremely Low dose). The structure of the set-up we presented is inspired by the soft X-ray microscope developed by Wachulak and collaborators [7], but it has the novelty of an array of Fresnel zone plates coupled to the detector in order to make the first soft X-ray plenoptic microscope. Within the chapter, the role of each element of the set-up was commented and the choice of the Fresnel zone plates among all the available optics was dis-

cussed. The design of the experiment was challenging, as each optical element had to match the geometrical properties of the plenoptic camera with the Fresnel zone plates features. We ended up that better performances could be achieved by using as main lens a multilayer optic (for instance an elipsoidal mirror or a Schwarzschild), or by tuning the wavelength source in order to fit with a natural crystal.

At the moment XPCT can provide only a qualitative assessment about nanoparticles distribution. As future perspective, we believe that an improvement of the K-edge technique could be helpful to isolate nanoparticles signal from that of surrounding elements. It will allow to provide quantitative information about nanoparticle deposits in tissues and pheraps also to discriminate nanoparticles from amyloid deposits.
VOXEL project is still open and it aims at prototyping soft and hard X-rays plenoptic cameras soon. Today the soft X-ray plenoptic camera is still under test at Laboratoire d'Optique Appliquée, while the hard X-ray plenoptic camera that will be dedicated to small animal imaging is under development at Imagine Optic in Bordeaux, France. With one or few exposures to achieve a 3D image compared to the thousands projections required in X-ray tomography, X-ray plenoptic camera will have a huge impact for bio-medical applications as it would lead to a drastic reduction of the X-ray dose transmitted to specimens.
The first experiment planned for our soft X-ray plenoptic camera will be the biolocalisation of theranostic nanoparticles in cells with 100 nm spatial resolution. In parallel, X-ray nanotomography with synchrotron light will be considered as benchmark for our novel desktop size system.

Appendix A

X-rays matter interaction

Following matter irradiation, three different phenomena can occur: the photoelectric effect, the Compton effect (or incoherent scattering) and the coherent scattering [27].
The photoeletric effect takes place when X-ray photons, of energy greater than the binding energy of an electron, cause the emission of a photo-electron from an inner level of an atom. Subsequently, an electron of an outer-level at higher energy immediately replaces this electron vacancy, thus producing characteristic X-ray radiation. The probability that a photoelectric interaction occurs, P, is inversely proportional to the X-ray energy, E:

$$P \propto E^{-3} \tag{5.15}$$

Therefore, the probability to have photoelectric effect is higher at low X-ray energies. At the same time, the photoelectric effect is also proportional to the cube of the atomic number of the considered material [27]:

$$P \propto Z^3. \tag{5.16}$$

The Compton effect concerns X-ray photons of medium energy, roughly between $30 - 70$ keV. It takes place when the incident radiation colliding with a free electron, or an electron belonging to an outer-level, causes the release of the electron itself. This is called "recoil electron". At the same time, the incoming radiation is scattered between 0° and 180° with a partial loss of its initial energy. Low-energy photons are preferentially backscattered (i.e. they are deflected with an angle larger than 90°), whereas high-energy photons are forward scattered (i.e. they are deflected with an angle smaller than 90°). After a Compton interaction,

most of the energy is held by the deflected photon that could be involved in other collisions before exiting the object. Thus, the absorbed energy by the sample is smaller than that can be absorbed during a photoelectric mechanism, leading to a minor attenuation effect. Compared to photoelectric effect, the probability that a Compton interaction occurs depends only on the electron density of a material, and not on its atomic number.
The third phenomenon is the coherent scattering. During this mechanism, it happens that the incident radiation penetrates the section of an object without interacting with it, but only causing a change of its direction. As it does not activate ionization process, it is less interesting for the interpretation of X-ray medical images [27].
Energy radiation of diagnostic interest is comprised between 20 keV and 140 keV. In this scenario, the photoelectric effect is the most interesting mechanism for medical imaging since it can provide the strongest attenuation.
The graphics in Fig. 5.19 and 5.20 compare the mass attenuation coefficients of photoelectric effect, of the sum of Compton and incoherent scattering and the total sum of these three phenomena as a function of the energy [40].

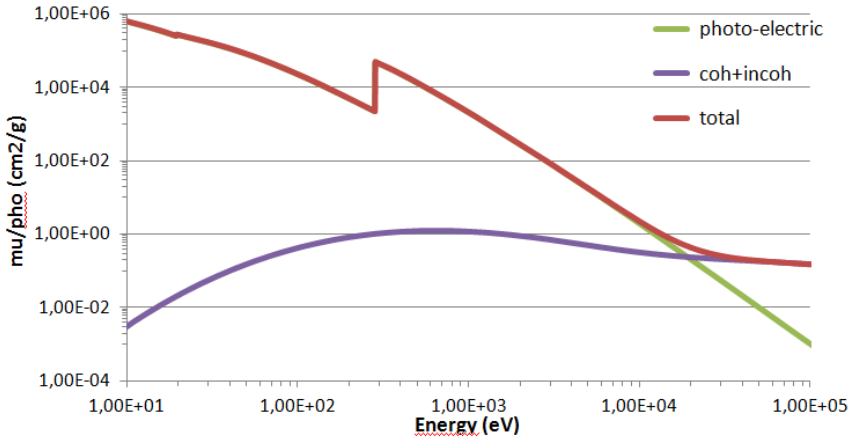

Figure 5.19: Plot of the mass attenuation coefficients for photoelectric, coherent and incoherent scattering and the sum of these three effects as a function of the energy for a mixture of carbon and oxygen.

In detail, the plot in Fig. 5.19 shows the trend for a mixture of carbon and oxygen that are the most representive elements of a biologic tissue, while Fig.

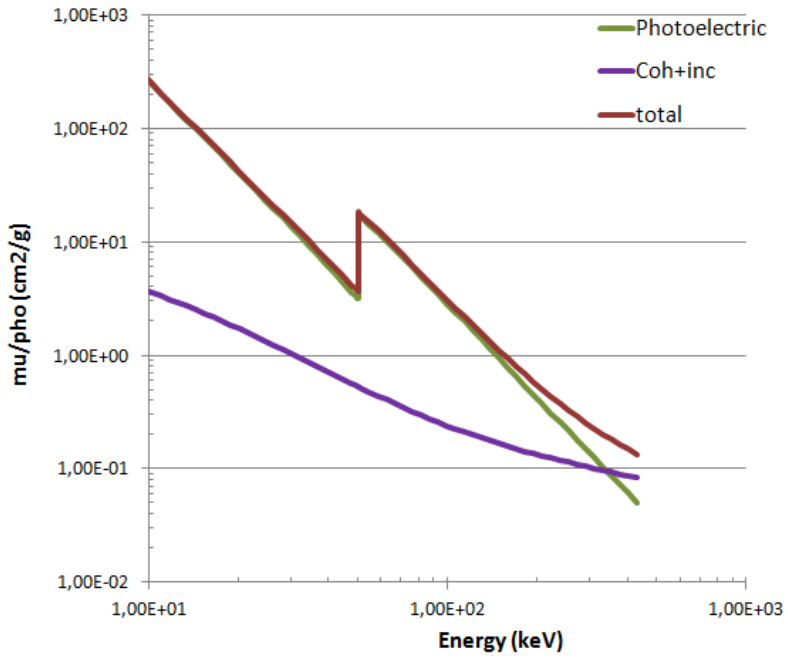

Figure 5.20: Plot of the mass attenuation coefficients for photoelectric, Compton and coherent scattering and the sum of these three effects in function of the energy for gadolinium.

5.20 shows the trend of the mass attenuation coefficients for a high-Z metal, like gadolinium. In both cases photoelectric effect is dominant in respect with the scattering phenomena, especially at low X-ray energies for the mixture carbon/ oxygen simulating the behavior of a soft tissue.

Appendix B

Attenuation law

When X-rays pass through the section of a material, a certain percentage is absorbed. The penetration depth of the radiation, or attenuation, depends on several factors: the selected wavelength and the physical properties of the used material like atomic number, density and thickness. For a monochromatic X-ray beam and an object made up of a single material, the transmitted radiation can be expressed by the Lambert-Beer law:

$$I = I_0 e^{-\frac{\mu L}{\rho}} \tag{5.17}$$

where I_0 is the incident radiation, μ the total linear attenuation coefficient including the contributions of photoelectric and Compton effects, L is the thickness of the material and, ρ its density.
From equation (5.17) it shows that materials with higher values of μ are those more attenuating. The linear attenuation coefficient is linked to the atomic number and density of a material. Attenuation is enhanced for materials made up of elements having high-atomic number, because the probability of photoelectric interaction is proportional to the cube of the atomic number of the considered material (see Eq. 5.16). At the same time, attenuation is also accentuated in case of high density materials because the chance of radiation-matter interaction is higher.
Radiological images are displayed according to a grayscale map varying from black to white. The more attenuating is the imaged object and, the more it looks white, such as bones, teeth, contrast agents based on high-Z elements, nanoparticles. The more the imaged object favours X-ray transmission and more it looks black, such as empty spaces.

Fig. 5.21 compares the mass attenuation coefficients, μ/ρ, in function of the energy of an adipose tissue (orange curve) and of gold (blue curve) that is a heavy metal with Z=79. The values plotted in the graph come from National Institute of Standards and Technology (NIST) [40].

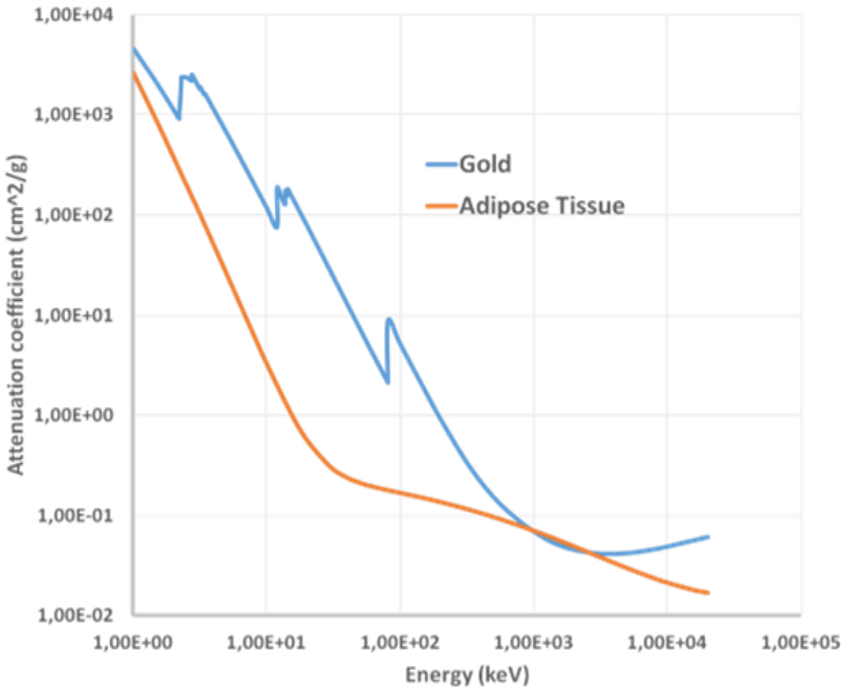

Figure 5.21: Comparison between the mass attenuation coefficients of gold and adipose tissue.

As it can be observed, gold has attenuation values higher than those of adipose tissue. Although the mass attenuation coefficients of both curves tend to dicrease with the increase of the energy, the gold profile shows some discontinuities. They are the gold absorption edges and correspond to the binding energies of the electrons belonging to the M, L and K shells, respectively. The large difference of attenuation lengths between gold and adipose tissue favours the observation of gold-based agents uptaken in biological materials, especially above gold K-edege at 80.72 keV. In fact, at this value the difference in attenuation between gold and adipose tissue is maximum. Thus, high-Z elements like gold appear more opaque than biological materials and, they can be better identified.

Appendix C

Refractive index in the X-ray range

The optical properties of a material are characterized by its refractive index. By definition, "the refractive index of a material is the sum of the forward-scattered radiation from all atoms that interfer with the incoming radiation to produce a modified propagating wave" [25].
Typically for visible light, the refractive index is greater than unit and this is associeted to a low radiation phase-velocity. The opposite occurs for the extreme ultraviolet and X-ray radiation, instead. In this energy range, X-rays propagate in materials at high phase-velocities; thus, the index of refraction is smaller than one.
Following the interaction with short wavelength radiation such as X-rays, absorption is the physical phenomenon that takes over. The total atomic scattering, indicated with $f^0(\omega)$, involves elastic and inelastic processes and is a complex number:

$$f^0(\omega) = f_1^0(\omega) - if_2^0(\omega). \tag{5.18}$$

with ω representing the frequency. Its components $f_1^0(\omega)$ and $f_2^0(\omega)$ are related to the refractive index, n, of a material that, in turn, is a complex number depending on ω.
Therefore, in the X-ray range the refractive index is known as:

$$n(\omega) = 1 - \delta - i\beta, \tag{5.19}$$

where δ, a slight deviation from unity, and β are related to the phase change and

the attenuated radiation intensity coming out of the object, respectively. More precisely, δ and β can be expressed in terms of $f_1^0(\omega)$ and $f_2^0(\omega)$ following:

$$\delta = \frac{n_a r_e \lambda^2}{2\pi} f_1^0(\omega) \tag{5.20}$$

and

$$\beta = \frac{n_a r_e \lambda^2}{2\pi} f_2^0(\omega). \tag{5.21}$$

where λ is the wavelength, n_a the atomic density and, r_e the electron radius. Basically, δ and β may be retrieved by means of phase-shift and absorption measurements, respectively [25]. In fact, β is the physical parameter directly involved in the X-ray absorption tomography measurements, whereas δ in those of XPCT. β might be also expressed as a function of the linear absorption coefficient, μ, defined in appendix B, by:

$$\beta = \frac{\lambda \mu}{4\pi}. \tag{5.22}$$

This equation is interesting to link the value of β with the absorption. Below it is given the real, δ, and imaginary part, β, of the index of refraction for different pure elements contained in brain. For this calculation, the density of the gas (around 10^{-3} g/cc) is used for hydrogen, nitrogen and oxygen that significantly differs from the density of molecules composing the brain (density around 1 g/cc). This explains the difference between carbon and gadolinium on the one hand and hydrogen, nitrogen and oxygen on the other hand.

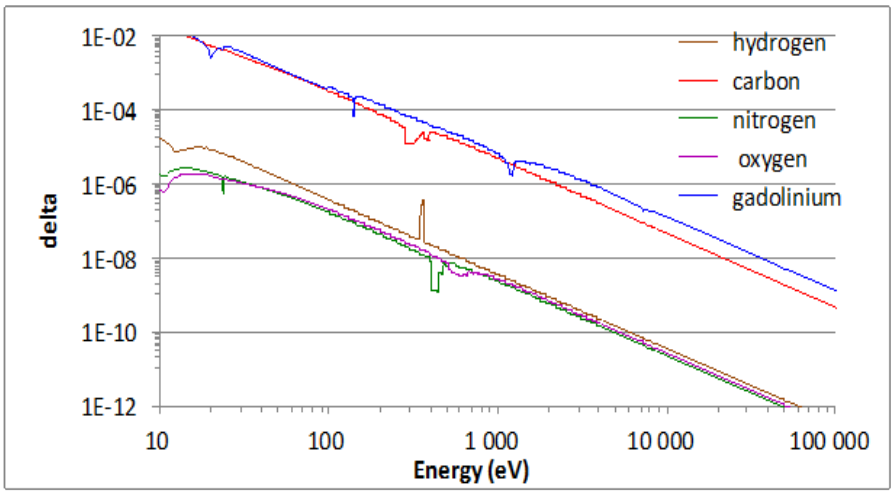

Figure 5.22: Real part of the refractive index (δ) for several pure elements versus photon energy.

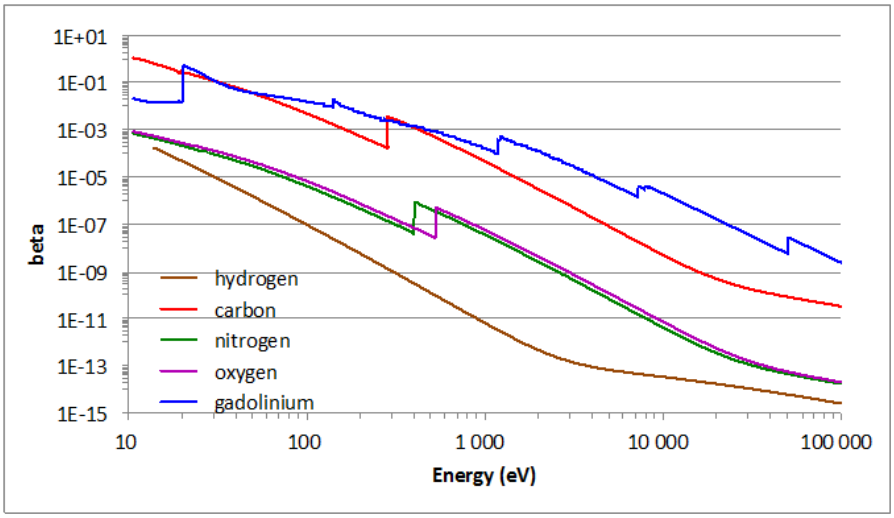

Figure 5.23: Imaginary part of the refractive index (β) for several pure elements versus photon energy.

Appendix D

Anatomical plane

The 3D information obtained with X-ray tomography can be visualized in a slice-by-slice mode. In order to be able to interpret the information contained in a tomographic dataset, a conventional coordinate system allows distinguishing three orthogonal planes in a sample or body (if we refer to medical images):

- Frontal or coronal plane that divides the body into front and back sections;
- Sagittal plane that separates the body into right and left side;
- Axial or transverse plane that divides the body in upper and inferior sectors.

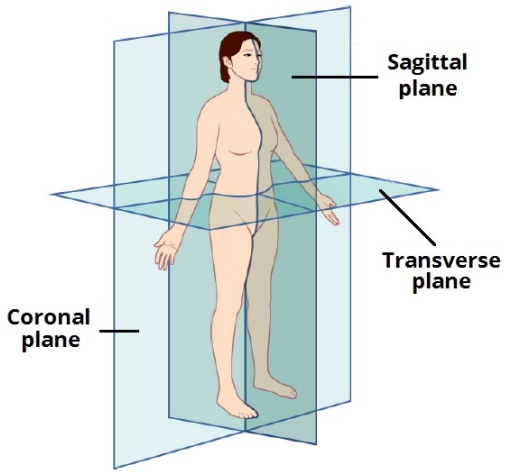

Figure 5.24: Anatomical planes of the human body.

Bibliography

[1] L. Sancey, V. Motto-Ros, B. Busser, S. Kotb, J. Benoit, A. Piednoir, F. Lux, O. Tillement, G. Panczer, and J. Yu, "Laser spectrometry for multi-elemental imaging of biological tissues," *Scientific Reports*, vol. 4, p. 6065, 2014. (Cited in pages VI, 1, 42, 45, 59 and 155.)

[2] M. A. Le Gros, G. McDermott, and C. A. Larabell, "X-ray tomography of whole cells," *Current Opinion in Structural Biology*, vol. 15, no. 5, pp. 593–600, 2005. (Cited in pages XIII, 4 and 134.)

[3] G. McDermott, M. A. Le Gros, C. G. Knoechel, M. Uchida, and C. A. Larabell, "Soft x-ray tomography and cryogenic light microscopy: The cool combination in cellular imaging," *Trends in Cell Biology*, vol. 19, no. 11, pp. 1587–595, 2009. (Cited in pages XIII, 134 and 135.)

[4] C. A. Larabell and K. A. Nugent, "Imaging cellular architecture with x-rays," *Current Opinion in Structural Biology*, vol. 20, no. 5, pp. 623–631, 2010. (Cited in pages XIII, 134 and 135.)

[5] A. Snigirev, V. Kohn, I. Snigireva, and B. Lengeler, "A compound refractive lens for focusing high-energy X-rays," *Nature*, vol. 384, pp. 49–51, 1996. (Cited in pages XIII, 137 and 138.)

[6] "Applied Nanotools Inc.." `https://www.appliednt.com/y`. (Cited in pages XIII, 140, 147 and 150.)

[7] P. W. Wachulak, A. Torrisi, A. Bartnik, D. Adjei, J. Kostecki, L. Wegrzynski, R. Jarocki, M. Szczurek, and H. Fiedorowicz, "Desktop water window microscope using a double-stream gas puff target source," *Appl. Phys. B*, vol. 118, pp. 573–578, 2015. (Cited in pages XIV, 4, 141, 142, 143 and 157.)

[8] L. Bregoli, D. Movia, J. D. Gavigan-Imedio, J. Lysaght, J. Reynolds, and A. Prina-Mello, "Nanomedicine applied to translational oncology: A future perspective on cancer treatment," *Nanomedicine: Nanotechnology, Biology and Medicine*, vol. 12, no. 1, pp. 81–103, 2016. (Cited in page 1.)

[9] J. F. Hainfeld, D. N. Slatkin, and H. M. Smilowitz, "The use of gold nanoparticles to enhance radiotherapy in mice," *Physics in Medicine and Biology*, vol. 49, no. 18, 2004. (Cited in pages 1 and 59.)

[10] G. R. Reddy, M. S. Bhojani, P. McConville, J. Moody, B. A. Moffat, D. E. Hall, G. Kim, Y. E. L. Koo, M. J. Woolliscroft, J. V. Sugai, T. D. Johnson, M. A. Philbert, R. Kopelman, A. Rehemtulla, and B. D. Ross, "Vascular targeted nanoparticles for imaging and treatment of brain tumors," *Clinical Cancer Research*, vol. 12, no. 22, pp. 6677–6686, 2006. (Cited in pages 1 and 59.)

[11] L. Sancey, F. Lux, S. Kotb, S. Roux, S. Dufort, A. Bianchi, Y. Crémillieux, P. Fries, J. L. Coll, C. Rodriguez-Lafrasse, M. Janier, M. Dutreix, M. Barberi-Heyob, F. Boschetti, F. Denat, C. Louis, E. Porcel, S. Lacombe, G. Le Duc, E. Deutsch, J. L. Perfettini, A. Detappe, C. Verry, R. Berbeco, K. T. Butterworth, S. J. McMahon, K. M. Prise, P. Perriat, and O. Tillement, "The use of theranostic gadolinium-based nanoprobes to improve radiotherapy efficacy," *British Journal of Radiology*, vol. 87, no. 1041, pp. 1–15, 2014. (Cited in pages 1 and 85.)

[12] S. Kotb, A. Detappe, F. Lux, F. Appaix, E. L. Barbier, V.-L. Tran, M. Plissonneau, H. Gehan, F. Lefranc, C. Rodriguez-Lafrasse, C. Verry, R. Berbeco, O. Tillement, and L. Sancey, "Gadolinium-Based Nanoparticles and Radiation Therapy for Multiple Brain Melanoma Metastases: Proof of Concept before Phase I Trial.," *Theranostics*, vol. 6, no. 3, pp. 418–427, 2016. (Cited in pages 1 and 44.)

[13] M. F. Kircher, U. Mahmood, R. S. King, M. F. Kircher, U. Mahmood, R. S. King, R. Weissleder, and L. Josephson, "A Multimodal Nanoparticle for Preoperative Magnetic Resonance Imaging and Intraoperative Optical Brain Tumor Delineation Advances in Brief A Multimodal Nanoparticle for Preoperative Magnetic Resonance Imaging and Intraoperative Optical Brain

Tumor Delinea," *Cancer Research*, vol. 63, no. 23, pp. 8122–8125, 2003. (Cited in pages 1 and 43.)

[14] B. Chertok, B. A. Moffat, A. E. David, F. Yu, C. Bergemann, B. D. Ross, and V. C. Yang, "Iron oxide nanoparticles as a drug delivery vehicle for MRI monitored magnetic targeting of brain tumors," *Biomaterials*, vol. 29, no. 4, pp. 487–496, 2008. (Cited in pages 1 and 43.)

[15] H.-Y. Lee, Z. Li, K. Chen, A. R. Hsu, C. Xu, J. Xie, S. Sun, and X. Chen, "PET/MRI Dual-Modality Tumor Imaging Using Arginine-Glycine-Aspartic (RGD)-Conjugated Radiolabeled Iron Oxide Nanoparticles," *Journal of Nuclear Medicine*, vol. 49, no. 8, pp. 1371–1379, 2008. (Cited in pages 1 and 43.)

[16] V. Motto-Ros, L. Sancey, X. C. Wang, Q. L. Ma, F. Lux, X. S. Bai, G. Panczer, O. Tillement, and J. Yu, "Mapping nanoparticles injected into a biological tissue using laser-induced breakdown spectroscopy," *Spectrochimica Acta - Part B Atomic Spectroscopy*, vol. 87, pp. 168–174, 2013. (Cited in pages 1, 42, 45 and 155.)

[17] J. Panyam, S. K. Sahoo, S. Prabha, T. Bargar, and V. Labhasetwar, "Fluorescence and electron microscopy probes for cellular and tissue uptake of poly(D,L-lactide-co-glycolide) nanoparticles," *International Journal of Pharmaceutics*, vol. 262, no. 1-2, pp. 1–11, 2003. (Cited in pages 2 and 42.)

[18] X. Huang, X. Teng, D. Chen, F. Tang, and J. He, "The effect of the shape of mesoporous silica nanoparticles on cellular uptake and cell function," *Biomaterials*, vol. 31, no. 3, pp. 438–448, 2010. (Cited in page 2.)

[19] L. Sancey, S. Kotb, C. Truillet, F. Appaix, A. Marais, E. Thomas, B. Van Der Sanden, J. P. Klein, B. Laurent, M. Cottier, R. Antoine, P. Dugourd, G. Panczer, F. Lux, P. Perriat, V. Motto-Ros, and O. Tillement, "Long-term in Vivo clearance of gadolinium-based AGuIX nanoparticles and their biocompatibility after systemic injection," *ACS Nano*, vol. 9, no. 3, pp. 2477–2488, 2015. (Cited in pages 2, 44, 45 and 47.)

[20] A. Bravin, P. Coan, and P. Suortti, "X-ray phase-contrast imaging: From pre-clinical applications towards clinics," *Physics in Medicine and Biology*, vol. 58, no. 1, 2013. (Cited in pages 2, 15, 16 and 24.)

[21] S. Williams, X. Zhang, C. Jacobsen, d. L. S. Kirz, J. a, J. Van't Hof, and S. S. Lamm, "Measurements of wet metaphase chromosomes in the scanning transmission X-ray microscope," *Journal of Microscopy*, vol. 170, no. 2, pp. 155 – 165, 1993. (Cited in pages 2 and 135.)

[22] P. M. Bennett, G. F. Foster, C. J. Buckey, and R. E. Burge, "The effect of soft X-radiation on myofibrils," *Journal of Microscopy*, vol. 172, no. 2, pp. 109 – 119, 1993. (Cited in pages 2 and 135.)

[23] R. Ng, *Digital light field photography*. PhD thesis, 2006. (Cited in pages 2, 102, 103, 117, 119, 122, 124 and 156.)

[24] R. Magnin, F. Rabusseau, F. Salabartan, S. Mriaux, J.-F. Aubry, D. Le Bihan, E. Dumont, and B. Larrat, "Magnetic resonance-guided motorized transcranial ultrasound system for blood-brain barrier permeabilization along arbitrary trajectories in rodents," *Journal of Therapeutic Ultrasound*, vol. 3, no. 22, 2015. (Cited in page 3.)

[25] D. Attwood, "Soft X-rays and Extreme Ultraviolet Radiation: Principles and Applications," *Cambridge University Press*, 1999. (Cited in pages 4, 133, 165 and 166.)

[26] A. C. Kak and S. Malcolm, "Principles of Computerized Tomographic Imaging," *Society of Industrial and Applied Mathematics*, 2001. (Cited in page 7.)

[27] J. Hsieh, "Computed Tomography: Principles, Design, Artifacts, and Recent Advances ," *SPIE Press*, 2003. (Cited in pages 7, 8, 26, 28, 32, 35, 36, 159 and 160.)

[28] S. Fourmaux, S. Corde, K. Ta Phuoc, P. Lassonde, G. Lebrun, S. Payeur, F. Martin, S. Sebban, V. Malka, A. Rousse, and J. C. Kieffer, "Single shot phase contrast imaging using laser-produced betatron x-ray beams," *Optics Letters*, vol. 36, no. 13, pp. 2426–2428, 2011. (Cited in page 8.)

[29] J. Wenz, S. Schleede, K. Khrennikov, M. Bech, P. Thibault, M. Heigoldt, F. Pfeiffer, and S. Karsch, "Quantitative x-ray phase-contrast microtomography from a compact laser-driven betatron source," *Nature Communications*, vol. 6, no. 7568, 2015. (Cited in page 8.)

[30] A. Döpp, L. Hehn, J. Götzfried, J. Wenz, M. Gilljohann, H. Ding, S. Schindler, F. Pfeiffer, and S. Karsch, "Quick x-ray microtomography using a laser-driven betatron source," *Optica*, vol. 5, no. 2, pp. 199–203, 2018. (Cited in page 8.)

[31] J. Götzfried, A. Döpp, M. Gilljohann, H. Ding, S. Schindler, J. Wenz, L. Hehn, F. Pfeiffer, and S. Karsch, "Research towards high-repetition rate laser-driven X-ray sources for imaging applications," *Nuclear Inst. and Methods in Physics Research, A*, 2018. (Cited in page 8.)

[32] F. Zernike, "How i discovered phase contrast," *Science*, vol. 121, no. 3141, pp. 345–349, 1955. (Cited in page 14.)

[33] D. Gabor, "A new microscopic principle," *Nature*, vol. 161, no. 777, 1948. (Cited in page 14.)

[34] U. Bonse and M. Hart, "An x-ray interferometer," *Applied Physics Letters*, vol. 6, no. 8, pp. 155–156, 1965. (Cited in page 14.)

[35] A. Szöke, "X-ray and electron holography using a local reference beam," *AIP Conference Proceedings*, vol. 147, no. 361, 1986. (Cited in page 14.)

[36] A. Snigirev, I. Snigireva, V. Kohn, S. Kuznetsov, and I. Schelokov, "On the possibilities of x-ray phase contrast by coherent high-energy synchrotron radiation," *Review of Scientific Instruments*, vol. 66, no. 12, pp. 5486–5492, 1995. (Cited in pages 14 and 16.)

[37] S. W. Wilkins, "Phase-contrast imaging using polychromatic hard x-rays," *Nature*, vol. 384, pp. 335–8, 1996. (Cited in pages 14, 16 and 22.)

[38] T. Weitkamp, D. Haas, D. Wegrzynek, and A. Rack, "ANKAphase: Software for single-distance phase retrieval from inline X-ray phase-contrast radiographs," *Journal of Synchrotron Radiation*, vol. 18, no. 4, pp. 617–629, 2011. (Cited in pages 14, 15 and 24.)

[39] S. C. Mayo, A. W. Stevenson, and S. W. Wilkins, "In-Line Phase Contrast X-ray Imaging and Tomography for Material Science," *Materials*, vol. 5, pp. 937–965, 2012. (Cited in page 15.)

[40] "HDF5." `https://physics.nist.gov/PhysRefData/FFast/html/form.html`. (Cited in pages 15, 160 and 164.)

[41] E. Forster, K. Goetz, and P. Zaumseil, "Double crystal diffractometry for the characterization of targets for laser fusion experiments.," *Krist. Tech*, vol. 15, pp. 937–945, 1980. (Cited in page 16.)

[42] T. J. Davis, T. E. Gureyev, D. Gao, and S. Wilkins, "X-ray image contrast from a simple phase-object.," *Phys. Rev.Lett.*, vol. 74, pp. 3173–3176, 1995. (Cited in page 16.)

[43] T. Weitkamp, A. Diaz, C. David, F. Pfeiffer, M. Stampanoni, P. Cloetens, and E. Ziegler, "X-ray phase imaging with a grating interferometer," *Optics Express*, vol. 13, no. 16, p. 6296, 2005. (Cited in page 16.)

[44] F. Pfeiffer, O. Bunk, C. David, M. Bech, G. Le Duc, A. Bravin, and P. Cloetens, "High-resolution brain tumor visualization using three-dimensional x-ray phase contrast tomography," *Physics in Medicine and Biology*, vol. 52, no. 23, pp. 6923–6930, 2007. (Cited in pages 16 and 59.)

[45] A. Olivo and R. Speller, "A coded-aperture technique allowing X-ray phase contrast imaging with laboratory sources.," *Phys. Rev.Lett.*, vol. 91, p. 074106, 2007. (Cited in page 16.)

[46] G. Schmahl, D. Rudolph, G. Schneider, P. Guttman, and B. Niemann, "Phase Contrast X-ray microscopy studies," *Optik*, vol. 97, pp. 181–182, 1994. (Cited in page 16.)

[47] D. Sayre and H. N. Chapman, " X-ray microscopy," *Acta. Cryst.*, vol. A51, pp. 237–252, 1995. (Cited in page 16.)

[48] P. C. Diemoz, C. K. Hagen, M. Endrizzi, and A. Olivo, "Sensitivity of laboratory based implementations of edge illumination X-ray phase-contrast imaging," *Applied Physics Letters*, vol. 103, no. 24, 2013. (Cited in page 16.)

[49] G. R. Myers, T. E. Gureyev, D. M. Paganin, and S. C. Mayo, "The binary dissector: phase contrast tomography of two- and three-material objects from few projections," *Optic Express*, vol. 16, no. 14, p. 10736, 2008. (Cited in pages 20 and 24.)

[50] M. R. Teague, "Deterministic phase retrieval: a Green's function solution," *Journal of the Optical Society of America*, vol. 73, no. 11, p. 1434, 1983. (Cited in pages 20, 21 and 28.)

[51] D. Paganin, S. C. Mayo, T. E. Gureyev, P. R. Miller, and S. W. Wilkins, "Simultaneous phase and amplitude extraction from a single defocused image of a homogeneous object," *Journal of Microscopy*, vol. 206, no. 1, pp. 33–40, 2002. (Cited in pages 20, 21, 24 and 28.)

[52] J. Moosmann, R. Hofmann, and T. Baumbach, "Single-distance phase retrieval at large phase shifts," *Optics Express*, vol. 19, no. 13, p. 12066, 2011. (Cited in pages 20 and 28.)

[53] M. A. Beltran, D. M. Paganin, K. K. W. Siu, A. Fouras, S. B. Hooper, D. H. Reser, and M. J. Kitchen, "Interface-specific x-ray phase retrieval tomography of complex biological organs," *Phys. Med. Biol.*, vol. 56, pp. 7353–7369, 2011. (Cited in page 20.)

[54] A. Pogany, D. Gao, and S. W. Wilkins, "Contrast and resolution in imaging with a microfocus x-ray source," *Review of Scientific Instruments*, vol. 68, no. 7, p. 2774, 1997. (Cited in page 24.)

[55] F. Brun, L. Massimi, M. Fratini, D. Dreossi, F. Billé, A. Accardo, R. Pugliese, and A. Cedola, "SYRMEP Tomo Project: a graphical user interface for customizing CT reconstruction workflows," *Advanced Structural and Chemical Imaging*, vol. 3, no. 1, p. 4, 2017. (Cited in pages 25 and 28.)

[56] W. van Aarle, W. J. Palenstijn, J. De Beenhouwer, T. Altantzis, S. Bals, K. J. Batenburg, and J. Sijbers, "The ASTRA Toolbox: A platform for advanced algorithm development in electron tomography," *Ultramicroscopy*, vol. 157, pp. 35–47, 2015. (Cited in page 25.)

[57] "HDF5." `http://www.hdfgroup.org`. (Cited in page 25.)

[58] F. De Carlo, D. Gürsoy, F. Marone, M. Rivers, D. Y. Parkinson, F. Khan, N. Schwarz, D. J. Vine, S. Vogt, S. C. Gleber, S. Narayanan, M. Newville, T. Lanzirotti, Y. Sun, Y. P. Hong, and C. Jacobsen, "Scientific data exchange: A schema for HDF5-based storage of raw and analyzed data," *Journal of Synchrotron Radiation*, vol. 21, no. 6, pp. 1224–1230, 2014. (Cited in page 25.)

[59] F. E. Boas and D. Fleischmann, "CT artifacts: Causes and reduction techniques," *Imaging Med.*, vol. 4, no. 2, pp. 229–240, 2012. (Cited in pages 26 and 32.)

[60] V. Van Nieuwenhove, J. De Beenhouwer, F. De Carlo, L. Mancini, F. Marone, and J. Sijbers, "Dynamic intensity normalization using eigen flat fields in X-ray imaging," *Optics Express*, vol. 23, no. 21, p. 27975, 2015. (Cited in page 26.)

[61] N. T. Vo, M. Drakopoulos, R. C. Atwood, and C. Reinhard, "Reliable method for calculating the center of rotation in parallel-beam tomography," *Optics Express*, vol. 22, no. 16, p. 19078, 2014. (Cited in page 26.)

[62] C. Raven, "Numerical removal of ring artifacts in microtomography," *Review of Scientific Instruments*, vol. 69, no. 8, pp. 2978–2980, 1998. (Cited in page 27.)

[63] M. Boin and A. Haibel, "Compensation of ring artefacts in synchrotron tomographic images," *Optics Express*, vol. 14, no. 25, p. 12071, 2006. (Cited in page 27.)

[64] B. Münch, P. Trtik, F. Marone, and M. Stampanoni, "Stripe and ring artifact removal with combined wavelet Fourier filtering," *Optic Express*, vol. 17, no. 10, pp. 1844–1856, 2009. (Cited in pages 27, 32 and 33.)

[65] M. Oimoen, "An effective filter for removal of production artifacts in US Geological Survey 7.5-minute digital elevation models," *... of the Fourteenth International Conference on Applied ...*, no. November 2000, pp. 6–8, 2000. (Cited in page 27.)

[66] P. Gilbert, "Iterative methods for the three-dimensional reconstruction of an object from projections," *Journal of Theoretical Biology*, vol. 36, no. 1, pp. 105–117, 1972. (Cited in page 28.)

[67] A. H. Andersen and A. C. Kak, "Simultaneous Algebraic Reconstruction Technique (SART): A superior implementation of the ART algorithm," *Ultrasonic Imaging*, vol. 6, no. 1, pp. 81–94, 1984. (Cited in page 28.)

[68] J. A. Scales, "Tomographic inversion via the conjugate gradient method," *Geophysics*, vol. 52, no. 2, pp. 179–185, 1987. (Cited in page 28.)

[69] J. Miao, F. Förster, and O. Levi, "Equally sloped tomography with oversampling reconstruction," *Phys. Rev. B- Condensed Matter and Materials Physics*, vol. 72, no. 5, p. 052103, 2005. (Cited in page 28.)

[70] D. M. Pelt and K. J. Batenburg, "Improving Filtered Backprojection Reconstruction by Data-Dependent Filtering," *IEEE Transactions on Image Processing*, vol. 23, no. 11, pp. 4750–4762, 2014. (Cited in page 28.)

[71] L. A. Shepp and B. Logan, "The Fourier Reconstruction of a Head Section," *IEEE Transactions on Nuclear Science*, vol. 21, no. 3, pp. 21–43, 1974. (Cited in page 30.)

[72] J. Schindelin and al., "Fiji: an open-source platform for biological- image analysis," *Nature Methods*, vol. 9, no. 7, pp. 676–682, 2012. (Cited in page 30.)

[73] M. S. Nixon and A. S. Aguado, "Feature Extraction and Image Processing," *Academic Press*, p. 88, 2008. (Cited in page 31.)

[74] B. Preim and D. Bartz, "Visualization in Medicine: Theory, Algorithms, and Applications," *The Morgan Kaufmann series in computer graphics*, pp. 137–152, 2007. (Cited in page 38.)

[75] B. Preim and D. Bartz, "Visualization in Medicine: Theory, Algorithms, and Applications," *The Morgan Kaufmann series in computer graphics*, pp. 261–263, 2007. (Cited in page 38.)

[76] K. Yin Win and S. S. Feng, "Effects of particle size and surface coating on cellular uptake of polymeric nanoparticles for oral delivery of anticancer

drugs," *Biomaterials*, vol. 26, no. 15, pp. 2713–2722, 2005. (Cited in page 42.)

[77] T. D. Rane and A. M. Armani, "Two-photon microscopy analysis of gold nanoparticle uptake in 3D cell spheroids," *PLoS ONE*, vol. 11, no. 12, pp. 1–13, 2016. (Cited in page 42.)

[78] H. Lin, S. P. Centeno, L. Su, B. Kenens, S. Rocha, M. Silwa, J. Hofkens, and H. Uji-i, "Mapping of surface-enhanced fluorescence on metal nanoparticles using super-resolution photoactivation localization microscopy," *Chemphyschem*, vol. 13, no. 4, pp. 973 –981, 2012. (Cited in page 42.)

[79] P. Bon, N. Bourg, S. Lécart, S. Monneret, E. Fort, J. Wenger, and S. Lévque-Fort, "Three-dimensional nanometre localization of nanoparticles to enhance super-resolution microscopy," *Nature Communications*, vol. 6, no. 7764, 2015. (Cited in page 42.)

[80] Y. Gimenez, B. Busser, F. Trichard, A. Kulesza, J. M. Laurent, V. Zaun, F. Lux, J. M. Benoit, G. Panczer, P. Dugourd, O. Tillement, F. Pelascini, L. Sancey, and V. Motto-Ros, "3D Imaging of Nanoparticle Distribution in Biological Tissue by Laser-Induced Breakdown Spectroscopy," *Scientific Reports*, vol. 6, no. July, pp. 1–9, 2016. (Cited in page 42.)

[81] A. Vogel and V. Venugopalan, "Mechanisms of Pulsed Laser Ablation of Biological Tissues," *Chem. Rev.*, vol. 103, no. 2, pp. 577–644, 2003. (Cited in page 42.)

[82] M. Fratini, I. Bukreeva, G. Campi, F. Brun, G. Tromba, P. Modregger, D. Bucci, G. Battaglia, R. Spanò, M. Mastrogiacomo, H. Requardt, F. Giove, A. Bravin, and A. Cedola, "Simultaneous submicrometric 3D imaging of the micro-vascular network and the neuronal system in a mouse spinal cord.," *Scientific reports*, vol. 5, p. 8514, 2015. (Cited in page 43.)

[83] B. R. Pinzer, M. Cacquevel, P. Modregger, S. A. McDonald, J. C. Bensadoun, T. Thuering, P. Aebischer, and M. Stampanoni, "Imaging brain amyloid deposition using grating-based differential phase contrast tomography," *NeuroImage*, vol. 61, no. 4, pp. 1336–1346, 2012. (Cited in pages 43, 86 and 92.)

[84] A. Mignot, C. Truillet, F. Lux, L. Sancey, C. Louis, F. Denat, F. Boschetti, L. Bocher, A. Gloter, O. St??phan, R. Antoine, P. Dugourd, D. Luneau, G. Novitchi, L. C. Figueiredo, P. C. De Morais, L. Bonneviot, B. Albela, F. Ribot, L. Van Lokeren, I. Dchamps-Olivier, F. Chuburu, G. Lemercier, C. Villiers, P. N. Marche, G. Le Duc, S. Roux, O. Tillement, and P. Perriat, "A top-down synthesis route to ultrasmall multifunctional Gd-based silica nanoparticles for theranostic applications," *Chemistry - A European Journal*, vol. 19, no. 19, pp. 6122–6136, 2013. (Cited in page 43.)

[85] F. Lux, A. Mignot, P. Mowat, C. Louis, S. Dufort, C. Bernhard, F. Denat, F. Boschetti, C. Brunet, R. Antoine, P. Dugourd, S. Laurent, L. V. Elst, R. Muller, L. Sancey, V. Josserand, J. L. Coll, V. Stupar, E. Barbier, C. Rmy, A. Broisat, C. Ghezzi, G. Le Duc, S. Roux, P. Perriat, and O. Tillement, "Ultrasmall rigid particles as multimodal probes for medical applications," *Angewandte Chemie - International Edition*, vol. 50, no. 51, pp. 12299–12303, 2011. (Cited in pages 43 and 44.)

[86] "NH TherAguixl." `http://nhtheraguix.com/`. (Cited in page 43.)

[87] E. Porret, L. Sancey, A. Martn-Serrano, M. I. Montaez, R. Seeman, A. Yahia-Ammar, H. Okuno, F. Gomez, A. Ariza, N. Hildebrandt, J.-B. Fleury, J.-L. Coll, and X. Le Guével, "Hydrophobicity of gold nanoclusters influences their interactions with biological barriers," *Chemistry of Materials*, vol. 29, no. 17, pp. 7497–7506, 2017. (Cited in page 44.)

[88] X. Le Guevel, M. Henry, V. Motto-Ros, E. Longo, M. I. Montanez, F. Pelascini, O. De la Rochefoucauld, P. Zeitoun, J.-L. Coll, V. Josserand, and L. Sancey, "Elemental and optical imaging evaluation of zwitterionic gold nanoclusters in glioblastoma mouse models," *Nanoscale*, 2018. (Cited in pages 44, 47 and 49.)

[89] "ID17-Biomedical Beamline." `http://www.esrf.eu/UsersAndScience/Experiments/CBS/ID17`. (Cited in page 44.)

[90] A. Mittone, I. Manakov, L. Broche, C. Jarnias, P. Coan, and A. Bravin, "Characterization of a sCMOS-based high-resolution imaging system," *Journal of Synchrotron Radiation*, vol. 24, no. 6, pp. 1226–1236, 2017. (Cited in page 44.)

[91] W. S. Cho, M. Cho, J. Jeong, M. Choi, B. S. Han, H. S. Shin, J. Hong, B. H. Chung, J. Jeong, and M. H. Cho, "Size-dependent tissue kinetics of PEG-coated gold nanoparticles," *Toxicology and Applied Pharmacology*, vol. 245, no. 1, pp. 116–123, 2010. (Cited in page 44.)

[92] S. Dufort, L. Sancey, and J. L. Coll, "Physico-chemical parameters that govern nanoparticles fate also dictate rules for their molecular evolution," *Advanced Drug Delivery Reviews*, vol. 64, no. 2, pp. 179–189, 2012. (Cited in pages 44 and 47.)

[93] S. Han, J. Lee, K. Ahn, Y. Kim, J. Kim, J. Lee, J. Shin, K. Jeon, W. Cho, N. Song, M. Gulumian, B. Shin, and I. Yu, "Size-dependent clearance of gold nanoparticles from lungs of Sprague-Dawley rats after short-term inhalation exposure.," *Arch. Toxicol.*, vol. 89, no. 7, pp. 1083 –1094, 2015. (Cited in page 44.)

[94] J.-L. Bridot, A.-C. Faure, S. Laurent, C. Rivière, C. Billotey, B. Hiba, M. Janier, V. Josserand, J.-L. Coll, L. Vander Elst, R. Muller, S. Roux, P. Perriat, and O. Tillement, "Hybrid gadolinium oxide nanoparticles: multimodal contrast agents for in vivo imaging," *Journal of the American Chemical Society*, vol. 129, no. 16, pp. 5076–5084, 2007. (Cited in page 44.)

[95] D. Kryza, J. Taleb, M. Janier, L. Marmuse, I. Miladi, P. Bonazza, C. Louis, P. Perriat, S. Roux, O. Tillement, and C. Billotey, "Biodistribution study of nanometric hybrid gadolinium oxide particles as a multimodal spect/mr/optical imaging and theragnostic agent," *Bioconjugate Chemistry*, vol. 22, no. 6, pp. 1145–1152, 2011. (Cited in page 44.)

[96] I. Miladi, G. Le Duc, D. Kryza, A. Berniard, P. Mowat, S. Roux, J. Taleb, P. Bonazza, P. Perriat, F. Lux, O. Tillement, C. Billotey, and M. Janier, "Biodistribution of ultra small gadolinium-based nanoparticles as theranostic agent: Application to brain tumors," *Journal of Biomaterials Applications*, vol. 28, no. 3, pp. 385–394. (Cited in page 44.)

[97] A. Bianchi, S. Dufort, F. Lux, A. Courtois, O. Tillement, J.-L. Coll, and Y. Crmillieux, "Quantitative biodistribution and pharmacokinetics of multimodal gadolinium-based nanoparticles for lungs using ultrashort te mri," *Magma*, vol. 27, no. 4, p. 303316, 2014. (Cited in page 44.)

[98] R. R. Arvizo, O. R. Miranda, D. F. Moyano, C. A. Walden, K. Giri, R. Bhattacharya, J. D. Robertson, V. M. Rotello, J. M. Reid, and P. Mukherjee, "Modulating Pharmacokinetics, Tumor Uptake and Biodistribution by Engineered Nanoparticles," *PLOS ONE*, vol. 6, no. 9, pp. 1–6, 2011. (Cited in page 47.)

[99] H. Soo Choi, W. Liu, P. Misra, E. Tanaka, J. P. Zimmer, B. Itty Ipe, M. G. Bawendi, and J. V. Frangioni, "Renal clearance of quantum dots," *Nature Biotechnology*, vol. 25, pp. 1165–1170, 2007. (Cited in page 47.)

[100] J. Liu, M. Yu, C. Zhou, and J. Zheng, "Renal clearable inorganic nanoparticles: a new frontier of bionanotechnology," *Materials Today*, vol. 16, no. 12, pp. 477 – 486, 2013. (Cited in page 47.)

[101] X.-D. Zhang, Z. Luo, J. Chen, S. Song, X. Yuan, X. Shen, H. Wang, Y. Sun, K. Gao, L. Zhang, S. Fan, D. T. Leong, M. Guo, and J. Xie, "Ultrasmall Glutathione-Protected Gold Nanoclusters as Next Generation Radiotherapy Sensitizers with High Tumor Uptake and High Renal Clearance," *Scientific Reports*, vol. 5, no. 8869, 2015. (Cited in page 47.)

[102] E. Longo, A. Bravin, F. Brun, I. Bukreeva, A. Cedola, M. Fratini, X. L. Guevel, L. Massimi, L. Sancey, O. Tillement, P. Zeitoun, and O. de La Rochefoucauld, "3d map of theranostic nanoparticles distribution in mice brain and liver by means of x-ray phase contrast tomography," *Journal of Instrumentation*, vol. 13, no. 1, 2018. (Cited in page 47.)

[103] E. Sadauskas, H. Wallin, M. Stoltenberg, U. Vogel, P. Doering, A. Larsen, and G. Danscher, "Kupffer cells are central in the removal of nanoparticles from the organism," *Particle and Fibre Toxicology*, vol. 4, no. 10, 2007. (Cited in page 48.)

[104] E. Longo, A. Bravin, F. Brun, I. Bukreeva, A. Cedola, O. De La Rochefoucauld, M. Fratini, L. Le Guevel, X. Massimi, L. Sancey, O. Tillement, and P. Zeitoun, "3d imaging of theranostic nanoparticles in mice organs by means of x-ray phase contrast tomography," *Proc.SPIE*, vol. 10573, pp. 10573 – 10577, 2018. (Cited in page 49.)

[105] A. Jemal, M. J. Thun, L. A. G. Ries, H. L. Howe, H. K. Weir, M. M. Center, E. Ward, X.-C. Wu, C. Eheman, R. Anderson, U. A. Ajani, B. Kohler,

and B. K. Edwards, "Annual report to the nation on the status of cancer, 19752005, featuring trends in lung cancer, tobacco use, and tobacco control," *Journal of the National Cancer Institute*, vol. 100, no. 23, pp. 1672–1694, 2008. (Cited in page 55.)

[106] S. Dufort, A. Bianchi, M. Henry, F. Lux, G. Le Duc, V. Josserand, C. Louis, P. Perriat, Y. Cremillieux, O. Tillement, and J. L. Coll, "Nebulized gadolinium-based nanoparticles: A theranostic approach for lung tumor imaging and radiosensitization," *Small*, vol. 11, no. 2, pp. 215–221, 2015. (Cited in pages 55 and 59.)

[107] N. R. Labiris and M. B. Dolovich, "Pulmonary drug delivery. part ii: The role of inhalant delivery devices and drug formulations in therapeutic effectiveness of aerosolized medications," *British Journal of Clinical Pharmacology*, vol. 56, no. 6, pp. 600–612, 2003. (Cited in page 55.)

[108] C. Storti, V. Le Noci, M. Sommariva, E. Tagliabue, A. Balsari, and L. Sfondrini, "Aerosol delivery in the treatment of lung cancer," *Current Cancer Drug Targets*, vol. 15, no. 7, pp. 604–612, 2015. (Cited in page 55.)

[109] J. F. Hainfeld, F. A. Dilmanian, D. N. Slatkin, and H. M. Smilowitz, "Radiotherapy enhancement with gold nanoparticles," *Journal of Pharmacy and Pharmacology*, vol. 60, no. 8, pp. 977–985, 2008. (Cited in pages 55 and 59.)

[110] M.-Y. Chang, A.-L. Shiau, Y.-H. Chen, C.-J. Chang, H. H.-W. Chen, and C.-L. Wu, "Increased apoptotic potential and dose-enhancing effect of gold nanoparticles in combination with single-dose clinical electron beams on tumor-bearing mice," *Cancer Science*, vol. 99, no. 7, pp. 1479–1484, 2008. (Cited in pages 55 and 59.)

[111] E. Porcel, S. Liehn, H. Remita, N. Usami, K. Kobayashi, Y. F. Furusawa, C. Le Sech, and S. Lacombe, "Platinum nanoparticles: a promising material for future cancer therapy?," *Nanotechnology*, vol. 21, no. 8, p. 85103, 2010. (Cited in pages 55 and 59.)

[112] J. Li, Y. Wang, R. Liang, X. An, K. Wang, G. Shen, Y. Tu, J. Zhu, and J. Tao, "Recent advances in targeted nanoparticles drug delivery to melanoma," *Nanomedicine: Nanotechnology, Biology, and Medicine*, vol. 11, no. 3, pp. 769–794, 2015. (Cited in page 58.)

[113] J. Zakrzewski, L. Geraghty, and A. Rose, "Clinical variables and primary tumor characteristics predictive of the development of melanoma brain metastasis and post-brain metastasis survival," vol. 117, no. 8, pp. 1711–1720, 2012. (Cited in page 58.)

[114] A. Sandru, S. Voinea, E. Panaitescu, and A. Blidaru, "Survival rates of patients with malignant melanoma," *Journal of Medicine and Life*, vol. 7, no. 4, pp. 572–576, 2014. (Cited in page 58.)

[115] Partdrige W., "The blood-brain barrier: bottlneck in brain drug development," *NeuroRx*, vol. 2, no. January, pp. 3–14, 2005. (Cited in page 59.)

[116] P. et al., "Postoperative radiotherapy in the treatment of single metastases to the brain: A randomized trial," *JAMA*, vol. 280, pp. 1485–1489, nov 1998. (Cited in page 59.)

[117] M. P. Mehta, P. Rodrigus, C. H. Terhaard, A. Rao, J. Suh, W. Roa, L. Souhami, A. Bezjak, M. Leibenhaut, R. Komaki, C. Schultz, R. Timmerman, W. Curran, J. Smith, S. C. Phan, R. A. Miller, and M. F. Renschler, "Survival and neurologic outcomes in a randomized trial of motexafin gadolinium and whole-brain radiation therapy in brain metastases," *Journal of Clinical Oncology*, vol. 21, no. 13, pp. 2529–2536, 2003. (Cited in page 59.)

[118] P. M. Foreman, B. E. Jackson, K. P. Singh, A. K. Romeo, B. L. Guthrie, W. S. Fisher, K. O. Riley, J. M. Markert, C. D. Willey, M. Bredel, and J. B. Fiveash, "Postoperative radiosurgery for the treatment of metastatic brain tumor: Evaluation of local failure and leptomeningeal disease," *Journal of Clinical Neuroscience*, vol. 49, pp. 48–55, 2018. (Cited in page 59.)

[119] B. J. Blyth and P. J. Sykes, "Radiation-Induced Bystander Effects: What Are They, and How Relevant Are They to Human Radiation Exposures?," *Radiation Research*, vol. 176, no. 2, pp. 139–157, 2011. (Cited in page 59.)

[120] H. Xin, X. Sha, X. Jiang, W. Zhang, L. Chen, and X. Fang, "Anti-glioblastoma efficacy and safety of paclitaxel-loading Angiopep-conjugated dual targeting PEG-PCL nanoparticles," *Biomaterials*, vol. 33, no. 32, pp. 8167–8176, 2012. (Cited in pages 59 and 156.)

[121] Y. Cheng, R. A. Morshed, B. Auffinger, A. L. Tobias, and M. S. Lesniak, "Multifunctional nanoparticles for brain tumor imaging and therapy," *Advanced Drug Delivery Reviews*, vol. 66, pp. 42–57, 2014. (Cited in pages 59 and 156.)

[122] Y. Zheng and L. Sanche, "Gold Nanoparticles Enhance DNA Damage Induced by Anti-cancer Drugs and Radiation," *Radiation Research*, vol. 172, no. 1, pp. 114–119, 2009. (Cited in page 59.)

[123] R. I. Berbeco, H. Korideck, W. Ngwa, R. Kumar, J. Patel, S. Sridhar, S. Johnson, B. D. Price, A. Kimmelman, and G. M. Makrigiorgos, "DNA Damage Enhancement from Gold Nanoparticles for Clinical MV Photon Beams," *Radiation Research*, vol. 178, no. 6, pp. 604–608, 2012. (Cited in page 59.)

[124] C. Sicard-Roselli, E. Brun, M. Gilles, G. Baldacchino, C. Kelsey, H. McQuaid, C. Polin, N. Wardlow, and F. Currell, "A new mechanism for hydroxyl radical production in irradiated nanoparticle solutions," *Small*, vol. 10, no. 16, pp. 3338–3346, 2014. (Cited in page 59.)

[125] P. Mowat, A. Mignot, W. Rima, F. Lux, O. Tillement, C. Roulin, M. Dutreix, D. Bechet, S. Huger, L. Humbert, M. Barberi-Heyob, M. T. Aloy, E. Armandy, C. Rodriguez-Lafrasse, G. Le Duc, S. Roux, and P. Perriat, "In Vitro Radiosensitizing Effects of Ultrasmall Gadolinium Based Particles on Tumour Cells," *Journal of Nanoscience and Nanotechnology*, vol. 11, no. 9, pp. 7833–7839, 2011. (Cited in page 59.)

[126] M. Luchette, H. Korideck, M. Makrigiorgos, O. Tillement, and R. Berbeco, "Radiation dose enhancement of gadolinium-based AGuIX nanoparticles on HeLa cells," *Nanomedicine: Nanotechnology, Biology, and Medicine*, vol. 10, no. 8, pp. 1751–1755, 2014. (Cited in page 59.)

[127] I. Miladi, M. T. Aloy, E. Armandy, P. Mowat, D. Kryza, N. Magné, O. Tillement, F. Lux, C. Billotey, M. Janier, and C. Rodriguez-Lafrasse, "Combining ultrasmall gadolinium-based nanoparticles with photon irradiation overcomes radioresistance of head and neck squamous cell carcinoma," *Nanomedicine: Nanotechnology, Biology, and Medicine*, vol. 11, no. 1, pp. 247–257, 2015. (Cited in page 59.)

[128] H. Yoo, E. Jung, H. S. Gwak, S. H. Shin, and S. H. Lee, "Surgical outcomes of hemorrhagic metastatic brain tumors," *Cancer Research and Treatment*, vol. 43, no. 2, pp. 102–107, 2011. (Cited in page 67.)

[129] "American Cancer Society." `https://cancerstatisticscenter.cancer.org/`. (Cited in page 73.)

[130] D. Rigel, J. Russak, and R. Friedman, "The evolution of melanoma dignosis: 25 years beyond the ABCDs," *Ca Cancer J Clin*, vol. 60, pp. 301–316, 2010. (Cited in page 73.)

[131] B. Bandarchi, L. Ma, R. Navab, A. Seth, and G. Rasty, "From Melanocyte to Metastatic Malignant Melanoma," *Dermatology Research and Practice 2010*, vol. 2010, no. 583748, 2010. (Cited in page 73.)

[132] J. He, N. Wang, H. Tsurui, M. Kato, M. Iida, and T. Kobayashi, "Non-invasive, label-free, three-dimensional imaging of melanoma with confocal photothermal microscopy: Differentiate malignant melanoma from benign tumor tissue," *Scientific Reports*, vol. 6, no. 30209, 2016. (Cited in page 73.)

[133] T. E. Matthews, I. R. Piletic, M. A. Selim, M. J. Simpson, and W. S. Warren, "Pump-Probe Imaging Differentiates Melanoma from Melanocytic Nevi," *Science Translational Medicine*, vol. 3, no. 71, p. 71ra15, 2011. (Cited in page 73.)

[134] B. Zitová and J. Flusser, "Image registration methods: A survey," *Image and Vision Computing*, vol. 21, no. 11, pp. 977–1000, 2003. (Cited in page 76.)

[135] Chinga, G. & Syverud, K., "Quantification of paper mass distributions within local picking areas," *Nordic Pulp and Paper Research Journal*, vol. 22, no. 04, pp. 441–446, 2007. (Cited in page 76.)

[136] H. Braak and K. Del Tredici, "The preclinical phase of the pathological process underlying sporadic Alzheimer's disease," *Brain*, vol. 138, no. 10, pp. 2814–2833, 2015. (Cited in page 85.)

[137] A. Coimbra, D. S. Williams, and E. Hostetler, "The role of MRI and PET/ SPECT in Alzheimer's disease," *Journal of Neuroscience*, vol. 6, no. 6, pp. 629 – 647, 2006. (Cited in page 85.)

[138] L. Mosconi, V. Berti, L. Glodzik, A. Pupi, S. De Santi, and M. J. De Leon, "Pre-Clinical Detection of Alzheimer's Disease Using FDG-PET, with or without Amyloid Imaging," *Journal of Alzheimer's disease*, vol. 20, no. 3, pp. 843 –854, 2010. (Cited in page 85.)

[139] A. Petiet, M. Santin, A. Bertrand, C. J. Wiggins, F. Petit, D. Houitte, P. Hantraye, J. Benavides, T. Debeir, T. Rooney, and M. Dhenain, "Gadolinium-staining reveals amyloid plaques in the brain of Alzheimer's transgenic mice," *Neurobiology of Aging*, vol. 33, no. 8, pp. 1533 – 1544, 2012. (Cited in page 85.)

[140] M. Plissonneau, J. Pansieri, L. Heinrich-Balard, J.-F. Morfin, N. Stransky-Heilkron, P. Rivory, P. Mowat, M. Dumoulin, R. Cohen, r. Allmann, v. Tth, M. J. Saraiva, C. Louis, O. Tillement, V. Forge, F. Lux, and C. Marquette, "Gd-nanoparticles functionalization with specific peptides for -amyloid plaques targeting," *Journal of Nanobiotechnology*, vol. 60, no. 14, 2016. (Cited in page 86.)

[141] J. F. Jordao, E. Thvenot, K. M. Coultes, T. Scarcelli, Y.-Q. Weng, K. Xhima, M. O'Reilly, Y. Huang, J. McLaurin, K. Hynynen, and I. Aubert, "Amyloid-plaque reduction, endogenous antibody delivery and glial activation by brain-targeted, transcranial focused ultrasound," *Experimental Neurology*, vol. 248, pp. 16 – 29, 2013. (Cited in page 86.)

[142] J. H. Viles, "Metal ions and amyloid fiber formation in neurodegenerative diseases. Copper, zinc and iron in Alzheimer's, Parkinson's and prion diseases," *Coordination Chemistry Reviews*, vol. 256, pp. 2271 –2284, 2012. (Cited in page 87.)

[143] H. Rositi, V. Hubert, L. Weber, E. Ong, L. P. Berner, C. Frindel, D. Rousseau, C. Olivier, M. Langer, T. H. Cho, N. Nighoghossian, Y. Berthezéne, F. Peyrin, F. Chauveau, and M. Wiart, "High throughput three-dimensional imaging of myelin fibers in the whole mouse brain," *User-*

Dedicated Microsymposium 2 (UDM2) ESRF user meeting 2017 - Quantitative coherent X-ray diffraction imaging, Feb 2017, Grenoble, France. (Cited in page 89.)

[144] H. Oakley, S. Cole, S. Logan, E. Maus, P. Shao, J. Craft, A. Guillozet-Bongaarts, M. Ohno, J. Disterhoft, L. Van Eldik, R. Berry, and R. Vassar, "Intraneuronal betaamyloid aggregates, neurodegeneration, and neuron loss in transgenic mice with five familial Alzheimer's disease mutations: potential factors in amyloid plaque formation," *Journal of Neuroscience*, vol. 26, pp. 10129 – 10140, 2006. (Cited in page 92.)

[145] S. Jawhar, A. Trawicka, C. Jenneckens, T. Bayer, and O. Wirths, "Motor deficits, neuron loss, and reduced anxiety coinciding with axonal degeneration and intraneuronal AB aggregation in the 5XFAD mouse model of Alzheimer's disease," *Neurobiology of Aging*, vol. 30, no. 1, pp. 196.e29 – 196.e40, 2012. (Cited in page 92.)

[146] T. Dickson and J. Vickers, "The morphological phenotype of -amyloid plaques and associated neuritic changes in Alzheimer's disease," *Neuroscience*, vol. 105, no. 1, pp. 99 – 107, 2001. (Cited in page 92.)

[147] M. D. Meadowcroft, J. R. Connor, M. B. Smith, and Q. X. Yang, "Magnetic resonance imaging and histological analysis of beta-amyloid plaques in both human alzheimer's disease and app/ps1 transgenic mice," *Journal of magnetic resonance imaging: JMRI*, vol. 29, no. 5, pp. 997–1007, 2009. (Cited in page 92.)

[148] M. W. Bourassa, A. C. Leskovjan, R. V. Tappero, E. R. Farquhar, C. A. Colton, W. E. Van Nostrand, and L. M. Miller, "Elevated copper in the amyloid plaques and iron in the cortex are observed in mouse models of alzheimer's disease that exhibit neurodegeneration," *Biomedical spectroscopy and imaging*, vol. 2, no. 2, pp. 129–139, 2013. (Cited in page 96.)

[149] A. C. Kak and M. Slaney, "Principles of Computerized Tomographic Imaging," *IEEE Press.*, 1988. (Cited in page 99.)

[150] M. Levoy, R. Ng, A. Adams, M. Footer, and M. Horowitz, "Light Field Microscopy," *ACM Transactions on Graphics - Proc. SIGGRAPH 2006*, vol. 25, no. 3, p. 825, 2006. (Cited in pages 99, 100, 109, 111 and 133.)

[151] N. Viganò, H. D. Sarkissian, C. Herzog, O. de la Rochefoucauld, R. van Liere, and K. J. Batenburg, "Tomographic approach for the quantitative scene reconstruction from light field images," *Opt. Express*, vol. 26, no. 18, pp. 22574–22602, 2018. (Cited in page 99.)

[152] G. Lippmann, "Épreuves réversibles donnant la sensation du relief," *J. Phys. Theor. Appl.*, vol. 7, no. 1, pp. 821–825, 1908. (Cited in page 100.)

[153] H. Ives, "Parallax Panoramagrams Made With a Large Diameter Lens," *Journal of the Optical Society of America*, vol. 20, no. 6, pp. 332–340, 1930. (Cited in page 100.)

[154] E. H. Adelson and J. R. Bergen, "The plenoptic function and the elements of early vision," *Computational Models of Visual Processing*, pp. 3–20, 1991. (Cited in pages 100 and 101.)

[155] E. H. Adelson and J. Y. A. Wang, "Single Lens Stereo with a Plenoptic Camera," *IEEE Transactions on Pattern Analysis and Machine Intelligence*, vol. 14, no. 2, pp. 99–106, 1992. (Cited in pages 100 and 117.)

[156] M. Levoy and P. Hanrahan, "Light field rendering," *Proceedings of the 23rd annual conference on Computer graphics and interactive techniques - SIGGRAPH '96*, pp. 31–42, 1996. (Cited in pages 100 and 101.)

[157] A. Gershun, "The light field," *J. Math. and Physics*, vol. 18, pp. 51–151, 1936. (Cited in page 100.)

[158] A. Isaksen, L. McMillan, and S. J. Gortler, "Dynamically reparameterized light fields," *Proceedings of the 27th annual conference on Computer graphics and interactive techniques - SIGGRAPH '00*, pp. 297–306, 2000. (Cited in pages 100 and 123.)

[159] M. Levoy, B. Chen, V. Vaish, M. Horowitz, I. McDowall, and M. Bolas, "Synthetic aperture confocal imaging," *ACM Transactions on Graphics*, vol. 23, p. 825, 2004. (Cited in pages 100 and 126.)

[160] R. Ng, "Fourier slice photography," *ACM SIGGRAPH 2005 Papers on - SIGGRAPH '05*, p. 735, 2005. (Cited in pages 100, 102, 117, 120, 122 and 127.)

[161] "Lytro." `https://support.lytro.com/hc/en-us`. (Cited in page 100.)

[162] A. Lumsdaine and T. Georgiev, "The Focused Plenoptic Camera," *2009 IEEE International Conference on Computational Photography (ICCP)*, pp. 1–8, 2009. (Cited in pages 100 and 106.)

[163] "Adobe." `http://lightfield-forum.com/light-field-camera-prototypes/adobe-lightfield-camera-protypes/`. (Cited in page 100.)

[164] "Raytrix." `https://raytrix.de/`. (Cited in page 100.)

[165] E. Y. Lam, "Computational photography with plenoptic camera and light field capture: tutorial," *Journal of the Optical Society of America A*, vol. 32, no. 11, p. 825, 2015. (Cited in pages 101, 103 and 104.)

[166] S. J. Gortler, R. Grzeszczuk, R. Szeliski, and M. F. Cohen, "The Lumigraph," *Siggraph*, pp. 43–54, 1996. (Cited in page 101.)

[167] T. Georgiev and A. Lumsdaine, "Reducing Plenoptic Camera Artefacts," *COMPUTER GRAPHICS forum*, vol. 29, no. 6, pp. 1955–1968, 2010. (Cited in page 106.)

[168] "ImagineOptic." `https://www.imagine-optic.com/`. (Cited in page 112.)

[169] R. Ramamoorthi and P. Hanrahan, "On the relationship between radiance and irradiance: determining the illumination from images of a convex Lambertian object," *Journal of the Optical Society of America A*, vol. 18, pp. 2448–2459, 2001. (Cited in page 122.)

[170] L. Stroebel, J. Compton, J. Current, and R. Zakia, "Photographic Materials and Processes," *Boston: Focal Press*, 1986. (Cited in page 122.)

[171] M. A. Le Gros, G. McDermott, B. P. Cinquin, E. A. Smith, M. Do, W. L. Chao, P. P. Naulleau, and C. A. Larabell, "Biological soft x-ray tomography on beamline 2.1 at the advanced light source," *Journal of microscopy*, vol. 21, no. 6, pp. 1370–1377, 2014. (Cited in page 134.)

[172] C. A. Larabell and T. Le Gros, Mark A. Pollard, "X-ray tomography generates 3-d reconstructions of the yeast, saccharomyces cerevisiae, at 60-nm resolution," *Molecular Biology of the Cell*, vol. 15, no. 3, pp. 957–962, 2004. (Cited in page 134.)

[173] E. A. Smith, B. P. Cinquin, G. McDermott, M. A. Le Gros, D. Y. Parkinson, H. T. Kim, and C. A. Larabell, "Correlative microscopy methods that maximize specimen fidelity and data completeness, and improve molecular localization capabilities," *Journal of Structural Biology*, vol. 184, no. 1, pp. 12 – 20, 2013. (Cited in page 134.)

[174] W. Chao, P. Fischer, T. Tyliszczak, S. Rekawa, E. Anderson, and P. Naulleau, "Real space soft x-ray imaging at 10 nm spatial resolution," *Opt. Express*, vol. 20, no. 9, pp. 9777–9783, 2012. (Cited in page 134.)

[175] J. Kirz, C. Jacobsen, and M. Howells, "Soft x-ray microscopes and their biological applications," *Quarterly Reviews of Biophysics*, vol. 28, no. 1, pp. 33–130, 1995. (Cited in page 135.)

[176] H. N. Chapman, C. Jacobsen, and S. Williams, "A characterisation of dark-field imaging of colloidal gold labels in a scanning transmission x-ray microscope," *Ultramicroscopy*, vol. 62, no. 3, pp. 191 – 213, 1996. (Cited in page 135.)

[177] W. Meyer-llse, D. Hamamoto, A. Nair, S. Lelivre, G. Denbeaux, L. Johnson, A. Pearson, D. Yager, M. Legros, and C. Larabell, "High resolution protein localization using soft x-ray microscopy," *Journal of microscopy*, vol. 201, no. 3, pp. 395 – 403, 2001. (Cited in page 135.)

[178] S. Suehiro, H. Miyaji, and H. Hayashi, "Refractive lens for X-ray focus," *Nature*, vol. 352, pp. 385–386, 1991. (Cited in page 136.)

[179] A. G. Michette, "No X-ray lens," *Nature*, vol. 353, p. 510, 1991. (Cited in page 136.)

[180] B. X. Yang, "Fresnel and refractive lenses for X-ray," *Nucl. Instrum. Methods A*, vol. 328, pp. 578–587, 1993. (Cited in page 136.)

[181] "X-Ray Data Booklet/Section 4.MULTILAYERS AND CRYSTALS." `http://xdb.lbl.gov/Section4/Sec_4-1.html`. (Cited in page 138.)

[182] M. Ishino and O. Yoda, "Fabrication of multilayer mirrors consisting of oxide and nitride layers for continual use across the k-absorption edge of carbon," *Applied Optics*, vol. 43, no. 9, pp. 1849–1855, 2004. (Cited in page 138.)

[183] W. Chao, J. Kim, S. Rekawa, P. Fischer, and E. H. Anderson, "Demonstration of 12 nm Resolution Fresnel Zone Plate Lens based Soft X-ray Microscopy," *Optics Express*, vol. 17, no. 20, pp. 17669–17677, 2009. (Cited in page 140.)

[184] "X-Ray Data Booklet/Section 4.4 ZONE PLATES." `http://xdb.lbl.gov/Section4/Sec_4-4.html`. (Cited in page 141.)

[185] P. W. Wachulak, A. Torrisi, A. Bartnik, H. Fiedorowicz, T. Feigl, R. Jarocki, J. Kostecki, R. Rakowski, P. Rudawski, M. Sawicka, M. Szczurek, A. Szczurek, and Z. Zawadzki, "A compact, quasi-monochromatic laser-plasma EUV source based on a double-stream gas-puff target at 13.8 nm wavelength," *Appl. Phys. B*, vol. 100, no. 3, pp. 461–469, 2010. (Cited in page 141.)

[186] K. W. Kim, Y. Kwon, K. Y. Nam, J. H. Lim, K. G. Kim, K. S. Chon, B. H. Kim, D. E. Kim, J. G. Kim, B. N. Ahn, H. J. Shin, S. Rah, K. H. Kim, J. S. Chae, D. G. Gweon, D. W. Kang, S. H. Kang, J. Y. Min, K. S. Choi, S. E. Yoon, E. A. Kim, Y. Namba, and K. H. Yoon, "Compact soft x-ray transmission microscopy with sub-50 nm spatial resolutiion," *Phys. Med. Biol.*, vol. 51, no. 6, pp. 99–107, 2006. (Cited in page 141.)

[187] P. A. C. Takman, G. A. Stollberg, G. A. Johansson, A. Holmberg, M. Lindblom, and H. M. Hertz, "High-resolution compact X-ray microscopy," *Journal of Microscopy*, vol. 226, no. 2, pp. 175–181, 2007. (Cited in page 141.)

[188] G. A. C. Johansson, A. Holmberg, H. M. Hertz, and M. Berglund, "Design and performance of a laser-plasma-based compact soft x-ray microscope," *Review of Scientific Instruments*, vol. 73, no. 3, pp. 1193–1197, 2002. (Cited in page 141.)

[189] "Thales." `https://www.thalesgroup.com/en/activities/market-specific-solutions/lasers`. (Cited in page 142.)

[190] "ATTOTECH." `http://attotech.se/GR020.html`. (Cited in page 142.)

[191] "Luxel." `https://luxel.com/`. (Cited in page 142.)

[192] "Rigaku." `https://www.rigaku.com/en`. (Cited in page 144.)

[193] "Princeton Instruments." `https://www.princetoninstruments.com/`. (Cited in page 151.)

[194] H. Labriet, C. Nemoz, M. Renier, P. Berkvens, T. Brochard, R. Cassagne, H. Elleaume, F. Estve, C. Verry, J. Balosso, J. F. Adam, and E. Brun, "Significant dose reduction using synchrotron radiation computed tomography: first clinical case and application to high resolution ct exams," *Scientific Reports*, vol. 8, no. 12491, 2018. (Cited in page 156.)

université PARIS-SACLAY | ÉCOLE DOCTORALE Ondes et Matière (EDOM)

Titre : De la tomographie X à la première caméra plénoptique à rayons X pour la bio-localisation des nanoparticules

Mots clés : Tomographie X à contraste de phase, Plénoptique X, Nanoparticules, Fenêtre de l'eau

Résumé : La tomographie par rayons X est une technique d'imagerie non-invasive qui permet de réaliser des images en 3D par l'acquisition de multiples images en 2D. La tomographie X par contraste de phase (XPCT) a été utilisée pour étudier la biodistribution de nanoparticules métalliques (NPs) dans des souris. Ces NPs sont très utilisées comme radiosensibilisants dans la recherche de traitements contre les cancers mais aussi pour marquer des plaques amyloïdes de la maladie d'Alzheimer chez la souris. Grace à la grande brillance du synchrotron ESRF, des images XPCT en haute résolution ont été obtenues et traitées pour produire des modèles en 3D d'organes de souris dopés aux NPs de gadolinium, d'or ou de platine.
En parallèle, dans le cadre du projet Européen VOXEL (Volumetric X-ray Extremely Low dose), un microscope compact à rayons X mous a été développé pour l'imagerie cellulaire. Ce microscope fonctionne dans la « fenêtre de l'eau », une région spectrale pour laquelle un bon contraste de la structure cellulaire est réalisable naturellement. Ce microscope est conçu pour réaliser de l'imagerie plénoptique, une technique actuellement testée uniquement dans le visible. Ce système est composé d'une lentille principale et d'une matrice de micro-lentilles couplée à un détecteur, permettant d'enregistrer les composantes angulaires et spatiales des rayons arrivant au niveau du détecteur. Il est ainsi possible de produire des images en 3D à partir d'une seule exposition. Adapter cette technique disruptive aux rayons X aura, un très grand impact pour les applications biomédicales car cela permettra de réduire fortement la dose absorbée par les échantillons par rapport à la méthode conventionnelle de tomographie X.

Title : From X-ray tomography to the first X-ray plenoptic camera for nanoparticles bio-localization

Keywords : X-ray Phase-Contrast Tomography, X-ray Plenoptic, Nanoparticles, Water Window

Abstract : X-ray tomography is a non-invasive imaging technique that allows producing 3D images following the acquisition of multiple 2D images at many angles. In particular, X-ray Phase-Contrast Tomography (XPCT) has been exploited for resolving the biodistribution of metal-based theranostic nanoparticles (NPs) in mice. These NPs are widely used as radiosensitizers for researches on cancer therapies and, recently to mark amyloid plaques in Alzheimer's disease in mice. Thanks to the high brightness of ESRF synchrotron, high resolution XPCT images were obtained and thus processed for producing 3D models of mice organs doped with gadolinium, gold or platinum NPs.
In parallel, in the framework of a European project, named VOXEL (Volumetric X-ray Extremely Low dose), a compact desktop-size soft X-ray microscope was developed aiming at biological cell imaging. The microscope was designed to be suitable in the so-called "water window" spectral range, where a natural good contrast of the cellular structures is achievable. The microscope was conceived to perform plenoptic imaging, a technology currently tested only in the visible domain. This device is composed of a main lens and a microlens array coupled to a detector, allowing recording the spatial and the angular components of the light rays travelling up to the detector and thus enabling producing 3D images in a single exposure. By adapting this disrupting technology to X-rays, a huge impact for bio-medical applications is foreseen, since it would lead to a drastic decrease of the dose absorbed by samples, compared to traditional X-ray tomography methods.

Université Paris-Saclay
Espace Technologique / Immeuble Discovery
Route de l'Orme aux Merisiers RD 128 / 91190 Saint-Aubin, France